



# **HURRICANE LOSS MITIGATION PROGRAM**

## **2022 ANNUAL REPORT**

*January 1, 2023*

Prepared by  
Florida Division of Emergency Management

Ron DeSantis  
Governor

Kevin Guthrie  
Director

# TABLE OF CONTENTS

Executive Summary.....	3
Background.....	4
Hurricane Loss Mitigation Program Activities.....	6
Hurricane Loss Mitigation Program Analysis.....	8
Hurricane Loss Mitigation Program Goals and Recommendations.....	10
Shelter Retrofit Program Activities.....	11
Shelter Retrofit Program Goals and Recommendations.....	15
Appendix A: FY 2022 Annual Report for Mobile Home Tie Down Program	
Appendix B: FY 2022 Annual Report for Florida International University	

## EXECUTIVE SUMMARY

Pursuant to Subsection 215.559 (6), Florida Statutes (F.S.), this document provides a full report and accounting of activities and evaluation of such activities conducted by the Hurricane Loss Mitigation Program (HLMP). The period covered by this report is July 1, 2021, through June 30, 2022, or State Fiscal Year (FY) 2022. Section 215.559 (1), F.S., establishes the Hurricane Loss Mitigation Program in the Division of Emergency Management (Division). The Division receives an annual appropriation of \$10 million from the investment income of the Florida Hurricane Catastrophe Fund, authorized under the Florida General Appropriation Act and Section 215.555 (7) (c), F.S. The Shelter Retrofit Program, Tallahassee Community College's (TCC) Mobile Home Tie-Down Program, and Florida International University's (FIU) Hurricane Research Program account for a combined \$6.5 million, or sixty-five (65%) percent of the FY 2022 \$10 million appropriation. The remaining thirty-five (35%) percent distributes a community mitigation grant that includes flood and wind mitigation of Florida residences and public outreach and education about retrofits to citizens, local government officials, and their staff.

The Shelter Retrofit Program and TCC's Mobile Home Tie-Down Program have separate reporting requirements under Section 252.385, F.S., and Section 215.559(2)(a), F.S., respectively. This report includes a project analysis of the Shelter Retrofit Program, an annual report for the Tallahassee Mobile Home Tie-Down Program, a detailed summary of FIU's Hurricane Research Program progress, and a programmatic analysis of the Hurricane Loss Mitigation Program.

Section 215.559 was supposed to sunset on June 30, 2022; however, Senator Ed Hooper sponsored bill SB 578 in the 2022 General Session to repeal HLMP's sunset to June 30, 2032. SB 578 was ultimately Laid on Table, and companion bill CS/CS/HB 837 passed. Other than the sunset repeal, the bill transferred the Mobile Home Tie-Down Program from TCC to Gulf Coast State College (GCSC) and expanded the Shelter Retrofit Program to include new construction. This bill is in effect as of July 1, 2022.

## BACKGROUND

In the aftermath of Hurricane Andrew, the Florida Legislature created a series of programs to stabilize the economy and insurance industry. These programs consist of the following:

- Citizens Property Insurance Corporation (formed from a merger of the Florida Windstorm Underwriting Association and the Florida Residential Property and Casualty Joint Underwriting Association), the state insurance plan for residents unable to obtain a conventional homeowner's insurance policy;
- The Florida Hurricane Catastrophe Fund, Section 215.555 F.S., a re-insurance fund established to limit insurance exposure after a storm;
- The Bill Williams Residential Safety and Preparedness Act, which in 1999 created the Hurricane Loss Mitigation Program, Section 215.559 F. S., with an annual appropriation of \$10 million.

Section 215.559 (1), F.S., establishes the Hurricane Loss Mitigation Program in the Division of Emergency Management (Division). The Division receives an annual appropriation of \$10 million from the investment income of the Florida Hurricane Catastrophe Fund authorized under the Florida General Appropriation Act and Section 215.555 (7) (c) F. S. The annual appropriation provides funding to local governments, state agencies, public and private educational institutions, and non-profit organizations to support programs improving hurricane preparedness, reducing potential losses in the event of a hurricane, and providing research and education to reduce hurricane losses.

## **Specific Program Areas and Funding Levels**

**Shelter Retrofits** - Pursuant to Section 215.559(2)(a), F. S., \$3 million of the annual \$10 million appropriation for the Hurricane Loss Mitigation Program directs retrofits to existing facilities to enable them for use as public shelters. An annual report of the state's shelter retrofit program, entitled the Shelter Retrofit Report, is prepared annually and separately submitted to the Governor and the Legislature pursuant to Section 252.385, F.S. The remaining \$7 million of the appropriation is allocated according to different subsections in Section 215.559, F. S., as described below.

**Tallahassee Community College (TCC)** – Pursuant to Section 215.559(2)(a), F. S., TCC receives an annual allocation of \$2.8 million, or forty (40%) percent of the remaining \$7 million. TCC administers these funds and use them to mitigate future losses for mobile homes and to provide tie-downs for mobile homes in communities throughout Florida. See Appendix A for TCC's FY 2022 Annual Report.

**Florida International University (FIU)** – Pursuant to Section 215.559(3), F. S., FIU receives \$700,000, or ten (10%) percent, of the remaining \$7 million. FIU administers these funds and dedicates them to hurricane research at the Type I Center of the State University System to support hurricane loss reduction devices and techniques. See Appendix B for FIU's FY 2022 Final Report.

**Hurricane Loss Mitigation Program (HLMP)** – The remaining \$3.5 million provides grant funding to governmental entities, non-profit organizations, and qualified for-profit organizations as a means to improve the resiliency of residential, community, and government structures within their communities. HLMP advertises funding through a Request for Proposal (RFP), which utilizes a Benefit-Cost Analysis (BCA) for each of the submitted projects to ensure that the recommended mitigation retrofits remain cost-effective.

# Hurricane Loss Mitigation Program

## PROGRAM ACTIVITIES

### **HLMP Funding Distribution -**

In June 2020, the Division issued a Request for Proposal (RFP) for FY 2021 projects. A review panel appointed by the Division selected eligible applicants based on priority, need, benefit, and alignment with local mitigation strategy projects. Based on this evaluation process, 26 projects became eligible for funding. However, due to the limitation of funds, 14 of 26 were awarded.

Instead of posting another RFP for FY 2022, HLMP leadership decided to fund the remaining eligible 12 applicants from FY 2021 for FY 2022, and 11 applicants accepted. These grant recipients are: Banyan Community Health Center, DeSoto County Board of County Commissioners, City of Chattahoochee, Escambia County Board of County Commissioners, City of Bristol, Adopt a Hurricane Family, Inc. dba Crisis Housing Solutions, Emerald Coast Regional Council, City of Flagler Beach, West Palm Beach Housing Authority, City of Edgewater, and City of Panama City. The project agreements have an initial period of performance closeout date of June 30, 2022.

Due to statewide concerns surrounding the COVID-19 pandemic, extensions were granted as needed for December 31, 2022. The extensions were granted due to the halting of many projects and the supply chain bottlenecks of construction equipment and materials.

### **HLMP Outreach –**

Pursuant to Section 215.559, F. S., the Hurricane Loss Mitigation Program was set to expire on June 30, 2022. Outreach efforts were limited due to the statute expiration and mainly focused on the FloridaDisaster.org website for public outreach. This site provides citizens and potential recipients with all the information and forms needed to apply to the HLMP program. It also includes an additional hurricane retrofit guide to help citizens make informed decisions on preparing their homes for potentially hazardous weather.

## **Program Management -**

HLMP is working toward adopting processes that have proven success in the Mitigation Bureau's federal grant programs. HLMP project and grant management training programs are continuously evolving to include the best practices experienced by the state-funded grant program and federal grant management programs. Additionally, custom scope templates have been designed for the various newly permissible mitigation project types that HLMP manages. These new scopes are Florida-specific, project-specific, and provide explicit instruction on the compliance requirements set forth by the State of Florida, the Division of Emergency Management, and the Bureau of Mitigation.

## PROGRAM ANALYSIS

### FY 2022 Recipients

Figure 1.1 shows the awards and amounts spent to date for FY 2022. Due to supply chain issues, many of these projects were extended to December 31, 2022. Due to these extensions, the current amount spent is much lower than in previous years. All currently active projects are proceeding on schedule and are projected to close with most, if not all, funds spent.

Recipient	Award Amount	Spent to Date	Project Type
DEM-HL00040 Banyan Community Health Center, Inc.	\$ 194,000.00	\$ 87,891.80	Commerical Wind Mitigation
DEM-HL00049 DeSoto County Board of County Commissioners	\$ 194,000.00	\$ -	Public Building Wind Mitigation
DEM-HL00050 City of Chattahoochee	\$ 194,000.00	\$ -	Residential Wind Mitigation
DEM-HL00051 Escambia County Board of County Commissioners	\$ 194,000.00	\$ 60,000.00	Residential Wind Mitigation
DEM-HL00052 City of Bristol	\$ 194,000.00	\$ -	Residential Wind Mitigation
DEM-HL00053 Adopt a Hurricane Family, Inc. dba Crisis Housing Solutions	\$ 194,000.00	\$ 24,050.00	Residential Wind Mitigation
DEM-HL00054 Emerald Coast Regional Council	\$ 194,000.00	\$ 31,475.70	Residential Wind Mitigation
DEM-HL00055 City of Flagler Beach (WITHDRAWN)	\$ 194,000.00	\$ 3,156.05	Public Building Wind Mitigation
DEM-HL00056 West Palm Beach Housing Authority	\$ 194,000.00	\$ 154,472.67	Residential Wind Mitigation
DEM-HL00057 City of Edgewater	\$ 194,000.00	\$ -	Public Building Wind Mitigation
DEM-HL00058 City of Panama City	\$ 194,000.00	\$ -	Residential Wind Mitigation
<b>Total</b>	<b>\$ 2,134,000.00</b>	<b>\$ 361,046.22</b>	

Figure 1.1

### Benefit-Cost Analysis

Figure 1.2 shows the Benefit-Cost Analysis (BCA) on FY 2022 projects.

Recipient	BCA Benefits	Cost	Return on Investment
DEM-HL00040 Banyan Community Health Center, Inc.	\$ 650,544.00	\$ 256,685.00	153.44%
DEM-HL00049 DeSoto County Board of County Commissioners	\$ 52,304.00	\$ 45,749.00	14.33%
DEM-HL00050 City of Chattahoochee	\$ 212,933.00	\$ 116,270.00	83.14%
DEM-HL00051 Escambia County Board of County Commissioners	\$ 212,933.00	\$ 116,270.00	83.14%
DEM-HL00052 City of Bristol	\$ 162,546.00	\$ 161,026.00	0.94%
DEM-HL00053 Adopt a Hurricane Family, Inc. dba Crisis Housing Solutions	\$ 218,179.00	\$ 146,114.00	49.32%
DEM-HL00054 Emerald Coast Regional Council	\$ 186,840.00	\$ 182,001.00	2.66%
DEM-HL00055 City of Flagler Beach (WITHDRAWN)	\$ -	\$ -	
DEM-HL00056 West Palm Beach Housing Authority	\$ 337,750.00	\$ 151,120.00	123.50%
DEM-HL00057 City of Edgewater	\$ 162,101.00	\$ 161,912.00	0.12%
DEM-HL00058 City of Panama City	\$ -	\$ -	
<b>TOTAL</b>	<b>\$ 2,196,130.00</b>	<b>\$ 1,337,147.00</b>	<b>64.24%</b>

Figure 1.2



## Closed Projects

Figure 1.3 shows all completed projects during FY 2022, which had over \$2.3 million spent retrofitting residential and public properties.

Closed Project	Award Amount	Amount Spent	Project Type
DEM-HL00006 Boynton Beach Faith Based CDC	\$ 150,000.00	\$ 150,000.00	Mitigation Reconstruction
DEM-HL00009 City of Plantation	\$ 194,000.00	\$ 194,000.00	Public Building Wind Mitigation
DEM-HL00012 The ARC Tampa Bay	\$ 194,000.00	\$ 170,537.28	Residential Wind Mitigation
DEM-HL00020 Flagler County	\$ 194,000.00	\$ 194,000.00	Residential Wind Mitigation
DEM-HL00035 Centro Campesino Farmworker Center	\$ 194,000.00	\$ 190,700.00	Residential Wind Mitigation
DEM-HL00036 City of Pompano Beach	\$ 194,000.00	\$ 194,000.00	Residential Wind Mitigation
DEM-HL00037 City of Carrabelle	\$ 194,000.00	\$ 191,990.78	Residential Wind Mitigation
DEM-HL00038 Miami-Dade County	\$ 194,000.00	\$ 188,339.32	Residential Wind Mitigation
DEM-HL00039 St. Lucie Habitat for Humanity, Inc.	\$ 194,000.00	\$ 194,000.00	Residential Wind Mitigation
DEM-HL00041 City of Bradenton	\$ 194,000.00	\$ 186,097.51	Residential Wind Mitigation
DEM-HL00042 City of Lauderdale Lakes	\$ 194,000.00	\$ 193,339.94	Residential Wind Mitigation
DEM-HL00043 City of Deerfield Beach	\$ 194,000.00	\$ 150,566.67	Residential Wind Mitigation
DEM-HL00045 City of North Lauderdale	\$ 194,000.00	\$ 184,791.67	Residential Wind Mitigation
DEM-HL00055 City of Flagler Beach	\$ 194,000.00	\$ 3,156.05	Government Building Wind Mitigation
<b>TOTAL</b>	<b>\$ 2,672,000.00</b>	<b>\$ 2,385,519.22</b>	

Figure 1.3

## FY 2023 New Projects

Figure 1.4 shows all the approved HLMP projects for FY 2023, which have a balanced set of residential and non-residential wind mitigation projects.

Newly Awarded Recipient	Award Amount	Project Type
DEM-HL00063 City of Fellsmere	\$ 194,000.00	Public Building Wind Mitigation
DEM-HL00064 Lake Support and Emergency Recovery, Inc.	\$ 194,000.00	Residential Wind Mitigation
DEM-HL00065 Eckerd College	\$ 194,000.00	Educational Building Wind Mitigation
DEM-HL00066 Miami Dade County - Community Action and Human Services Department	\$ 194,000.00	Residential Wind Mitigation
DEM-HL00067 Florida Keys Aqueduct Authority	\$ 194,000.00	Water Treatment Facility Wind Mitigation
DEM-HL00068 Centro Campesino Farmworker Center	\$ 194,000.00	Residential Wind Mitigation
DEM-HL00069 Emerald Coast Regional Council	\$ 194,000.00	Residential Wind Mitigation
DEM-HL00070 Jefferson County	\$ 194,000.00	Government Building Wind Mitigation
DEM-HL00071 St. Lucie Habitat for Humanity	\$ 194,000.00	Residential Wind Mitigation
DEM-HL00072 City of Lauderdale Lakes	\$ 194,000.00	Residential Wind Mitigation
DEM-HL00073 Miami Shores Village	\$ 194,000.00	Public Building Wind Mitigation
DEM-HL00074 Banyan Community Health Center, Inc.	\$ 194,000.00	Commercial Wind Mitigation
DEM-HL00075 City of North Lauderdale	\$ 194,000.00	Residential Wind Mitigation
DEM-HL00076 Pasco County Board of County Commissioners	\$ 194,000.00	Public Building Wind Mitigation
DEM-HL00077 Calhoun County	\$ 150,000.00	Residential Wind Mitigation

Figure 1.4

## PROGRAM GOALS AND RECOMMENDATIONS

The Division of Emergency Management is committed to developing programs to educate the public on ways to reduce the impact of a disaster. The Division must continue working with Florida homeowners, local governments, non-profit organizations, and state agencies to reduce the risk of hurricane losses. Research must continue to develop stronger wind mitigation measures to protect the residents of Florida and increase structural survivability for residences. Additionally, through a comprehensive outreach approach, more communities will have an opportunity to participate in the grant program.

The Division has the following goals for the Hurricane Loss Mitigation Program:

- Continue refining grant management activities in the Salesforce platform for better reporting and process improvement,
- Where possible, leverage HLMP funds with other funds from federal, state, local government, or private sources, and
- Partner with Recovery Regional Coordinators (RRC) to enhance HLMP outreach efforts.

Observations and Recommendations:

**Observation** - Grant recipients and contractors are continually under a confined time constraint for awarding and expending the appropriated funds within one fiscal year. Project solicitation, awarding, contracting, sub-contracting, actual mitigation retrofits and project closeout must be completed by the end of each fiscal year. This condensed time frame does not allow the Division or its participants sufficient time to take full advantage of the funding provided.

**Recommendation** – Extend the funding and budget authority for the annual appropriation for up to two years. This would allow the Division’s contracts to start upon full execution and have a period of performance that would expire at the end of the second fiscal year.

# Shelter Retrofit Program

## PROGRAM ACTIVITIES

### Shelter Retrofit Funding

In 2017, the Hurricane Loss Mitigation Program began managing the Shelter Survey and Retrofit Program's grants and contracting responsibilities. HLMP applies proven grant management processes to existing and new projects managed by the Shelter Retrofit Program. With the resources available to the Mitigation Bureau's Finance Unit, tracking shelter payments, contracting, and reporting streamlines processes for the Shelter Retrofit Program.

The Hurricane Loss Mitigation Program also works with the Mitigation Bureau's Technical Unit to verify the work done completed by Shelter Retrofit Program. Modernized Scopes of Work have been finalized with the collaboration of the Shelter Retrofit Program, Technical Unit, and Hurricane Loss Mitigation Program. New review processes and detailed requirements within the Scope of Work will strengthen regulation and monitoring while providing the recipient with a clearer understanding of their goals and objectives.

## Executed Projects

Figure 2.1 displays the shelter retrofit agreement executed in FY 2022, totaling \$280,000.00.

Recipient	Award Amount
DEM-SR00036 Jefferson County	\$ 280,000.00
<b>TOTAL</b>	<b>\$ 280,000.00</b>

Figure 2.1

## Closed Projects

Figure 2.2 below summarizes the eight projects closed during FY 2022, totaling \$1,587,909.15.

Recipient	Amount Spent
DEM-SR00028 Indian River State College	\$ 330,097.78
DEM-SR00031 Pinellas County	\$ 19,355.00
DEM-SR00013 Bay District Schools (Deer Point)	\$ 325,295.41
DEM-SR00014 Bay District Schools (Bozeman)	\$ 323,371.00
DEM-SR00036 Jefferson County School District	\$ -
DEM-SR00022 School Board of Brevard County	\$ 484,577.95
DEM-SR00029 Sumter County School Board	\$ 105,212.01
DEM-SR00025 Walton County BOCC (WITHDRAWN)	\$ -
<b>TOTAL</b>	<b>\$1,587,909.15</b>

Figure 2.2

## Active Projects

Figure 2.3 shows all twelve projects active at the end year of FY 2022. The projects divide into three major categories; Engineering Study, Genset, and Retrofit. An Engineering Study determines the viability of a building for retrofitting. A Genset project installs the necessary electrical components to connect a generator to a building. Retrofit projects focus on hardening the envelope of a building.

Recipient	Projects	Project Type	# of Locations
HLMPSR17-020 A Multi Clay County BOCC	Orange Park High School	Engineering Study	5
	Asbury Lake Jr High School	Gen Set	
	Oakleaf High School	Retrofit	
	Fleming Island High School	Retrofit	
	Keystone Heights High School	Retrofit	
DEM-SR00001 Seminole County BOCC	Winter Springs High School	Retrofit	4
	Teague Middle School	Gen Set	
	Teague Middle School	Retrofit	
	Lawton Chiles Middle School	Gen Set	
	Lawton Chiles Middle School	Retrofit	
	Lyman High School	Gen Set	
DEM-SR00005 Orange County BOCC	South Econ Rec Gym	Retrofit	5
	West Orange Rec Gym	Retrofit	
	Silver Star Rec Gym	Retrofit	
	Meadow Woods Rec Gym	Retrofit	
	Goldenrod Rec Gym	Retrofit	
DEM-SR00010 Walton County BOCC	Freeport High School	Gen Set	1
DEM-SR00018 Sarasota School Board	Taylor Ranch Elementary	Retrofit	3
	Gulf Gate Elementary	Retrofit	
	North Port High School	Retrofit	

Figure 2.3

(Figure 2.3 cont.)

<b>DEM-SR00020 Lake School Board</b>	East Ridge High School	Retrofit	17
	Carver Middle School	Retrofit	
	Eustis Middle School	Retrofit	
	Mt. Dora High School	Retrofit	
	Leesburg High School	Retrofit	
	Tavares High School	Retrofit	
	Umatilla High School	Engineering Study	
	Umatilla High School	Retrofit	
	Eustis Middle School	Retrofit	
	Astatula Elementary School	Retrofit	
	Astatula Elementary School	Gen Set	
	Villages Elementary School	Gen Set	
	Villages Elementary School	Retrofit	
	Lost Lake Elementary School	Retrofit	
	Lost Lake Elementary School	Gen Set	
	Leesburg Elementary School	Gen Set	
	Umatilla Elementary School	Gen Set	
Spring Creek Elementary Schools	Gen Set		
Round Lake Elementary School	Gen Set		
East Ridge Middle School	Gen Set		
Tavares Middle School	Retrofit		
<b>DEM-SR00021 DeSoto School District</b>	West Elementary School	Retrofit	3
	Nocatee Elementary School	Retrofit	
	DeSoto High School	Retrofit	
<b>DEM-SR00027 Marion County - Retrofit</b>	Belleview High School	Retrofit	6
	Belleview Middle School	Retrofit	
	Legacy Elementary School	Retrofit	
	Saddlewood Elementary School	Retrofit	
	South Ocala Elementary School	Retrofit	
	West Port High School	Retrofit	
<b>DEM-SR00030 The School Board of Polk County</b>	Ben Hill Griffin JR Elementary School	Retrofit	5
	Frostproof Middle Senior School	Retrofit	
	Ft Meade/SR High	Retrofit	
	Ridge Community High School	Gen Set	
	Berkley Charter Elementary School	Retrofit	
<b>DEM-SR00032 Alachua County BOCC</b>	Freedom Center	Retrofit	1
	Freedom Center	Gen Set	
<b>DEM-SR00033 Bay County BOCC</b>	Bay County Public Library	Retrofit	1
	Bay County Public Library	Gen Set	
<b>DEM-SR00035 Clay County School Board</b>	Rideout Elementary	Retrofit	1

Engineering Study	2
Retrofit	43
Gen Set	16
<b>Total</b>	<b>61</b>

## **PROGRAM GOALS AND RECOMMENDATIONS**

### **Shelter Retrofit Program**

Under the guidance of the Hurricane Loss Mitigation Program, the Shelter Retrofit Program has grown in scope and efficiency. By collaborating with the Infrastructure Section, the Program continues eradicating shelter deficits throughout the state. From better reporting to improved funding accountability, the Program looks forward to providing greater resiliency and preparedness for future disasters throughout the state.

The Division has the following goals to accomplish in the next Fiscal Year:

- Meet the Legislature's goal to eliminate the deficit of safe public hurricane evacuation shelter space in any region of the state,
- Develop standards of cost-effectiveness towards new construction,
- Continue refining grant management activities in the Salesforce platform for better reporting and process improvement,
- Maintain a strong relationship between the Infrastructure staff and Mitigation staff, and
- Coordinate with the Mitigation Technical Unit to be in more aspects of the Program.

**2021-2022 ANNUAL REPORT  
TALLAHASSEE COMMUNITY COLLEGE  
MOBILE HOME TIE DOWN PROGRAM**

The Mobile Home Tie-Down Program continued to be a successful program during the 2021-2022 fiscal year, however reduced homeowner participation due to COVID-19 continued.

**Program Highlights:**

- Extension of RFP 2020-04 was offered to vendors Storm Ready Services (M&B Enterprises) and Timberline Construction Group for statewide services. Timberline Construction Group elected not to extend their agreement.
- The use of Quality Assurance Inspectors was continued, both for the Individual component and for the Parks, as TCC was still under travel restrictions.
- The Florida Department of Highway Safety and Motor Vehicles (D.H.S.M.V.), Division of Motor Vehicles, Manufactured Housing Section completed a random inspection of a minimum of 10% of the homes for the Parks component. This inspection verifies the items were actually installed by the vendor and installed according to the manufacturer's specifications.

**Impact of COVID-19:**

COVID restrictions continued to significantly impact the services provided this program year. Priority was given to utilize the remaining FY21 NCE funds; completion numbers were included in the FY21 final report. In addition, most parks did not have the capability, or interest to host large HOA meetings with the recommended social distancing guidelines, although some allowed for multiple HOA meetings outside and/or with small groups.

**Final Numbers:**

During the 2021-2022 program year fourteen (14) initial resident meetings were conducted by the Program Contractors. In several parks, meetings had to be repeated to maximize resident participation and reduce participant count for social distancing. These meetings were conducted with homeowner's association board members, volunteers and, on many occasions, most residents of a particular community. Many parks did not allow for HOA meetings to be held due to COVID concerns and program information had to be disseminated "door-to-door" within the community, which also affected participation.

- Interviews with management and/or homeowner association representatives.
- Visual inspections of all homes within the community.
- Intake training for the homeowners' association representatives.



TCC completed **five hundred thirty-four (534)** homes this past year as compared to two thousand ninety-eight (2,098) homes the previous year. The program was successfully completed in fifteen (15) mobile home communities, across nine (9) different Florida counties. **Six hundred ninety-four thousand five hundred fourteen (\$694,514)** was utilized of the **FY2022 DEM-HL00059 grant, or 25% grant utilization.**

Community/Park Name	Address	City	County	# Homes Served
Oak Springs	10 Manatee St	Sorrento	Lake	13
Citrus Grove Estates	15 Parkwood	Bradenton	Manatee	9
Eagles Nest Mobile Home Park	7801 34th Avenue North	St. Petersburg	Pinellas	14
Lake Point (Prev Holiday Mobile Park)	44B Dale Dr	Tavares	Lake	26
Southgate Mobile Home Park	8817 North Atlantic Ave	Cape Canaveral	Brevard	31
Holiday Acres / University Sun Estates MHP	306 Holiday Acres Dr	Orlando	Orange	11
Sunrise Village	799 Clearlake Rd	Cocoa	Brevard	30
Palm Ridge	1424 Flora Lee Dr	Leesburg	Lake	29
Heather Hills Estates	4907 4th St. W	Bradenton	Manatee	4
Pointe West	12651 Seminole Blvd	Largo	Pinellas	54
Colony In The Wood	17 Palm in the Wood	Port Orange	Volusia	188
Crystal Lakes	9941 Tarpon Key Court	Fort Myers	Lee	41
Lakeshore Landings	1907 Onaka Dr	Orlando	Orange	31
Tidevue Estates	4214 11 Street Court E	Ellenton	Manatee	41
Alafaya Palms	13600 Wesleyan Blvd	Orlando	Orange	12

#### Moving Forward:

- At the end of FY2021 NCE and use of FY2022 funding, 20 parks remain on the waiting list ready to serve, 20 ‘sister parks’ (owned by managers with other parks previously served under the program) were listed as interested, and roughly 30 parks who did not return phone calls were moved to ‘previously reviewed.’
- The statute regulating the Mobile Home Tie-down Program funds awarded the grant to Gulf Coast State College effective July 1, 2022.
- TCC has shared current contracts, RFP, and invited GCSC to participate in the MHTDP Steering Committee meetings.
- All files including current waiting list, parks served, and park databases have been prepared and will be uploaded to the DEM provided SharePoint for GCSC.

Please refer any questions relating to this report or the Program in general to:

Amy Bradbury  
Director of Financial Services  
Tallahassee Community College  
444 Appleyard Drive  
Tallahassee, FL 32304  
850.201.8519  
[amy.bradbury@tcc.fl.edu](mailto:amy.bradbury@tcc.fl.edu)



*A Resource for the State of Florida*

# **HURRICANE LOSS REDUCTION FOR HOUSING IN FLORIDA**

## **FINAL REPORT**

**For the Period November 18, 2021 to June 30, 2022**

*A Research Project Funded by:*  
**The State of Florida Division of Emergency Management  
Through Contract #DEM-HL00060**

*Prepared by*  
The International Hurricane Research Center (IHRC)  
Florida International University (FIU)

July 31, 2022

# Final Report

## Table of Contents

Executive Summary	Section 1
Understanding Hurricane Effects on Manufactured Homes (Chowdhury, Zisis, Elawady, Sutley, Dao)	Section 2
The Role of Slowly-Varying Downburst Wind Directions on the Resulting Aerodynamic Loading on Buildings (Elawady)	Section 3
Wind Flow Separation of T-Shape Bluff Bodies (Zisis)	Section 4
Investigation and Incorporation of WOW testing outputs in the Florida Public Hurricane Loss Model (Gurley and Pinelli )	Section 5
Education and Outreach Programs to Convey the Benefits of Various Hurricane Loss Mitigation Devices and Techniques (PI: Erik Salna)	Section 6

## **Section 1 Executive Summary**

Five major research efforts were identified by the International Hurricane Research Center (IHRC) for the Hurricane Loss Mitigation Program (HLMP) Fiscal Year 2021-22. Funding was dedicated to areas of structural mitigation analysis, economic loss analysis, and education and outreach. In keeping with the comprehensive agenda of the research topics for this project, the IHRC organized a multidisciplinary team of researchers, students and support staff to complete the stated objectives. The following is a summary of research findings:

### **Research Area 1: Understanding Hurricane Effects on Manufactured Homes (Chowdhury, Zisis, Elawady, Sutley, Dao)**

Manufactured Housing (MH) units are one of the most vulnerable residential structures to windstorms, including hurricanes. The overall goal of this research is to provide the fundamental knowledge needed to reduce the physical vulnerability of manufactured homes to wind events. While extensive research has been conducted on more traditional residential construction methods (e.g. light-frame wood construction - LFWC) little research exists on MHs. Of particular importance is the performance of anchorage systems of MHs, with limited research that does not capture many observed failure modes, including roof and wall cladding loss. Also, previous research doesn't capture the critical role of aerodynamic effects of the crawlspace beneath the units. In addition, there is no available knowledge regarding the interference effects caused by interactions between multiple units in a mobile home park. With an estimated 2.7 million MH units located within mobile home parks in the U.S., we strongly believe that there is an important gap in understanding hurricane effects on manufactured homes.

Three universities including Florida International University (FIU), Kansas University (KU) and University of Alabama (UA), will collaborate in this research which will address the significant gaps through a series of research tasks to be carried out over three years (total period envisioned to complete all research tasks discussed).

#### *Part A: Large-scale Wind Tunnel Testing of Manufactured Home Communities (Florida International University)*

Manufactured homes are structures built almost entirely off-site in a factory and then transported to the building site for final assembly. They help fill a demand for affordable housing and currently shelter more than 20 million people in the US. These homes were proved to be more vulnerable to extreme wind events than conventional residential houses, potentially due to higher structural and envelope damage susceptibilities resulting from outdated building standards. In addition, more than 10% of the manufactured homes in the US are in coastal and hurricane-prone areas. These increased vulnerabilities also cascade into higher fatalities and pronounced socio-economic impacts as most manufactured homes shelter low-income and most often uninsured communities. However, literature on the evaluation of realistic wind loads on manufactured homes and their communities, as well as wind resistance assessment of their envelope components, is limited. Therefore, this research aims to investigate the aerodynamics of

manufactured homes using large-scale wind tunnel experiments at the NSF-NHERI Wall of Wind Experimental Facility at FIU. The study also investigates the interference effects generated by the presence of multiple units in a mobile home park that may affect the wind loading on the manufactured home of interest. In this regard, both isolated and sheltered model configurations were considered by replicating manufactured home arrangements as seen in selected mobile home parks located in coastal areas. For the isolated case, a large-scale model of a typical manufactured home was instrumented with pressure taps to measure the wind-induced pressures and forces on the roof, walls, and floor. Then, to simulate the sheltering effects, the same instrumented model was surrounded by dummy models which represent the neighboring units in a mobile home park. Pressure, force, and moment coefficients obtained from this study showed that MHs are vulnerable to high peak wind loads. Moreover, these wind loads were found to be significantly lower for fully and partially shielded MHs. Furthermore, the collected data from this study were used to inform building component testing and numerical simulations of the behavior of mobile homes during extreme wind events. Most importantly, the findings of this study can be used to help improve MH design provisions in current codes and standards.

*Part B: Nonlinear Dynamic Analysis of Manufactured Homes subject to Hurricane-induced Wind Loads: Numerical Modeling - Initial Study (University of Alabama)*

As the housing affordability crisis has deepened in the United States, manufactured home units (MHU) are gaining traction as a viable alternative to meet rural and low-income households' long-term, affordable housing needs. However, there are major shortcomings in current building codes for connections and components of MHUs that make them vulnerable to damage from hurricane-induced wind loads. There is limited existing work on numerical modeling approaches to light-frame wood construction (LFWC) subject to wind loads. It is noted, however, that light-frame wood structures and MHUs differ in size of members, types of materials, methods of construction, weights of resulting structures, and failure mechanisms, and, therefore, they need to be studied separately.

Most nonlinear numerical models for light-frame wood buildings focus on seismic effect studies with an emphasis on shear wall (in-plane) modeling for seismic loading performed numerical analysis to provide the basic understanding required for the development of improved design procedures for light-frame wood buildings subject to lateral loads. Unlike seismic loading, wind loads on buildings often cause out-of-plane failure in the building envelope, such as roof sheathings or walls, and uplift failure due to a deficient vertical load path. Additionally, in earthquake engineering, hysteresis model used to predict the cyclic behavior of the structural component needs to account for both the positive and negative displacements. In wind engineering, depending on the modeled components, the cyclic loading may include only one-side (either negative or positive) or two-side (negative and positive) displacements. Therefore, the hysteresis model needs to be adjusted accordingly.

The objective of this study is to develop the numerical (FE) model to investigate the short-term cumulative damage on the MHU structural system under dynamic wind loads. The numerical model for structural components, such as fasteners and roof-sheathing, will use nonlinear load-deflection relationships to predict the responses under high deflections in extreme wind conditions. The model will be calibrated with the pressure coefficient time histories obtained from the experimental study by K.U. and the test data on pressure coefficient will be used to apply input

aerodynamic loading on MHU's roof, wall, and the under-deck surfaces. The wind pressure data measured at taps will be interpolated at nodal coordinates and integrated into wind load time histories at element nodes for numerical structural dynamic model. The hysteresis behavior of components and connections, for the nonlinear load-displacement curves, will be applied based on the findings from the experiment.

The development of performance-based design (PBD) in the field of structural wind engineering requires the numerical model to be capable of predicting the explicit performance of structure beyond the capacity and first failure of the building envelope. For example, uplift of the edge of the roof sheathing panel under wind loads may require a nonlinear roof sheathing fastener model that can accurately represent the unique characteristics of fastener/wood fiber interaction by considering the effect of load eccentricity on the coupled withdrawal-moment capacity.

In the first year of current study, the conceptual numerical model of roof of a single-story MHU in Wind Zone II will be analyzed under dynamic wind loads using a three-dimensional (3D) nonlinear finite element (FE) formulation of MHU components—roof sheathing, truss members, and fasteners (nails) to predict roof performance. In the first year of this study, UA team has successfully developed the conceptual numerical model for nail connections and other MHU substructures components used in Matlab program for analysis of a roof structure of MHU. Even though only the roof of a MHU was analysis in this report, the analysis can be extended for full MHU when longer running time allowed. The initial results show a reasonable range given the nail connection parameters were assumed during the analysis given that the connection tests are conducting at KU.

#### *Part C: Understanding Hurricane Effects on Manufactured Homes (Kansas University)*

Manufactured housing units (MHUs) are extremely vulnerable to windstorms, including hurricanes. The overall goal of this research is to provide the fundamental and practical knowledge needed to significantly reduce the physical vulnerability of manufactured homes to wind events. While extensive research has been conducted on light-frame wood construction (LFWC) little research exists on MHUs. Limited research exists on anchorage systems, but do not capture many observed failure modes, including roof and wall cladding loss.

With an estimated 2.7 million MHUs located within mobile home parks in the U.S., including approximately 7% of Florida's households, there is an important gap in understanding hurricane effects on manufactured homes. Through the creation of critical fundamental knowledge that can change code provisions, policies, and manufacturing processes, the innovative approaches proposed here have the potential to provide transformative impacts to new and existing mobile home parks and to manufactured housing units.

There were two primary goals motivating stakeholder engagement for this project, including (1) gaining insight from academics, practitioners, and others with working knowledge of physical and social problems associated with manufactured housing; and (2) to build momentum behind the need for the research community to more intentionally address disparities with manufactured housing construction and performance.

Thus, we identified a community of people interested in advancing the safety of manufactured homes and organized a workshop to bring these stakeholders together. Stakeholders were identified through the research team's personal and professional networks and peer-reviewed literature. The SAC provided critical feedback to the research team and should be a continued component of future research. Future research should (a) perform a benchmark study comparing wind loads produced on manufactured homes in different areas of Florida following HUD Code in comparison to ASCE 7 (2022) provisions, and (b) produce the results of a risk assessment demonstrating cost and benefit tradeoffs for Wind Zones I, II, and III manufactured homes, as well as in comparison to homes with remedial measures for improved wind performance. Continuing experimental testing to be able to produce a viable finite element model of manufactured housing is critical for a realistic risk assessment.

The primary goal of the experimental portion of this project was to provide a quantitative measurement of the performance of key connection(s) needed for advancing the finite element model being developed at the University of Alabama (UA). Based on this goal, the most important connection identified by the UA team was the roof sheathing to rafter connection, and thus was the sole focus of this portion of the project. Although withdrawal capacity is known for various fastener and wood combinations, the cyclic behavior of this connection has never been tested and was critical for the finite element model. Furthermore, as discussed by the SAC, the most common failure mode for Wind Zone II homes is failure at the roof, and thus important for initially focusing the component testing.

Fastener component monotonic testing informed cyclic testing protocols. Subsequent cyclic testing of various sheathing fastener configurations provided data that will be used in detailed finite element models of MHU structures. As shown in the results of this report, the mean capacities for the nail connections in SYP lumber are substantially (2.5 to 3 times) less than the mean capacities for screw connections in SPF. Similarly, the COV was always 2.5 times higher for the nail connections in SYP compared with the screw connections in SPF. Given that nail connections are the more common connection used in the actual construction of Wind Zone II manufactured homes which have roof failure as the most common observed failure mode in the field, switching fasteners from nails to screws is expected to provide significantly higher performance. More research is needed to understand this relationship for edge fasteners, as well as for the roof-to-wall connection. Additionally, more research is needed to understand the material and labor cost difference that is associated with using screws instead of nails in the construction of these homes.

## **Research Area 2: The Role of Slowly-Varying Downburst Wind Directions on the Resulting Aerodynamic Loading on Buildings (Elawady)**

Downbursts are non-stationary, transient, localized high winds that causes severe damage to buildings. Downbursts differ from synoptic ABL winds, which makes assessing their effects on buildings and other structures a complex process. This study examines how bluff body aerodynamics change during downburst velocity evolution with and without the effect of slowly varying wind direction. To replicate a real event that took place on June 19, 2003 in Lubbock,



Texas, at the WOW lab, the event was scaled down using appropriate time, length, and velocity scales. Downburst experiments began with scaled downburst flow characterization followed by static aerodynamic tests for wind direction (180°, 225°, 270°) and dynamic aerodynamic tests for wind direction varying between (260° to 290°). The maximum moving mean velocity at the building model roof mean height was 12.1 m/s using a time average window of 0.5 s. It was observed that pressure coefficient ( $C_p$ ) distribution across the building is similar to that typically observed for Atmospheric Boundary Layer wind events for all static directions. It was also observed that all surfaces have higher  $C_p$  values for the dynamic cases compared to the static cases. Future studies are needed to better codify downburst impact on buildings and the effect of the rotating wind direction on the wind loading of the building. In future analysis, peak pressure distributions will further be evaluated. The findings of this study and the planned future study of this new research topic will help improve design provisions in current codes and standards.

### **Research Area 3: Wind Flow Separation of T-Shape Bluff Bodies (Zisis)**

Wind engineering research aims at minimizing the impact of extreme wind events on people and the built environment. For instance, prediction of peak pressure coefficients on the surface of buildings is critical in understanding their behavior during a storm event and minimizing wind related damage to the building's envelope and structural system. The motivation for this project, was the 2016 FL Division of Emergency Management (DEM) funded research on canopies attached to mid-rise buildings. Some of the findings of that research revealed an unconventional distribution of pressures/suction on the canopies.

The focus of the current research was the concept of synchronous flow separation on T-shaped bluff bodies. This very specific flow phenomenon occurs when wind separates simultaneously due to interaction with both the main bluff body (e.g., building) and with the attached plate (e.g., canopy or balcony). Right after the flows are separated a very complex interaction is initiated that results in non-conventional wind-induced loading patterns on the surfaces of both the bluff body and the plate. Thus, this phenomenon could have great influence on aerodynamic performance of the building itself as well as the building components that are attached to it.

The wind tunnel testing on 1:100 models provided valuable information on the flow characteristics and corresponding wind pressure patterns. The geometric ratios of the constructed models resulted in some significant differences and revealed the impact of the bluff body volume on the separated flow and its reattachment on both the bluff body as well as the flat plate. The high suction zones were observed to move downwind and further from the leading edges which has some direct implications on the characterization of the design zones in typical north American building codes and wind standards. The findings proved that further research is needed to better understand the complexity of such fluid-structure interaction.

### **Research Area 4: Investigation and Incorporation of WOW testing outputs in the Florida Public Hurricane Loss Model (Gurley and Pinelli)**

One of the key components of a better mitigated and therefore more disaster-resilient Florida involves recovery and reconstruction funding for homeowners, and a key element of that funding derives from insurance coverage, which is increasingly driven by cost considerations. The Florida Public Hurricane Loss Model (FPHLM), which has been supported by the State, provides a means

of evaluating hazard insurance rate requests independently of the proprietary models used by private insurers. The model is continually refined to both satisfy the standards issued by the Florida Commission on Hurricane Loss Projection Methodology, and incorporate the current state-of-knowledge in the methodologies employed by the meteorological, engineering, actuarial, statistical, and computer science teams.

The Wall of Wind (WOW) research is largely focused on filling critical gaps in the engineering state-of-knowledge on building performance in hurricane winds via experimental methods. Recent FDEM-funded WOW work included the uplift loads on roof to wall connections of residential buildings, the influence of construction defects and their associated leakage paths on the building internal pressure during high winds, and the exterior building loads experienced by non-rectangular plan low-rise buildings. In a recent report the FPHLM research team evaluated the suitability of these research outputs for incorporation in the FPHLM. The conclusion was that they could be incorporated in the FPHLM with further research.

For the current performance period, four tasks, corresponding to four sections in this report, were proposed to investigate the possible incorporation of recent FIU wall of wind (WOW) experimental outcomes within the FPHLM.

#### Sections 1 to 3.

This sections of the report focus on possible updates to the FPHLM in response to both recent data provided by the FIU WOW facility, and changes to the Florida Building Code (FBC) as a response to adopting ASCE 7-16 Wind Load Provisions. FIU WOW research on the distribution of roof uplift loads to roof to wall (r2w) connections was used to verify the current assumptions employed in the FPHML. This expedited the development of a new variant in the strong residential model to reflect appropriate changes to component capacities that result in less vulnerable structures. This new strong variant will be submitted in the 2022 model certification cycle with the Florida Commission on Hurricane Loss Prediction Methodology (FCHLPM). The FIU WOW investigation of internal pressure for enclosed buildings was the basis for an investigation into the assumptions currently used in the FPHLM. The work from the 2020-2021 DEM report was updated to include the influence of model internal pressure modifications on overall vulnerability functions. The implementation of the new modeling schemes with modified internal pressure will be compared with new hurricane loss insurance claims data in the coming year to determine the disposition of this internal pressure modification. The FIU WOW investigation of loads and roof decking vulnerability on non-rectangular shaped residential structures guided the creation of a roadmap to determine the efficacy of developing non-rectangular models within FPHLM. As a part of future model calibrations based on new insurance claims data, alternative shapes will be considered to add an additional degree of freedom to the calibration process.

#### Section 4

With support from the FDEM, the WoW tested water ingress through a full-scale sliding glass door system installed on a large-scale building mock-up in 2021. The FPHLM models non-breach related leakage paths for sliders and other components to account for water ingress. In this report the FPHLM engineering team compared the WoW test outputs against the FPHLM water leak model. The comparisons centered on the rate of water penetration, expressed in volume of water per unit of effective area of the slider and per unit of time.

The water penetration in a non-breached component is a function of the size of the defect if any, the wind driven rain (WDR) impinging on the component and its associated run-off, the wind speed, and the wind direction, Similarly to what is observed in nature, the wind driven rain (WDR) rates for different storm durations in the FPHLM rain hazard model are not uniform. In fact, the mean WDR rates from the rain model are much smaller than the ones used in the WoW tests for the same wind speeds. The comparisons of the water penetration rate through the slider defects indicate that the FPHLM estimates higher water intrusion at low wind speeds and lower intrusion at high wind speeds.

Further research is needed to understand the discrepancy between the test results and the numerical model. That additional research could include WoW tests with different combinations of wind speed, wind direction, and duration, but with WDR rates similar to the FPHLM, and for different types of breaches to reflect the different strengths of the FPHLM models.

### **Research Area 6: Education and Outreach Programs to Convey the Benefits of Various Hurricane Loss Mitigation Devices and Techniques (PI: Erik Salna)**

The IHRC developed and coordinated education and outreach activities to build on the foundation of previous work under this grant and showcased the hurricane-loss mitigation objectives of the HLMP.

For the 2021-22 performance period, the below mentioned educational partnerships, community events, and outreach programs were developed:

*Wall of Wind Mitigation Challenge (WOW! Challenge): Thursday, March 31st, 2022*  
(The 2022 competition was done virtually.)

The International Hurricane Research Center (IHRC), located on the campus of Florida International University (FIU), has developed the Wall of Wind Mitigation Challenge (WOW! Challenge), a judged competition for South Florida high school students. As the next generation of engineers to address natural hazards and extreme weather, this STEM education event features a competition between high school teams to develop innovative wind mitigation concepts and real-life human safety and property protection solutions. The mitigation concepts are tested live at the FIU NSF-NHERI Wall of Wind (WOW) Experimental Facility (EF), located on FIU's Engineering Campus.

- The objective for the 2022 Wall of Wind Mitigation Challenge was for students to reduce the wind-induced force on a building's foundation, by optimizing its overall shape.
- The student teams prepared three components for the competition: a physical test, an oral presentation, and a written technical paper.
- The competition included teams from six South Florida high schools.
- *First Place* was awarded to Miami Coral Park Senior High School.  
*Second Place* was awarded to North Miami Senior High School.  
*Third Place* was awarded to G. Holmes Braddock Senior High School.

- A complete scoring summary can be found on the following link:  
[https://www.ihrc.fiu.edu/wp-content/uploads/2022/05/2022\\_WOW\\_CHALLENGE\\_RESULTS\\_SUMMARY.pdf](https://www.ihrc.fiu.edu/wp-content/uploads/2022/05/2022_WOW_CHALLENGE_RESULTS_SUMMARY.pdf)

Media exposure resulted in great positive visibility for the IHRC, FIU and FDEM's message of mitigation:

- NSF-NHERI DesignSafe News: <https://www.designsafe-ci.org/community/news/2022/june/fiu-wall-wind-mitigation-challenge-inspires-next-gen-engineers/>

*Eye of the Storm (Science, Mitigation & Preparedness) In-Person Event: May 14th, 2022*

The Museum of Discovery & Science (MODS), located in Fort Lauderdale, FL, assisted the IHRC in planning, coordinating and facilitating this free admission public education event that showcased special hands-on, interactive activities and demonstrations teaching hurricane science, mitigation and preparedness.

- A record 3,897 visitors attended Eye of the Storm, showcasing special interactive activities and demonstrations teaching hurricane science, mitigation and preparedness.
- A Participant Post Survey showed 86% of respondents increased their knowledge about wind engineering and mitigating hurricane damage and 90% will be taking steps to mitigate hurricane damage.
- Media Release and Flyer: [2022 Eye of the Storm – Hurricane \(Science, Mitigation & Preparedness\) Free Museum Event, Saturday, May 14th, 10am to 5pm | IHRC Website \(fiu.edu\)](#)

Special Guests:

- Grant Goodwin, HLMP Program Manager, Florida Division of Emergency Management
- Dana McGeehan, Region 7 Recovery Coordinator, Florida Division of Emergency Management

Media exposure resulted in great positive visibility in the community for the IHRC, FIU and FDEM's message of mitigation.

- [FIU News Website "University helps community prepare for hurricane season."](#) June 7, 2021.

NOAA Hurricane Awareness Tour: IHRC did not participate because there was not a Florida city on this year's tour. The tour conducted two events near Washington D.C. and in New York City.

Get Ready, America! The National Hurricane Survival Initiative: Cancelled due to lack of sponsorships.



*A Resource for the State of Florida*

**SECTION 2 PART A:**  
**Large-scale Wind Tunnel Testing of Manufactured Home  
Communities**  
**FINAL REPORT**  
**(Period: 2022)**

*A Research Project Funded by:*  
**The State of Florida Department of Emergency Management**

*Prepared by*  
*Dr. Arindam Gan Chowdhury*  
*Dr. Ioannis Zisis*  
*Dr. Amal Elawady*

*Graduate Student*  
*Ameyu Tolera*  
*Johnny Estephan*  
*Luis Pappaterra*

## **Executive Summary**

Manufactured homes are structures built almost entirely off-site in a factory and then transported to the building site for final assembly. They help fill a demand for affordable housing and currently shelter more than 20 million people in the US. These homes were proved to be more vulnerable to extreme wind events than conventional residential houses, potentially due to higher structural and envelope damage susceptibilities resulting from outdated building standards. In addition, more than 10% of the manufactured homes in the US are in coastal and hurricane-prone areas. These increased vulnerabilities also cascade into higher fatalities and pronounced socio-economic impacts as most manufactured homes shelter low-income and most often uninsured communities. However, literature on the evaluation of realistic wind loads on manufactured homes and their communities, as well as wind resistance assessment of their envelope components, is limited. Therefore, this research aims to investigate the aerodynamics of manufactured homes using large-scale wind tunnel experiments at the NSF-NHERI Wall of Wind Experimental Facility at Florida International University. The study also investigates the interference effects generated by the presence of multiple units in a mobile home park that may affect the wind loading on the manufactured home of interest. In this regard, both isolated and sheltered model configurations were considered by replicating manufactured home arrangements as seen in selected mobile home parks located in coastal areas. For the isolated case, a large-scale model of a typical manufactured home was instrumented with pressure taps to measure the wind-induced pressures and forces on the roof, walls, and floor. Then, to simulate the sheltering effects, the same instrumented model was surrounded by dummy models which represent the neighboring units in a mobile home park. Pressure, force, and moment coefficients obtained from this study showed that MHs are vulnerable to high peak wind loads. Moreover, these wind loads were found to be significantly lower for fully and partially shielded MHs. Furthermore, the collected data from this study were used to inform building component testing and numerical simulations of the behavior of mobile homes during extreme wind events. Most importantly, the findings of this study can be used to help improve MH design provisions in current codes and standards.

# 1 Introduction

Manufactured homes (MHs) are structures built almost entirely off-site in a factory and then transported to the building site for final assembly. They help fill a demand for affordable housing and currently shelter more than 20 million people in the US. In 2021, the U.S. Census reported that the industry shipped 105,772 homes with an average unit price of \$108,417 and an average floor area of 1,600 square feet (U.S. Census 2022). As shown in **Figure 1a**, shipments to Texas, Florida, South Carolina, North Carolina, Alabama, and Louisiana account for more than 45% of the total shipments made in 2021. The shipments to the state of Florida alone account for more than 7.2% of the entire trade. Furthermore, these high MH occupancy areas are consistent with the high wind speed areas in the American Society of Civil Engineers 7-22 Standard (ASCE 2022) [see **Figure 1b**].

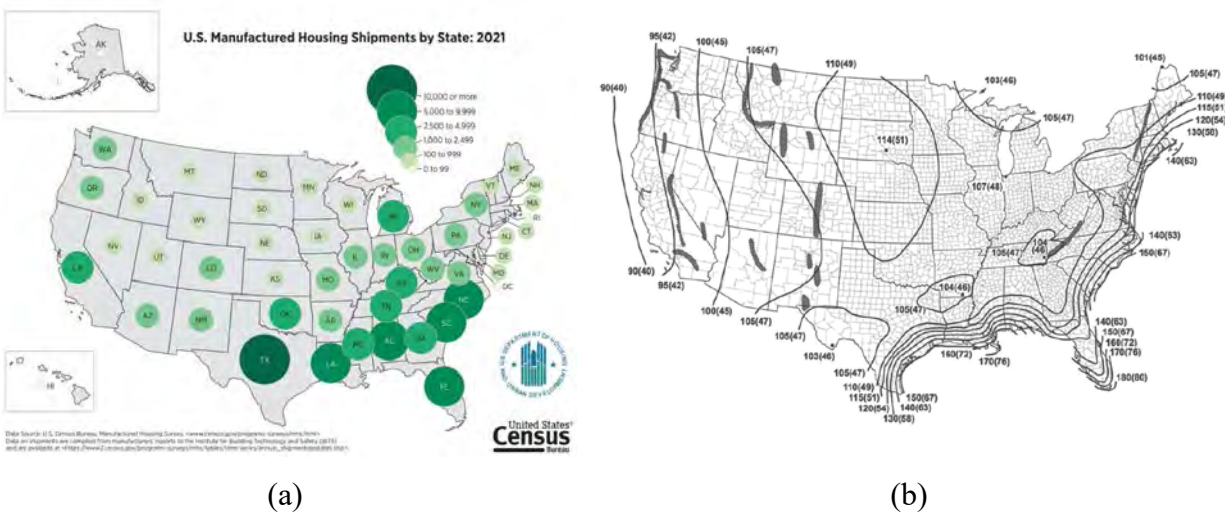


**Figure 1.** (a) U.S. manufactured housing shipment by state (U.S. Census 2022); (b) Basic wind speed for buildings and other structures (ASCE 2022).

Previous hurricanes showed that MHs are more vulnerable to wind damage than conventional residential houses. Hurricane Andrew, for example, was responsible for the damage of more than 10,000 MHs in 1992 (Sutley et al. 2020). Even though Hurricane Andrew was one of the most destructive hurricanes for both manufactured and conventional homes alike, still conventional residential houses standing adjacent to some MHs showed a significantly better wind performance (Marshall 1993). Similar observations were also made for Hurricane Charley in 2004 and Hurricanes Katrina and Rita in 2005 (FEMA 2004, 2006; IBTS 2005; Sutley et al. 2020). More

recently, Sutley et al. (2020) conducted post-hurricane imagery and damage assessment on MHs after Hurricanes Irma (2017) and Michael (2018) in Florida. The authors highlighted the physical vulnerabilities of MHs and the need for further research to enhance their wind resistance.

The relative vulnerabilities of MHs in comparison to conventional residential houses could potentially be due to differences in their wind loading and wind resistance mechanisms. In general, the wind damage mechanism to the MHs is similar to those observed in conventional homes, which is mainly due to envelope failure. In both cases, failure of the building components often time results in internal pressurization that imposes additional structural loads on the main wind force resisting system which could lead to severe damage [see **Figures 2a** and **2b**]. However, in addition to envelope failures, MHs are also vulnerable to foundation failures such as the trailer sliding off the foundation and overturning failure which are not common for conventional low-rise buildings (IBTS 2005; Sutley et al. 2020). **Figure 2c** shows a trailer sliding off that caused a permanent tilting of its concrete block footing during Hurricane Michael in 2018 (Sutley et al. 2020). This figure also shows the failure of the skirt covering the crawl space underneath the floor leaving it fully exposed. Moreover, attached structures such as carports and porches could also incur failure potentially resulting in the loss of the members themselves, or even failure initiation of the envelope component [see **Figure 2d**].



(a)



(b)





(c)



(d)

**Figure 2.** Wind damage to (a) MH, (b) conventional residential house, (c) foundation, and (d) carport (Sutley et al. 2020)

Besides differences in wind loading mechanisms, previous studies have also shown higher structural and envelope damage susceptibilities for MHs in comparison with conventional houses resulting from outdated building standards (Sutley et al. 2020). Even though similar wind performance is expected between the two structures, MHs are currently designed using building standards that are not in step with the current body of knowledge. The latest wind load provision update to the Manufactured Home Construction and Safety Standards Code (MHCSC) was made in the early 1990s. On January 14, 1994, the US Department of Housing and Urban Development (HUD) modified the MHCSC to improve wind load provisions based on ASCE 7-88 (Longinow 2004). In the improved standard, the HUD classifies the U.S. into three zone areas [See **Figure 3**], where Zones II and III pertain to high wind areas for which basic design wind speeds of 100 mph and 110 mph, respectively (HUD 2021). These wind speeds are significantly lower than the current ASCE 7-22 wind speed provisions shown in **Figure 1b**. Moreover, besides the wind speeds in high wind zone areas, the HUD's design wind pressures for MH anchorage, main wind force resisting system, components and cladding have not been recently updated. Furthermore, to update these provisions, literature on the evaluation of realistic wind loads on MHs and their communities, as well as wind resistance assessment of their envelope components, is limited. To date, wind load evaluation of MHs was conducted by Marshall (1977) who investigated wind loads on a full-scale MH placed in an open terrain environment.

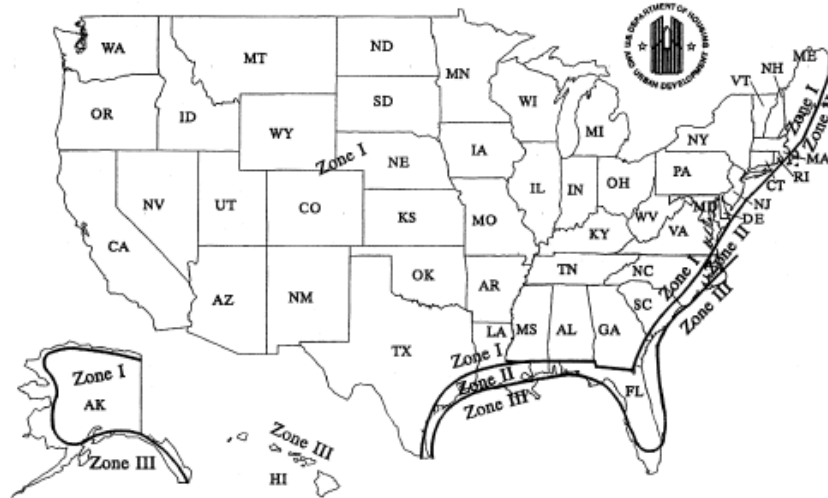


**Figure 3.** Basic wind zone map for manufactured housing (HUD 2021)

Therefore, this research aims to investigate the aerodynamics of MHs using large-scale wind tunnel experiments at the NSF-NHERI Wall of Wind (WOW) Experimental Facility (EF) at Florida International University (FIU). The study also investigates the interference effects generated by the presence of multiple units in a mobile home park that may affect the wind loading on the MH of interest. In this regard, both isolated and sheltered model configurations were considered by replicating MH arrangements as seen in selected mobile home parks located in the State of Florida. Details on the selected mobile home parks and MH arrangements along with the experimental procedure adopted are presented in Section 2. Pressure, force, and moment coefficients obtained from this study are then discussed in Section 3. Finally, concluding remarks and recommendations for future work are presented in Section 4. The data obtained from this study will be used to inform building component testing and numerical simulations of the behavior of mobile homes during extreme wind events. Most importantly, the findings of this study can be also used to help improve the provisions in building design codes and standards as well as risk assessment models.

## 2 Methodology

### 2.1 MH model, test configurations, and instrumentation

Three main manufactured home sites in Florida, shown in **Figure 4**, were adopted in this study based on reconnaissance surveys conducted after the impacts of Hurricanes Irma in 2017 and Michael in 2018 (Sutley et al. 2020). These MH communities are located in South Naples, Coppitt

Key, and Estero, which represent typical community layouts. Based on that, four main test configurations were considered in this study: one isolated MH model and three grouped MH communities [see **Figure 5**]. For the isolated case, a large-scale model of a typical manufactured home was instrumented with pressure taps to measure the wind-induced pressures and forces on the roof, walls, and floor. Then, to simulate the sheltering effects, the same instrumented model was surrounded by dummy models which represent the neighboring units in a mobile home park. Moreover, similar tests were conducted with a fully open crawl space to investigate the effects of the skirt's failure on the wind loads.



**Figure 4.** Selected manufactured home communities in Florida: (a) South Naples; (b) Big Coppitt Key; (c) Estero.

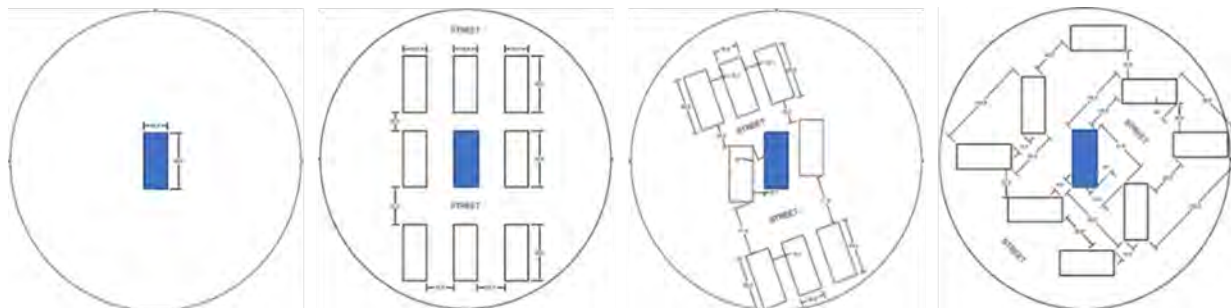


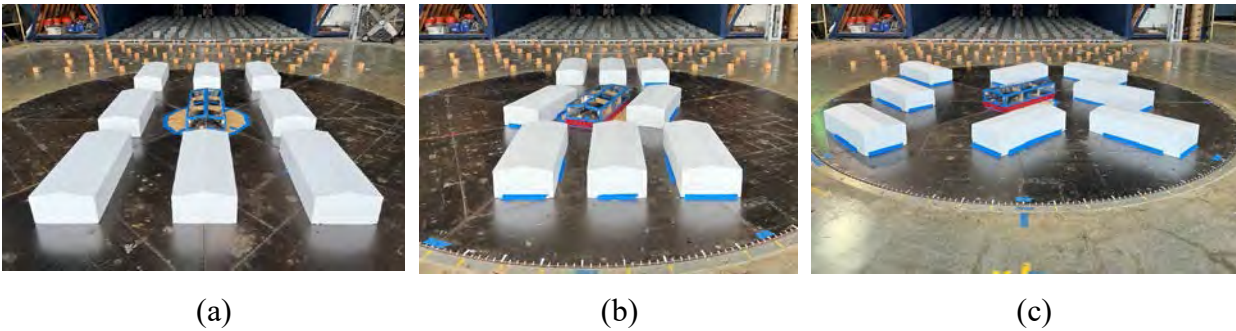
**Figure 5.** Test configurations with the MH of interest located at the center

A large-scale MH model with typical full-scale dimensions of 8m ( $W$ )  $\times$  18.2m ( $L$ )  $\times$  4.2m ( $H$ ) (26.2ft  $\times$  59.8ft  $\times$  13.8ft) was used for the experiments. The 1:20 scale model, shown in **Figure 6**, has a gable roof of 2:12 slope and is supported on 24 piers of 1.2m (4ft) height, 4m (13ft) on-center spacing along the building's width, and 2.4m (8ft) on-center spacing along the building's length. The model was constructed with 6mm (0.25in) thick polycarbonate sheets supported by wooden

frames. Following common MH construction practices, a skirt (also referred to as screen) with a 50% porosity was used to cover the crawl space, as shown in **Figure 6a**. In addition, **Figure 6b** shows the isolated model with an open crawl space. Foam blocks with similar dimensions to those of the MH of interest were placed around the main building model to simulate the various MH community layouts [see **Figure 7**].



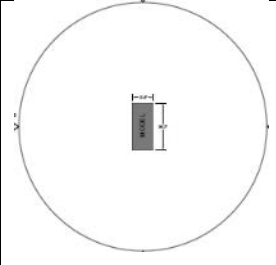
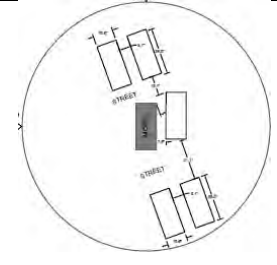
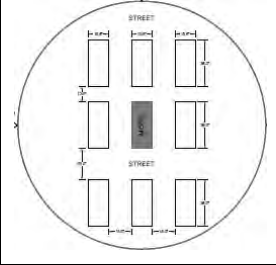
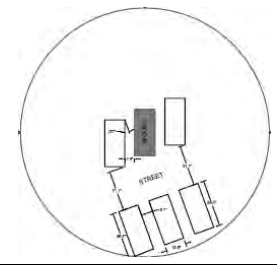
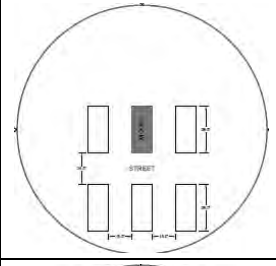
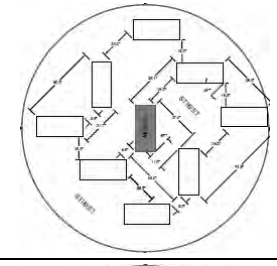
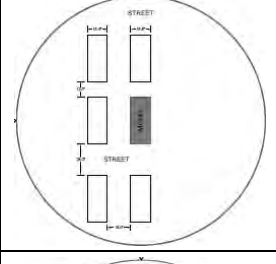
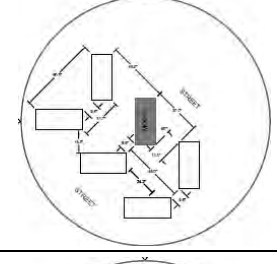
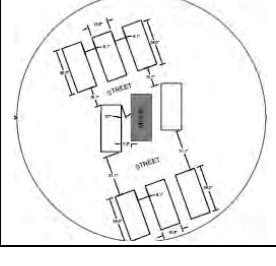
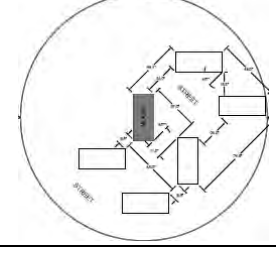
**Figure 6.** Isolated MH model with (a) partially-enclosed crawl space and (b) open crawl space



**Figure 7.** MH community layouts in (a) South Naples, (b) Big Coppitt Key, and (c) Estero.

A total of 17 configurations were considered for the experiments: Configuration numberings with the letter “a” denote partially-enclosed crawl space (with the skirt on), whereas those with the letter “b” refer to the models with open crawl space. **Table 1** summarizes the various MH model configurations which can be grouped into 3 categories: isolated (Configurations 1a and 1b), fully shielded (Configurations 2a, 2b, 5a, 5b, 8a, and 8b), and partially shielded (Configurations 3a, 4a, 4b, 6a, 6b, 7a, 9a, 9b, and 10a).

**Table 1.** Test model configurations

Configuration #	Schematic	Configuration #	Schematic
1a and 1b		6a and 6b	
2a and 2b		7a	
3a		8a and 8b	
4a and 4b		9a and 9b	
5a and 5b		10a	

To measure the wind-induced external pressures, a total of 372 pressure taps were installed throughout the building model surfaces, as shown in **Figure 8**. Specifically, 48 pressure taps were installed on each of the two gable ends (North and South walls), 55 taps on each of the East and West walls, 110 taps on the gable roof, and 56 taps on the floor. The pressure taps were connected to a ZOC33/DSM4000 Scanivalve data acquisition system, which sampled pressures at a rate of

520 Hz. A tubing transfer function was used to correct the collected pressure data for distortion effects introduced by the tubing length (Irwin et al. 1979).

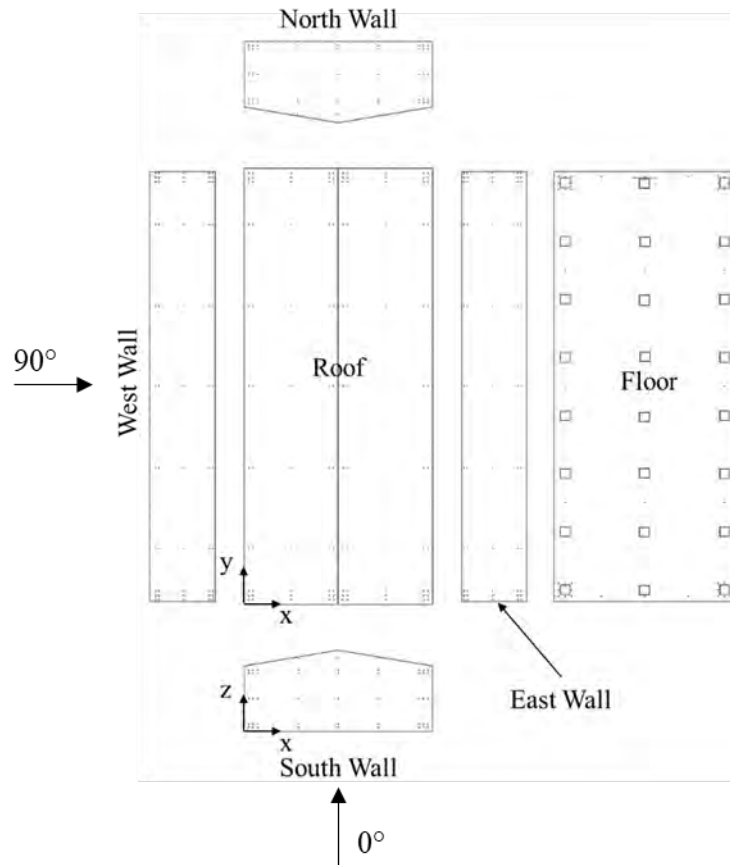


**Figure 8.** Pressure tap layout

## 2.2 Wind flow simulation and test protocol

The 12-fan WOW EF, shown in **Figure 9a**, is a full- and large-scale testing facility, capable of generating wind speeds up to 70 m/s (157 mph) and turbulence characteristics similar to those recorded in Category 5 hurricanes on the Saffir-Simpson scale (Chowdhury et al. 2017, 2018). Equipped with spires and floor roughness elements (**Figure 9b**), the WOW is capable of simulating Atmospheric Boundary Layer (ABL) wind flows under various terrain conditions. Free-stream wind speeds were measured using Turbulent Flow Instruments cobra probes installed at full-scale heights of 2.5m (8.2ft), 4.2m (13.8ft), 6m (19.7ft), 8m (26.3ft), and 10m (32.8ft). The mean wind speed  $\bar{U}_m$  of the simulated open terrain flow was 16m/s (36mph) at the mean roof height  $H_{ref}$  of 4.2m.



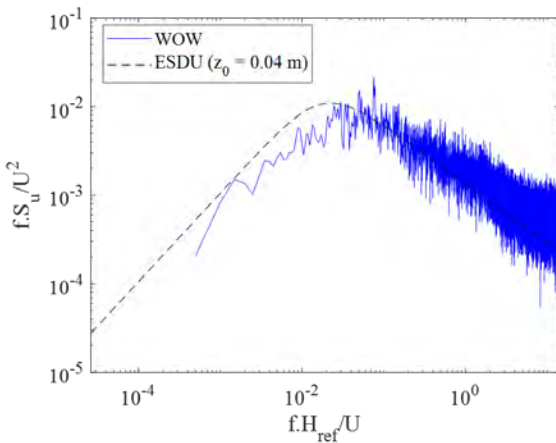
(a)



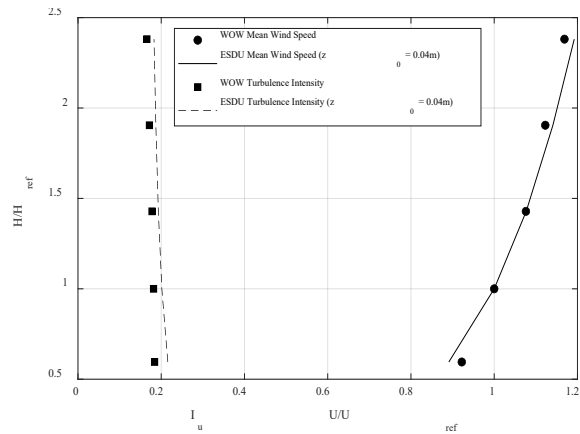
(b)

**Figure 9.** (a) 12-fan WOW EF; (b) spires and floor roughness elements

**Figure 10a** shows the power spectral density (PSD) of the WOW longitudinal velocity fluctuations at the mean roof height along with the full-scale Von-Karman PSD based on ESDU item 85020 (ESDU 2001) for a roughness length  $z_0 = 0.04\text{m}$ . The mean wind velocity and turbulence intensity profiles are presented in **Figure 10b**.



(a)



(b)

**Figure 10.** (a) PSD of the longitudinal wind velocity fluctuations; (b) Mean wind speed and turbulence intensity profiles

A summary of the simulated wind flow characteristics and those of the full-scale counterpart are presented in Table 2. The ratio of the longitudinal integral length scale to the mean wind speed  $xL_{um}/\bar{U}_m$  is equal to 4.14, which exceeds the minimum requirement of 3, as provided by (ASCE 2021). Based on these comparisons, it can be concluded that both the low- and high-frequency components of the full-scale turbulence were adequately simulated at the WOW. The model was

placed on the automated turntable and aerodynamic experiments were conducted for a 1-min duration at 40 wind directions (0:10:350°, 45°, 135°, 225°, and 315°).

**Table 2.** Wind flow characteristics

Parameter	Full-scale	WOW Model (1:20)
Turbulence Intensity (%)	$I_{up} = 20$	$I_{um} = 18$
Integral length scale (m)	${}^xL_{up} = 39$	${}^xL_{um} = 0.87$
Mean roof height (m)	$H_p = 4.2$	$H_m = 0.21$
Sampling duration (min)	$t_p = 15$	$t_m = 1$
Mean wind speed (m/s)	$\bar{U}_p = 21$	$\bar{U}_m = 16$

### 2.3 Data Analysis

Wind-induced external pressure data were collected on the walls, roof, and floor of the MH model for the 17 test configurations. Time histories of the pressure coefficients  $C_p(\theta, t)$  were calculated using Equation (1), where  $P(\theta, t)$  is the pressure time series in Pa (psf),  $P_0$  is the static reference pressure in Pa (psf),  $\rho$  is the air density in  $\text{Kg/m}^3$  (slugs/ft<sup>3</sup>),  $\theta$  is the wind azimuth, and  $\bar{U}$  is the mean wind speed in m/s (mph) at the mean roof height.

$$C_p(\theta, t) = \frac{P(\theta, t) - P_0}{\frac{1}{2}\rho\bar{U}^2} \quad (1)$$

Net force  $C_F(\theta, t)$  and moment  $C_M(\theta, t)$  coefficient time series were also computed for the x, y, and z directions, accordingly. These coefficients represent the drag, lift, and overturning moment coefficients depending on the wind azimuth  $\theta$ , as described in Equations (2) to (6), where  $d$  and  $H$  in m (ft) refer to the moment arm and mean roof height, respectively.

$$C_{F_x}(\theta, t) = \frac{\sum_i \left( C_{p_{East,i}}(\theta, t) - C_{p_{West,i}}(\theta, t) \right) \cdot A_i}{\sum_i A_i} \quad (2)$$

$$C_{F_y}(\theta, t) = \frac{\sum_i \left( C_{p_{South,i}}(\theta, t) - C_{p_{North,i}}(\theta, t) \right) \cdot A_i}{\sum_i A_i} \quad (3)$$

$$C_{F_z}(\theta, t) = \frac{\sum_i \left( C_{p_{Roof,i}}(\theta, t) - C_{p_{Floor,i}}(\theta, t) \right) \cdot A_i}{\sum_i A_i} \quad (4)$$



$$C_{M_x}(\theta, t) = \frac{\sum_i C_{F_{y,i}}(\theta, t) \cdot d_i}{H} \quad (5)$$

$$C_{M_y}(\theta, t) = \frac{\sum_i C_{F_{x,i}}(\theta, t) \cdot d_i}{H} \quad (6)$$

Peak pressure, force, and moment coefficients, referenced by the 3-sec full-scale gust wind speed  $\hat{U}_{3s} = \bar{U}_{1hr} \cdot (1 + 3.4I_{u,p})$ , were estimated for a 1-hr storm duration using Extreme Value Analysis with 100 subintervals. Specifically, the peaks were fitted into a Fisher Tippet Type-I distribution based on a non-exceedance probability of 0.78 (Lieblein 1974).

### 3 Results and Discussion

Results of the large-scale aerodynamic experiments on MHs are presented in this section for a range of wind directions. The mean and peak pressure, force, and moment coefficients on the isolated MH model are discussed in Section 3.1. The results of the shielding effects on wind loads are then examined in Section 3.2 for the fully and partially shielded cases. In addition, the effects of crawl space opening on the floor wind loads are assessed for both the isolated and shielded MH configurations.

#### 3.1 Aerodynamics of an isolated MH

##### 3.1.1 Spatial distribution of pressure coefficients

The aerodynamics of an MH followed those of a typical bluff body under the action of wind flows. The distribution of mean pressure coefficients  $\bar{C}_p$  on the roof and walls of the isolated MH model are presented in **Figure 11** for normal ( $0^\circ$  and  $90^\circ$ ) and cornering wind directions ( $45^\circ$  and  $225^\circ$ ). For normal winds, the highest roof suctions are observed at the leading edges under the separation bubble. The suctions are larger along the roof's length than those along its width [e.g.,  $\bar{C}_p(0^\circ) = -1.0$  and  $\bar{C}_p(90^\circ) = -2.0$ ]. This is due to the flow separation being more significant on the leading edge parallel to the ridge. As the distance from the leading edge increases,  $\bar{C}_p$  tend to decrease in magnitude from -2.0 to -0.5 for  $90^\circ$  due to flow reattachment. For cornering winds, high suctions were observed at the upwind corner and leading edges due to the formation of conical vortices [e.g.,  $\bar{C}_p(45^\circ)$  and  $\bar{C}_p(225^\circ)$  of -2.0]. The windward wall was subjected to positive  $\bar{C}_p$  of 0.5, while suctions between -0.5 and -0.75 were observed on the leeward and side walls. Due to the presence

of the skirt covering the crawl space, floor suction were small in magnitude for all wind directions ( $\bar{C}_p$  between -0.25 and -0.5).

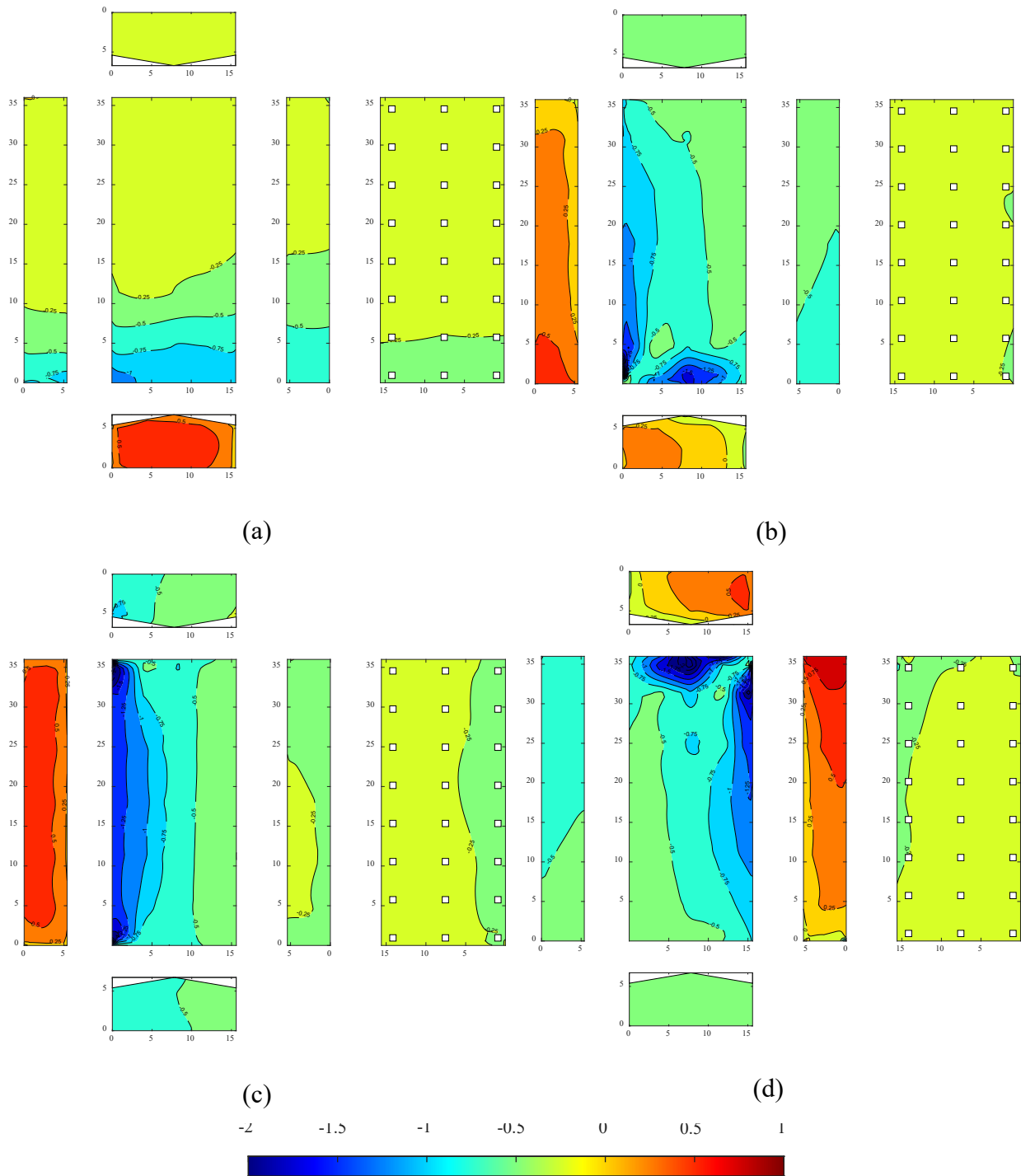


**Figure 11.**  $\bar{C}_p$  for Configuration 1a: (a)  $0^\circ$ , (b)  $45^\circ$ , (c)  $90^\circ$ , and (d)  $225^\circ$

In addition to  $\bar{C}_p$ , critical peak pressure coefficients  $\hat{C}_p$  (maximum and minimum) from all wind directions are presented for Configurations 1a and 1b in **Figure 12**. Similar  $\hat{C}_p$  distributions were observed on the roof and walls for both Configurations. More specifically, the roof corners experienced the highest peak suction of -6.0, while positive maximum  $\hat{C}_p$  of 1.0 were detected on the walls.

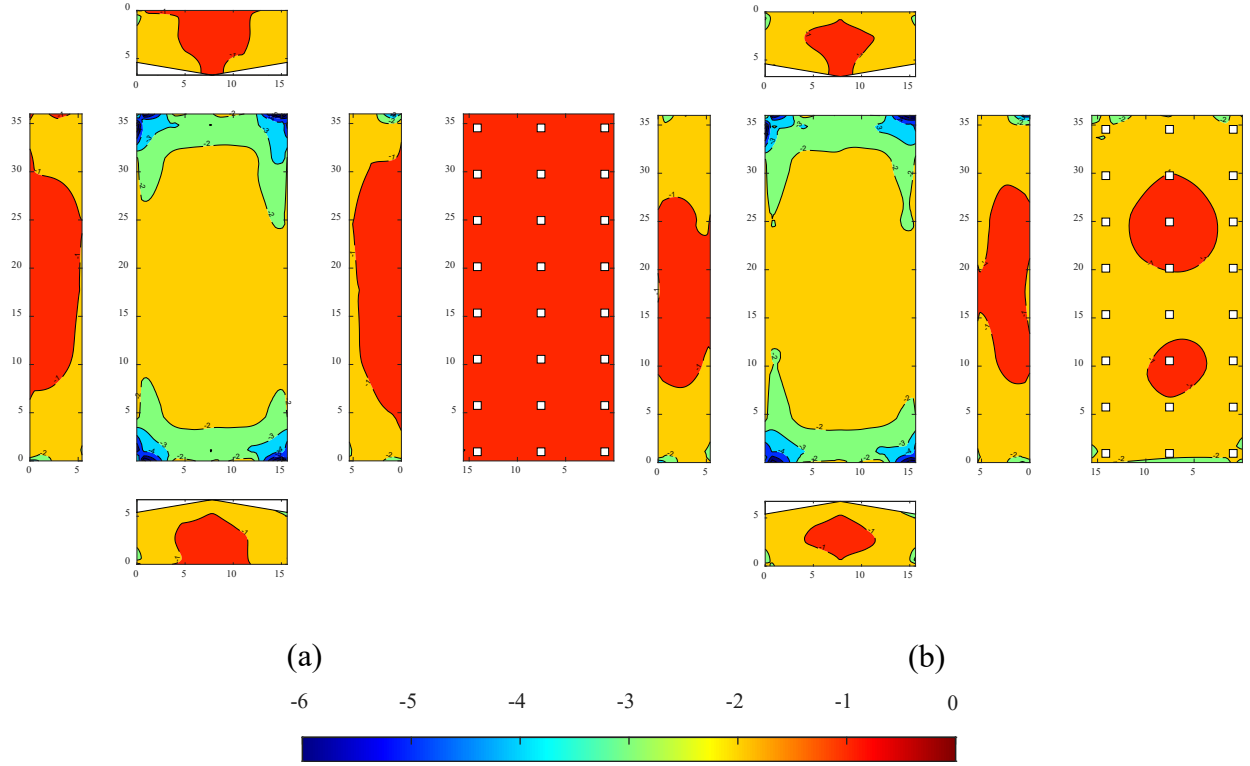


**Figure 12.** Critical minimum  $\hat{C}_p$  from all wind directions for Configuration (a) 1a and (b) 1b

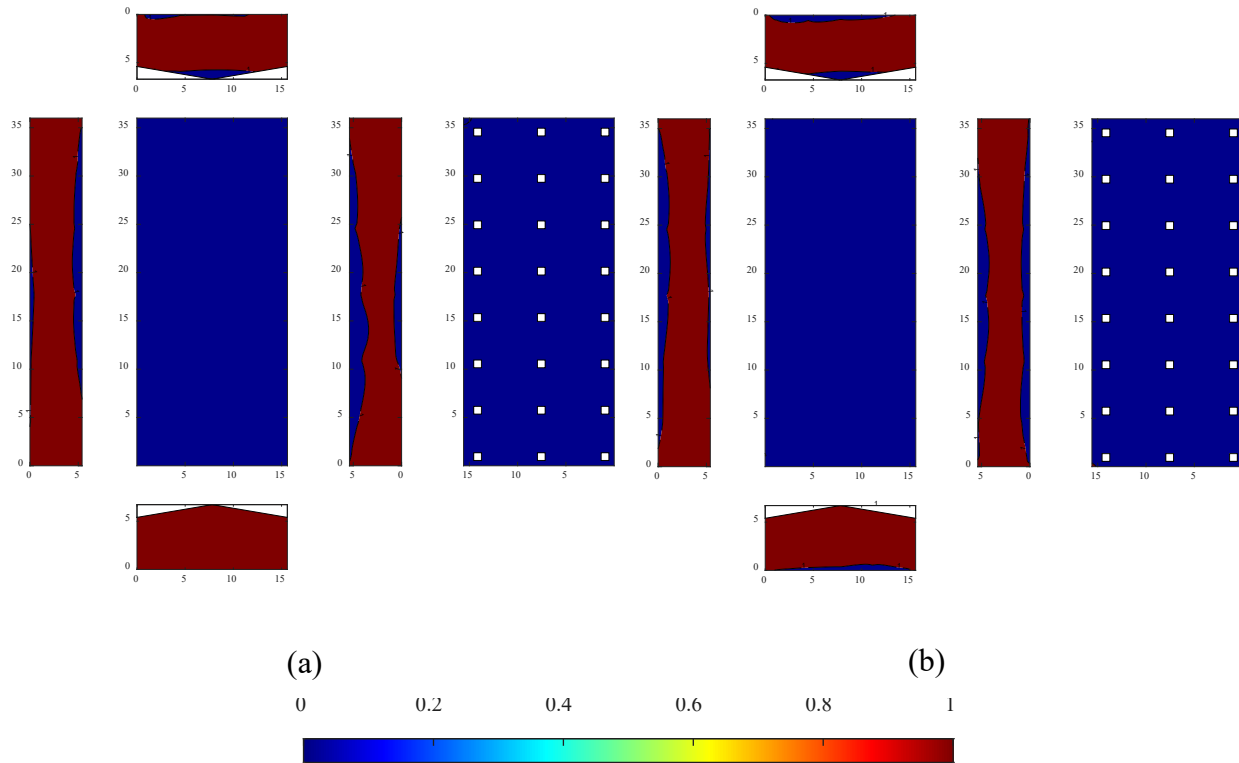


**Figure 13.** Critical maximum  $\hat{C}_p$  from all wind directions for Configuration (a) 1a and (b) 1b

The crawl space opening was shown to affect the  $\hat{C}_p$  distribution on the floor surface of the isolated MH model. For Configuration 1a where the skirt is present, a constant minimum  $\hat{C}_p$  of -1.0 was observed over the whole floor area. For open crawl space (as in Configuration 1b), the minimum  $\hat{C}_p$  ranged between -1.0 and -3.0 with the lowest magnitudes being detected at the floor center. The highest peak suctions occurred near the floor leading edges due to flow separation being significant in the absence of the skirt. Maximum  $\hat{C}_p$  on the floor surface were close to 0, meaning that the floor is subjected to suctions only.

### 3.1.2 Force and moment coefficients

Mean and peak force ( $\bar{C}_F$  and  $\hat{C}_F$ ) and moment ( $\bar{C}_M$  and  $\hat{C}_M$ ) coefficients are presented in **Figure 14** and **Figure 15** for the isolated MH model (Configurations 1a and 1b) for the range of wind directions between  $0^\circ$  and  $350^\circ$ .

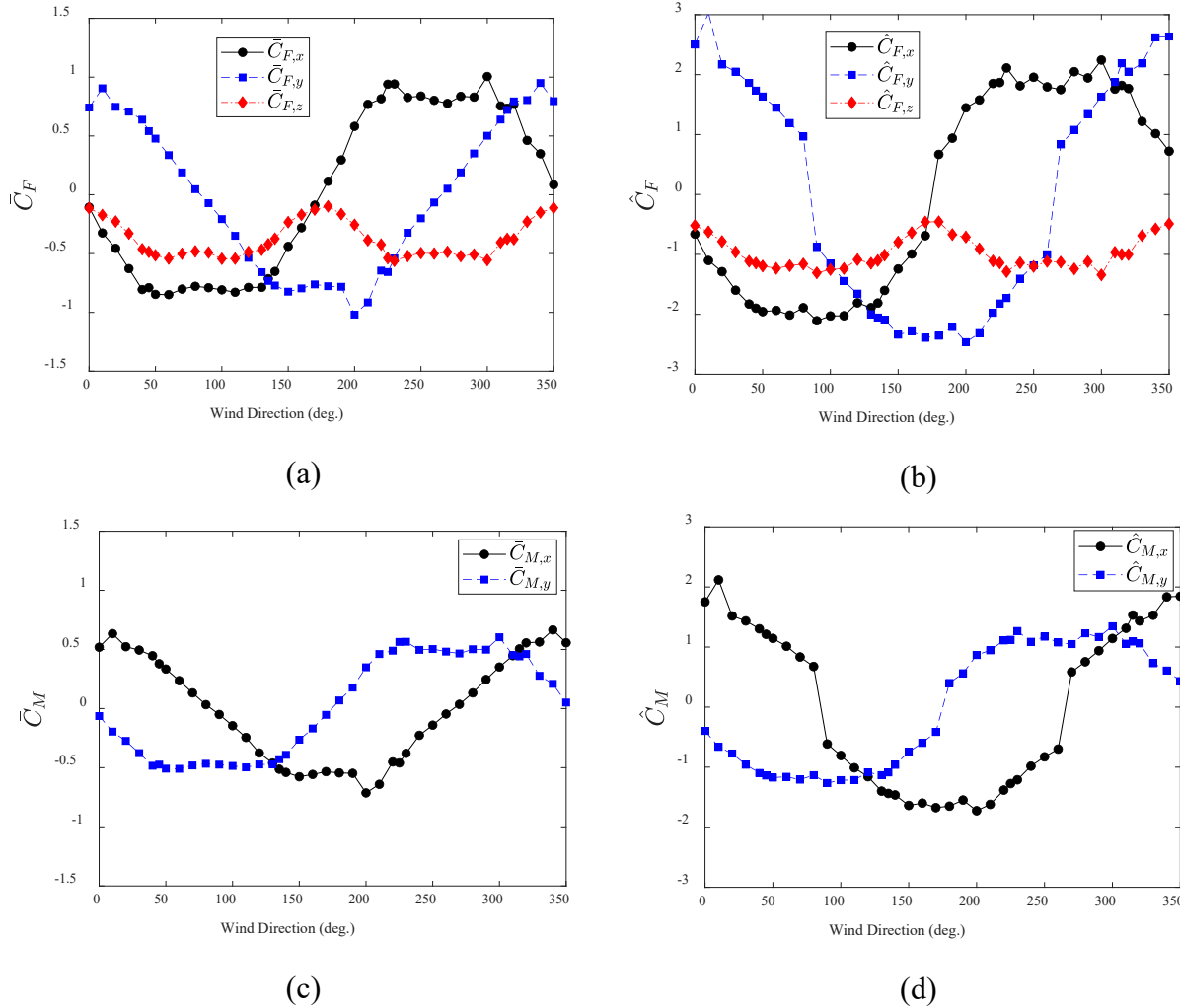


**Figure 14.** Configuration 1a: (a)  $\bar{C}_F$ , (b)  $\hat{C}_F$ , (c)  $\bar{C}_M$ , and (d)  $\hat{C}_M$

From a design perspective, force and moment coefficients can be used to calculate the base shear and base overturning moments, important loads in the wind design of the foundation system. The largest  $\bar{C}_{Fx}$  of +/-1.0 and  $\hat{C}_{Fx}$  of +/-2.0 acting normal to the East and West walls (parallel to the ridge) were observed for wind directions of 90° and 270°. On the other hand,  $\bar{C}_{Fy}$  and  $\hat{C}_{Fy}$  acting normal to the gable ends are the largest for 0° and 180° wind directions ( $\bar{C}_{Fy} = 1.0$  and  $-1.0$ ;  $\hat{C}_{Fy} = 3.0$  and  $-2.5$  for 0° and 180°, respectively). In addition, it was observed that the magnitude of  $\bar{C}_{Fx}$  and  $\hat{C}_{Fx}$  increased as  $\bar{C}_{Fy}$  and  $\hat{C}_{Fy}$  decreased, and vice versa. This indicates that the drag coefficients  $C_{Fx}$  and  $C_{Fy}$  are the most critical when they are parallel to the wind direction. Similar observations were made for the moment coefficients: the largest  $\bar{C}_{Mx}$  of +/-0.7 and  $\hat{C}_{Mx}$  of +/-2.0

were detected for  $0^\circ$  and  $180^\circ$ , while the largest  $\bar{C}_{My}$  of  $\pm 0.5$  and  $\hat{C}_{My}$  of  $\pm 1.5$  were observed for  $0^\circ$  and  $90^\circ$ , which are in line with the critical directions of  $C_{Fy}$  and  $C_{Fx}$ , respectively.

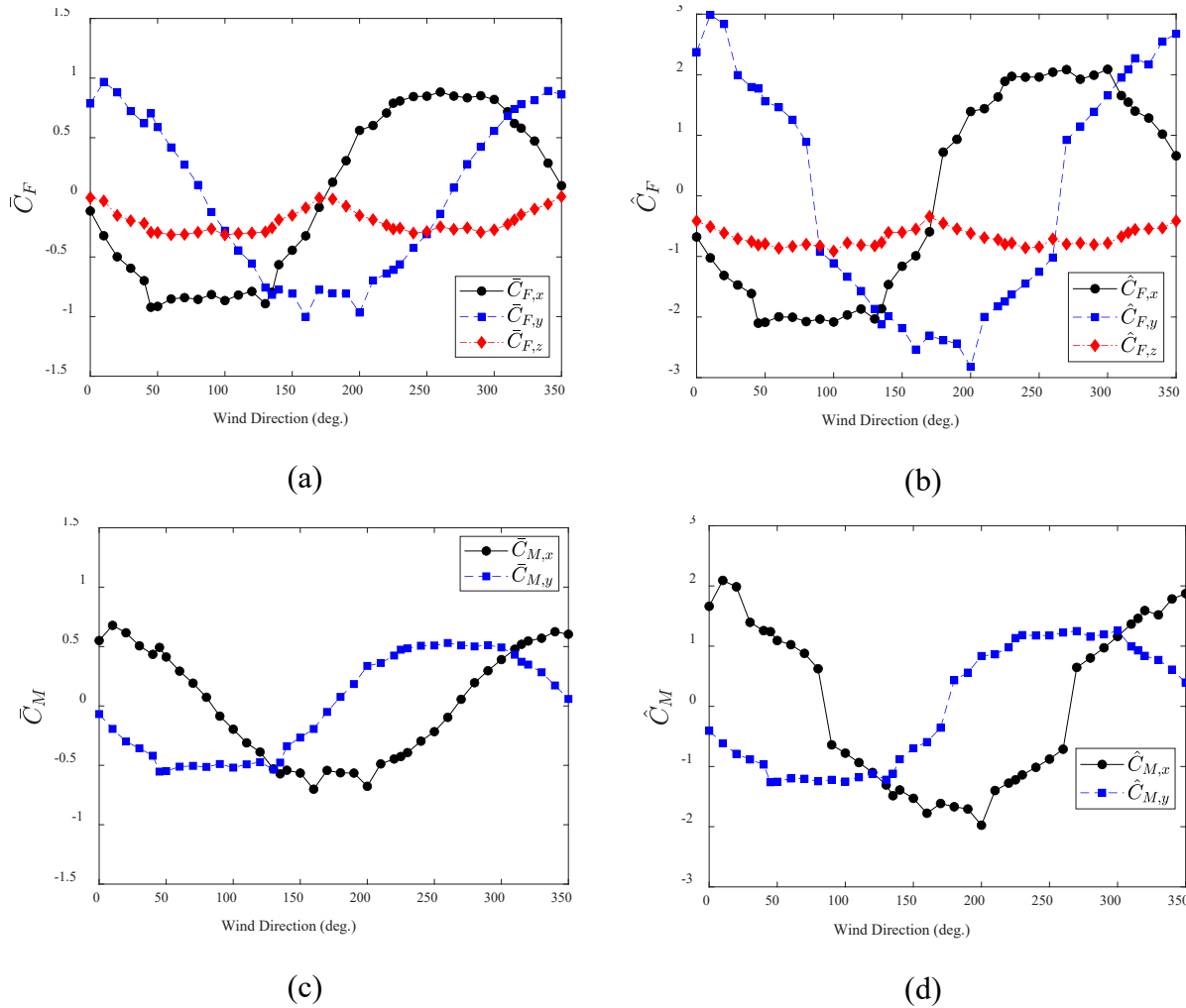


**Figure 15.** Configuration 1b: (a)  $\bar{C}_F$ , (b)  $\hat{C}_F$ , (c)  $\bar{C}_M$ , and (d)  $\hat{C}_M$

The mean and peak lift coefficients  $\bar{C}_{Fz}$  and  $\hat{C}_{Fz}$ , acting normal to the roof surface, are the highest for cornering winds. For instance, the lift coefficients were higher in magnitude for Configuration 1a than 1b (e.g.,  $\hat{C}_{Fz} = -1.5$  versus  $-1.0$  for  $45^\circ$ ). This is due to the floor suction being more significant for Configuration 1b, thus alleviating the overall lift coefficients on the MH with open crawl space.

## 3.2 Shielding effects on the wind loading

### 3.2.1 Fully shielded cases with skirt

The peak force and moment coefficients are presented in **Figure 16** for the fully shielded configurations with partially-enclosed crawl space (i.e., Configurations 2a, 5a, and 8a) as a function of wind direction. Comparative analysis revealed that Configuration 8a is the most critical among the three fully shielded configurations being considered. More specifically, the largest  $\hat{C}_{Fx}$  of +/-2.0,  $\hat{C}_{Fy}$  of +/-3.0, and  $\hat{C}_{Fz}$  of -1.5 were observed for Configuration 8a, compared to peaks of +/-1.0, +/-1.8, and -0.8 for Configuration 5a, respectively. For  $\hat{C}_{Mx}$  and  $\hat{C}_{My}$  of Configuration 8a, the values were +/-2.0 and +/-1.5 compared to +/-1.0 and +/-0.5, respectively. This may be attributed to the shielded community layout of Configuration 8a being the most irregular with larger spacing between the adjacent MH units.

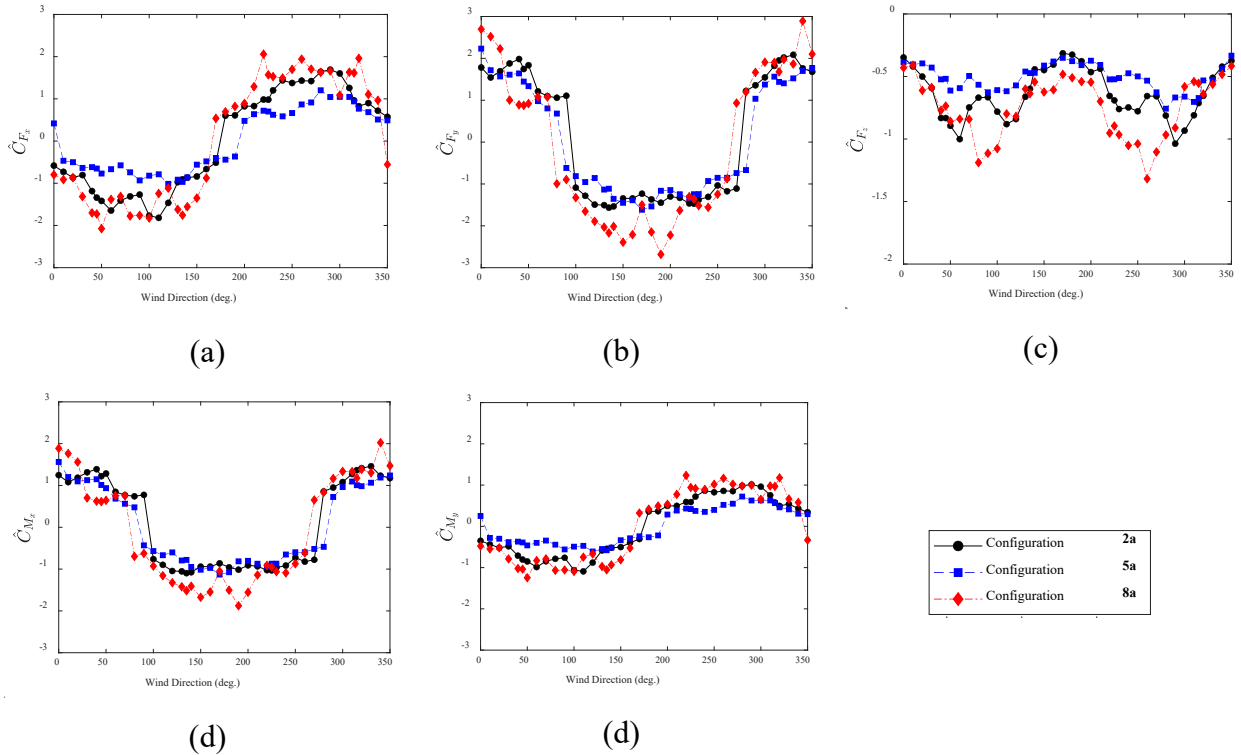


**Figure 16.** Fully shielded cases with skirt: (a)  $\hat{C}_{Fx}$ , (b)  $\hat{C}_{Fy}$ , (c)  $\hat{C}_{Fz}$ , (d)  $\hat{C}_{Mx}$ , and (e)  $\hat{C}_{My}$

The largest peak suctions were observed at the roof corners for Configuration 8a, as shown in **Figure 17**, due to the flow separation being more significant for this particular MH arrangement. In addition, a speed-up in the wind flow caused larger peak positive wind loads on the walls. Compared to the isolated MH of Configuration 1a, peak force and moment coefficients were

shown to be alleviated by up to 50% for Configurations 2a and 5a due to the shielding effects. For example,  $\hat{C}_{FX}$ ,  $\hat{C}_{FY}$ , and  $\hat{C}_{FZ}$  of +/-1.0, +/-1.5, and -0.8, respectively, were observed for Configuration 5a, compared to values of +/-2.0, +/-2.5, and -1.5 for Configuration 1a, respectively.

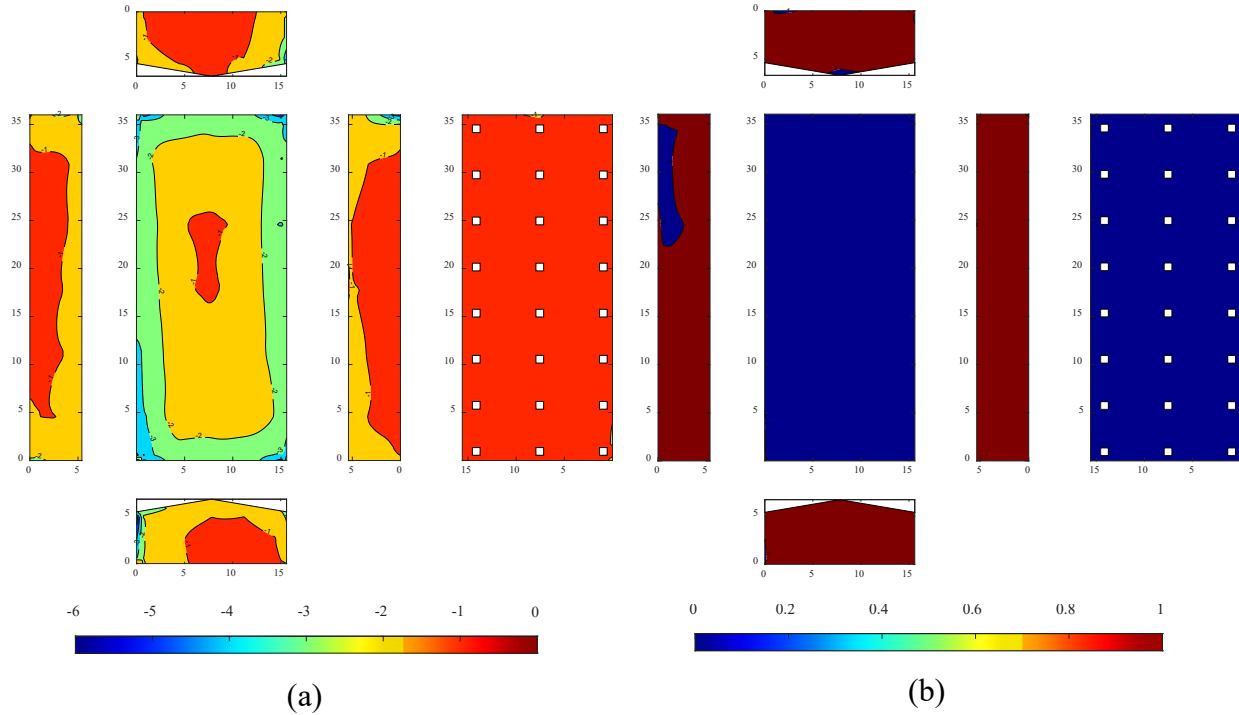


**Figure 17.** Critical (a) minimum and (b) maximum  $\hat{C}_p$  from all wind directions for Configuration 8a

### 3.2.2 Partially shielded cases with skirt

The peak force and moment coefficients are presented in **Figure 18** for the partially shielded configurations with a skirt (i.e., Configurations 3a, 4a, 6a, 7a, 9a, and 10a) as a function of wind direction. No significant differences were observed between the peak wind loads for the different partially shielded cases. In addition, the largest peak force and moment coefficients for the partially shielded cases are comparable to the most critical fully shielded case (Configuration 8a). This indicates that the wind-induced on the foundation (i.e., base shear and overturning moments) may not be affected by the shielding extent. Such effects would rather be more significant for local pressures [see **Figure 19**], needed for the design of components and cladding.



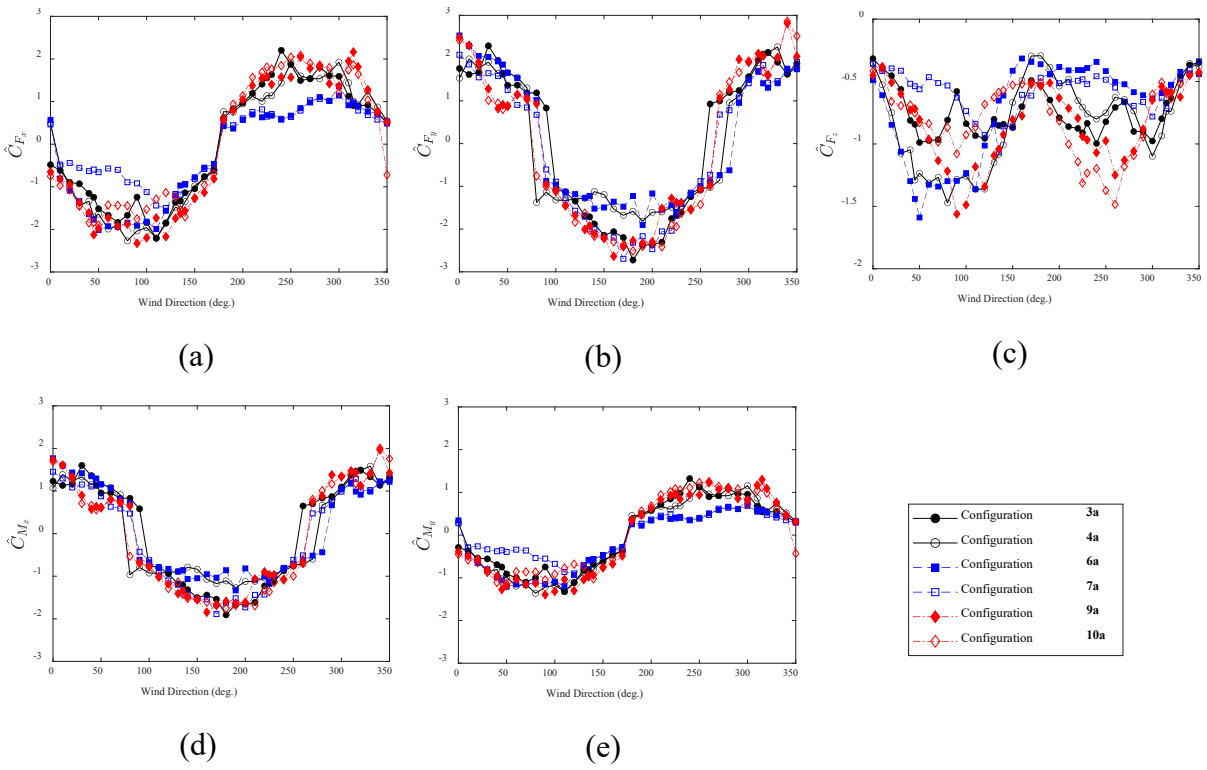


**Figure 18.** Partially shielded cases with skirt: (a)  $\hat{C}_{F_x}$ , (b)  $\hat{C}_{F_y}$ , (c)  $\hat{C}_{F_z}$ , (d)  $\hat{C}_{M_x}$ , and (e)  $\hat{C}_{M_y}$

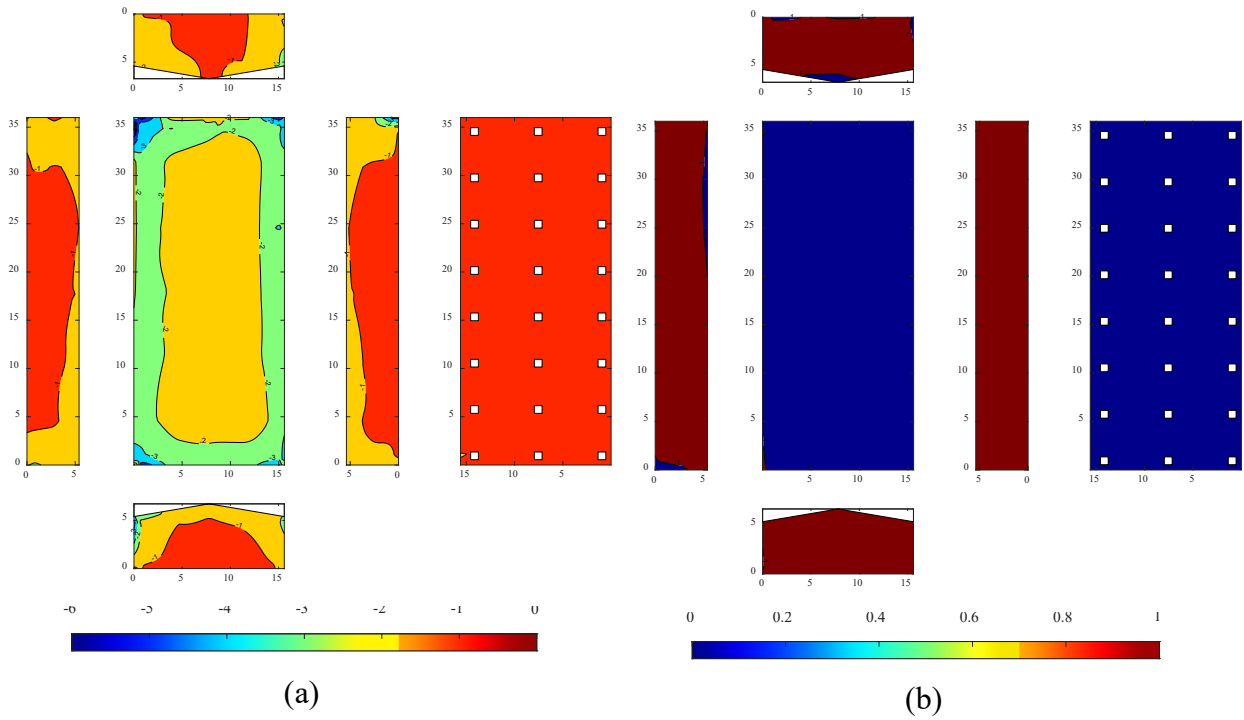


**Figure 19.** Critical (a) minimum and (b) maximum  $\hat{C}_p$  from all wind directions for Configuration 9a

#### **4 Concluding Remarks**

This study evaluated wind loads on manufactured home (MH) communities using a large-scale state-of-the-art experimental facility. The main objective of the study was to investigate wind loads on both isolated and shielded MHs by considering typical community layouts in Florida. This entailed conducting aerodynamic experiments on 17 test configurations which were engulfed in simulated open terrain boundary layer flows at the WOW EF. Moreover, the study also considered the effect of open crawl spaces often caused by skirt failure. Statistics of pressure, force, and moment coefficients obtained from the collected pressure time histories were used to assess wind effects on MHs. Based on these results, the following concluding remarks are provided:

- The spatial pressure distribution on isolated MHs is similar to that of typical low-rise buildings. Critical peak roof suctions of up to -6.0 were recorded near the corners and leading edges.
- Floor pressures were significantly influenced by the porosity of the crawl space opening. While the use of a partially enclosed (50% porosity ratio) skirt resulted in lower suctions, the fully opened case caused higher suction on the edges of the floor and walls due to flow separation.
- The results showed that shielding effects can alleviate wind loads on MHs. The reduction in the base shear and moment was observed to be as much as 50%. In addition, shielding effects were found to be similar between the simulated community layouts with consistent observations between the fully- and partially shielded cases.

The findings of this study can be used to help improve the MH design provisions in current building design codes and standards as well as risk assessment models.

#### **Benefits to the State of Florida**

The research that was carried out has the potential to provide transformative impacts to new and existing mobile home parks, and to manufactured housing units through critical fundamental and practical knowledge that can change code provisions, policies, and manufacturing processes. The findings can inform new ASCE 7 provisions and lead to significantly improved HUD design standards for MH units. The findings can also be shared with MH builders and park owners and residents, as well as FEMA to inform new site development for post-disaster temporary housing

that uses manufactured homes. Findings are applicable beyond MH units used as permanent housing including post-disaster temporary shelters and housing used in the U.S. and internationally.

The research is important for Florida and Floridians (and the entire U.S.) in terms of understanding and reducing the vulnerability of MH units. The research activities helped in training students in three universities with expertise in hurricane damage mitigation.

### **Acknowledgment**

The authors would like to acknowledge the financial support from the State of Florida Division of Emergency Management (FDEM). The experiments at the NSF NHERI WOW EF were greatly facilitated by the fine work of WOW staff members Dr. Steven Diaz, Walter Conklin, Dr. Dejiang Chen, James Erwin, and Manuel Matus. The opinions, findings, conclusions, or recommendations expressed in this article are solely those of the authors and do not represent the opinions of the funding agencies.

## References

- ASCE. (2021). *Wind tunnel testing for buildings and other structures. ASCE Standard*, American Society of Civil Engineers (ASCE), Reston, VA, USA.
- ASCE. (2022). *Minimum Design Loads and Associated Criteria for Buildings and Other Structures*. American Society of Civil Engineers (ASCE), Reston, VA, USA.
- Chowdhury, A. G., Vutukuru, K. S., and Moravej, M. (2018). “Full- and Large-Scale Experimentation Using the Wall of Wind to Mitigate Wind Loading and Rain Impacts on Buildings and Infrastructure Systems.” *Proceedings of the 11th Structural Engineering Convention (SEC18)*, Jadavpur University, Kolkatta, India.
- Chowdhury, A. G., Zisis, I., Irwin, P., Bitsuamlak, G., Pinelli, J. P., Hajra, B., and Moravej, M. (2017). “Large-scale experimentation using the 12-fan wall of wind to assess and mitigate hurricane wind and rain impacts on buildings and infrastructure systems.” *Journal of Structural Engineering (United States)*, 143(7), 1–16.
- ESDU. (2001). “Characteristics of the Atmospheric Boundary Layer, Part II: Single Point Data for Strong Winds (Neutral Atmosphere) (Item 85020). Engineering Sciences Data Unit.” Engineering Science Data Unit.
- FEMA. (2004). *Mitigation Assessment Team Report: Hurricane Charley in Florida*.
- FEMA. (2006). *Summary Report on Building Performance: Hurricane Katrina 2005*.
- HUD. (2021). “MANUFACTURED HOME CONSTRUCTION AND SAFETY STANDARDS.” US Department of Housing and Urban Development.
- IBTS. (2005). *Assessment of Damage to Manufactured Homes Caused by Hurricane Charley*.
- Irwin, H., Cooper, K. R., and Girard, R. (1979). “Correction of distortion effects caused by tubing systems in measurements of fluctuating pressures.” *Journal of Wind Engineering and Industrial Aerodynamics*, Elsevier, 5(1–2), 93–107.
- Lieblein, J. (1974). *Efficient methods of extreme-value methodology. NBSIR 74-602*, Washington DC.
- Longinow, A. (2004). “Wind Loads and Anchoring for Manufactured Housing.” *Practice*

*Periodical on Structural Design and Construction*, 9(4), 207–210.

Marshall, R. D. (1977). “The Measurement of Wind Loads on a Full-Scale Mobile Home.” (September), 142.

Marshall, R. D. (1993). “Wind Load Provisions of the Manufactured Home Construction and Safety Standards - A Review and Recommendations for Improvement.” 103.

Sutley, E. J., Vazquez, K., Kim, J. H., Dao, T., Johnston, B., and Hunt, J. (2020). “Performance of Manufactured Housing during Hurricanes Irma and Michael.” *Journal of Performance of Constructed Facilities*, 34(4), 1–11.

U.S. Census. (2022). “U.S. Manufactured Housing Shipments by State: 2021.” <<https://www.census.gov/library/visualizations/2021/econ/2021-shipments-map.html>> (Jul. 27, 2022).



*A Resource for the State of Florida*

**Section 2 Part B**  
**Nonlinear Dynamic Analysis of Manufactured Homes subject to  
Hurricane-induced Wind Loads: Numerical Modeling - Initial  
Study**

*A Research Project Funded by:*  
**The State of Florida Department of Emergency Management**

**Investigators:** Thang Dao  
Associate Professor  
Associate Editor, ASCE Journal of Structural Engineering  
Civil, Construction, and Environmental Engineering  
[The University of Alabama](#)

Farhan Chowdhury  
Postdoctoral Research Aide  
Civil, Construction, and Environmental Engineering  
[The University of Alabama](#)

## I. Introduction

As the housing affordability crisis has deepened in the United States, manufactured home units (MHU) are gaining traction as a viable alternative to meet rural and low-income households' long-term, affordable housing needs. However, there are major shortcomings in current building codes for connections and components of MHUs that make them vulnerable to damage from hurricane-induced wind loads. There is limited existing work on numerical modeling approaches to light-frame wood construction (LFWC) subject to wind loads. It is noted, however, that light-frame wood structures and MHUs differ in size of members, types of materials, methods of construction, weights of resulting structures, and failure mechanisms, and, therefore, they need to be studied separately.

Most nonlinear numerical models for light-frame wood buildings focus on seismic effect studies with an emphasis on shear wall (in-plane) modeling for seismic loading (Filiatrault and Folz, 2002; Christovasilis and Filiatrault, 2010; Xu and Dolan, 2009; van de Lindt et al., 2012; Hafeez et al., 2014). Collins et al. (2005) performed numerical analysis to provide the basic understanding required for the development of improved design procedures for light-frame wood buildings subject to lateral loads. Unlike seismic loading, wind loads on buildings often cause out-of-plane failure in the building envelope, such as roof sheathings or walls, and uplift failure due to a deficient vertical load path. Additionally, in earthquake engineering, hysteresis model used to predict the cyclic behavior of the structural component needs to account for both the positive and negative displacements. In wind engineering, depending on the modeled components, the cyclic loading may include only one-side (either negative or positive) or two-side (negative and positive) displacements. Therefore, the hysteresis model needs to be adjusted accordingly.

The **objective** of this study is to develop the numerical (FE) model to investigate the short-term cumulative damage on the MHU structural system under dynamic wind loads. The numerical model for structural components, such as fasteners and roof-sheathing, will use nonlinear load-deflection relationships to predict the responses under high deflections in extreme wind conditions. The model will be calibrated with the

pressure coefficient time histories obtained from the experimental study by K.U. and the test data on pressure coefficient will be used to apply input aerodynamic loading on MHU's roof, wall, and the under-deck surfaces. The wind pressure data measured at taps will be interpolated at nodal coordinates and integrated into wind load time histories at element nodes for numerical structural dynamic model. The hysteresis behavior of components and connections, for the nonlinear load-displacement curves, will be applied based on the findings from the experiment.

The development of performance-based design (PBD) in the field of structural wind engineering requires the numerical model to be capable of predicting the explicit performance of structure beyond the capacity and first failure of the building envelope. For example, uplift of the edge of the roof sheathing panel under wind loads may require a nonlinear roof sheathing fastener model that can accurately represent the unique characteristics of fastener/wood fiber interaction by considering the effect of load eccentricity on the coupled withdrawal-moment capacity (Dao and van de Lindt, 2008).

In the first year of **current study**, the conceptual numerical model of roof of a single-story MHU in Wind Zone II will be analyzed under dynamic wind loads using a three-dimensional (3D) nonlinear finite element (FE) formulation of MHU components—roof sheathing, truss members, and fasteners (nails) to predict roof performance.

## II. Background on Manufactured Homes

According to the Manufactured Housing Institute's National Communities Council (MHINCC), manufactured homes "are homes built entirely in the factory under a federal building code administered by the U.S. Department of Housing and Urban Development (HUD). The Federal Manufactured Home Construction and Safety Standards (commonly known as the HUD Code) went into effect June 15, 1976. Manufactured homes may be single- or multi-section and are transported to the site and installed." The MHINCC distinguishes among several types of factory-built housing: manufactured homes, modular



homes, panelized homes, pre-cut homes, and mobile homes. Mobile home “is the term used for manufactured homes produced prior to June 15, 1976, when the HUD Code went into effect.”

According to MHI, more than 43,000 land-lease manufactured/mobile home communities exist in the U.S., with an estimated 4.3 million home sites, providing accommodation for nearly 22 million people.

Current building codes and practices, for either manufactured or site-built homes, are not designed to withstand severe tornadoes. A direct hit from a tornado will bring about severe damage or destruction of any home in its path—site-built or manufactured. With winds more than 140 miles-per-hour, thousands of site-built and manufactured homes suffered extensive damage from **Hurricane Andrew** in 1992. In July 1994, HUD issued revisions to the wind safety provision of the HUD Code, with further updates issued in 2005–2007. Now, in areas prone to hurricane-force winds (known as Wind Zones II and III according to HUD’s Basic Wind Zone Map), the standards for manufactured homes are equivalent to the current regional and national building codes for site-built homes in these wind zones ([Manufactured Housing Institute, 2017](#)).

### III. Literature Review

[Dao and van de Lindt \(2013; 2014\)](#) investigated the **seismic** performance of an innovative light-frame cold-formed steel (CFS) frame for midrise building by performing a series of reversed-cyclic tests of subassembly structures and developed a numerical model for nonlinear time history analysis using an 11-parameter **hysteretic** spring model for v-braced panels built upon the work of [Folz and Filiatrault \(2001\)](#) on light-frame wood shear walls and fitted to the test data. They found that the framing system performed very well at both the individual panel and global building levels in a moderate earthquake and provided good ductility because of energy dissipation of the connections. The global and local responses were smaller than the drift limits set by the performance expectation levels of life safety (LS) and collapse prevention (CP) during the Northridge earthquake of 1994 at DBE and MCE level, and the CP performance level controls the design, which is typical for midrise buildings.

Other numerical studies involving phenomenological hysteretic model for building lateral load resisting systems under reverse-cyclic loading include [Boudaud et al. \(2015\)](#) and [Usefi et al. \(2019\)](#). The first paper presents the seismic behavior of a finite element (FE) model of timber-framed shear wall under dynamic load based on a 16-parameter hysteretic constitutive law for nail joints modeled using asymmetric Bezier curve and calibrated with quasi-static test data. The refined FE model predictions were in good agreement with the shake table experimental data under seismic loading. The second paper reviews several numerical studies for seismic response of cold-formed steel (CFS) shear walls involving different hysteresis models with or without strength degradation parameters, and remarks on their strengths and limitations.

[Lacourt et al. \(2016\)](#), [Lim et al. \(2017\)](#), [Izzi et al. \(2018\)](#), and [Dong et al. \(2021\)](#) all present various form of hysteresis models in their numerical studies on dowel-type timber joints and nail connections.

All hysteresis models discussed above are focused on seismic behavior of structural components and no hysteresis model is found that's specifically developed for wind response on structures.

[Dao and van de Lindt \(2008\)](#) proposed a new nonlinear roof sheathing fastener (nail) model described using a nonlinear spring element that possesses six degrees of freedom (**6-DOF**) at each node. This nail model is targeted for use in finite element **wind load** applications of wood-frame roof systems and is a function of not only the uplift pressure acting on the roof sheathing, but also the effective moment arm (not just the moment) acting on the edge nails. The model is shown to result in a significantly reduced capacity when compared to finite element models that assume only nail withdrawal.

In their next paper, [van de Lindt and Dao \(2009\)](#) presented a fragility-based approach to performance-based design (**PBD**) of wood-frame buildings for wind load, where they included their new 6-DOF nail model to the finite-element analysis (FEA) of a light-frame wood building. Additionally, shell elements formulated using eight-node elements were used to model the oriented strand board (OSB) roof sheathing panel. Beam elements were used for the truss members. When shear walls were modeled for lateral capacity in the

structural integrity limit state, a nonlinear spring element was used, which is consistent with the state-of-the-art earthquake pushover analysis. In the numerical analyses, the pressure applied on the panel was divided into steps small enough so that the axial force and displacement in the nails were able to follow their empirical relationship. Four performance expectation levels were addressed in this study linking them to a peak 3-s gust and fragilities were developed.

In the above-mentioned study, wind forces acting on the structure and components were calculated using ASCE 7-05 ([ASCE 2005](#)) wind pressures, even though the focus was intended to be on PBD and not on ASCE 7. The wind force was modeled based on [Ellingwood \(1999\)](#), as

$$\bar{w} = 0.8w_n$$

$$\sigma_w = 0.35\bar{w}$$

where  $\bar{w}$ =mean of the wind force;  $w_n$ =nominal wind force; and  $\sigma_w$ =standard deviation of the wind force.

The ASCE 7 directional procedure of wind load calculation is based on **static** analysis, and therefore, the motivation of the current study described in this paper would be to apply **dynamic** analysis procedure for wind force calculation based on the wind tunnel test results.

[He et al. \(2017; 2018\)](#) reviewed and studied the performance of light-frame wood low-rise buildings under wind loads through wind tunnel test and validated finite-element models.

[Estephan et al. \(2021\)](#) performed characterization of wind-induced pressure on membrane roofs based on full-scale wind tunnel testing at FIU to study the effect of roof flexibility on wind-induced pressure. However, their study did not include the dynamic aspect and geometrical nonlinearity of the load-bearing behavior for membrane structures.

[Jeong et al. \(2021\)](#) carried out performance-based wind design (PBWD) of RC building using time-history wind load generated from power spectral density (PSD) functions, as opposed to conducting wind tunnel tests.

Mohammadi et al. (2019) presented a performance-based evaluation of an existing 47-story steel moment frame high-rise building under extreme wind loads using a 3-D nonlinear finite-element model and an **incremental dynamic analysis (IDA)**. The nonlinear cyclic response of **shear tab gravity connections** was considered in this model by incorporating the OpenSEES *Pinching4* element with the parameters calibrated by Elkady and Lognos (2015) using the experimental data by Liu and Astaneh-Asl (2000).

#### IV. Nail Withdrawal Test (K.U.)

K.U. researchers performed nail withdrawal tests to obtain the hysteresis model parameters of nails. The data will be provided to University of Alabama (UA) team for calibration of the numerical model. Full analysis of the connection behavior will be provided by UA team when the data is available.

#### V. Wind Tunnel Test (F.I.U.)

Wind load statistics for each roof sheathing panel (RSP) for each **hurricane hour** considered must be determined (Dao and van de Lindt, 2012; Dao et al., 2012).

Wind tunnel test data from FIU were used to estimate the mean value of the **pressure coefficient** on the RSP of the manufactured home unit under consideration.

A set of boundary-layer wind tunnel tests was conducted on a 1:20 scaled model gable roof structure with pressure taps installed on the roof. The tests were performed in the 12-fan WOW facility at FIU. The pressure at each tap on the roof was recorded as a **time series** for different wind directions, from which the pressure coefficient time history was calculated. Dimensional analysis would be performed to scale up the time series data.

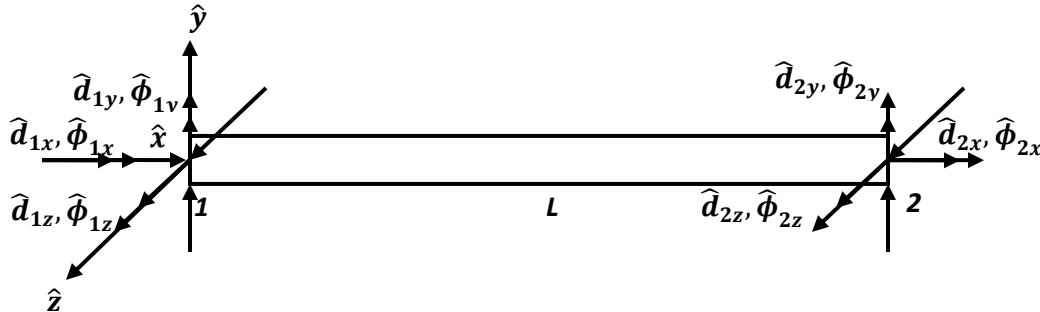
## VI. Numerical Analysis (U.A.)

### 1. Finite-Element Formulation

The failures of wood-frame structures under wind load will typically occur at the connections between structural components, e.g., the nails that connect the OSB to the trusses in roof systems, and not the members themselves. To transfer the force and moment from the OSB to the truss members, the nail elements are modeled after [Dao and van de Lindt \(2008\)](#) using a **nonlinear spring** with six degrees of freedom (three translational and three rotational DOFs) at each node. Eight-node plate and shell elements are used to model the OSB roof sheathing panels. Truss members, wood beams, and columns are modeled using beam elements. Shear walls, when present, are modeled using a nonlinear spring element.

#### 1.1. Member Elements:

Beam element is used to model wall studs, roof trusses, and other beam/joist structures.



$\hat{d}_{1x}, \hat{d}_{1y}, \hat{d}_{1z}$  are translational displacements at end 1

$\hat{d}_{2x}, \hat{d}_{2y}, \hat{d}_{2z}$  are translational displacements at end 2

$\hat{\phi}_{1x}, \hat{\phi}_{1y}, \hat{\phi}_{1z}$  are rotational displacements at end 1

$\hat{\phi}_{21x}, \hat{\phi}_{2y}, \hat{\phi}_{2z}$  are rotational displacements at end 2

$\hat{x}, \hat{y}, \hat{z}$  are local coordinates

*Figure 1-Local coordinates for member element*

Local stiffness matrix:

Each member element includes two ends (Figure 3.1), six dofs for each end, therefore each member element has 12 dofs. The stiffness matrix  $[K_e]$  in local coordinates can be derived by shape functions or directly from the displacement method, both of which yield the same result. This stiffness matrix can be expressed as

$$[K_e] = \begin{bmatrix} \frac{EA}{L} & 0 & 0 & 0 & 0 & 0 & -\frac{EA}{L} & 0 & 0 & 0 & 0 & 0 \\ 0 & \frac{12EI_z}{L^3} & 0 & 0 & 0 & \frac{6EI_z}{L^2} & 0 & -\frac{12EI_z}{L^3} & 0 & 0 & 0 & \frac{6EI_z}{L^2} \\ 0 & 0 & \frac{12EI_y}{L^3} & 0 & -\frac{6EI_y}{L^2} & 0 & 0 & 0 & -\frac{12EI_y}{L^3} & 0 & -\frac{6EI_y}{L^2} & 0 \\ 0 & 0 & 0 & \frac{GJ}{L} & 0 & 0 & 0 & 0 & 0 & -\frac{GJ}{L} & 0 & 0 \\ 0 & 0 & -\frac{6EI_y}{L^2} & 0 & \frac{4EI_y}{L} & 0 & 0 & 0 & \frac{6EI_y}{L^2} & 0 & \frac{2EI_y}{L} & 0 \\ 0 & \frac{6EI_z}{L^2} & 0 & 0 & 0 & \frac{4EI_z}{L} & 0 & -\frac{6EI_z}{L^2} & 0 & 0 & 0 & \frac{2EI_z}{L} \\ -\frac{EA}{L} & 0 & 0 & 0 & 0 & 0 & \frac{EA}{L} & 0 & 0 & 0 & 0 & 0 \\ 0 & -\frac{12EI_z}{L^3} & 0 & 0 & 0 & -\frac{6EI_z}{L^2} & 0 & \frac{12EI_z}{L^3} & 0 & 0 & 0 & -\frac{6EI_z}{L^2} \\ 0 & 0 & -\frac{12EI_y}{L^3} & 0 & \frac{6EI_y}{L^2} & 0 & 0 & 0 & \frac{12EI_y}{L^3} & 0 & \frac{6EI_y}{L^2} & 0 \\ 0 & 0 & 0 & -\frac{GJ}{L} & 0 & 0 & 0 & 0 & 0 & \frac{GJ}{L} & 0 & 0 \\ 0 & 0 & -\frac{6EI_y}{L^2} & 0 & \frac{2EI_y}{L} & 0 & 0 & 0 & \frac{6EI_y}{L^2} & 0 & \frac{4EI_y}{L} & 0 \\ 0 & \frac{6EI_z}{L^2} & 0 & 0 & 0 & \frac{2EI_z}{L} & 0 & -\frac{6EI_z}{L^2} & 0 & 0 & 0 & \frac{4EI_z}{L} \end{bmatrix} \quad (1)$$

where  $A$  is the cross-sectional area,  $E$  is the elastic modulus,  $L$  is the length of the member;  $I_y$  and  $I_z$  are moment of inertia in  $y$  and  $z$  direction and  $I_x$  is the torsional constant of the member.

The force vector:

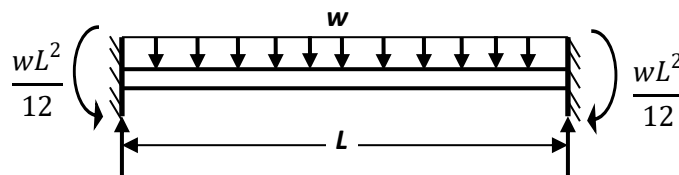


**Figure 2-End reactions of member under uniform distributed load**

For a uniformly distributed load  $q$  applied on each member, the force vector in local coordinates is formulated as

$$\{\mathbf{F}_{ed}\} = \begin{bmatrix} \frac{w_x L}{2} & \frac{w_y L}{2} & \frac{w_z L}{2} & 0 & -\frac{w_z L^2}{12} & \frac{w_y L^2}{12} & \frac{w_x L}{2} & \frac{w_y L}{2} & \frac{w_z L}{2} & 0 & \frac{w_z L^2}{12} & -\frac{w_y L^2}{12} \end{bmatrix} \quad (2)$$

where  $w_x, w_y, w_z$  are the uniformly distributed force in the  $\hat{x}, \hat{y}$  and  $\hat{z}$  directions, respectively;  $L$  is the length of the member.

*The transformation matrix*

In order to solve the stiffness equation for the structure, the expressions in local coordinates must be expressed in global coordinates. In the local coordinate system, the equilibrium equation can be expressed as

$$[\mathbf{K}_e]\{\mathbf{d}_e\} = \{\mathbf{F}_{ed}\} \quad (3)$$

where  $[\mathbf{K}_e]$  is the local stiffness matrix,  $\{\mathbf{d}_e\}$  is the local displacement vector;  $\{\mathbf{F}_{ed}\}$  is the local force vector due to the distributed load. The relationships between the global displacement vector and the local displacement vector can be expressed as:

$$\{\mathbf{d}_e\} = [\mathbf{T}]\{\mathbf{d}\} \quad (4)$$

where  $[\mathbf{T}]$  is the transformation matrix,  $\{\mathbf{d}\}$  is the global displacement vector. Substituting equation (4) into equation (3) yields

$$[\mathbf{K}_e][\mathbf{T}]\{\mathbf{d}\} = \{\mathbf{F}_{ed}\} \quad (5)$$

Multiplying  $[\mathbf{T}]^T$  with both sides of equation (3.5) gives

$$[\mathbf{T}]^T[\mathbf{K}_e][\mathbf{T}]\{\mathbf{d}\} = [\mathbf{T}]^T\{\mathbf{F}_{ed}\} \quad (6)$$

but since

$$[\mathbf{T}]^T[\mathbf{K}_e][\mathbf{T}] = [\mathbf{K}]_M \quad (7)$$

and 
$$[\mathbf{T}]^T \{\mathbf{F}_{ed}\} = \{\mathbf{F}\}_M \quad (8)$$

where  $[\mathbf{K}]_M$  is member global stiffness matrix and  $\{\mathbf{F}\}_M$  is member global force vector, one can write

$$[\mathbf{K}]_M = [\mathbf{T}]^T [\mathbf{K}_e] [\mathbf{T}] \quad (9)$$

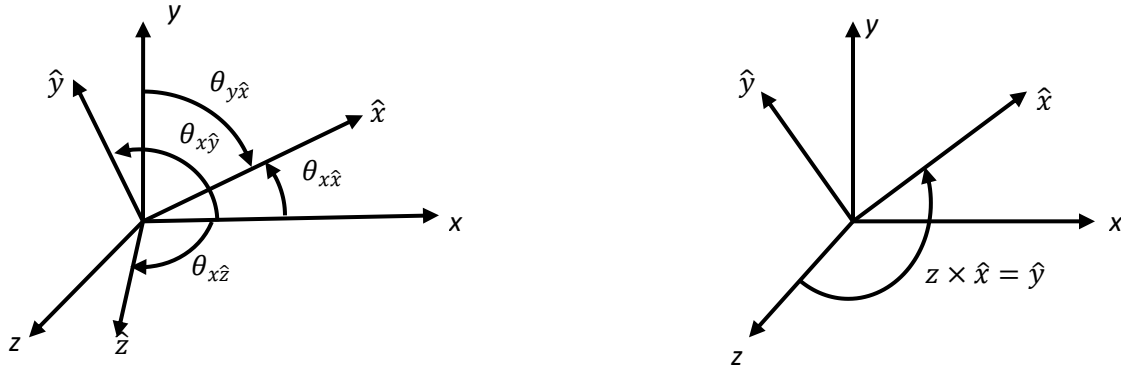


*Figure 3-Local and global coordinates*

In order to compute transformation matrix  $[\mathbf{T}]$ , we assume that the local  $y$  coordinates of members always parallel to  $xOy$  surface of global coordinates. We have:

$$[\mathbf{T}] = \begin{bmatrix} [\mathbf{T}_{3D}] & [\mathbf{O}] & [\mathbf{O}] & [\mathbf{O}] \\ [\mathbf{O}] & [\mathbf{T}_{3D}] & [\mathbf{O}] & [\mathbf{O}] \\ [\mathbf{O}] & [\mathbf{O}] & [\mathbf{T}_{3D}] & [\mathbf{O}] \\ [\mathbf{O}] & [\mathbf{O}] & [\mathbf{O}] & [\mathbf{T}_{3D}] \end{bmatrix}; \quad (10)$$

$$[\mathbf{T}_{3D}] = \begin{bmatrix} l & m & n \\ -\frac{m}{D} & \frac{l}{D} & 0 \\ -\frac{l \cdot n}{D} & -\frac{m \cdot n}{D} & D \end{bmatrix} \quad (11)$$

and 
$$[\mathbf{O}] = \begin{bmatrix} 0 & 0 & 0 \\ 0 & 0 & 0 \\ 0 & 0 & 0 \end{bmatrix} \quad (12)$$

$$l = \frac{x_2 - x_1}{L}; m = \frac{y_2 - y_1}{L}; n = \frac{z_2 - z_1}{L}; D = \sqrt{l^2 + m^2} \quad (13)$$

If  $D = 0$ , and  $n \geq 0$  then 
$$[\mathbf{T}_{3D}] = \begin{bmatrix} 0 & 0 & 1 \\ 0 & 1 & 0 \\ -1 & 0 & 0 \end{bmatrix} \quad (14)$$



$$\text{If } D = 0 \text{ and } n < 0 \text{ then } [\mathbf{T}_{3D}] = \begin{bmatrix} 0 & 0 & -1 \\ 0 & 1 & 0 \\ 1 & 0 & 0 \end{bmatrix} \quad (15)$$

Where  $(x_1, y_1, z_1)$  and  $(x_2, y_2, z_2)$  are coordinates of member's ends.

## 1.2. Shell elements

Shell element is used to model structural panels such as roof or wall sheathings.

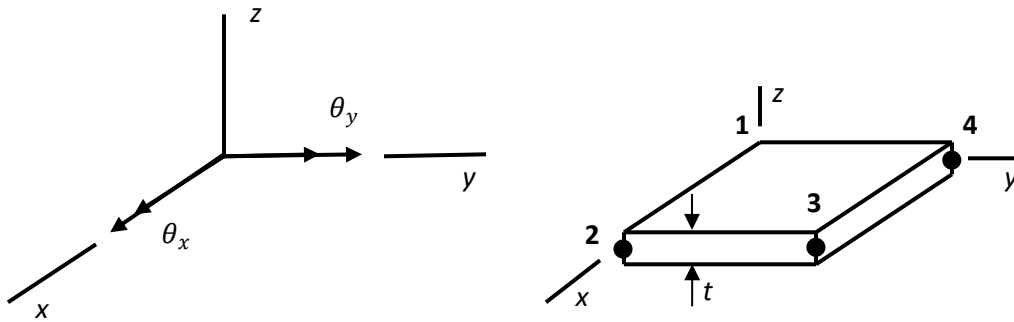


**Figure 4-Nodal degrees of freedom for shell elements in local coordinates**

To keep the degrees of freedom consistent with the member elements, one should use Mindlin plates for the models. Mindlin defined the displacement field for shell elements

$$u = z \times \theta_y(x, y); v = -z \times \theta_x(x, y); w = w(x, y)$$

Where  $\theta_x(x, y)$  and  $\theta_y(x, y)$  are the rotations of straight line normal to undeformed midsurface from the original position in  $x$  and  $y$  direction, respectively.

The stiffness matrix of shell elements can be obtained by coupling bending and membrane components.

*Bending component:*

From the displacement field defined, we can compute strains in shells:

$$\begin{aligned} \epsilon_x &= z \times \theta_{y,x}; & \gamma_{xy} &= z(\theta_{y,y} - \theta_{x,x}) \\ \epsilon_y &= -z \times \theta_{x,y}; & \gamma_{yz} &= w_{,y} - \theta_x \end{aligned} \quad (16)$$

$$\varepsilon_z = 0; \quad \gamma_{zx} = w_{,x} + \theta_y$$

Where  $\theta_{x,x}$ ,  $\theta_{x,y}$ ,  $\theta_{y,x}$ ,  $\theta_{y,y}$ ,  $w_{,x}$  and  $w_{,y}$  are the derivatives of  $\theta_x(x, y)$ ,  $\theta_y(x, y)$  and  $w(x, y)$  versus  $x$  and  $y$ , respectively.

Stresses in shell element are computed as:

$$\begin{aligned} \sigma_x &= \frac{z}{1-\nu^2} (E_x \theta_{y,x} - \nu E_y \theta_{x,y}); \quad \tau_{xy} = Gz(\theta_{y,y} - \theta_{x,x}) \\ \sigma_y &= \frac{z}{1-\nu^2} (\nu E_x \theta_{y,x} - E_y \theta_{x,y}); \quad \tau_{yz} = KG(w_{,y} - \theta_x) \\ \sigma_z &= 0; \quad \tau_{zx} = KG(w_{,x} + \theta_y) \end{aligned} \quad (17)$$

And:

$$M_x = \int_{-\frac{t}{2}}^{\frac{t}{2}} \sigma_x z dz = \int_{-\frac{t}{2}}^{\frac{t}{2}} \frac{z^2}{1-\nu^2} (E_x \theta_{y,x} - \nu E_y \theta_{x,y}) dz = \frac{t^3}{12(1-\nu^2)} (E_x \theta_{y,x} - \nu E_y \theta_{x,y})$$

$$M_x = (D_x \theta_{y,x} - \nu D_y \theta_{x,y})$$

$$M_y = \int_{-\frac{t}{2}}^{\frac{t}{2}} \sigma_y z dz = \int_{-\frac{t}{2}}^{\frac{t}{2}} \frac{z^2}{1-\nu^2} (\nu E_x \theta_{y,x} - E_y \theta_{x,y}) dz = \frac{t^3}{12(1-\nu^2)} (\nu E_x \theta_{y,x} - E_y \theta_{x,y})$$

$$M_y = (\nu D_x \theta_{y,x} - D_y \theta_{x,y})$$

$$M_{xy} = \int_{-\frac{t}{2}}^{\frac{t}{2}} \tau_{xy} z dz = \int_{-\frac{t}{2}}^{\frac{t}{2}} Gz^2 (\theta_{y,y} - \theta_{x,x}) dz = \frac{Gt^3}{12} (\theta_{y,y} - \theta_{x,x})$$

$$M_{xy} = \frac{(D_x + D_y)(1-\nu)}{4} (\theta_{y,y} - \theta_{x,x})$$

$$Q_x = \int_{-\frac{t}{2}}^{\frac{t}{2}} \tau_{xz} dz = \int_{-\frac{t}{2}}^{\frac{t}{2}} KG_x (w_{,x} + \theta_y) dz$$

$$Q_x = KG_x t(w_{,x} + \theta_y)$$

$$Q_y = \int_{-\frac{t}{2}}^{\frac{t}{2}} \tau_{yz} dz = \int_{-\frac{t}{2}}^{\frac{t}{2}} KG_y (w_{,y} - \theta_x) dz$$

$$Q_y = KG_y t(w_{,y} - \theta_x)$$

From stresses and strains, taking integration throughout the volume for strain energy density gives us:

$$\begin{aligned}
 U &= \frac{1}{2} \int_A \int_{-\frac{t}{2}}^{\frac{t}{2}} (\sigma_x \varepsilon_x + \sigma_y \varepsilon_y + \tau_{xy} \gamma_{xy} + \tau_{yz} \gamma_{yz} + \tau_{zx} \gamma_{zx}) dz dA \\
 &= \frac{1}{2} \int (M_x \theta_{y,x} - M_y \theta_{x,y} - M_{xy} (\theta_{x,x} - \theta_{y,y}) + Q_x (\theta_y + w_{,x}) - Q_y (\theta_x - w_{,y})) dA
 \end{aligned} \tag{18}$$

Where  $M_x$ ,  $M_y$  are moment in  $x$  and  $y$  directions;  $M_{xy}$  is the twist in  $x$  and  $y$  direction;  $Q_x$  and  $Q_y$  are shear forces in  $x$  and  $y$  directions.

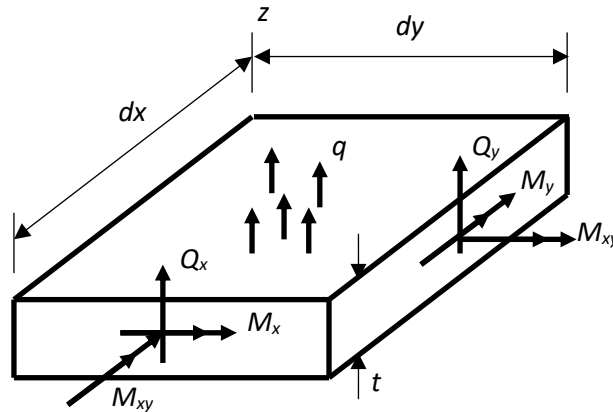


**Figure 5-Resultant force vectors**

In matrix form:

$$U = -\frac{1}{2} \int [\mathbf{R}] \{\mathbf{K}_M\} dA \quad (19)$$

$$\text{Where: } [\mathbf{R}] = [M_x \ M_y \ M_{xy} \ Q_x \ Q_y] \quad (20)$$

$$\{\mathbf{K}_M\} = \begin{Bmatrix} \theta_{y,x} \\ -\theta_{x,y} \\ -\theta_{x,x} + \theta_{y,y} \\ \theta_y + w_{,x} \\ -\theta_x + w_{,y} \end{Bmatrix} \quad (21)$$

And:

$$\{\mathbf{K}_M\} = \begin{Bmatrix} \theta_{y,x} \\ -\theta_{x,y} \\ -\theta_{x,x} + \theta_{y,y} \\ \theta_y + w_{,x} \\ -\theta_x + w_{,y} \end{Bmatrix} = \begin{bmatrix} 0 & 0 & 0 & 0 & N_x & 0 \\ 0 & 0 & 0 & -N_y & 0 & 0 \\ 0 & 0 & 0 & -N_x & N_y & 0 \\ 0 & 0 & N_x & 0 & N & 0 \\ 0 & 0 & N_y & -N & 0 & 0 \end{bmatrix} \begin{Bmatrix} u \\ v \\ w \\ \theta_x \\ \theta_y \\ \theta_z \end{Bmatrix} = [\mathbf{B}_b] \{\mathbf{d}\} \quad (22)$$

Where  $N$  is shape function;  $N_x$  and  $N_y$  are derivatives of shape function versus  $x$  and  $y$ , respectively.

$$\begin{aligned} \{\mathbf{R}\} &= \begin{Bmatrix} M_x \\ M_y \\ M_{xy} \\ Q_x \\ Q_y \end{Bmatrix} = \begin{bmatrix} D_x & \nu D_y & 0 & 0 & 0 \\ \nu D_x & D_y & 0 & 0 & 0 \\ 0 & 0 & \frac{(D_x + D_y)(1-\nu)}{4} & 0 & 0 \\ 0 & 0 & 0 & KG_x t & 0 \\ 0 & 0 & 0 & 0 & KG_y t \end{bmatrix} \cdot \begin{Bmatrix} \theta_{y,x} \\ -\theta_{x,y} \\ -\theta_{x,x} + \theta_{y,y} \\ \theta_y + w_{,x} \\ -\theta_x + w_{,y} \end{Bmatrix} \\ &= [\mathbf{D}_b] \cdot \{\mathbf{K}_M\} \end{aligned} \quad (23)$$

$$[\mathbf{R}] = [\mathbf{K}_M] \cdot [\mathbf{D}_b]^T = [\mathbf{K}_M] \cdot [\mathbf{D}_b] = [\mathbf{d}] \cdot [\mathbf{B}_b]^T \cdot [\mathbf{D}_b] \quad (24)$$

Substituting equation (22) and (24) into equation (19) gives us:

$$U = \frac{1}{2} \int [\mathbf{d}] \cdot [\mathbf{B}_b]^T \cdot [\mathbf{D}_b] \cdot [\mathbf{B}_b] \cdot \{\mathbf{d}\} dA \quad (25)$$

Taking variation for both sides of equation (25) leads to:

$$\delta U = \int [\delta \mathbf{d}] \cdot [\mathbf{B}_b]^T \cdot [\mathbf{D}_b] \cdot [\mathbf{B}_b] \cdot \{\mathbf{d}\} dA \quad (26)$$

The stiffness matrix due to bending component:

$$[\mathbf{K}_{SB}] = \int [\mathbf{B}_b]^T \cdot [\mathbf{D}_b] \cdot [\mathbf{B}_b] dA \quad (27)$$

*Membrane component:*

Membrane component yields constant stresses across the thickness of shells. The displacement fields of membrane component are defined as:

$$u = u(x, y); v = v(x, y); w = const; \quad (28)$$

There are only three non-zero stress components:

$$\begin{aligned} \sigma_x &= \frac{1}{1-\nu^2} (E_x \varepsilon_x + \nu E_y \varepsilon_y) = \frac{1}{1-\nu^2} \left( E_x \frac{\partial u}{\partial x} + \nu E_y \frac{\partial v}{\partial y} \right) \\ \sigma_y &= \frac{1}{1-\nu^2} (\nu E_x \varepsilon_x + E_y \varepsilon_y) = \frac{1}{1-\nu^2} \left( \nu E_x \frac{\partial u}{\partial x} + E_y \frac{\partial v}{\partial y} \right) \\ \tau_{xy} &= G_{xy} \gamma_{xy} = G_{xy} \left( \frac{\partial u}{\partial y} + \frac{\partial v}{\partial x} \right) \end{aligned} \quad (29)$$

Strain energy:

$$\begin{aligned} \mathbf{U} &= \frac{1}{2} \int (\sigma_x \varepsilon_x + \sigma_y \varepsilon_y + \tau_{xy} \gamma_{xy}) dV \\ &= \frac{1}{2} t \int (\sigma_x \varepsilon_x + \sigma_y \varepsilon_y + \tau_{xy} \gamma_{xy}) dA \end{aligned} \quad (30)$$

In matrix form:

$$\mathbf{U} = \frac{1}{2} t \int [\sigma_x \quad \sigma_y \quad \tau_{xy}] \cdot \begin{Bmatrix} \varepsilon_x \\ \varepsilon_y \\ \gamma_{xy} \end{Bmatrix} dA \quad (31)$$

Constitutive laws give us:

$$[\sigma_x \quad \sigma_y \quad \tau_{xy}] = \frac{1}{1-\nu^2} \cdot \begin{bmatrix} E_x & \nu E_y & 0 \\ \nu E_x & E_y & 0 \\ 0 & 0 & \frac{1-\nu}{2} \end{bmatrix} \cdot \begin{Bmatrix} \varepsilon_x \\ \varepsilon_y \\ \gamma_{xy} \end{Bmatrix} \quad (32)$$

From equilibrium conditions, we have:

$$\begin{Bmatrix} \varepsilon_x \\ \varepsilon_y \\ \gamma_{xy} \end{Bmatrix} = \begin{Bmatrix} \frac{\partial u}{\partial x} \\ \frac{\partial v}{\partial y} \\ \frac{\partial u}{\partial y} + \frac{\partial v}{\partial x} \end{Bmatrix} = \begin{bmatrix} N_x & 0 & 0 & 0 & 0 & 0 \\ 0 & N_y & 0 & 0 & 0 & 0 \\ N_y & N_x & 0 & 0 & 0 & 0 \end{bmatrix} \cdot \begin{Bmatrix} u \\ v \\ w \\ \theta_x \\ \theta_y \\ \theta_z \end{Bmatrix} = [\mathbf{B}_m] \cdot \{\mathbf{d}\} \quad (33)$$

Substitute equation (33) and equation (32) into equation (31) we get:

$$\mathbf{U} = \frac{1}{2} \int [\mathbf{d}] \cdot [\mathbf{B}_m]^T \cdot [\mathbf{D}_m] \cdot [\mathbf{B}_m] \cdot \{\mathbf{d}\} dA \quad (34)$$

$$\text{Where } [\mathbf{D}_m] = \frac{t}{1-\nu^2} \cdot \begin{bmatrix} E_x & \nu E_y & 0 \\ \nu E_x & E_y & 0 \\ 0 & 0 & \frac{1-\nu}{2} \cdot \frac{E_x + E_y}{2} \end{bmatrix} \quad (35)$$

Taking variation both sides of equation (3.34) gives us:

$$\delta \mathbf{U} = \int [\delta \mathbf{d}] \cdot [\mathbf{B}_m]^T \cdot [\mathbf{D}_m] \cdot [\mathbf{B}_m] \cdot \{\mathbf{d}\} dA \quad (36)$$

Stiffness matrix due to membrane component:

$$[\mathbf{K}_{SM}] = \int [\mathbf{B}_m]^T \cdot [\mathbf{D}_m] \cdot [\mathbf{B}_m] dA \quad (37)$$

*Solution for stress: Bending component:*

From equation (17), one can have:

$$\begin{Bmatrix} \sigma_x \\ \sigma_y \\ \tau_{xy} \\ \tau_{xz} \\ \tau_{yz} \end{Bmatrix} = \begin{bmatrix} A_x & \nu A_y & 0 & 0 & 0 \\ \nu A_x & A_y & 0 & 0 & 0 \\ 0 & 0 & \frac{(A_x + A_y)(1-\nu)}{4} & 0 & 0 \\ 0 & 0 & 0 & KG_x & 0 \\ 0 & 0 & 0 & 0 & KG_y \end{bmatrix} \cdot \begin{Bmatrix} \theta_{y,x} \\ -\theta_{x,y} \\ -\theta_{x,x} + \theta_{y,y} \\ \theta_y + w_{,x} \\ -\theta_x + w_{,y} \end{Bmatrix}$$

$$= [\mathbf{S}_b] \cdot \{\mathbf{K}_M\} = [\mathbf{S}_b] \cdot [\mathbf{B}_b] \cdot \{\mathbf{d}\} \tag{38}$$

Where

$$A_x = \frac{E_x z}{1 - \nu^2}; \quad A_y = \frac{E_y z}{1 - \nu^2} \tag{39}$$

$$\{\sigma\} = [\mathbf{S}_b] \cdot [\mathbf{B}_b] \cdot \{\mathbf{d}\} \tag{40}$$

*Solution for stress: Membrane component:*

From equation (29) we have:

$$\sigma_x = \frac{1}{1 - \nu^2} (E_x \varepsilon_x + \nu E_y \varepsilon_y) = \frac{1}{1 - \nu^2} \left( E_x \frac{\partial u}{\partial x} + \nu E_y \frac{\partial v}{\partial y} \right)$$

$$\sigma_y = \frac{1}{1 - \nu^2} (\nu E_x \varepsilon_x + E_y \varepsilon_y) = \frac{1}{1 - \nu^2} \left( \nu E_x \frac{\partial u}{\partial x} + E_y \frac{\partial v}{\partial y} \right)$$

$$\tau_{xy} = G_{xy} \gamma_{xy} = G_{xy} \left( \frac{\partial u}{\partial y} + \frac{\partial v}{\partial x} \right) \tag{41}$$

$$\begin{Bmatrix} \sigma_x \\ \sigma_y \\ \tau_{xy} \end{Bmatrix} = \begin{bmatrix} C_x & \nu C_y & 0 \\ \nu C_x & C_y & 0 \\ 0 & 0 & \frac{1-\nu}{2} C_{xy} \end{bmatrix} \cdot \begin{Bmatrix} \varepsilon_x \\ \varepsilon_y \\ \gamma_{xy} \end{Bmatrix} \quad C = \frac{E}{1-\nu^2} \tag{42}$$

Substitute equation (33) into equation (42) one can get:

$$\{\sigma\} = [\mathbf{S}_m] \cdot [\mathbf{B}_m] \cdot \{\mathbf{d}\}$$

### 1.3.New non-linear nail model

### Finite Element Formulation

In current state-of-the-art axial nail models used in finite element analyses, there is only one degree of freedom per node, and the nail is allowed to displace in the axial direction only (Figure 3.6). In order to perform much of the analysis in this dissertation, a new more versatile nail model was needed. For the new nail model, the nail is assumed to possess six degrees of freedom for each node, and specifically accounts for the coupling of axial force and rotational stiffness. This type of model provides more accuracy in the estimation of overall capacity and incremental deformation of roof panels.

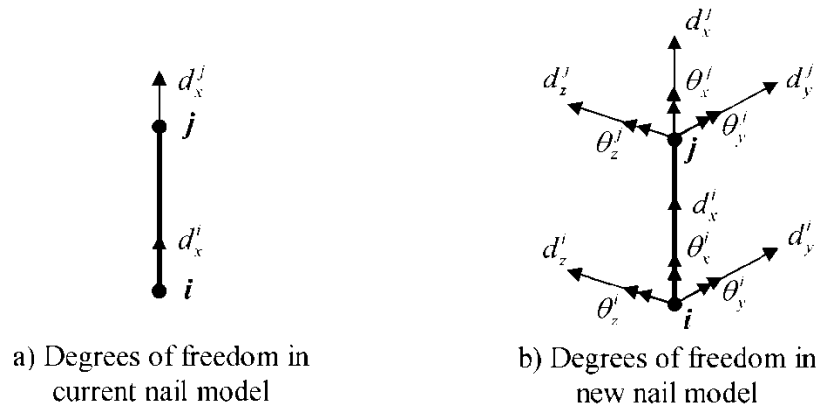


Figure 6 – Degrees of freedom in current and new nail models

In wood structural analysis, wood beams and columns can be modeled using beam elements. Sheathing such as oriented strand board (OSB) can be modeled using plate and shell elements with in-plane isotropic elastic models for approximation of components such as stress, strain, and displacement. The failures typically occur at the connections between structural components, e.g. the nails that connect the OSB to the trusses in roof systems, and not the members themselves. In the present study, the aforementioned nail model, which is intended for use in finite element analyses, is described as a non-linear spring with six degrees of freedom (DOF).

In order to transfer the force and moment from the OSB to the truss members, the nail is modeled as a spring with six components including three components in translation and three components in rotation. As



previously mentioned, the OSB is modeled using shell elements and the truss members are modeled as beam elements. Now, imagine the forces and moments need to be transferred from one node on the OSB to another node on a truss element via the nails. At the element level, the spring equation can be written simply as

$$[K]_S \{U\}_S = \{F\}_S \quad (44)$$

$$\{U\}_S = \{U\}_i - \{U\}_j \quad (45)$$

where  $\{U\}_S$  is the spring displacement,  $\{U\}_i$  is the displacement at node  $i$  on the OSB and  $\{U\}_j$  is the displacement at node  $j$  on the truss,  $[K]_S$  is the secant spring stiffness matrix for the six components and  $\{F\}_S$  is the spring force. The spring stiffness matrix  $[K]_S$  is estimated at each load level based on the  $\{U\}_S$  just obtained and the curves from experimental data.

The bending component of the stiffness matrix follows the beam bending stiffness equation described before (1) and the axial component are modeled using the hysteresis curve described in the next section.

The element stiffness matrix is transformed into global coordinates and then added to the global stiffness matrix. It should be noted that there are some finite element modeling integration details that are not obvious. For example, when integrating the nail model into a finite element program, node  $i$  and  $j$  initially have the same coordinates (before loading), therefore the nail direction vector should be specified and used to create the transformation matrix. The positive directions (node  $i$  to node  $j$ , translational and rotational) should also be specified so that they can be checked at each load step, if each displacement component is negative, the spring stiffness in that direction  $k_{ii}$  should then be set to an “infinite” value. The flowchart in Figure 3.7 shows the iterative procedure for assembly of the nail element stiffness in the global stiffness matrix.

### *Hysteresis Model*

In this study, both the panels and nails are modeled with nonlinear phenomenological hysteretic behavior. An **11-parameter hysteretic model** for reverse-cyclic seismic loading was borrowed from [Dao and van de Lindt \(2013\)](#) and repurposed for use with wind loading. This model itself was a slight modification of the 10-parameter hysteresis model introduced by [Folz and Filiatrault \(2001\)](#). In that hysteresis model, the envelope monotonic loading curve (hysteretic backbone) was described by five parameters,  $F_0$ ,  $K_0$ ,  $r_1$ ,  $r_2$ , and  $\delta_u$ , and unloading and reloading paths are described by another five parameters,  $F_1$ ,  $r_3$ ,  $r_4$ ,  $\alpha$ , and  $\beta$ ; the monotonic loading curve starts at the origin of the force-displacement coordinate with slope  $K_0$  and following the curve  $F = \text{sgn}(\delta)(F_0 + r_1 K_0 |\delta|)[1 - \exp(-(K_0 |\delta|)/F_0)]$ , where  $F$  and  $\delta$  are force and displacement, respectively, whose relationship is described by the hysteretic model. The ultimate load is at displacement  $\delta_u$  and  $F_u = (F_0 + r_1 K_0 \delta_u)[1 - \exp(-K_0 \delta_u/F_0)]$ . At the ultimate loading point, the curve has slope  $r_1 K_0$ . When the displacement goes beyond  $\delta_u$ , the force starts to decrease with slope  $r_2 K_0$  to the failure point. Unloading off the envelope curve follows a path with unloading slope  $r_3 K_0$ . If it continues unloading, the response moves onto a pinching path with slope  $r_4 K_0$ . This pinching path always passes the pinching points  $(0, F_1)$  for positive displacement increment and  $(0, -F_1)$  for negative displacement increment. If it continues the reloading, then the response follows a path with degrading stiffness  $K_p = K_0(\delta_0/\delta_{max})^\alpha$ , where  $\delta_0 = F_0/K_0$  and  $\delta_{max} = \beta \delta_{un}$ ,  $\delta_{un}$  is the largest unloading displacement experienced by the model to that point, and  $\alpha$  and  $\beta$  are hysteretic parameters defining the degrading stiffness,  $K_p$ . The 10 parameters are obtained by fitting the model to the test data. Additionally, a single parameter was included to account for the degradation of the unloading slope described as parameter  $r_3$  in the [Folz and Filiatrault \(2001\)](#) model:

$$r_3 = r_3^{\delta_u} \left( \frac{\delta_u}{\delta_{max}} \right)^\gamma \quad (46)$$

where  $r_3^{\delta_u}$  = unloading slope coefficient ( $r_3^{\delta_u} K_0$  = unloading slope), when  $\delta_{max} = \delta_u$ , and  $\gamma$  = parameter describing the unloading stiffness degradation. Figs. 7 shows the sample hysteresis fit using the 11-parameter model for the panels and nails.

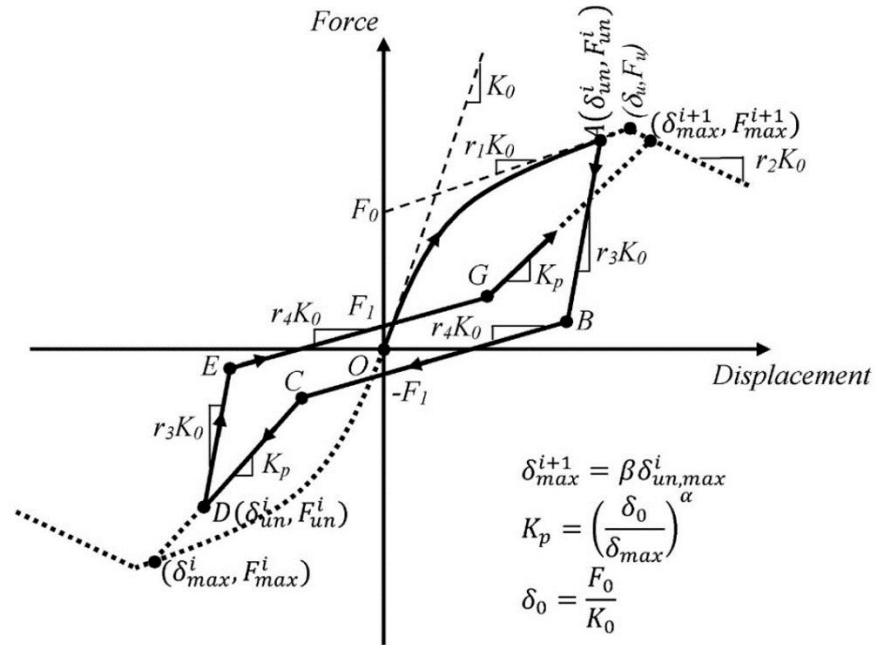


Figure 7 – Hysteresis model

### *P – Δ Effect*

The *P – Δ* effect must be included for nonlinear analysis of columns that carry the vertical load transferred by the panels. To do this, the geometric stiffness matrix is calculated at every time step during the nonlinear analysis and added to the elastic stiffness matrix before assembling it into the global stiffness matrix of the system.

To include the *P – Δ* effect from dead load and an applicable portion of the live load in the **nonlinear dynamic analysis**, a nonlinear static analysis with dead load and 25% of live load is conducted prior to the dynamic analysis. The resulting displacement of the system is set as the initial displacement for dynamic analysis. Then, by upgrading the internal force and the geometric stiffness matrix for all columns within the structural system, the *P – Δ* effect is included.

## 2. Integration of wind loads

In non-linear time-history analysis, at each time step, wind pressures all the taps on the roof are calculated and interpolated at (shell) element nodes. The interpolation is conducted using shape functions at the taps

at local coordinates. The shape function is defined for each tap column in local  $x$  direction and each tap row for local  $y$  direction. The shape function of a tap is the product of shape function in  $x$  and  $y$  directions. The shape function in each row and column is calculated by equations:

$$N_i(y) = \frac{(y-y_1)(y-y_2)\dots(y-y_{i-1})(y-y_{i+1})\dots(y-y_n)}{(y_i-y_1)(y_i-y_2)\dots(y_i-y_{i-1})(y_i-y_{i+1})\dots(y_i-y_n)} \quad (47)$$

$$N_j(x) = \frac{(x-x_1)(x-x_2)\dots(x-x_{j-1})(x-x_{j+1})\dots(x-x_m)}{(x_j-x_1)(x_j-x_2)\dots(x_j-x_{j-1})(x_j-x_{j+1})\dots(x_j-x_m)} \quad (48)$$

And the shape function of tap  $k$  at row  $i$  and column  $j$  is calculated by equation:

$$N_k(x, y) = N_{ij}(x, y) = N_i(y) \cdot N_j(x) \quad (49)$$

where  $x$  and  $y$  are local coordinates of the face where pressure taps are installed.

The wind pressure of an element node at coordinate  $(x, y)$  on the face is calculated by equation:

$$p(x, y) = \sum_{k=1}^{\text{number of taps}} N_k(x, y) \cdot p_k \quad (50)$$

in which  $p_k$  is the pressure at tap  $k$  at the current time step.

After pressures at nodes on the face are calculated, the wind load at each node is calculated by integration of the pressure using virtual work principle:

$$\delta W = \delta u \cdot F_w = \int_A p \cdot \delta u \cdot dA = \int_A [\delta u] \cdot [N]^T \cdot [N] \cdot [p] \cdot dA \quad (51)$$

Or

$$[F_w] = \int_A [N]^T \cdot [N] \cdot [p] \cdot dA \quad (52)$$

where  $[F_w]$  is wind force vector at element nodes,  $[N]$  is row matrix of element nodal shape functions, and  $[p]$  is vector of nodal pressures.

### 3. Time-History Analysis

Code-based wind load is derived by a frequency domain analysis. However, a frequency domain analysis is invalid in an inelastic system [Jeong et al. \(2021\)](#). To conduct inelastic PBWD and verification, a time-history wind load is required. Wind tunnel testing is recognized as a reasonable means for determining wind loads. Because the structure remained in the elastic range under **habitability evaluation load** (1-year return period), directional loads were considered separately, and correlation of directional loads were used for inelastic analysis.

Nonlinear time-history analysis (NTHA) was performed for each of the wind load cases, namely the along-wind, across-wind, and torsional-wind loads. The duration of wind load is much longer than that of the

seismic load. For wind load, extremely large computation is required for NTHA. **Conventional time integration method** was employed as opposed to the fast nonlinear analysis (FNA) where the geometric nonlinearity cannot be considered. The time-history plots are shown in Figs. 2 and 3.

The building numerical model was subjected to dynamic time-history wind loading using 256 time-history point loads around the building surface. The duration of the analyses for each wind direction was approximately 4000 sec, including more than one hour of wind loading and a linear ramp-up, gradually increasing the forces in the first several seconds, from zero to the initial amount of the wind loading to avoid a dynamic impact effect. A critical damping ratio equal to 2%, using the **Rayleigh damping method**, was applied in the nonlinear response history analyses. To avoid the spurious damping forces, the damping matrix was assembled based on the tangent stiffness.

A simulation video of the building motion near collapse indicates that the building is actually responding in a combination of along-wind, cross-wind, and torsional deformations.

A well-know numerical integration method, Newmark- $\beta$ , is used for time history analysis in this study since the non-linear hysteresis model can be exerted into the model.

#### 4. FE Model of MHU Roof

In the preliminary stage of the numerical study, a roof structure of MHU was analyzed using the Matlab program developed by UA team. The roof structure is shown in Figure 8, in which the roof trusses are installed every 24 inches. The model includes roof trusses, roof sheathing panel, and nail connections. In the model,  $4ft \times 8ft \times \frac{15}{32} in.$  roof sheathings are modeled using 8-node shell elements. Truss members are built from  $2 \times 4 in.$  wood lumbers and modeled using beam element with hinge connections at the ends. Nails connections are modeled as spring elements with bending components modeled by beam stiffness matrix and axial component is modeled using non-linear hysteresis model as mentioned earlier. Nails are used to attach roof sheathings and truss members, and there is no blocking (joist members at panel edges)

for roof sheathing. Since nail connection data is not available at the time of the report, assumptions of hysteresis parameter are assumed for the model.

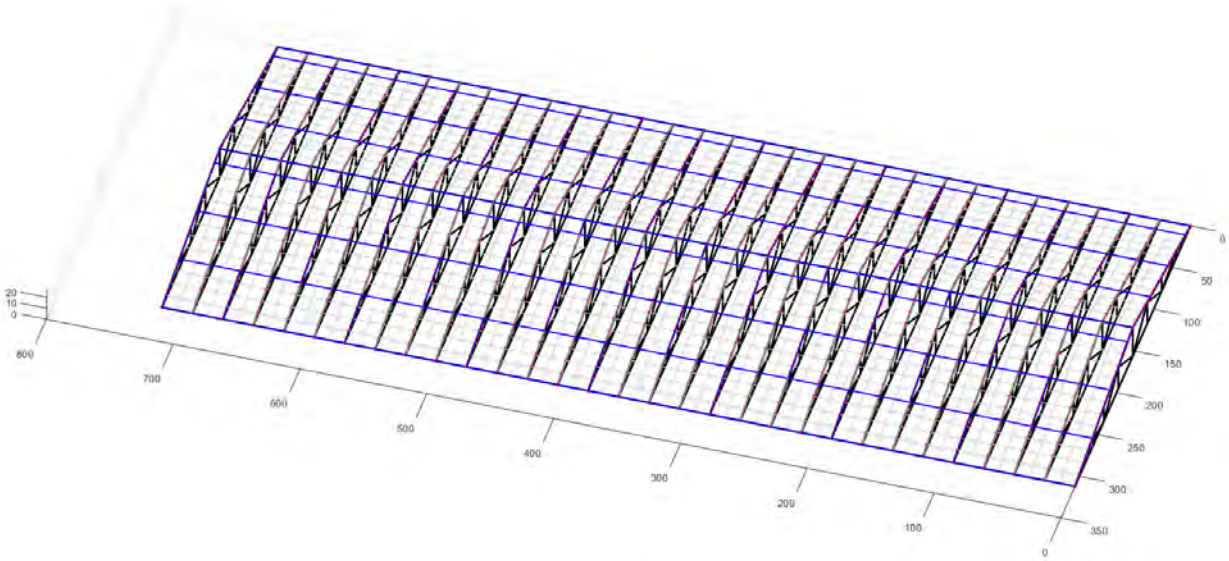


Figure 8 - Roof Structure Model

In Figure 9, the blue lines show the sheathing panel edges, the red dots are location of nail connections. The light lines show the shell element meshing.

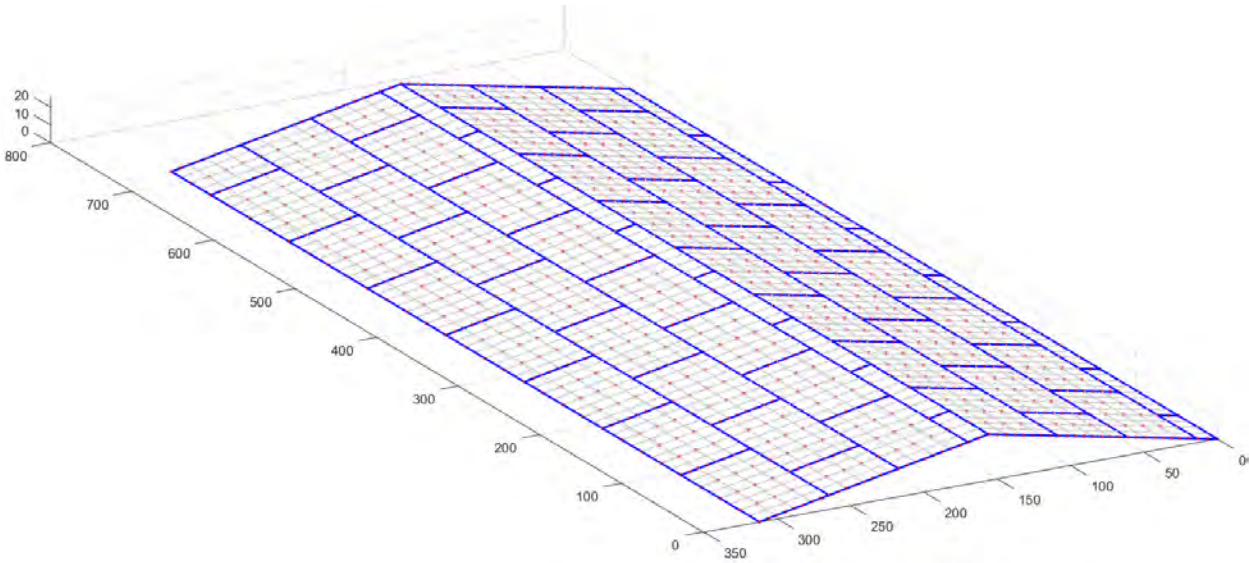
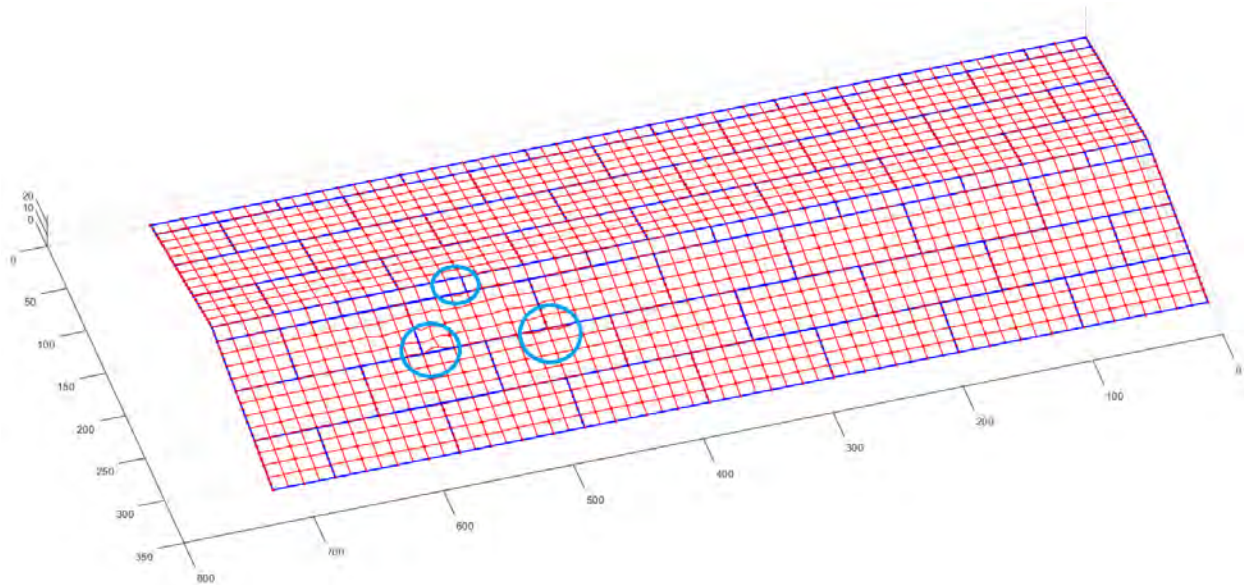


Figure 9 - Roof sheathing panels, element mesh, and nail connections

Edge nails are installed every 6 inches while field nails spacing is 12 inches.

## 5. Initial Results



*Figure 10 – Roof sheathing deformation (Displacement scale = 5.0)*

Initial analysis of the roof of a MHU show that under wind load of wind speed  $V = 21.4 \text{ m/s}$  (48.15 mph) at mean-roof height, there is some small gap opening on the edge of roof sheathing panel where there is no nail connection attachment as shown at circles in Figure 10. Further detailed analysis of MHU structure will be conducted when connection test data available for model calibration and application into the program.

## VII. Summary and Conclusions

In the first year of this study, UA team has successfully developed the conceptual numerical model for nail connections and other MHU substructures components used in Matlab program for analysis of a roof structure of MHU. Even though only the roof of a MHU was analysis in this report, the analysis can be extended for full MHU when longer running time allowed. The initial results show a reasonable range given the nail connection parameters were assumed during the analysis given that the connection tests are conducting at KU.

## VIII. References

- ASCE. (2005). "Minimum design loads for buildings and other structures." *ASCE/SEI 7-05*, ASCE, Reston, Va.
- Boudaud, C., Humbert, J., Baroth, J., Hameury, S., and Daudeville, L. (2015). "Joints and wood shear walls modelling II: Experimental tests and FE models under seismic loading." *Eng. Struct.*, *101*, 743-749.
- Christovasilis, I. P., and Filiatrault, A. (2010). "A two-dimensional numerical model for the seismic collapse assessment of light-frame wood structures." In *Structures Congress 2010* (pp. 832-843).
- Collins, M., Kasal, B., Paevere, P., and Foliente, G. C. (2005). "Three-dimensional model of light frame wood buildings. I: Model description." *J. Struct. Eng.*, *131*(4), 676-683.
- Dao, T. N. (2010). "The development of performance-based wind engineering for residential structures: From concepts to application." *Colorado State University*.
- Dao, T. N., and van de Lindt, J. W. (2012). "Loss analysis for wood frame buildings during hurricanes. I: Structure and hazard modeling." *J. Perform. Constr.*, *26*(6), 729-738.
- Dao, T. N., and van de Lindt, J. W. (2008). "New nonlinear roof sheathing fastener model for use in finite-element wind load applications." *J. Struct. Eng.*, *134*(10), 1668-1674.
- Dao, T. N., and van de Lindt, J. W. (2014). "Numerical Seismic Performance of an Innovative CFS Midrise Building Designed Using DDD." *J. Perform. Constr.*, *28*(5), 04014018.
- Dao, T. N., and van de Lindt, J. W. (2013). "Seismic performance of an innovative light-frame cold-formed steel frame for midrise construction." *J. Struct. Eng.*, *139*(5), 837-848.
- Dao, T. N., van de Lindt, J. W., Prevatt, D. O., and Gupta, R. (2012). "Probabilistic procedure for wood-frame roof sheathing panel debris impact to windows in hurricanes." *Eng. Struct.*, *35*, 178-187.



Dong, H., He, M., Wang, X., Christopoulos, C., Li, Z., and Shu, Z. (2021). “Development of a uniaxial hysteretic model for dowel-type timber joints in OpenSees.” *Constr Build Mater.*, 288, 123112.

Elkady, A., and Lignos, D. G. (2015). “Effect of gravity framing on the overstrength and collapse capacity of steel frame buildings with perimeter special moment frames.” *Earthq Eng Struct Dyn*, 44(8), 1289-1307.

Ellingwood, B. R. (1999). “A comparison of general design and load requirements in building codes in Canada, Mexico, and the United States.” *Eng. J.*, 36(2), 67–80.

Estephan, J., Feng, C., Chowdhury, A. G., Chavez, M., Baskaran, A., and Moravej, M. (2021). “Characterization of wind-induced pressure on membrane roofs based on full-scale wind tunnel testing.” *Eng. Struct.*, 235, 112101.

Filiatrault, A., and Folz, B. (2002). “Performance-based seismic design of wood framed buildings.” *J. Struct. Eng.*, 128(1), 39-47.

Folz, B., and Filiatrault, A. (2001). “Cyclic analysis of wood shear walls.” *J. Struct. Eng.*, 127(4), 433-441.

Hafeez, G., Mustafa, A., Doudak, G., and McClure, G. (2014). “Predicting the fundamental period of light-frame wood buildings.” *J. Perform. Constr.*, 28(6), A4014004.

He, J., Pan, F., and Cai, C. S. (2017). “A review of wood-frame low-rise building performance study under hurricane winds.” *Eng. Struct.*, 141, 512-529.

He, J., Pan, F., Cai, C. S., Habte, F., and Chowdhury, A. (2018). “Finite-element modeling framework for predicting realistic responses of light-frame low-rise buildings under wind loads.” *Eng. Struct.*, 164, 53-69.

Izzi, M., Rinaldin, G., Polastri, A., and Fragiaco, M. (2018). “A hysteresis model for timber joints with dowel-type fasteners.” *Eng. Struct.*, 157, 170-178.

Jeong, S. Y., Alinejad, H., and Kang, T. H. K. (2021). “Performance-Based Wind Design of High-Rise Buildings Using Generated Time-History Wind Loads.” *J. Struct. Eng.*, 147(9), 04021134.

- Lacourt, P. A., Crisafulli, F. J., and Mirasso, A. E. (2016). "Finite element modelling of hysteresis, degradation and failure of dowel type timber joints." *Eng. Struct.*, 123, 89-96.
- Lim, H., Lam, F., Foschi, R. O., and Li, M. (2017). "Modeling load-displacement hysteresis relationship of a single-shear nail connection." *J. Eng. Mech.*, 143(6), 04017015.
- Liu, J., and Astaneh-Asl, A. (2000). "Cyclic testing of simple connections including effects of slab." *J. Struct. Eng.*, 126(1), 32-39.
- Manufactured Housing Institute. (2017). "Understanding Today's Manufactured Housing." *Manufactured Housing Institute*.
- Mohammadi, A., Azizinamini, A., Griffis, L., and Irwin, P. (2019). "Performance assessment of an existing 47-story high-rise building under extreme wind loads." *J. Struct. Eng.*, 145(1), 04018232.
- Usefi, N., Sharafi, P., and Ronagh, H. (2019). "Numerical models for lateral behaviour analysis of cold-formed steel framed walls: State of the art, evaluation and challenges." *Thin-Walled Struct.*, 138, 252-285.
- van de Lindt, J. W., and Dao, T. N. (2009). "Performance-based wind engineering for wood-frame buildings." *J. Struct. Eng.*, 135(2), 169-177.
- van de Lindt, J. W., Pei, S., Pang, W., and Shirazi, S. M. H. (2012). "Collapse testing and analysis of a light-frame wood garage wall." *J. Struct. Eng.*, 138(4), 492-501.
- Xu, J., and Dolan, J. D. (2009). "Development of a wood-frame shear wall model in ABAQUS." *J. Struct. Eng.*, 135(8), 977-984.



*A Resource for the State of Florida*

**SECTION 2 PART C:  
UNDERSTANDING HURRICANE EFFECTS ON MANUFACTURED HOMES**

**FINAL REPORT  
(Period: 2022)**

*A Research Project Funded by:*  
**The State of Florida Department of Emergency Management**

*Prepared by  
Dr. Elaina J. Sutley  
Dr. William Collins*

*Graduate Student  
Afeez Badmus*

*Undergraduate Student  
Cyra Chronister*

## **Introduction**

Manufactured housing units (MHUs) are extremely vulnerable to windstorms, including hurricanes. The overall goal of this research is to provide the fundamental and practical knowledge needed to significantly reduce the physical vulnerability of manufactured homes to wind events. While extensive research has been conducted on light-frame wood construction (LFWC) little research exists on MHUs. Limited research exists on anchorage systems, but do not capture many observed failure modes, including roof and wall cladding loss.

With an estimated 2.7 million MHUs located within mobile home parks in the U.S. (Ferguson 2022), including approximately 7% of Florida's households (AHS 2019), there is an important gap in understanding hurricane effects on manufactured homes. Through the creation of critical fundamental knowledge that can change code provisions, policies, and manufacturing processes, the innovative approaches proposed here have the potential to provide transformative impacts to new and existing mobile home parks and to manufactured housing units. This report presents the research from Phase I of the project carried out at the University of Kansas.

## **Background**

The design of manufactured homes is governed by the U.S. Department of Housing and Urban Development standard *Manufactured Home Construction and Safety Standards, Part 3280*, (termed HUD Code herein) which has not seen significant updates since 1994, and in which the hazard maps of lower wind speeds (comparing to current ASCE-7 standard) are from the 1988 version of ASCE Standard 7. Manufactured housing units are the most vulnerable residential structures to windstorms, including hurricanes and tornadoes. Manufactured housing uses wood frame construction, but it is constructed fundamentally differently from site-built housing and thus must be studied specifically. Design provisions in the HUD Code are vague and leave a fair amount of interpretation for manufacturers. Our post-disaster field reconnaissance demonstrates high variability in manufactured home construction, within and across Wind Zones, which correlates to performance. There is no publicly available information on how manufactured homes are constructed. However, our team has obtained structural details from HUD and a major U.S. manufacturer of manufactured homes. Within these documents, there is significant variability. The true structural design level(s) of manufactured homes are unknown; quantifying such is a critical first step in being able to improve their wind performance.

## **Methodology**

### ***Stakeholder Engagement***

There were two primary goals motivating stakeholder engagement for this project, including (1) gaining insight from academics, practitioners, and others with working knowledge of physical and social problems associated with manufactured housing; and (2) to build momentum behind the need for the research community to more intentionally address disparities with manufactured housing construction and performance.

Thus, we identified a community of people interested in advancing the safety of manufactured homes and organized a workshop to bring these stakeholders together. Stakeholders were identified through the research team's personal and professional networks and peer-reviewed literature. A list of 29 individuals including (a) 14 individuals from academia, spanning atmospheric science, economics, geography, public policy, sociology, urban planning, and wind engineering disciplines; (b) 5 government employees with meteorology, geography, risk communication, and wind engineering expertise, including two building code officials in the State of Florida; (c) 7 individuals from industry, all in structural and/or wind engineering; (d) 2 individuals from non-profit organizations, including with public policy and wind engineering backgrounds; and (e) 1 individual from the national press. Nineteen of the 29 agreed to serve on a stakeholder advisory committee (SAC).

The SAC were requested to attend one two-hour virtual meeting in February to learn about the project and offer their input towards its initial direction, and attend one three-hour virtual meeting in June, at the end of the project, to learn about progress and provide feedback on next steps. During the first meeting, scheduled February 25, 2022. Sutley spent half an hour presenting the goals and methodology of the project, posing specific questions for feedback along the way. The remaining 90 minutes were spent interacting with the SAC members. The second meeting was held on June 28, 2022. The project team spent the first half hour presenting their progress to date; a member from each institution gave approximately 10-minute updates. The update was followed by a one-hour breakout session, a 15-minute break, a second 45-minute breakout session, 15 minutes of reporting out from the breakouts, and a short open-discussion and closing. Each breakout session split the attendees into three 'zoom rooms', providing smaller spaces to engage the SAC. The first breakout session discussed was guided by the prompt "What are the biggest needs, challenges, and barriers to improving the structural performance of manufactured housing?" The second breakout session was guided by the prompt "What are the biggest non-engineering research and practical needs for improving manufactured housing?"

The Results section of this report describes feedback gained from both SAC meetings; the Conclusions section provides the overall recommendations from the SAC. Team presentations are provided in Appendices A and B for the first and second SAC meetings, respectively.

### ***Components and Connection Testing***

The primary goal of the experimental portion of this project was to provide a quantitative measurement of the performance of key connection(s) needed for advancing the finite element model being developed at the University of Alabama (UA). Based on this goal, the most important connection identified by the UA team was the roof sheathing to rafter connection, and thus was the sole focus of this portion of the project. Although withdrawal capacity is known for various fastener and wood combinations, the cyclic behavior of this connection has never been tested and

was critical for the finite element model. Furthermore, as discussed by the SAC, the most common failure mode for Wind Zone II homes is failure at the roof, and thus important for initially focusing the component testing.

Using structural details provided by HUD and a major U.S. manufacturer, common components for Wind Zone II homes were tested to quantify behavior and thereby wind performance for the roof sheathing to rafter connection. A two-step quasi-static cyclic testing protocol, that started with monotonic testing to inform the second step of cyclic testing, was used to quantify fastener withdrawal capacity.

### *Test Configuration*

Roof sheathing to rafter connection details were selected to represent typical connection geometries found in Wind Zone II manufactured homes in the United States. One joint configuration, a single field fastener on 8 x 8 sheathing, was fabricated and tested under monotonic and quasi-static cyclic loading (see Figure 1).



**Figure 1.** Test specimen: 8 x 8 sheathing-to-rafter connection with single field fastener

All lumber and sheathing used in this study were purchased at a local lumber store. Test specimens were comprised of a rafter, sheathing, and fastener. Rafters were 2 x 4 southern yellow pine (SYP) or spruce-pine-fir (SPF) lumber, sheathing was oriented strand board (OSB) or 3-ply plywood, and fasteners were 8d common smooth shank nails or #8 screws. All lumber was graded No. 2 or better. In accordance with the National Design Specification (2018), information describing the fasteners used in the study, including diameter, length, and thread patterns, are described in Table 1, alongside the geometric properties for the wood materials used in this study. Nails were installed using a pneumatic nail gun; screws were installed using a cordless drill driver. Screw holes were not pre-drilled to mimic the condition of how these structures are built in practice. Table 2 summarizes the test parameters for the roof sheathing to rafter connection test specimens tested here. Of note, in typical Wind Zone II manufactured homes, nails are by far the more common fastener used in practice for roof sheathing to rafter connections. Screws are rarely, if ever, used, but are tested here to demonstrate the potential increase in capacity with the simple upgrade of fastener.

**Table 1.** Geometric Properties of Roof Sheathing to Rafter Connection Components

<b>Component</b>	<b>Description</b>	<b>Geometric Properties</b>			
Rafter	Spruce Pine Fir (SPF)	2 in. x 4 in.			
	Southern Yellow Pine (SYP)	2 in. x 4in.			
Sheathing	Oriented Strand Board (OSB)	7/16 in. thick			
	3-Ply Plywood	0.5 in. thick			
<b>Fastener</b>	<b>Type</b>	<b>Length (in.)</b>	<b>Shank Diameter (in.)</b>	<b>Head Diameter (in.)</b>	<b>Thread Length (in.)</b>
Smooth Shank Nail	8d common	2.375	0.113	9/32	n/a
Screw	#8	2.0	0.111	0.426	1.299

**Table 2.** Roof Sheathing to Rafter Test Matrix

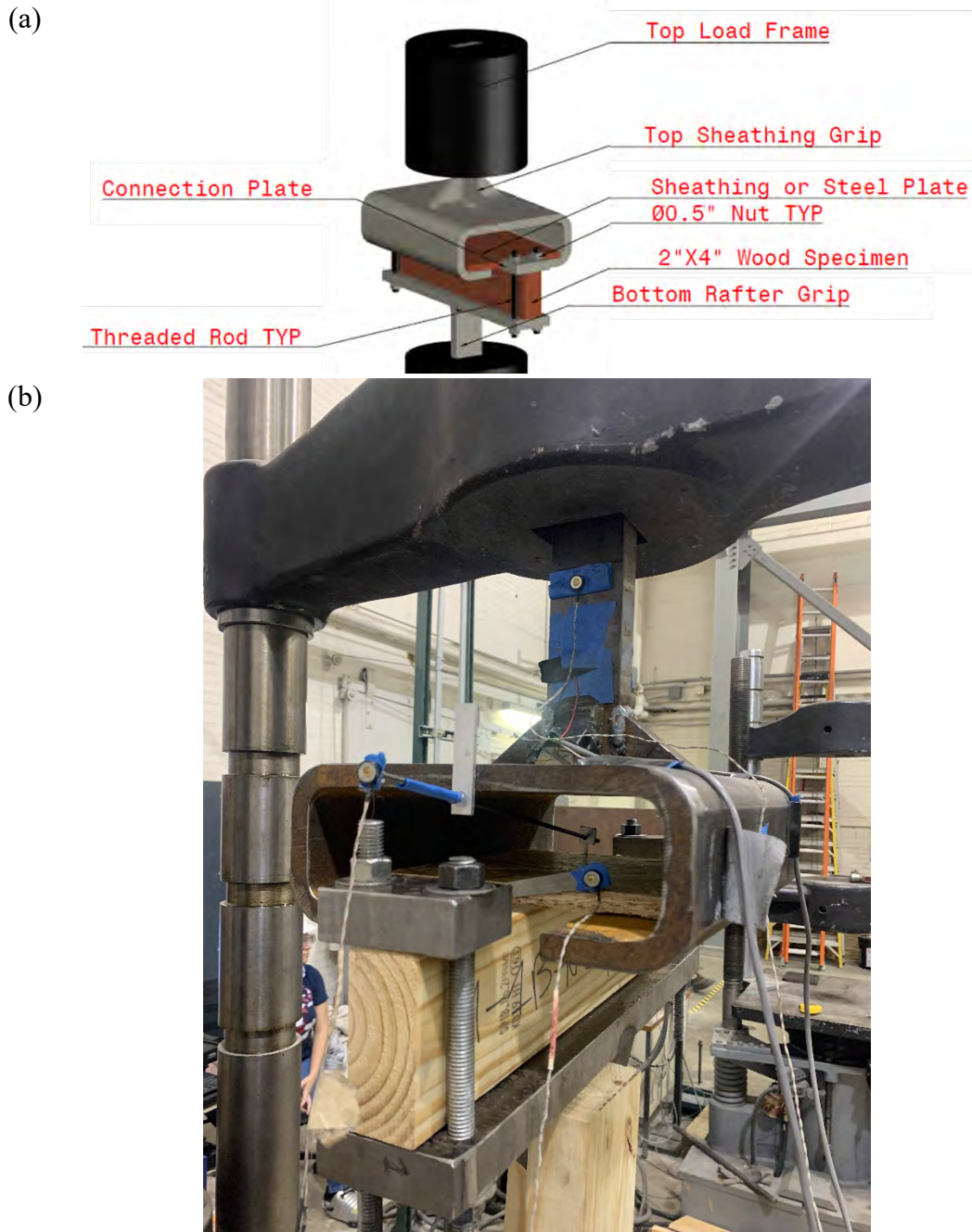
<b>Sheathing type (8 x8)</b>	<b>Rafter type</b>	<b>Fastener</b>	<b>Monotonic Tests</b>	<b>Cyclic Tests</b>
OSB	SPF	#8 screw	7	4
	SYP	8d box nail	5	3
Plywood (3-ply)	SPF	#8 screw	4	2

*Test Name Nomenclature*

Throughout this section of the report, the test name nomenclature corresponds to the test type, sheathing materials, rafter lumber species, fastener type, and fastener location. Monotonic tests are represented by an M; quasi-static cyclic tests are represented by a C. Sheathing material is denoted as O for OSB or P for plywood. Rafter lumber species is spelled out using the entire acronym for the species, either SPF or SYP. Fastener type is denoted as S for screw or N for nail; fastener location is denoted as F1 or F2 for one or two field fasteners, or E for edge. It should be noted that this report includes only single field, F1, fastener test results. Finally, the last number in the name designates the test number in the series of similar tests. For example, M-O-S-SPF-F1-1 corresponds to the first monotonic test on OSB sheathing connected via screw to a SPF rafter with one field fastener.

*Test Setup*

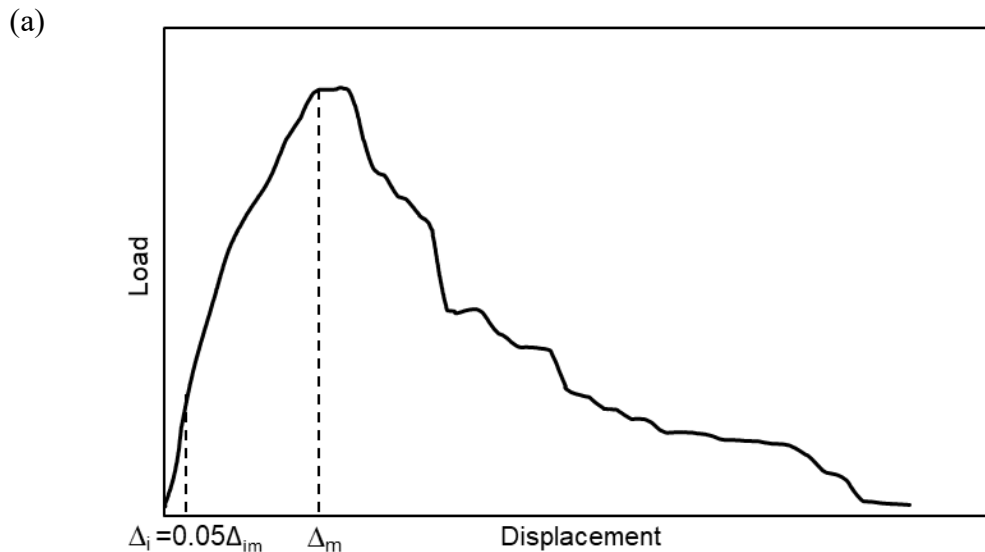
A steel fixture was designed and fabricated to hold the test specimen in the loading frame and transfer uplift force to the fasteners (Figure 2). All specimens were tested using a Baldwin machine with a capacity of 60 kips (266 kN). The bottom sheathing grip was fixed and designed to hold the 2 x 4 rafter in place, while the top sheathing grip imposed the uplift force effect on the sheathing mimicking wind uplift on roof sheathing by attempting to extract the fasteners vertically from the rafter.



**Figure 2.** Test Fixture: (a) Schematic; (b) Photograph



The two-part loading protocol involved monotonic testing and a two-step quasi-static cyclic protocol based on FEMA 461 procedures (2007). The monotonic test was performed at a constant displacement rate of 0.1 in./min (2.54 mm/min) in accordance with ASTM D 1761 standard (2020). The results obtained from the monotonic test were used to determine the appropriate displacement amplitude for the cyclic tests. FEMA 461 protocols require the identification of a displacement corresponding to initial damage,  $\Delta_0$ . The procedure then requires a minimum of 6 displacement cycles prior to reaching this initial damage state, with an additional 10 cycles prior to reaching  $\Delta_m$ , the displacement corresponding to maximum load. Due to the nature of sheathing connection failures, the procedure was modified for the current study. Based on the least ductile monotonic test result, the initial displacement for cyclic loading, defined herein as  $\Delta_i$  was taken to be 5% of  $\Delta_m$ . Subsequent displacement amplitudes were continuously increased by a factor of 1.4 until the load-carrying capacity of the connection was exceeded. At each displacement amplitude, two cycles were applied to the test specimen. An idealized loading history for a monotonic test is presented in Figure 3a, while a schematic loading protocol for quasi-static cyclic testing is shown in Figure 3b, with key displacement amplitudes labeled in each.



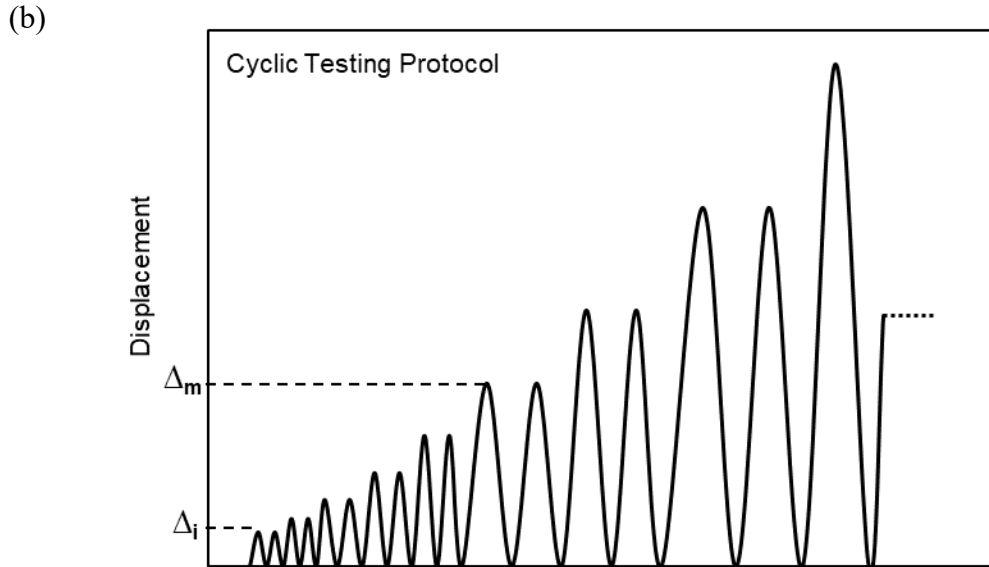


**Figure 3.** Schematic representation of a load protocol with key displacement parameters identified for the: (a) Monotonic test; (b) Cyclic test

### *Test Load Protocol*

Load response was recorded using the load frame built-in force transducer at a rate of 10 Hz. Three Optotrak markers, as shown in Figure 2, were utilized to measure vertical displacement at various locations. A marker was attached to the top sheathing grip to measure crosshead displacement, the sheathing centerline to allow for the removal of sheathing bending included in crosshead displacement, and the fastener head itself to allow for the determination of any relative displacement between the fastener and the sheathing. Pictures were taken to document the failure mode of each specimen at various testing stages.

## **Results**

### ***Stakeholder Engagement***

Both SAC meetings had good and diverse attendance and engagement. During the February 25, 2022 meeting, the SAC provided feedback on the park configurations and subsequent test protocols, including the orientation of units in a park and spacing, as well as emphasizing the need for an isolated test case. No one had direct information on specific connection details but agreed these were critical to performing meaningful experiments for development of the finite element model.

During the June 28, 2022 meeting, the SAC reinforced the need for an isolated test case, reinforced the need for nailed connections taking priority over screwed connections, and reinforced the need for both experimental efforts being necessary for continued advancement of the preliminary finite element model. The SAC asked about foundation connections, and why they were not included in the proposed Phase of research. The research team, and other members of the SAC discussed how Wind Zone I homes are still most often failing at their foundation, whereas Wind Zone II and III

homes most often fail at their roof-to-wall and wall-to-floor connections. Thus, the foundation requirements in Wind Zones II and III areas tend to be sufficient when installed properly.

In the breakout discussions, the various groups discussed how wind loads in the HUD Code Part 3280 are from 1988, and the major barrier created by disincentives of manufactured home manufacturers and process of the HUD Code Part 3280 committee. In the latter case, committee members terms are for three years, whereas the code cycle is six years, thus making it difficult to make change in the code without a structured and targeted effort of multiple team members rotating on and off the committee during a single cycle.

The SAC also discussed a viable option for policy changes could be the replacement of Wind Zone I and II homes with Wind Zone III homes under the notion that Wind Zone III homes may vary in quality and performance but meet the same performance as site-built housing. This assertion lacks validation but based on structural details of Wind Zone III homes and the low quality of site-built housing permitted in the greater part of the U.S., the research team believes it is likely true.

Finally, the SAC discussed the urgency for getting national and federal attention on the research topic. Suggestions were made for a media strategy and drafting a one-pager to share with relevant federal offices demonstrating the results of (1) a benchmark study comparing loads produced on manufactured homes from HUD Code Part 3280 with ASCE 7-22, and (2) the results of a risk assessment demonstrating costs versus benefit tradeoffs between Wind Zones I, II, and III homes.

### ***Components and Connection Testing Study***

This section presents the results of the roof sheathing to rafter connection testing. First, the pinching4 material model is introduced, which was used to model the behavior of the cyclic load-displacement relationship. Monotonic test results are shared and then compared with NDS values; then cyclic test results are shared and fit with the pinching4 material model.

#### ***Pinching4 Material Model***

The pinching4 material model is capable of simulating cyclic behavior of fasteners, and has been implemented in OpenSees (Lowes, et al. 2004). The backbone curve of the pinching4 material is multilinear and is used as the basis for defining points along the positive and negative response envelope. A typical pinching4 backbone is shown in Figure 4. Variables  $ePf_1$ ,  $ePf_2$ ,  $ePf_3$ , and  $ePf_4$  define the force points on the positive response envelope, while  $ePd_1$ ,  $ePd_2$ ,  $ePd_3$ , and  $ePd_4$  define deformation values on the same. As sheathing-to-fastener connections are not capable of reversed loading, this study modified the pinching4 model to only define the positive branch of the backbone. The results from the tested configurations were evaluated to characterize the behavior of roof sheathing to rafter connections.

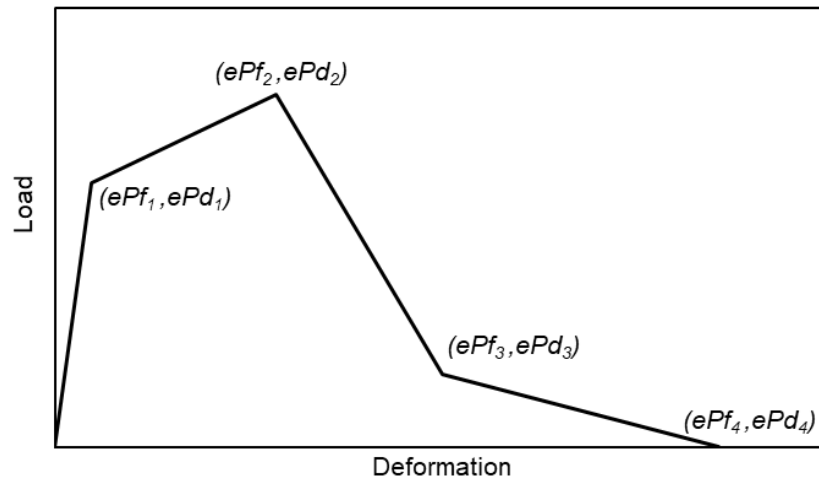


**Figure 4.** Modified pinching material backbone

*Monotonic Test Results*

Monotonic testing of screw and nail fasteners resulted in the two primary failure modes for this connection: pull-through and pull-out. Pull-through (PT) is described by the sheathing pulling through the fastener head as it remains embedded in the rafter. Pull-out (PO) is described by the fastener pulling out of the rafter and displacing with the sheathing. Screw fasteners exhibited both PT and PO failures. Nailed connections only exhibited pull-out failures, which is expected given the smooth shank and lower withdrawal capacity of nails relative to screws. Typical examples of PT and PO failure modes are presented in Figures 5a and 5b, respectively.

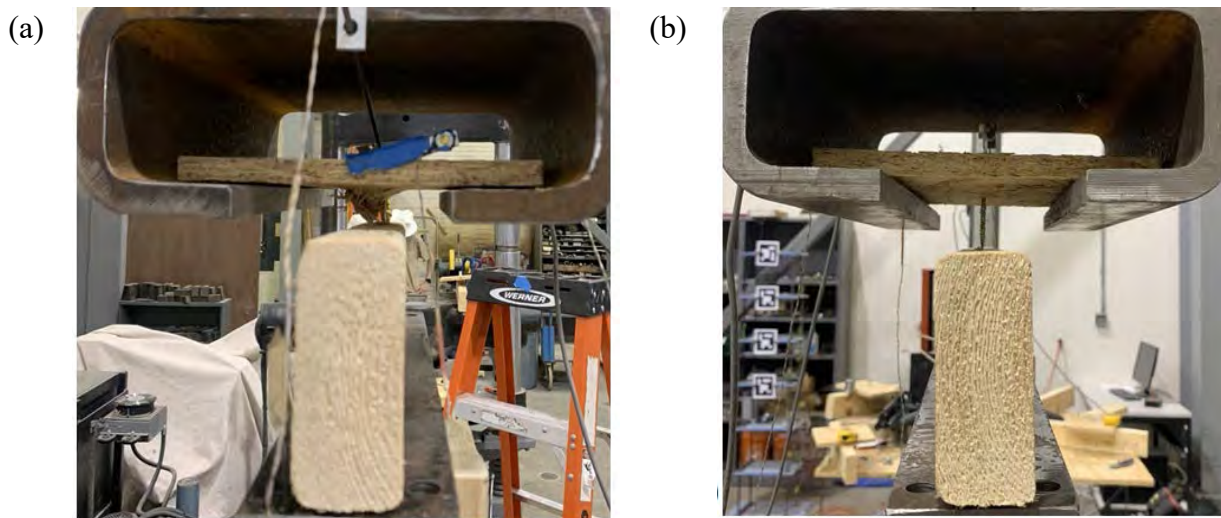


**Figure 5.** Screw test failure modes: (a) pull-through; (b) pull-out

A summary of monotonic test results is presented in Tables 3 through 6. Results include maximum load capacity and corresponding displacement, failure mode for each specimen, and mean capacity and coefficient of variation for all like specimens. Additionally, initial connection stiffness was determined for each test configuration by calculating the slope of the force-displacement curve up to load corresponding to 0.4  $P_{max}$  (ASTM 2018). As shown in Tables 3 through 6, the mean capacity of the nail connection in SYP lumber (Table 3) is 195 lbf which is approximately 40% of the mean capacity of the two screw connections. Furthermore, the coefficient of variation (COV) is approximately 2.5 times as high for the nail connected relative to the two screw connections.

**Table 3.** Monotonic test results for 8 x 8 plywood sheathing with single nail (SYP lumber)

Configuration	Load capacity $P_{max}$ N (lbf)	$\Delta_{max}$ mm (in.)	$0.4P_{max}$ N (lbf)	$\Delta_{0.4max}$ mm (in.)	Initial Stiffness $K_o$ N/mm (lbf/in.)	Failure mode	Mean Capacity N (lbf)	COV load
M-O-N-SYP-F1-1	517 (116)	6.13 (0.24)	207 (47)	0.17 (0.01)	1255 (7167)	PO	870 (195)	0.38
M-O-N-SYP-F1-2	453 (102)	0.3 (0.02)	181 (41)	0.13 (0.01)	1373 (7834)	PO		
M-O-N-SYP-F1-3	1236 (278)	0.46 (0.02)	494 (111)	0.33 (0.01)	1489 (8504)	PO		
M-O-N-SYP-F1-4	1210 (272)	3.71 (0.15)	484 (109)	0.15 (0.01)	3270 (18649)	PO		
M-O-N-SYP-F1-5	932 (210)	0.85 (0.03)	373 (84)	0.10 (0.01)	3671 (20963)	PO		

**Table 4.** Monotonic test results for 8 x 8 OSB sheathing with single screw (SPF lumber)

Configuration	Load Capacity $P_{max}$ N (lbf)	$\Delta_{max}$ mm (in.)	$0.4P_{max}$ N (lbf)	$\Delta_{0.4max}$ mm (in.)	Initial Stiffness $K_o$ N/mm (lbf/in.)	Failure Mode	Mean Capacity N (lbf)	COV Load
M-O-S-SPF-F1-1	2034 (457)	2.30 (0.09)	814 (183)	0.79 (0.03)	1033 (5898)	PO	2117 (476)	0.15
M-O-S-SPF-F1-2	2474 (556)	3.14 (0.12)	989 (222)	0.74 (0.03)	1344 (7669)	PO		
M-O-S-SPF-F1-3	2186 (491)	4.87 (0.19)	874 (196)	0.73 (0.03)	1195 (6822)	PT		
M-O-S-SPF-F1-4	2641 (594)	2.38 (0.09)	1056 (237)	1.27 (0.05)	832 (4748)	PT		
M-O-S-SPF-F1-5	1913 (430)	1.67 (0.07)	765 (172)	0.10 (0.01)	7530 (42983)	PT		
M-O-S-SPF-F1-6	1789 (402)	5.13 (0.20)	716 (161)	0.64 (0.03)	1127 (6432)	PT		
M-O-S-SPF-F1-7	1787 (402)	2.23 (0.09)	715 (161)	0.31 (0.01)	2345 (13382)	PO		

**Table 5.** Monotonic test results for 8 x 8 plywood sheathing with single screw (SPF lumber)

Configuration	Load Capacity $P_{max}$ N (lbf)	$\Delta_{max}$ mm (in.)	$0.4P_{max}$ N (lbf)	$\Delta_{0.4max}$ mm (in.)	Initial Stiffness $K_o$ N/mm (lbf/in.)	Failure Mode	Mean Capacity N (lbf)	COV Load
M-P-S-SPF-F1-1	2620 (589)	4.41 (0.17)	1048 (236)	0.93 (0.04)	1124 (6414)	PO	2360 (530)	0.13
M-P-S-SPF-F1-2	2678 (602)	5.85 (0.23)	1071 (240)	0.67 (0.03)	1599 (9127)	PT		
M-P-S-SPF-F1-3	2182 (491)	6.23 (0.25)	873 (196)	0.79 (0.03)	1103 (6296)	PT		
M-P-S-SPF-F1-4	1961 (441)	4.91 (0.19)	785 (176)	1.2 (0.05)	650 (3708)	PT		

*Comparison of test results with NDS values*

To compare test results with expected design values, the ASD and LRFD ultimate design capacities of these connections were determined based on the National Design Specification (NDS) (American Wood Council 2018). For nails, the ultimate withdrawal capacity is given by:

$$W_u = 6900 G^{2.5} D \quad \text{eq. (1)}$$

where  $G$  is equal to the specific gravity of wood ( $G = 0.55$  for SYP) and  $D$  is the fastener shank diameter ( $D = 0.113$  in.), which results in a value of  $W_u = 138$  lbf/in. The embedded length of the nail shank in the rafter member is 1.938 in., resulting in an ultimate withdrawal capacity of 267 lbf.

For wood screws, the ultimate withdrawal (pull-out) capacity,  $W_u$ , is given by:

$$W_u = 14250 G^2 D \quad \text{eq. (2)}$$

where  $G = 0.42$  for SPF and  $D$  is equal to the diameter of the screw shank ( $D = 0.164$  in. for #8), resulting in a value of  $W_u = 279$  lbf/in. Utilizing the length of the screw embedded in the rafter member (1.299 in.) results in an ultimate withdrawal capacity of 362 lbf.

Fastener head pull-through,  $W_H$ , is given by:

$$W_H = 690 \pi D_H G^2 t_{ns} \quad \text{eq. (3)}$$

where  $G$  is the specific gravity of the sheathing ( $G = 0.5$  for OSB),  $D_H$  is the fastener head diameter ( $D_H = 0.423$  in.), and  $t_{ns}$  is the net side member thickness ( $t_{ns} = 7/16$  in.), resulting in a value of  $W_H = 100$  lbf. As comparisons are being made with experimental data and capacity values are not being used for design, the implicit factor of safety of five that is empirically included in this calculation (Douglas et al 2018) was removed, resulting in an estimated pull-through capacity of 501 lbf.

Typical monotonic force-displacement (sheathing centerline displacement) behavior for the three connections tested here are presented in Figures 6 through 8. For easy comparison, the nominal ultimate capacities based on NDS calculation are plotted with monotonic test results. In all plots pull-out failures are represented by blue lines, while pull-through failures are represented by red lines. As shown in Figure 6, the nail connection peak load reached the nominal pull-out capacity in two of the five monotonic tests. The mean capacity shown in Table 3, however, was only 73% of the nominal pull-out capacity calculated through the NDS.

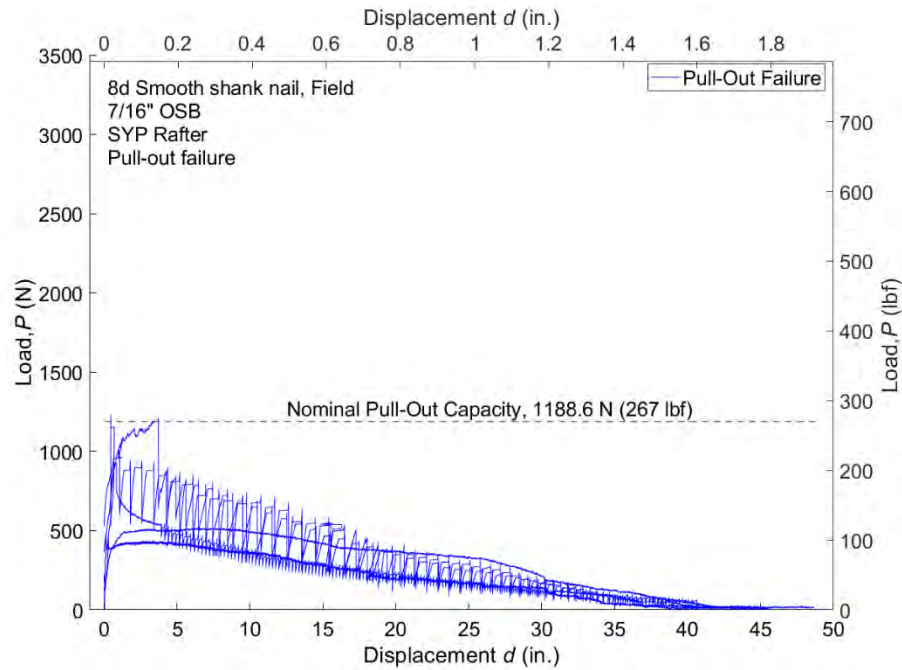


**Figure 6.** Monotonic load versus sheathing centerline displacement for nail, OSB to SYP connection

The monotonic test results for the screw connection in OSB sheathing are shown in Figure 7. The PO failure modes always exceeded the calculated nominal PO capacity, whereas three of the four tests which failure in PT did not reach the calculated nominal PT capacity. The mean capacity shown in Table 4, however, was 95% of the nominal PT capacity and over 100% of the nominal PO capacity calculated through the NDS.



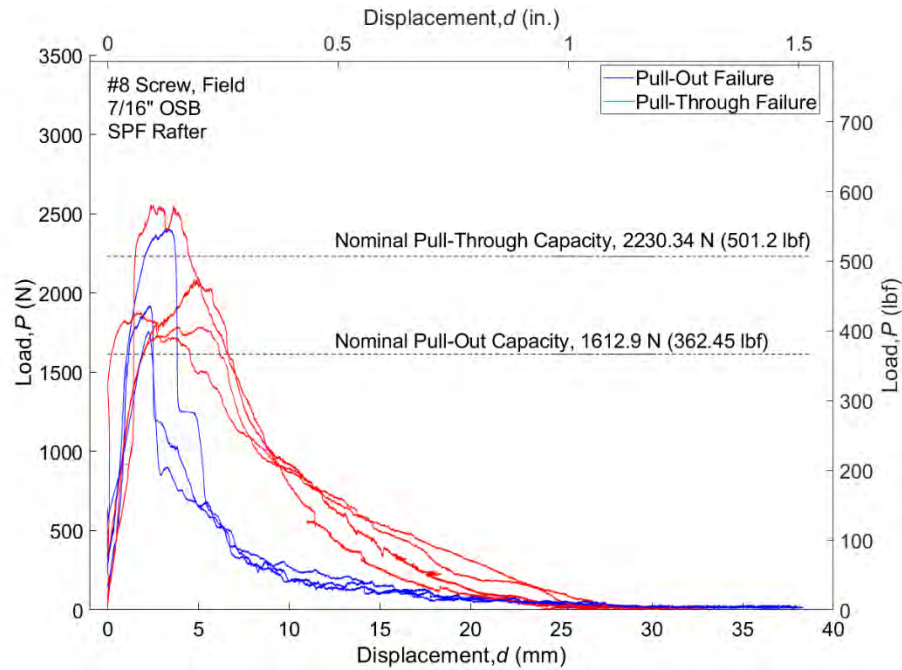


**Figure 7.** Monotonic load versus sheathing centerline displacement for single screw, OSB to SPF connection

Similarly, the monotonic test results for the screw connection in plywood sheathing are shown in Figure 8. The PO failure mode occurred in one of the four tests, and exceeded the calculated nominal PO capacity. The PT failure mode occurred in three of the four tests, where the calculated PT capacity was only exceeded in one of the three tests. The mean capacity shown in Table 5, however, was over 100% of the nominal PT and PO capacities calculated through the NDS.

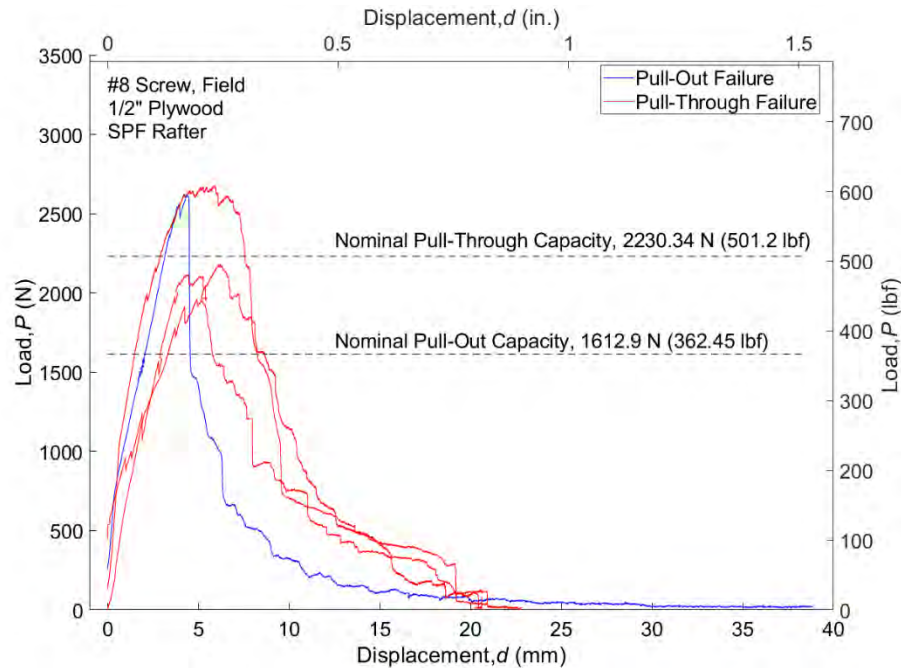


**Figure 8.** Monotonic load versus sheathing centerline displacement for single screw, plywood to SPF connection

### *Cyclic Test Results*

A typical cyclic force-deformation curve based on results of the monotonic tests and the modified FEMA 461 loading protocol described above is provided in Figure 9. The specific test specimen presented in Figure 9 is the nail, OSB to SYP connection. Additional plots of cyclic tests are provided in Appendix C. A summary of the test results is provided from Tables 6 through 8. Initial backbone curves (positive branch only) were constructed for each specimen. The positive backbone parameters were defined using Matlab's boundary command with a shrink factor of 1.0. The backbone parameters were fit to minimize the error between the force predictions and the test results. Tables 9 through 11 present the backbone curve parameters for all cyclic tests. The single screw in plywood sheathing produced the highest maximum displacements and highest maximum load capacities across all cyclic tests, which were both approximately three times higher than the maximum displacement and load capacities of the single nail in OSB connection.

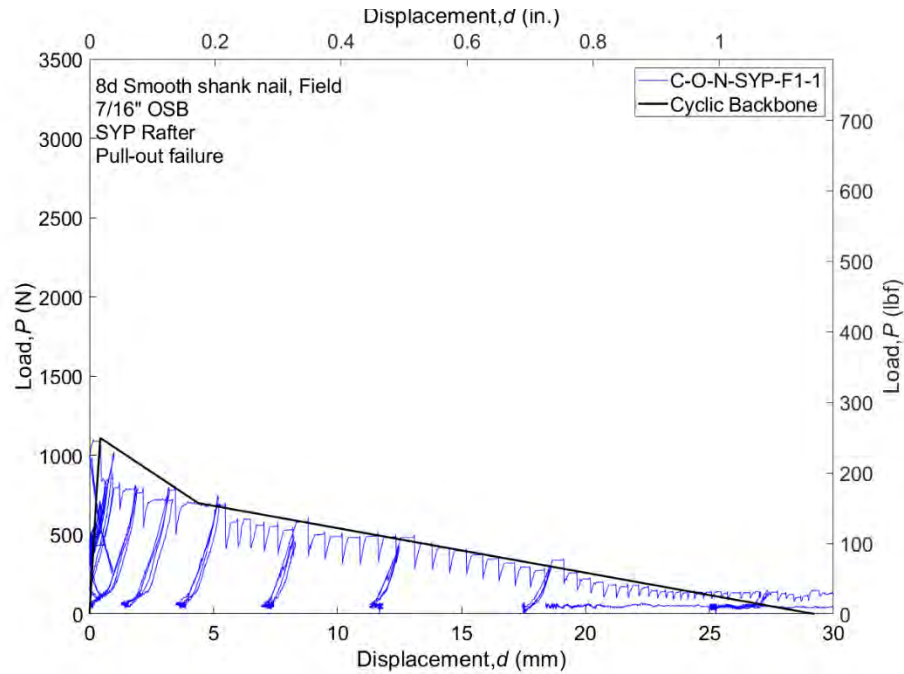


**Figure 9.** Cyclic force-deformation response for C-O-N-SYP-F1-1

**Table 6.** Cyclic test results for 8 x 8 OSB sheathing with single nail (SYP lumber)

Configuration	Load capacity $P_{max}$ N (lbf)	$\Delta_{max}$ mm (in.)	Failure mode	Mean Capacity N (lbf)	COV load
C-O-N-SYP-F1-1	1109 (249)	2.59 (0.102)	PO		
C-O-N-SYP-F1-2	992 (223)	1.39 (0.055)	PO	997 (224)	0.09
C-O-N-SYP-F1-3	889 (200)	2.15 (0.085)	PO		

**Table 7.** Cyclic test results for 8 x 8 OSB sheathing with single screw (SPF lumber)

Configuration	Load capacity $P_{max}$ N (lbf)	$\Delta_{max}$ (in.)	Failure mode	Mean Capacity (lbf)	COV load
C-O-S-SPF-F1-1	2139 (481)	2.59 (0.102)	PT	2282 (513)	0.06
C-O-S-SPF-F1-2	2370 (533)	2.23 (0.087)	PT		
C-O-S-SPF-F1-3	2159 (485)	1.80 (0.071)	PT		
C-O-S-SPF-F1-4	2457 (552)	1.52 (0.060)	PO		

**Table 8.** Cyclic test results for 8 x 8 plywood sheathing with single screw (SPF lumber)

Configuration	Load capacity $P_{max}$ N (lbf)	$\Delta_{max}$ mm (in.)	Failure mode	Mean Capacity N (lbf)	COV load
C-P-S-SPF-F1-1	2916 (656)	5.61 (0.22)	PO	2966 (667)	0.02
C-P-S-SPF-F1-2	3013 (677)	6.5 (0.26)	PO		

**Table 9.** Backbone parameters for 8 x 8 OSB sheathing with single screw (SPF lumber)

Configuration	ePd1 mm (in.)	ePd2 mm (in.)	ePd3 mm (in.)	ePd4 mm (in.)	ePf1 N (lbf)	ePf2 N (lbf)	ePf3 N (lbf)	ePf4 N (lbf)	Failure mode
C-O-S-SPF-F1-1	0.83 (0.03)	2.59 (0.10)	7.30 (0.23)	20.85 (0.82)	1605 (360)	2140 (480)	1284 (288)	0	PT
C-O-S-SPF-F1-2	0.45 (0.02)	2.23 (0.09)	6.23 (0.24)	17.81 (0.70)	1660 (373)	2371 (532)	1422 (319)	0	PT
C-O-S-SPF-F1-3	0.33 (0.01)	1.80 (0.07)	5.87 (0.23)	16.31 (0.64)	1512 (339)	2160 (485)	1317 (296)	0	PT
C-O-S-SPF-F1-4	0.49 (0.02)	1.53 (0.06)	3.71 (0.14)	9.90 (0.39)	1884 (423)	2458 (552)	1229 (276)	0	PO

**Table 10.** Backbone parameters for 8 x 8 plywood sheathing with single screw (SPF lumber)

<b>Configuration</b>	<b>ePd1</b> <b>mm</b> <b>(in.)</b>	<b>ePd2</b> <b>mm</b> <b>(in.)</b>	<b>ePd3</b> <b>mm</b> <b>(in.)</b>	<b>ePd4</b> <b>mm</b> <b>(in.)</b>	<b>ePf1</b> <b>N (lbf)</b>	<b>ePf2</b> <b>N (lbf)</b>	<b>ePf3</b> <b>N (lbf)</b>	<b>ePf4</b> <b>N (lbf)</b>	<b>Failure mode</b>
C-P-S-SPF-F1-3	1.81 (0.07)	5.61 (0.22)	7.23 (0.28)	18.0 (0.71)	1166 (262)	2917 (655)	496 (111)	0	PO
C-P-S-SPF-F1-4	1.40 (0.05)	6.52 (0.26)	7.22 (0.28)	20.0 (0.80)	1206 (271)	3015 (677)	935 (210)	0	PO

**Table 11.** Backbone parameters for 8 x 8 OSB sheathing with single nail (SYP lumber)

<b>Configuration</b>	<b>ePd1</b> <b>mm</b> <b>(in.)</b>	<b>ePd2</b> <b>mm</b> <b>(in.)</b>	<b>ePd3</b> <b>mm</b> <b>(in.)</b>	<b>ePd4</b> <b>mm</b> <b>(in.)</b>	<b>ePf1</b> <b>N</b> <b>(lbf)</b>	<b>ePf2</b> <b>N</b> <b>(lbf)</b>	<b>ePf3</b> <b>N (lbf)</b>	<b>ePf4</b> <b>N (lbf)</b>	<b>Failure mode</b>
C-O-N-SYP-F1-1	0.29 (0.01)	0.43 (0.02)	4.38 (0.17)	29.2 (1.15)	777 (174)	1110 (249)	699 (157)	0	PO
C-O-N-SYP-F1-2	0.30 (0.01)	1387 (0.05)	2.69 (0.11)	29.8 (1.17)	646 (145)	923 (207)	544 (122)	0	PO
C-O-N-SYP-F1-3	1.19 (0.04)	2.15 (0.08)	6.25 (0.25)	29.7 (1.17)	623 (140)	890 (200)	525 (118)	0	PO

## **Conclusions**

### ***Stakeholder Engagement***

The SAC provided critical feedback to the research team and should be a continued component of future research. The research team is pursuing an important research topic that is well-aligned with federal interests and initiatives. Future research should (a) perform a benchmark study comparing wind loads produced on manufactured homes in different areas of Florida following HUD Code in comparison to ASCE 7 (2022) provisions, and (b) produce the results of a risk assessment demonstrating cost and benefit tradeoffs for Wind Zones I, II, and III manufactured homes, as well as in comparison to homes with remedial measures for improved wind performance. Continuing experimental testing to be able to produce a viable finite element model of manufactured housing is critical for a realistic risk assessment.

### ***Components and Connection Testing Study***

Fastener component monotonic testing informed cyclic testing protocols. Subsequent cyclic testing of various sheathing fastener configurations provided data that will be used in detailed finite element models of MHU structures. As shown in the results of this report, the mean capacities for the nail connections in SYP lumber are substantially (2.5 to 3 times) less than the mean capacities for screw connections in SPF. Similarly, the COV was always 2.5 times higher for the nail connections in SYP compared with the screw connections in SPF. Given that nail connections are the more common connection used in the actual construction of Wind Zone II manufactured homes which have roof failure as the most common observed failure mode in the field, switching fasteners from nails to screws is expected to provide significantly higher performance. More research is needed to understand this relationship for edge fasteners, as well as for the roof-to-wall connection. Additionally, more research is needed to understand the material and labor cost difference that is associated with using screws instead of nails in the construction of these homes.

## References

American Housing Survey (AHS) (2019). 2019 Florida – General Housing Data – All Occupied Units. Accessed July 24, 2022. [https://www.census.gov/programs-surveys/ahs/data/interactive/ahstablecreator.html?s\\_areas=00012&s\\_year=2019&s\\_tablename=TABLE1&s\\_bygroup1=1&s\\_bygroup2=1&s\\_filtergroup1=1&s\\_filtergroup2=1](https://www.census.gov/programs-surveys/ahs/data/interactive/ahstablecreator.html?s_areas=00012&s_year=2019&s_tablename=TABLE1&s_bygroup1=1&s_bygroup2=1&s_filtergroup1=1&s_filtergroup2=1)

American Society of Civil Engineers (ASCE) (2022). Minimum Design Loads for Buildings and Other Structures, Standard 7. American Society of Civil Engineers, Reston, VA.

American Society for Testing and Materials (ASTM) (2020). Standard Test Methods for Mechanical Fasteners in Wood and Wood-Based Materials, ASTM D1761. West Conshohocken, PA.

Douglas, B., Line, P., and Douglas, K. (2018). Evaluation of Fastener Head Pull-Through Strength of Wood. American Wood Council, Leesburg, VA.

Federal Emergency Management Agency (FEMA) (2007). Interim Testing Protocols for Determining the Seismic Performance Characteristics of Structural and Nonstructural Components, FEMA 461. Prepared by the Applied Technology Council for the Federal Emergency Management Agency, Washington, D.C.

Ferguson, W. (2022). ‘Sitting on a time bomb’: Mobile home park residents at risk in red-hot housing market. *Manufactured Home News*, published on April 27, 2022. <https://www.manufacturedhomes.com/blog/red-hot-housing-market/>

National Design Specification (NDS) (2018). National Design Specification for Wood Construction, 2018 Edition. ANSI/AWC-NDS 2018. American Wood Council, Leesburg, VA.

U.S. Department of Housing and Urban Development (HUD) (2022). 24 Code of Federal Regulations Part 3280, Manufactured Home Construction and Safety Standards. Washington, D.C.

**Appendix**

*Appendix A – Project Team presentation to SAC on February 25, 2022*

*Appendix B – Project Team presentation to SAC on June 28, 2022*

*Appendix C – Specimen-level Cyclic Results*

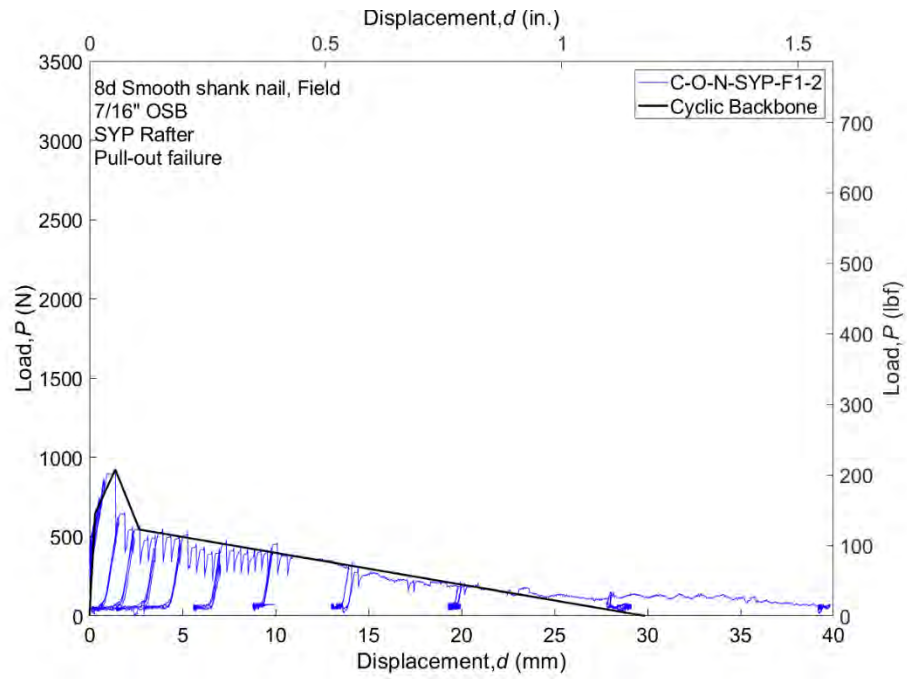


**Figure C1.** Cyclic force-deformation response for C-O-N-SYP-F1-2



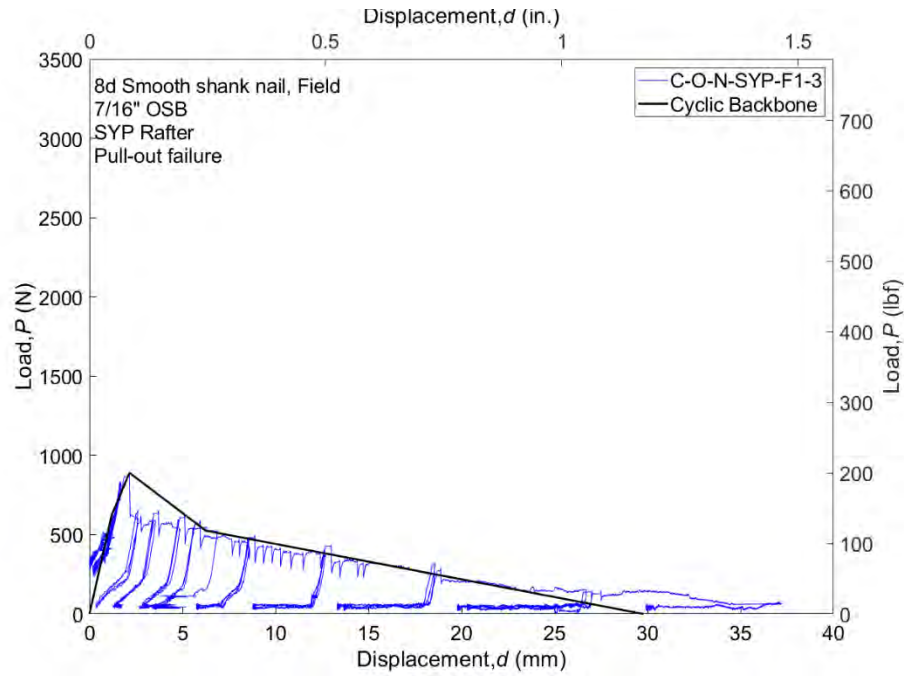


**Figure C2.** Cyclic force-deformation response for C-O-N-SYP-F1-3

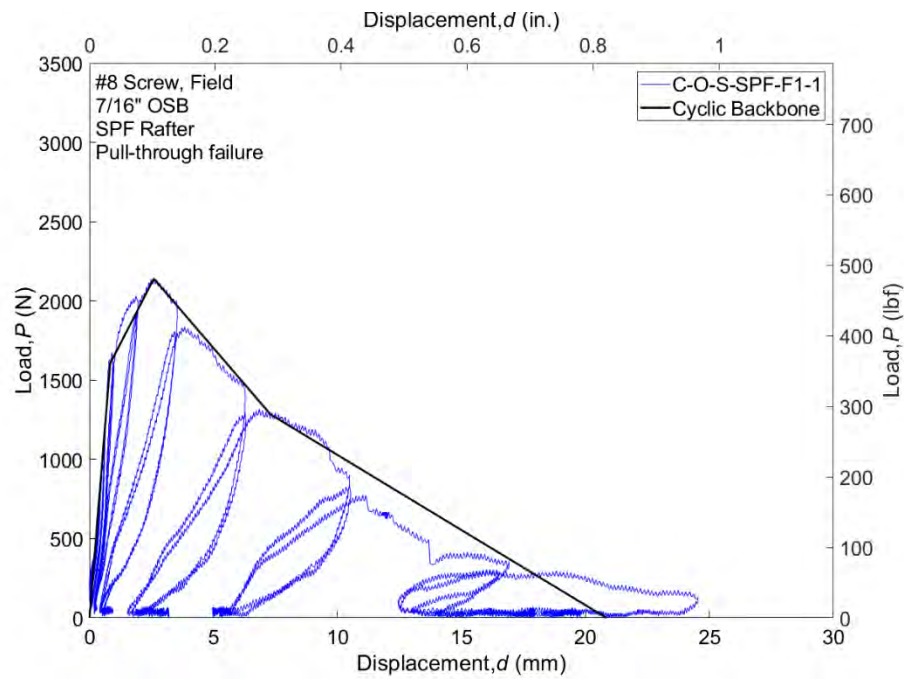


**Figure C3.** Cyclic force-deformation response for C-O-S-SPF-F1-1

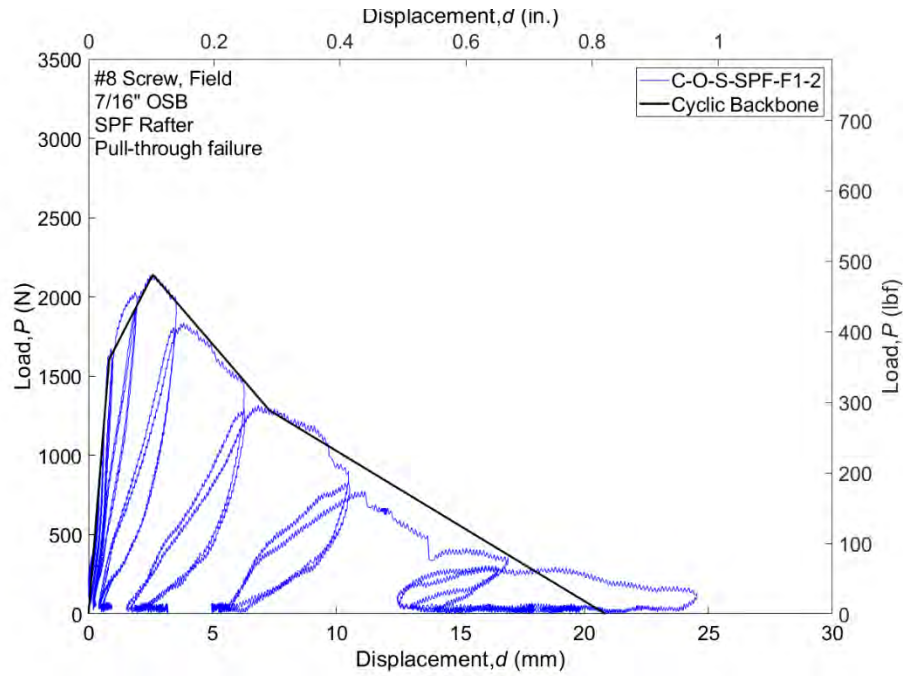


**Figure C4.** Cyclic force-deformation response for C-O-S-SPF-F1-2

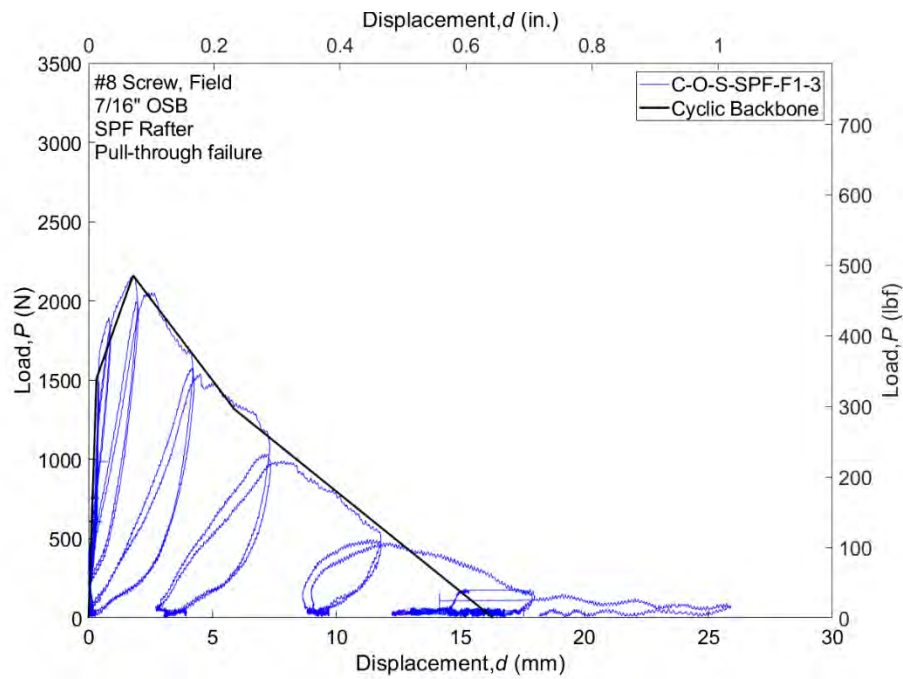


**Figure C5.** Cyclic force-deformation response for C-O-S-SPF-F1-3

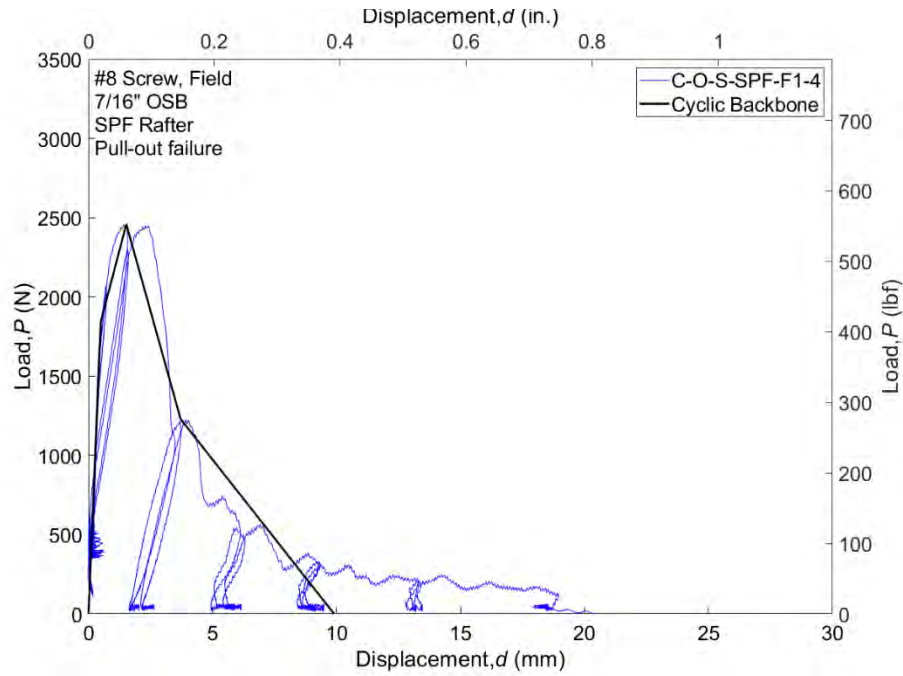


**Figure C6.** Cyclic force-deformation response for C-O-S-SPF-F1-4

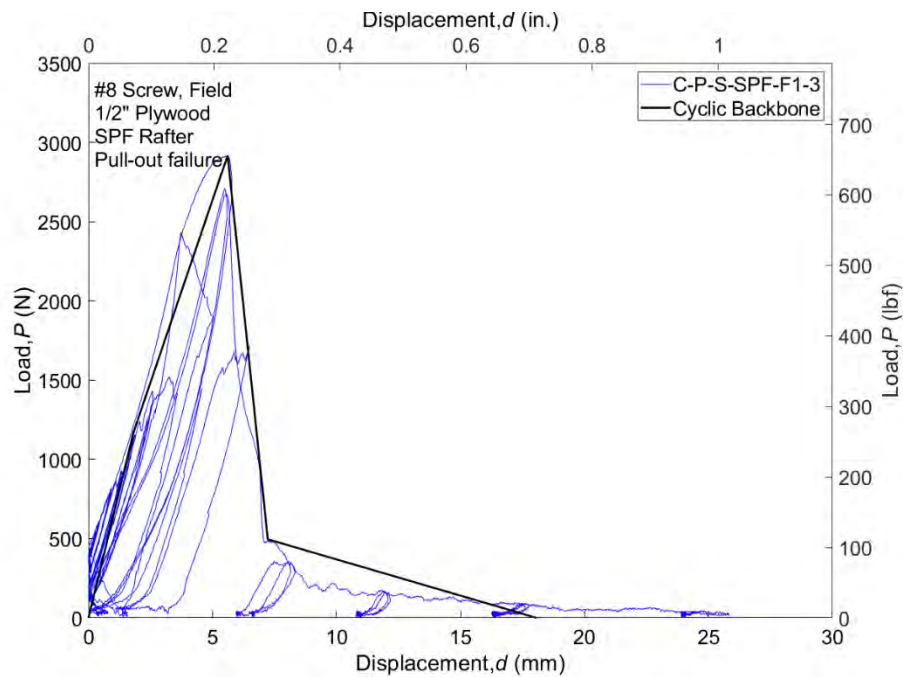


**Figure C7.** Cyclic force-deformation response for C-P-S-SPF-F1-3

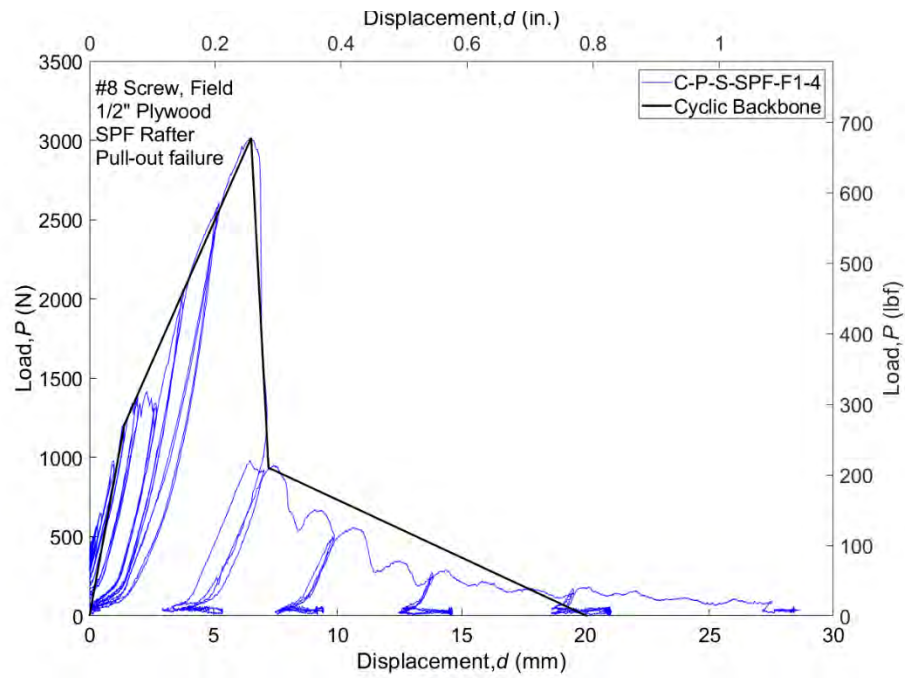


**Figure C8.** Cyclic force-deformation response for C-P-S-SPF-F1-4



*A Resource for the State of Florida*

### SECTION 3

## THE ROLE OF SLOWLY-VARYING DOWNBURST WIND DIRECTIONS ON THE RESULTING AERODYNAMIC LOADING ON BUILDINGS

**(Period: 2021-2022)**

*A Research Project Funded by:*  
**The State of Florida Department of Emergency Management**

*Prepared by*  
*Dr. Amal Elawady*  
*Fahim Ahmed, PhD Candidate, FIU*  
*Kehinde Alawode, PhD Candidate, FIU*

## **Executive Summary:**

Downbursts are non-stationary, transient, localized high winds that causes severe damage to buildings. Downbursts differ from synoptic ABL winds, which makes assessing their effects on buildings and other structures a complex process. This study examines how bluff body aerodynamics change during downburst velocity evolution with and without the effect of slowly varying wind direction. To replicate a real event that took place on June 19, 2003 in Lubbock, Texas, at the WOW lab, the event was scaled down using appropriate time, length, and velocity scales. Downburst experiments began with scaled downburst flow characterization followed by static aerodynamic tests for wind direction (180°, 225°, 270°) and dynamic aerodynamic tests for wind direction varying between (260° to 290°). The maximum moving mean velocity at the building model roof mean height was 12.1 m/s using a time average window of 0.5 s. It was observed that pressure coefficient ( $C_p$ ) distribution across the building is similar to that typically observed for Atmospheric Boundary Layer wind events for all static directions. It was also observed that all surfaces have higher  $C_p$  values for the dynamic cases compared to the static cases. Future studies are needed to better codify downburst impact on buildings and the effect of the rotating wind direction on the wind loading of the building. In future analysis, peak pressure distributions will further be evaluated. The findings of this study and the planned future study of this new research topic will help improve design provisions in current codes and standards.

## 1. Introduction

At the mature stage of a cell thunderstorm, a downburst form. Downburst winds are a falling mass of cold air that strikes the ground and transfers horizontally, causing significant radial outflow (Henry Liu, 1991). During the 18-year period between 1986 and 2003, downbursts caused more deaths and injuries than tornadoes and, in certain cases, hurricanes (Ashley & Mote, 2005). The damage caused by downbursts can be difficult to distinguish from that caused by tornadoes. This has led to a tendency in technical reports and damage assessment studies to combine the two occurrences and, in many circumstances, refer the damage to tornadoes effect only (F. Lombardo & Smith Douglas, 2009). However, the size of downburst events relative to that of tornadoes suggests that downbursts may have larger spatial impact than tornadoes. The size of downbursts cell can vary from 500 m to 4000 m which is translating to even larger spatial impact once it impinges on the ground and diverge radially in all directions (Richter et al., 2014). Downbursts are stochastic, nonstationary, localized, and highly turbulent extreme weather events that create high wind intensities in many places around the world (F. Lombardo & Smith, 2009; F. T. Lombardo et al., 2018).

Unlike hurricanes where the maximum wind speeds occur at high elevations, downburst maximum velocities are observed at low heights ranging between 5 m and 100 m, which is the normal range of building and infrastructure heights. These winds may cause damage to roofs, or total collapse of structures, particularly low-rise buildings, and other structures, to the same extent as catastrophic tornadoes (F2-F3).

Downbursts have different features compared to synoptic Atmospheric Boundary Layer (ABL) winds, which increases the difficulty of assessing their effects. The vertical profile of a downburst horizontal velocity exhibits a "nose shape" - one of the most distinguishing features of downbursts compared to regular ABL (Holmes, 2008). In addition, downburst velocity time history exhibits a short high intensity velocity spike consisting of a ramp-up, plateau, and a ramp-down. Such feature is expected to affect the dynamic response of flexible structures. Also, the temporal localization of the event means that downburst wind speeds have stochastic, non-stationary, and non-gaussian distribution nature. In addition, downbursts may exhibit varying wind directions during the short time period unlike synoptic winds which exhibit predominant wind direction. This

highlights the need to develop new design guidelines and data analysis methods suitable for the localized nature of downburst events and their impact on structures.

The focus of this study is to assess the impact of downbursts on low-rise buildings. Particularly, the study focuses on assessing the effect of slowly-varying downburst wind directions on the resulting aerodynamic loading on buildings. To achieve this goal, we have identified available data for a real downburst event occurred in Lubbock, Texas on June 19<sup>th</sup>, 2003, and its impact on a field building instrumented with pressure scanner along all surfaces. The wind and pressure data were made available to our team by Dr. Frank Lombardo, University of Illinois Urbana Champaign. Thus, the objectives of this study have twofold: (1) to experimentally assess the effect of the slowly-varying wind direction in comparison to downburst with predominant wind direction on the resulting surface pressure on a low-rise building model; (2) to compare the results obtained experimentally with those reported for other findings reported previously for experimental ABL testing on similar models.

## **2. Experimental Methodology**

The downburst wind profile is developed to be as accurate as possible to real-world conditions downburst recorded at Lubbock, Texas on June 19, 2003, using appropriate scaling. The automated turntable that is placed inside the testing chamber was used to adjust the direction of the downburst wind. A rotating transducer was used to record the rotation of the turntable with the building model. To get the surface pressure, pressure taps were employed on the scaled down building model. Three test types were adopted in the current study to assess the impact of the downburst with varying wind direction.

Test#1: Downburst flow characterization.

Test#2: Static downburst aerodynamic simulation. This test type represents the cases where the downburst flow was applied on the building without changing the direction during the event (i.e., no simultaneous changes in the wind direction during each test case).

Test#3: Dynamic downburst aerodynamic simulation. This test type represents the cases where the downburst flow was applied on the building with changing the direction during the event to replicate the scaled down Texas rotating downburst event.



Section 3 discusses the experimental facility used in this study, section 4 describes the field event of interest, section 5 discusses the scaling methodology, and section 6 explains the test protocol. In section 7, the flow characterization and aerodynamic results are provided and discussed. Conclusions and findings of this study are provided in section 8.

### **3. Experimental Facility**

#### *3.1 Wall of Wind*

The National Science Foundation-Natural Hazard Engineering Research Infrastructure (NHERI) Wall of Wind (WOW) is an open jet wind testing facility. The WOW is made up of a 12-propeller fan matrix arranged in 2 rows by 6 columns that generates massive amounts of wind that are then accelerated and shaped into a rectangular flow management box with a cross-sectional size of 6.1 m wide by 4.3 m high. The flow management box has a 9.75 m long fetch. The WOW has flow conditioning devices such as triangular spires and dynamic floor roughness components that provide straight line ABL flows for various terrain configurations of choosing.

Large turbulent wind fields generated by the WOW are capable of testing entire and large-scale structural models and their components to analyze the underlying weakness and vulnerability in their performance. The WOW is equipped with a 4.9 m diameter turntable, where the test models are mounted at their bases, receives the discharged flow from the open test section outside the region of the flow management box outlet. The turntable center is placed 6 m from the flow management box outlet allowing a large range of downstream locations where single point velocity measurements can be performed at varying heights and horizontal distances of interest. Figure 1 shows the WOW fans intake and the flow management box.



*Figure 1: FIU NHERI Wall of Wind experimental facility showing (a) rear end consisting of 12 fans positioned in an arch shaped, 2 rows by 12 columns and (b) front end consisting of the flow management box shooting the ABL wind flow jet.*

### *3.2 Downburst simulator at WOW*

A large-scale downburst simulator was recently added to the WOW, in front of the flow management box outlet. The downburst simulator aims to produce large-scale downburst outflows across the WOW testing section and reproduce transient aerodynamic loads on diverse structures. The WOW's incorporation of large-scale transient loads explores a new venue of hazard mitigation studies. Two louver-slats cover the simulator's lower 1.52 m by 5.94 m opening. The vertical slats open to a certain angle. The slat opening mechanism comprises of two counterweight systems (one on each side of the downburst simulator) coupled to the slats via stainless steel rope, pulleys, and winches. Counterweights hang while electromagnets hold louver slats. An Arduino system shuts power to the electro-magnets holding the slats closed. When the electromagnets lose power, they turn off, releasing the slats. The falling counterweights pull the ropes, opening both louver slats. Both slats are 5.89 m wide, 0.74 m long, 0.0127 m thick and weigh 133 kg each. The downburst simulator's upper part consists of blockage by aluminum 8020 framing and plywood sheathing to guide wind from the flow management box to the bottom region. A gravity gate (GG) placed behind the simulator blockage and electromagnet-suspended louver slats were employed to terminate the flow and reduce wind speeds when desired. The GG have counterweights that are used to control the rate of the drop. GG was attached with linear bearings. GG weighs 182 kg. The hanging electromagnet's power source was switched off after the louver slats opened so the gravity gate falls a 1.52 m. The GG was halted by shock absorbers located at the ground. Figure 2 shows the downburst simulator at WOW.



Figure 2: The WOW downburst simulator with the Cobra Probe at the Turntable Center

#### 4. June 19, 2003 Downburst Event Description

On June 19, 2003, a downburst hit Texas Tech University's Wind Engineering Research Field Laboratory (WERFL) in Lubbock, Texas. Instrumented WERFL anemometer tower captured the lower 50 m of the event at the five levels. The recorded wind speeds indicate that the maximum wind speed occurred at the WERFL mean roof height (4 m). The peak recorded (3 sec filtered) wind velocity  $V$  ( $V_{3\text{sec}}$ ), was 29.0 m/s (24.44 m/s) at the WERFL building's mean roof height (4 m) and 25.8 m/s (24.35 m/s) at the 10 m height. Wind direction ( $\theta$ ) at both heights was approximately 280 deg at the time instant corresponding to the maximum wind speed (Lombardo et al., 2018) . Figure 3 displays the 3-sec moving average velocity ( $V_{3\text{sec}}$ ) and direction ( $\theta_{3\text{sec}}$ ) time history for the downburst event with identification of the signature downburst ramp up and ramp down.

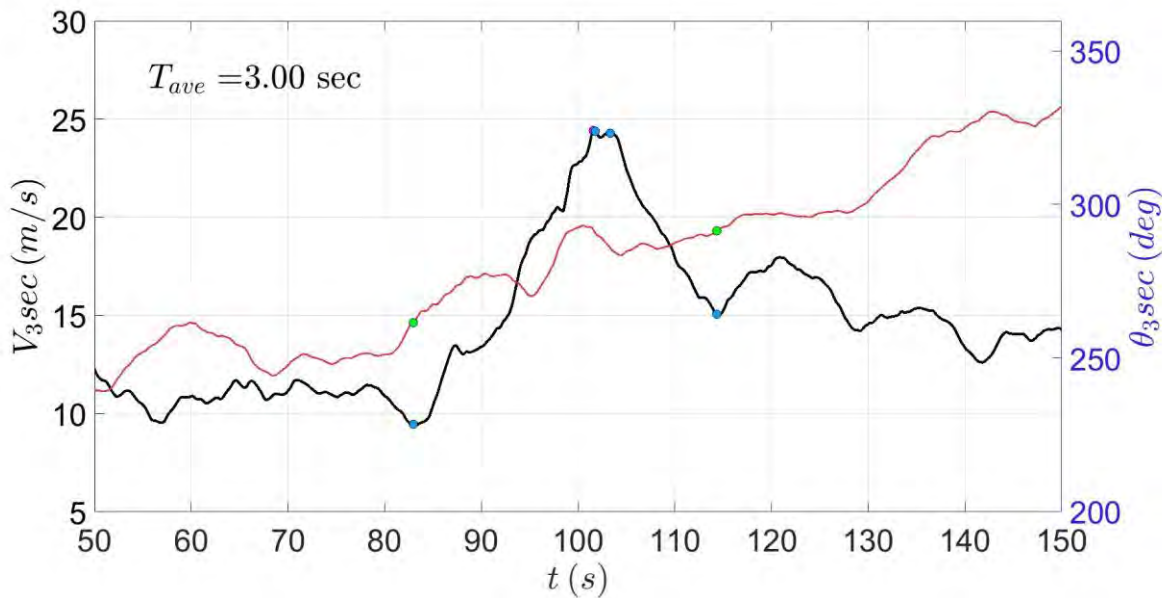


Figure 3: 3-sec moving average velocity ( $V_3$ ) and direction ( $\theta_3$ ) time history for the downburst event with identification of the ramp up start, peak, ramp down start and end (blue dot).

The initial record was 900s, however the first 150s are most significant to the downburst occurrence. Figure 3 highlights "ramp-up" and "ramp-down" phases before and after the peak wind gust. Wind direction changed from  $260^\circ$  to  $290^\circ$  in one minute between 83 and 114 seconds.  $V_{3sec}$  measured at building eaves height (4 m) was used to identify the ramp-up and ramp-down times. In the current study, flow accelerations were calculated from the smoothed record's gradients. Total ramp-up and ramp-down times were assessed to be 19.8s and 11.2s, respectively. Similar ramp-up and ramp-down durations were estimated for each WERFL tower height (Lombardo et al., 2018)

### 5. Scaling of the Downburst Event

To replicate the Texas downburst event at the WOW experimental facility, the event was scaled down using a length scale ( $\lambda_L$ ) = 1:20, time scale ( $\lambda_t$ ) = 1:11.20, which means the scaled down event (Model Event) duration is 2.8 s ( $\sim 3$  s). The velocity scale accordingly is ( $\lambda_V$ ) =  $\lambda_L / \lambda_t = 1:1.8$ . This gives the peak velocity of the scaled down event (Model Event) to 13.10 m/s.

The wind direction at the beginning of the downburst or at the start of the ramp up period was  $260^\circ$  deg and at the end of the downburst or ramp down period the direction was  $290^\circ$ . Thus, the wind direction change during the peak zone, the time zone of interest to structural engineering, was  $30^\circ$  in 2.8 s in the small scale simulations. So, the rate of wind direction changes in the scaled down event (Model Event) = 10.7 deg/s.

## 6. Test protocol

### 6.1 Model Configuration

WERFL building is a nominally sealed, rotatable low-rise building measuring 9.1 m x 13.7 m x 4.0 m and equipped with 204 differential pressure transducers measure external pressure on all faces of the building (Lombardo et al., 2018) (Lombardo et al., 2018) . The test model used in this study was a scaled-down (using length scale 1:20) model of this building made up of plexiglass and equipped with 204 pressure taps. The dimensions of the model building were 0.69 m x 0.46 m x 0.20 m. The building had a gable roof with a small slope of 1.27°. Figure 4 shows a photo of the WERFL building model mounted at the center of the turntable at the WOW.

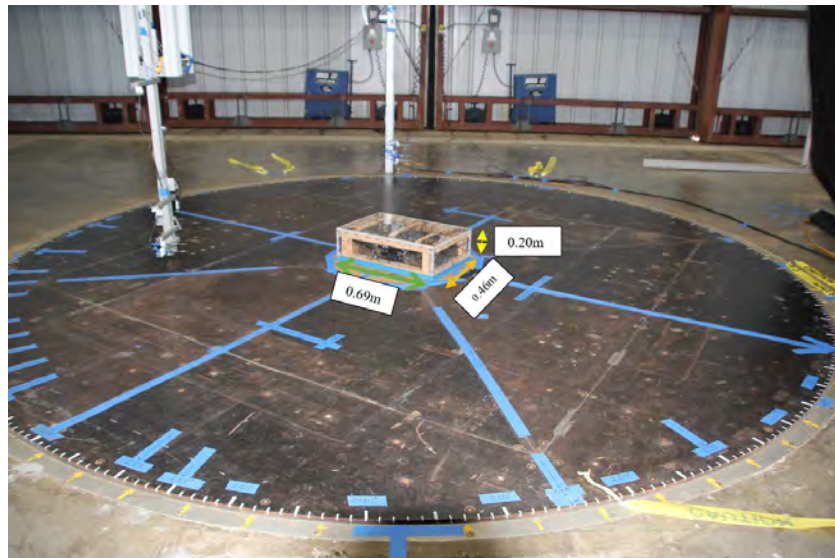


Figure 4: 1:20 scaled WERFL building with 204 taps

### 6.2 Instrumentation

To measure the free flow velocity, 5 Cobra probes were used with a sampling frequency of 625Hz. The Cobra probes monitor wind velocities in three directions. The cobra probes were placed at heights of 19, 152, 198, 304, 508 mm from the turntable. These heights were strategically selected to capture the peak velocity of the flow. Cobra probes were placed in a vertical rake that could move across the testing section in front of the downburst simulator. Figure 5 shows the cobra probes arrangement on the vertical rake.



*Figure 5: Location of the cobra probe to measure wind velocity*

When the downburst was desired, the slat angle was opened to at  $40^\circ$  to the horizontal plane and WOW fans throttle was set to 18%. The timer was fixed in such a way that the gravity gate will be released after 1 sec of opening the slat. Such setup enabled achieving the required peak zone duration of 3 sec at the turntable center.

Pressure on the surface of the model was captured through the pressure taps and pressure scanners. The pressure taps were connected to the ZOC33 Scanivalve pressure scanner module. Wind pressure data was acquired at 625Hz sampling frequency. A tubing transfer function (Irwin et al., 1979) was used in the analysis to account for the tube length.

The turntable rotation was measured with a rotating transducer device attached to the turntable at the WOW. This data was also sampled at 625Hz to ensure synchronization of the data.

### *6.3 Test Sequence*

The downburst experiments began with the flow characterization of the scaled downburst event. This phase of the tests involved figuring out (i) the location of the maximum wind speed along the vertical axis, (ii) the orientation of building before applying the turntable rotation to ensure the building was at the right angle when hit by the simulated downburst (iii) number of counter-weight blocks on the slat and gravity gate to ensure a similar outflow behavior as the Texas field event (i.e., rate of acceleration and deceleration of the flow during the peak zone of the time history). After each downburst flow calibration test, the wind velocity timeseries, and wind profiles were checked to ensure there were no errors and confirm the profiles match the expected scaled-down event.

The static pressure test of the building model was the next phase. The building model was fixed to the center of the turntable and subjected to the WOW downburst flow at 180°, 225°, 270° wind directions to investigate non-stationary, transient downburst surface pressures on each building surface (windward, leeward, side walls and roof). Each downburst aerodynamic test was conducted at 625 Hz/channel pressure sampling.

The dynamic test was the third and final phase of the study. In the dynamic test, 30° rotation was applied starting with various building orientation angle (i.e., 180°, 225°, 270°) with rotational speed of 10.7 deg/sec. During this test pressure data was recorded with 625 Hz/channel pressure sampling and the rotation of the turntable was recorded using a rotating transducer. The turntable rotation was started with certain degree offset to compensate for the acceleration of the turntable and to achieve the required speed 10.7 deg/sec. Figure 6 shows the variation of the turntable rotation speed (deg/sec) with variation of time (s). At 13.16s turntable started rotating and at 14.25s it reached the desired constant mean speed of 10.7 deg/sec. This speed remained constant up to 20.69s then it gradually started to lose speed and was completely stopped at 21.90s. The downburst occurred between 14.25s to 20.69s so that uniform direction change can be achieved.

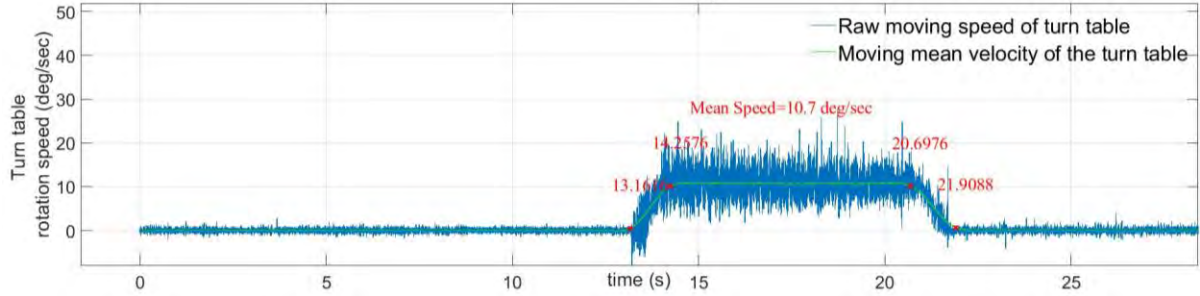


Figure 6: Variation of turn table rotation speed with time

## 7. Result and Discussion

This section starts with investigating the flow characteristics of the downburst outflows generated at the WOW test section. The mean and peak pressure coefficient ( $C_p$ ) distribution on each building face is calculated to assess the effect of downburst outflows on the buildings. Also, a comparative study is done after applying the rotational effect of the downburst to assess the role of the slowly-varying wind speed of the downburst flow on the resulting surface pressures

### 7.1 Flow characterization

The mean wind velocity was extracted using a moving mean time window  $T_{avg}$  based on classical decomposition methods suggested by (Holmes, 2008; Solari et al., 2015). Total instantaneous wind velocity of a downburst at any height, any time, and any downstream horizontal distance is defined as the vector summation of a central moving average wind velocity and a fluctuating wind velocity.

$$V(x, y, z, t) = \bar{V}(x, y, z, t) + v'(x, y, z, t)$$

where  $V(x, y, z, t)$  is the total instantaneous wind velocity at height  $z$  and time  $t$ ;  $\bar{V}(x, y, z, t)$  is the slowly-varying, non-turbulent, moving mean wind velocity;  $v'(x, y, z, t)$  is the residual turbulent fluctuation. The slowly varying mean  $\bar{V}(x, y, z, t)$  represents moving mean horizontal velocities based on a time moving window selected typically based on best visual fit to eliminate the fluctuation component. From these tests,  $T_{avg}$  of 0.5 s was applied to all cobra probe time histories. Figure 7 shows the raw and moving mean velocity time histories for the Free Flow Test (FFT) at the turntable center. The maximum moving mean velocity  $\bar{V}_{max} = 12.1$  m/s was achieved at the building eave height ( $z_{max}=198$  mm). As shown in the figure, the moving mean velocity time history follows the instantaneous velocity signal (Hjelmfelt, 1988a).



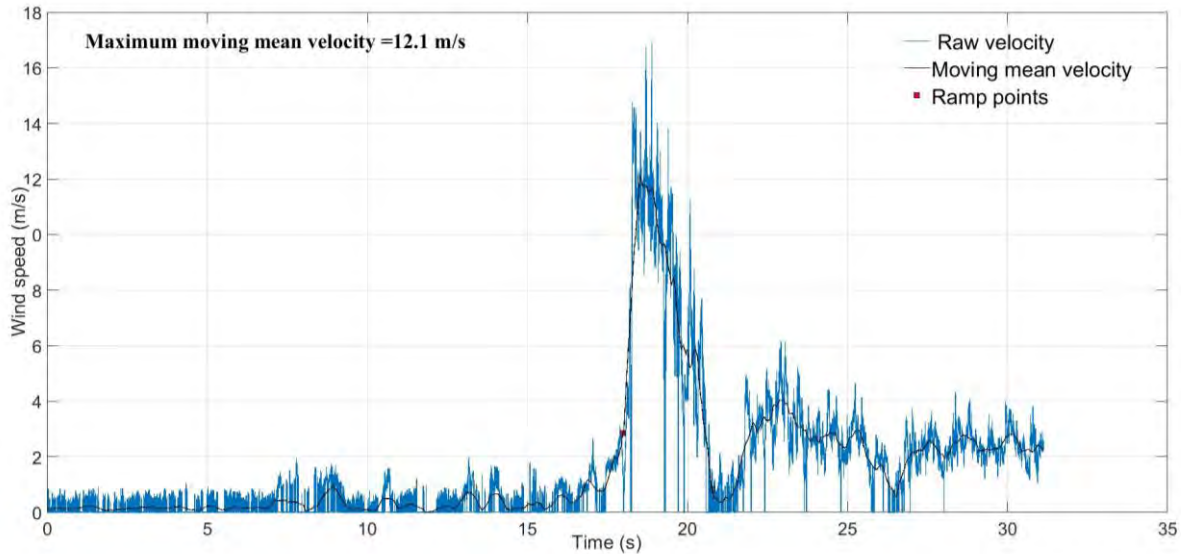


Figure 7: Velocity time history for Free Flow Test (FFT) at the turntable center, at building eave height of 198 mm

For each downburst test, the vertical profile of horizontal velocities at the Turntable Center (TTC) was normalized based on the maximum moving mean velocity ( $\bar{V}_{\max}$ ) from all five cobra probe locations.  $z_{\max}$  was the height of the maximum wind speed. For these experiments  $\bar{V}_{\max} = 12.1$  m/s and  $z_{\max} = 198$  mm, which was the eave height of the building, were used. Figure 8 compares the vertical profile of the normalized horizontal velocity constituting the 'nose' shape and measured at the TTC to real downburst events (Hjelmfelt, 1988a) and previous experiments from literature to assess the validity of the current tests.

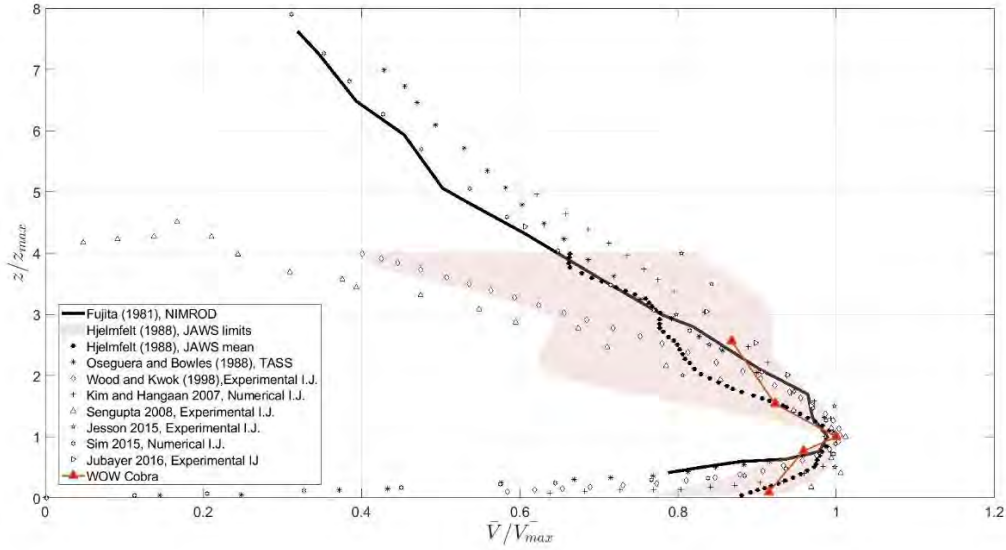


Figure 8: Vertical profile of horizontal wind velocities at the TTC for flow characterization with slat angles at 40 degrees.

## 7.2 Turbulence characterization

Downburst outflow dynamics and vortex development require a comprehensive analysis of statistical quantities such as turbulence intensity, integral length scale, Power Spectral Density (PSD), among others. The status quo of current data analysis methods for wind records are based on stationary gaussian events. The transient nature of downbursts yields to difficulty in evaluating statistical quantities representing the turbulence content. The following equation was used to define the instantaneous turbulence intensity of non-stationary winds, such as downbursts:

$$I_{u',T} = E \left[ \frac{\sigma_{v',T}}{\bar{V}_T(t)} \right]_T$$

where  $E [\cdot]$  is the expected value within a short time interval  $T$ ;  $\sigma_{v',T}$  is the standard deviation of the residual fluctuating wind velocity within a time interval  $T$  known herein as the peak zone defining the boundary of the ramp-up to ramp-down zone of the downburst time history and  $\bar{V}_T(t)$  is a time varying mean wind velocity which is considered herein to be equal to the maximum moving mean velocity within the peak zone.

Figure 9 shows the turbulence intensity profile for the downburst flow generated at the WOW measured at the TTC. Both field events (Lombardo et al., 2018) and laboratory simulated events (Le & Caracoglia, 2021) have indicated that downburst turbulence intensities reduce/taper off above the peak height which is also observed by the current study results.

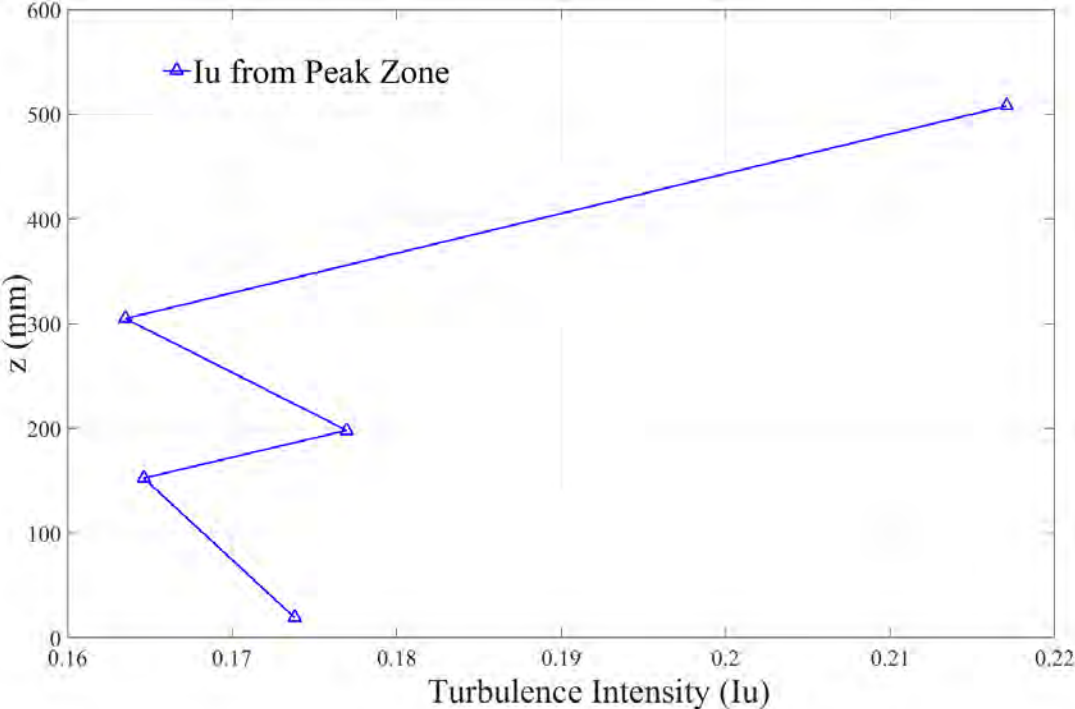


Figure 9: Vertical profile of turbulence intensity.

Figure 10 shows the non-dimensionalized PSD of the raw velocity V within the peak zone at the TTC. The downburst fluctuation has an adequate Von Karman model fit, and no deficiency is seen in the low frequency end. It was normalized using the raw velocity V within the peak zone. This match enabled us to proceed with the wind loading assessment as provided in the next section.

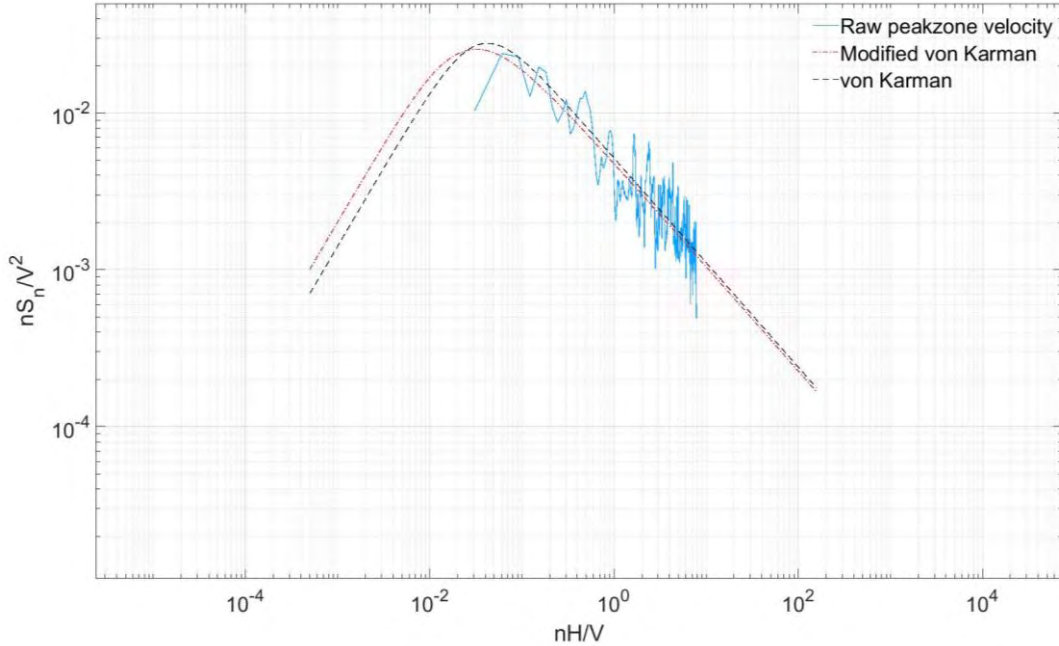


Figure 10: Non-dimensionalized Power Spectral Density for flow at the turn table center.

### 7.3 Building Aerodynamics

The natural dynamics of ABL and Downburst flows are different, so comparing wind loading in the form of pressure coefficients  $C_p$  requires several assumptions. The goal is to identify which method is best for determining  $C_p$  given downbursts' temporal localization character. In ABL wind loading, the surface differential pressure is normalized with respect to a reference velocity as follows:

$$C_{pmean} = \frac{p - p_{atmospheric}}{\frac{1}{2} \rho_{air} \bar{V}_{ref}^2}$$

where,  $\bar{V}_{ref}$  is the mean reference velocity recorded at the roof eave height of the appropriate building model during ABL events,  $p$  is the mean measured pressure. Because ABL flow is stationary, a single mean value can be applied to the complete pressure  $p$  and velocity  $\bar{V}_{ref}$  time series.

Downbursts cannot employ the same time averaging window as stationary events since they are shorter and temporally localized (Lombardo Franklin T., 2009). Several authors (Jesson et al.,

2015; Lombardo et al., 2018; Lombardo Franklin T., 2009) defined  $C_p$  with varied  $T_{avg}$  temporal averages. Asano et al., 2019 employed a mean pressure value and a maximum instantaneous wind velocity as reference velocity  $V_{max,T}$ . For this investigation, the following study is based on a  $T_{avg}$  of 0.5 sec applied to both the time-dependent moving pressure and velocity time histories.  $C_{p,mean\ Enve}(t)$  is the maximum mean pressure coefficient calculated at each tap irrespective of time and was calculated using the following equation.

$$C_{p,mean\ Enve}(t) = \frac{E[p(t) - p_{atmospheric}]_T}{\frac{1}{2}\rho_{air} \bar{V}_{max,ref,T}^2}$$

where  $E [ ]$  is the estimated differential pressure within the peak zone. Differential pressure is time dependent; within the peak zone duration.  $\bar{V}_{max,ref}$  represents the maximum moving mean velocity at eave height.

This report will focus on three principal external taps shown in Figure 11. The taps located along the dotted lines in South to North and East to West were also discussed. For all the tap arrangement see the appendix Figure a.

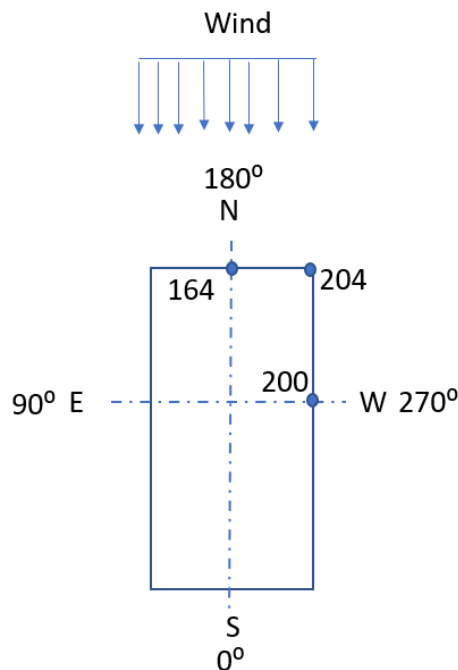


Figure 11: Principal pressure taps discussed in the report

Figure 12 shows the calculated  $C_{p,mean,Env}$  for the simulated static downburst event for  $180^\circ$ ,  $225^\circ$  and  $270^\circ$  wind directions. To calculate the envelop  $C_p$ , maximum moving mean velocity  $\bar{V}_{max}$  of 12.1 m/s was used. At  $180^\circ$  wind direction, the distribution of the  $C_p$  across the building (i.e., windward, lee ward, roof, side walls) are similar to the distribution resulting from an ABL wind event. Similarly, at  $225^\circ$  wind direction, pattern of the  $C_p$  across the building are similar to that resulting from an ABL wind event in the same direction, as conical vortices at the roof corners are evident by the high suction region. Same phenomena were observed for  $270^\circ$ .

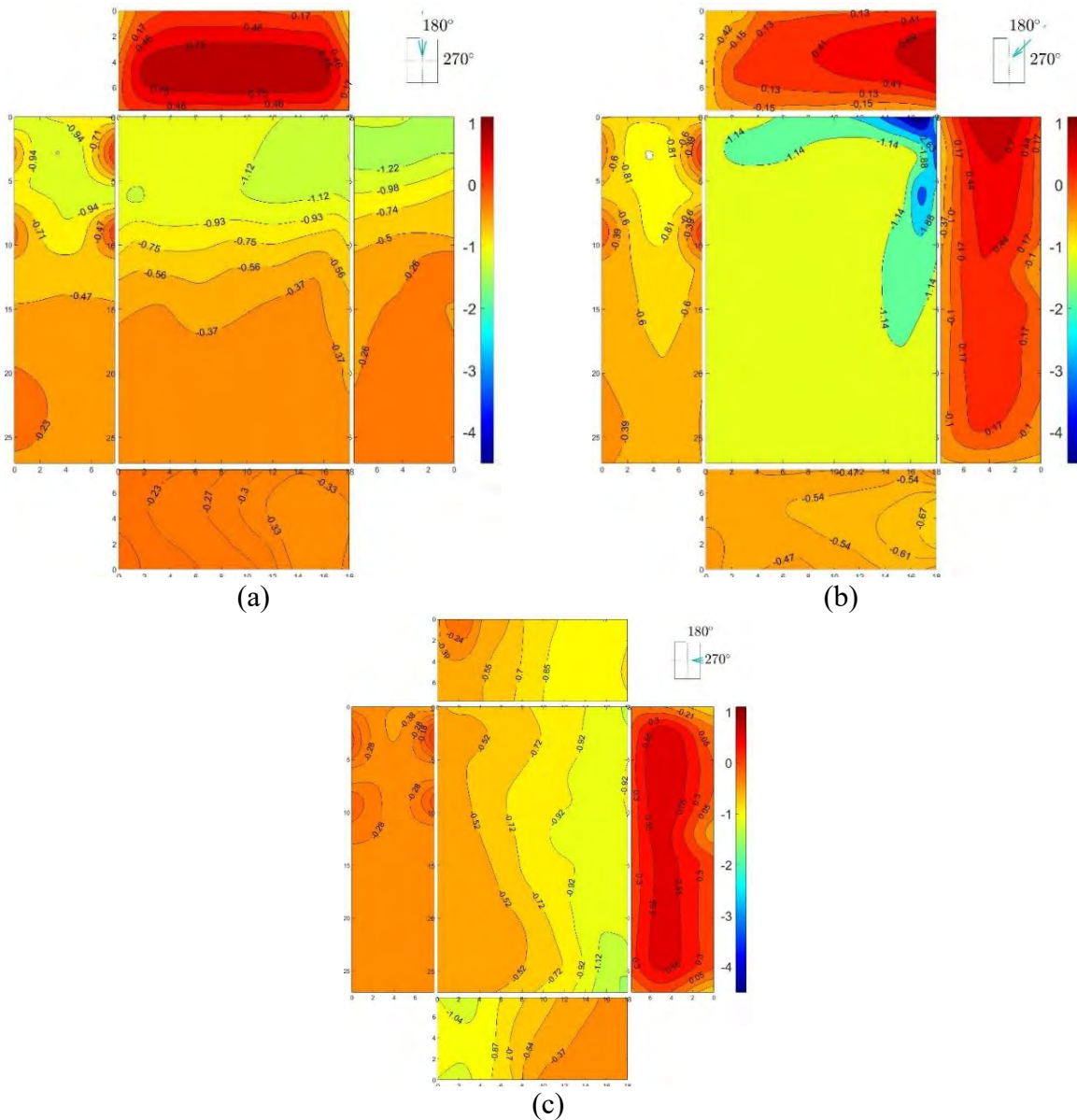


Figure 12: Maximum moving mean  $C_{p, envelop}$  for Downburst static case (a)  $180^\circ$  (b)  $225^\circ$  (c)  $270^\circ$

To calculate the instantaneous,  $C_{p,mean,t}$ , the following equation was used

$$C_{p,mean,t}(t) = \frac{[p(t) - p_{atmospheric}]_T}{\frac{1}{2} \rho_{air} \bar{V}_{max,ref,T}^2}$$

where differential pressure  $[p(t) - p_{atmospheric}]$  was at the instant in time when maximum pressure was recorded at a corner tap # 204 and  $\bar{V}_{max,ref,T}$  represents the maximum moving mean velocity at eave height.  $C_{p,mean,t}$  was calculated at the time when maximum pressure was recorded at a corner tap # 204. Pressure at this time instance for all the taps were determined to calculate the instantaneous mean  $C_{p,mean,t}$ .

Figure 13 shows the instantaneous mean  $C_{p,mean,t}$  for 225° deg wind direction. Similar to ABL flow, because of the creation of conical vortices as a result of the interaction of the building with the flow and the resulting flow separation at the roof edges, severe suction is noticed at the corner tap #204 and surrounding region. More discussion is provided in the next section.

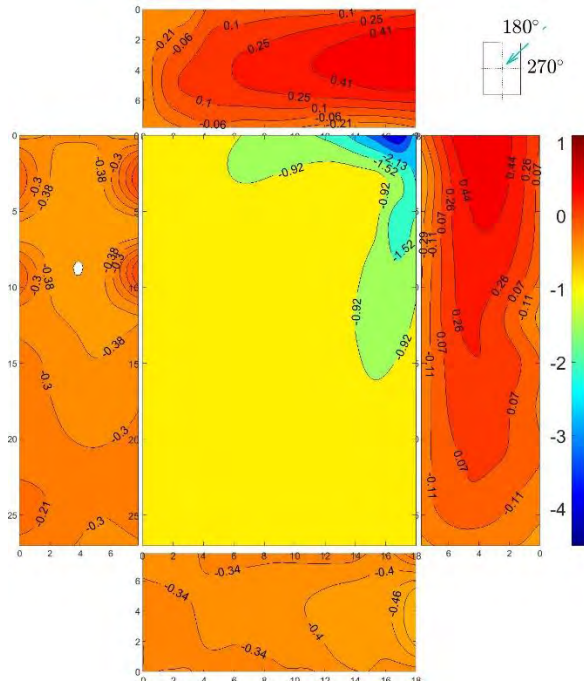


Figure 13: Instantaneous mean  $C_{p,t}$  for Downburst static case (wind direction 225°)

To understand the difference between static and dynamic test cases, the case of static wind direction  $270^\circ$  deg was adopted in this section. Figure 14 shows the calculated  $C_{p,mean,Env}$  for the simulated dynamic downburst event for occurring from  $260^\circ$  to  $290^\circ$  wind direction. The reference velocity was taken to be the maximum moving mean velocity  $\bar{V}_{max}$  of 12.1 m/s. Comparison between  $C_p$  values and patterns with  $270^\circ$  wind direction static case (as shown in Figure 12 (c)) mostly indicates similar distribution of  $C_p$  but higher values for dynamic case. For windward wall-static case ( $270^\circ$ ), a maximum value of  $C_p = 0.55$  and for dynamic case ( $260^\circ$  to  $290^\circ$ ), a maximum value of  $C_p = 0.61$  which is a 10.9% increase. For leeward wall-static case ( $270^\circ$ ), a maximum value of  $C_p = -0.38$  while for dynamic case ( $260^\circ$  to  $290^\circ$ ), a maximum value of  $C_p = -0.49$  is found resulting in a 28.94% increase. For north side walls-static case ( $270^\circ$ ), a maximum value of  $C_p = -0.85$  while for dynamic case ( $260^\circ$  to  $290^\circ$ ), a maximum value of  $C_p = -1.14$  resulting in a 34.12% increase. For south side walls-static case ( $270^\circ$ ), a maximum value of  $C_p = -1.04$  and for the dynamic case ( $260^\circ$  to  $290^\circ$ ), a maximum value of  $C_p = -1.22$  which is a 17.31% increase. For roof-static case ( $270^\circ$ ) a maximum value of  $C_p = -0.92$  is found while for the dynamic case ( $260^\circ$  to  $290^\circ$ ), maximum value of  $C_p = -1.69$  is found which is about 83.70% increase in suction.



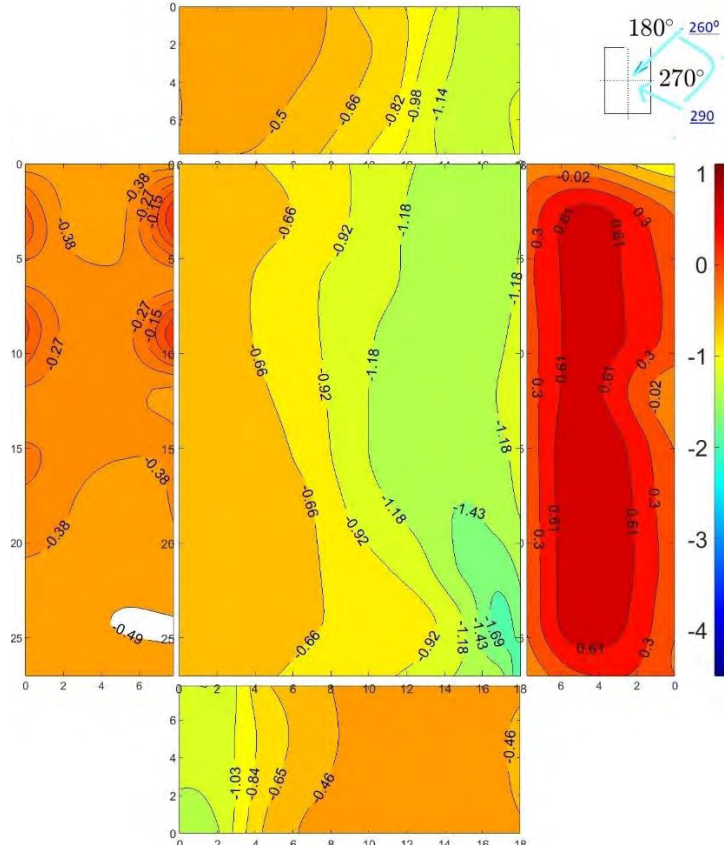
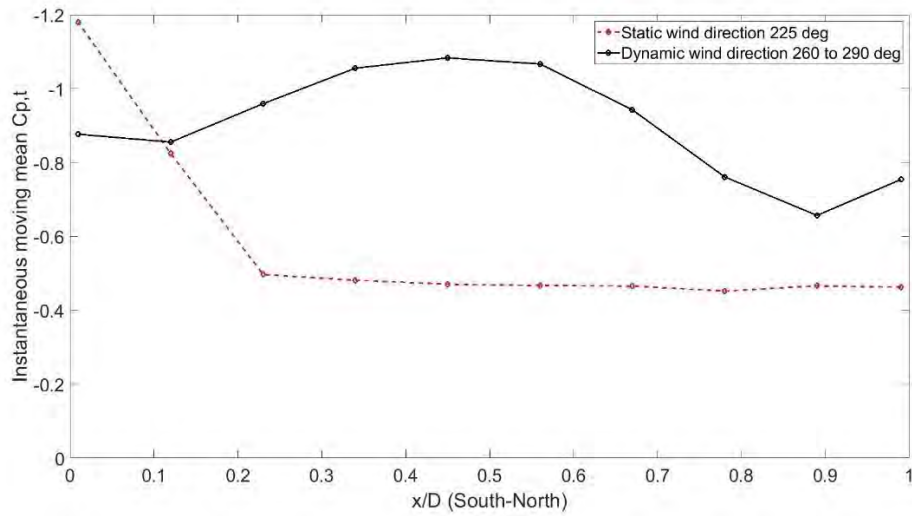
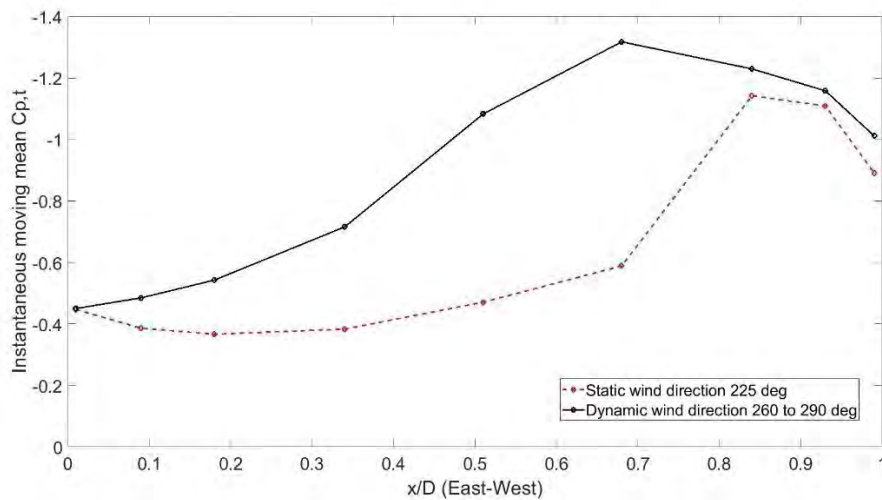


Figure 14: Maximum moving mean  $C_{p, envelop}$  for downburst dynamic case (wind direction  $260^\circ$  to  $290^\circ$ )

Figure 15 shows the variation of  $C_{p,mean,t}$  along south-north and east-west direction roof strips indicated earlier in Figure 11. Instantaneous pressure coefficients  $C_{p,mean,t}$  were calculated at the time corresponds to the maximum pressure recorded for Tap 204, for  $225^\circ$  static and  $260^\circ$  to  $290^\circ$  dynamic wind direction. The  $C_{p,mean,t}$  were negative for both cases. For static case south-north taps showed sharp reduction of  $C_{p,mean,t}$  values and then became constant. However, for dynamic case south-north taps showed an increment  $C_{p,mean,t}$  and then gradually decreased. For east-west taps, the suction pressure increases at the taps closest to the windward side, with the dynamic case showing higher suctions. However, the pattern is similar for both static and dynamic case.



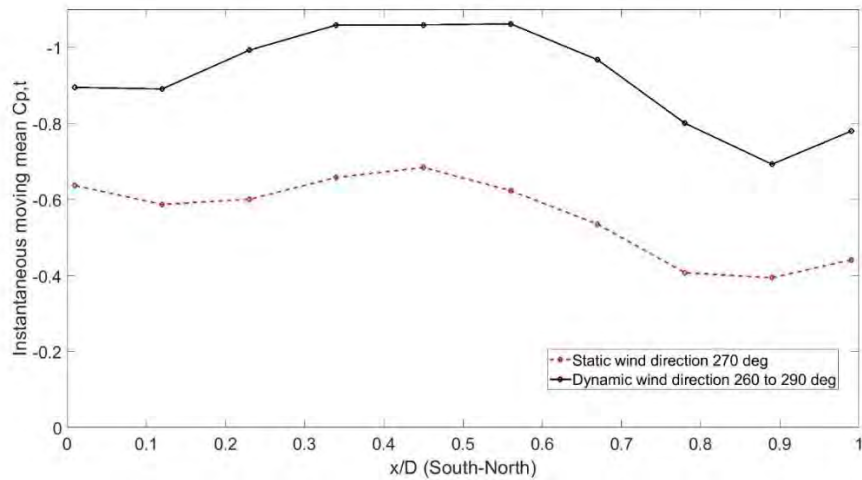
(a)



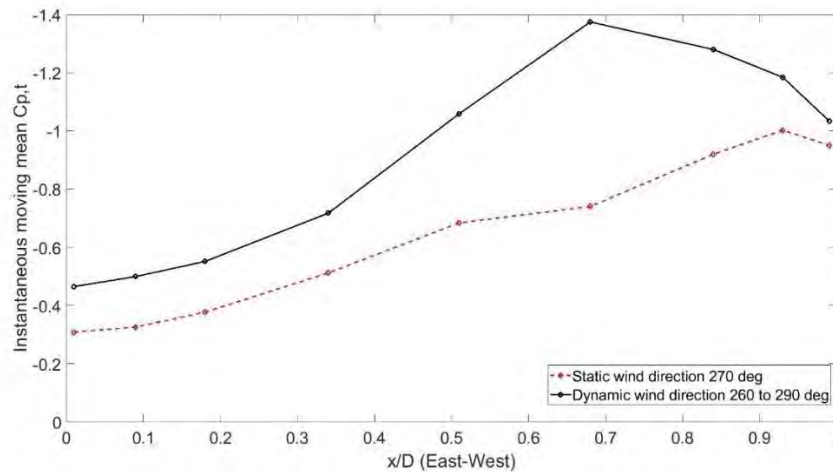
(b)

Figure 15: Distribution of instantaneous mean  $C_{p,mean,t}$  along the roof of the building for 225° static and 260° to 290° dynamic wind direction (a) south-north taps (b) east-west taps

Figure 16 shows the variation of  $C_{p,mean,t}$  along south-north and east-west direction.  $C_{p,mean,t}$  was calculated at maximum pressure on Tap 200 (see Figure 11 for tap locations), for 270° static and 260° to 290° dynamic wind direction. The  $C_{p,mean,t}$  were negative for both cases and the pattern is similar. Overall, the dynamic cases had the higher suction  $C_{p,mean,t}$  values.



(a)



(b)

Figure 16: Distribution of instantaneous mean  $C_{p,mean,t}$  along the roof of the building for  $270^\circ$  static and  $260^\circ$  to  $290^\circ$  dynamic wind direction (a) south-north taps (b) east-west taps

## 8. Conclusions

In this report, a scaled down downburst flow is reproduced at the Wall of Wind Experimental Facility to replicate a real downburst event. Flow characterization was done based on the targeted peak wind speed, duration of the event, and validation of the vertical profile compared to earlier reported downbursts. The model building was tested for various static wind direction ( $180^\circ$ ,  $225^\circ$ ,  $270^\circ$ ) and one dynamic wind direction ( $260^\circ$  to  $290^\circ$ ). The goal was to evaluate the variation of pressure distribution on the building with the slowly varying downburst wind direction and assess

how much the slowly-varying wind direction can alter the resulting pressure distribution and values. The following concluding remarks can be drawn from the experiment:

- The distribution of the  $C_p$  across the building for all the static cases ( $180^\circ$ ,  $225^\circ$ ,  $270^\circ$ ) were similar to that typically reported for ABL events for the same direction.
- $C_{p,mean,t}$  have similar distribution in both static and dynamic cases.
- The calculated  $C_{p,mean,Env}$  was higher for dynamic cases compared to static cases for all the surfaces. For windward, leeward, north and south side walls, the dynamic cases showed 10.9%, 28.94%, 34.12%, 17.31% higher  $C_{p,mean,Env}$  values, respectively. For the roof there was an 83.70% increase in  $C_{p,mean,Env}$  value.

The next step is to analyze the measured peak pressures and compare between the static and dynamic peak pressure distribution. Also, comparisons to the pressure measurements reported for the field event will help better validate the reported findings of this report.

### **Benefits to the State of Florida**

This research study focused on leveraging the new downburst simulator at the WOW to advance the fundamental knowledge and fill the current gap pertaining to effect of thunderstorm downbursts on residential structures which is not currently addressed in any building code around the world. While the differences between ABL and downburst events are quite well established in terms of wind flow characteristics, wind loading on buildings and infrastructure resulting from a downburst event as compared to a typical ABL wind event is not yet addressed which hinders achieving safe design for residential buildings. This project activities helped engaging two graduate students to perform innovative investigations in an experimental environment. The findings of this research will be disseminated through publications and will be discussed with building code and standards committees for potential inclusion in future editions.

## References

- Asano, K., Iida, Y., & Uematsu, Y. (2019). Laboratory study of wind loads on a low-rise building in a downburst using a moving pulsed jet simulator and their comparison with other types of simulators. *Journal of Wind Engineering and Industrial Aerodynamics*, *184*, 313–320. <https://doi.org/10.1016/J.JWEIA.2018.11.034>
- Ashley, W. S., & Mote, T. L. (2005). Derecho Hazards in the United States. *Bulletin of the American Meteorological Society*, *86*(11), 1577–1592. <https://doi.org/10.1175/BAMS-86-11-1577>
- Chowdhury, A. G., Asce, A. M., Zisis, ; I, Irwin, ; P, Asce, F., Bitsuamlak, ; G, Pinelli, J.-P., Hajra, ; B, Moravej, M., & Asce, S. M. (2017). Large-Scale Experimentation Using the 12-Fan Wall of Wind to Assess and Mitigate Hurricane Wind and Rain Impacts on Buildings and Infrastructure Systems. *Journal of Structural Engineering*, *143*(7), 04017053. [https://doi.org/10.1061/\(ASCE\)ST.1943-541X.0001785](https://doi.org/10.1061/(ASCE)ST.1943-541X.0001785)
- Henry Liu. (1991). *Wind Engineering: A Handbook for Structural Engineering* .
- Hjelmfelt, M. R. (1988a). Structure and life cycle of microburst outflows observed in Colorado. *J. APPL. METEOROL.*, *27*(8, Aug. 1988), 900–927. [https://doi.org/10.1175/1520-0450\(1988\)027<0900:salcom>2.0.co;2](https://doi.org/10.1175/1520-0450(1988)027<0900:salcom>2.0.co;2)
- Hjelmfelt, M. R. (1988b). Structure and Life Cycle of Microburst Outflows Observed in Colorado. *Journal of Applied Meteorology*, *27*. [https://journals.ametsoc.org/view/journals/apme/27/8/1520-0450\\_1988\\_027\\_0900\\_salcom\\_2\\_0\\_co\\_2.xml](https://journals.ametsoc.org/view/journals/apme/27/8/1520-0450_1988_027_0900_salcom_2_0_co_2.xml)
- Holmes, J. D. , H. H. M. , S. J. L. , L. C. W. , & O. K. D. (2008). A forensic study of the Lubbock-Reese downdraft of 2002. *Wind and Structures*.
- Irwin, H. P. A. H., Cooper, K. R., & Girard, R. (1979). Correction of distortion effects caused by tubing systems in measurements of fluctuating pressures. *Journal of Wind Engineering and Industrial Aerodynamics*, *5*(1–2), 93–107. [https://doi.org/10.1016/0167-6105\(79\)90026-6](https://doi.org/10.1016/0167-6105(79)90026-6)
- Jesson, M., Sterling, M., Letchford, C., & Haines, M. (2015). Aerodynamic forces on generic buildings subject to transient, downburst-type winds. *Journal of Wind Engineering and Industrial Aerodynamics*, *137*, 58–68. <https://doi.org/10.1016/J.JWEIA.2014.12.003>
- Le, V., & Caracoglia, L. (2021). Life-cycle cost assessment of vertical structures under nonstationary winds: Downburst vs. tornado loads. *Engineering Structures*, *243*. <https://doi.org/10.1016/J.ENGSTRUCT.2021.112515>
- Lombardo, F. T., Mason, M. S., & de Alba, A. Z. (2018). Investigation of a downburst loading event on a full-scale low-rise building. *Journal of Wind Engineering and Industrial Aerodynamics*, *182*, 272–285. <https://doi.org/10.1016/J.JWEIA.2018.09.020>

- Lombardo, F. T., & Smith, D. (2009). Analysis and Interpretation of Non-Stationary Wind Flow on a Bluff Body. *11th American Conference on Wind Engineering*. <http://iawe.org/Proceedings/11ACWE/11ACWE-Lombardo1.pdf>
- Lombardo Franklin T., D. A. S. (2009). Analysis and Interpretation of Non-Stationary Wind Flow on a Bluff Body. *11th American Conference on Wind Engineering*. <http://iawe.org/Proceedings/11ACWE/11ACWE-Lombardo1.pdf>
- Richter, H., Peter, J., & Collis, S. (2014). Analysis of a Destructive Wind Storm on 16 November 2008 in Brisbane, Australia. *Monthly Weather Review*, *142*(9), 3038–3060. <https://doi.org/10.1175/MWR-D-13-00405.1>
- Solari, G., Burlando, M., de Gaetano, P., & Repetto, M. P. (2015). Characteristics of thunderstorms relevant to the wind loading of structures. *Wind and Structures*, *20*(6), 763–791. <https://doi.org/10.1>

# Appendix

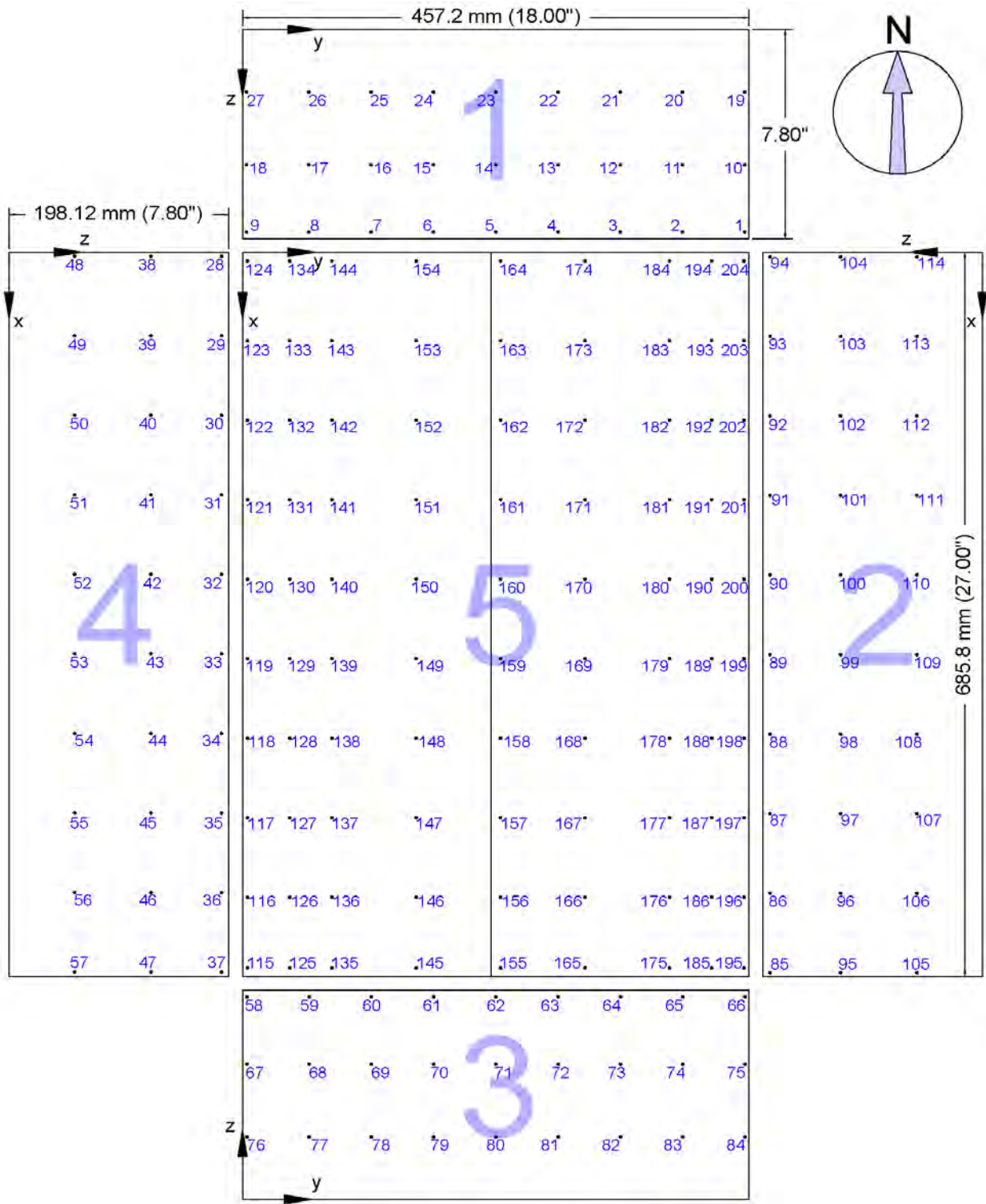
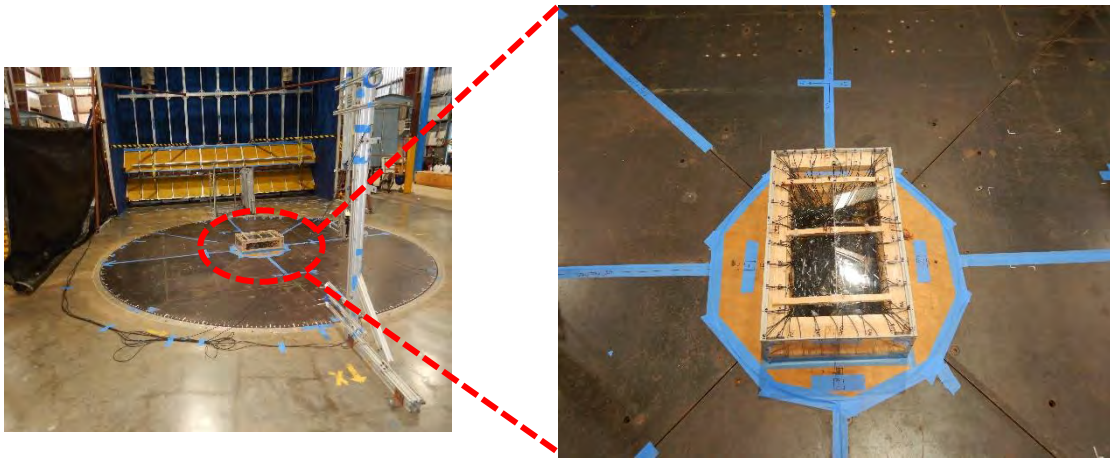
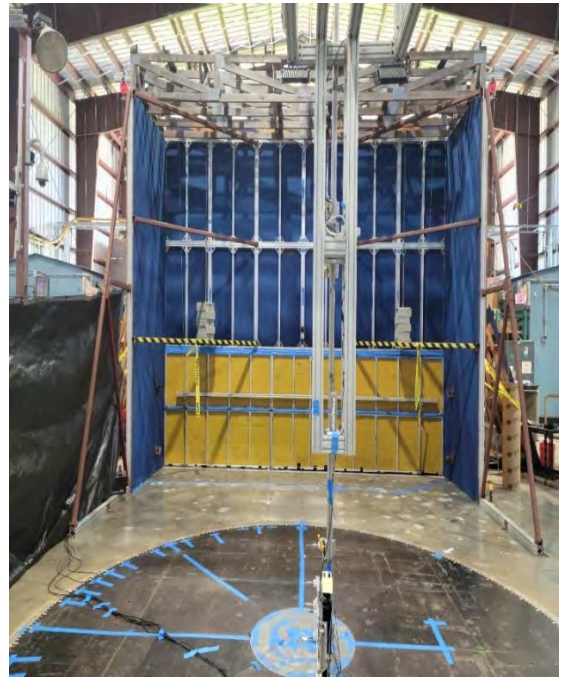


Figure a : Tap layout for 1:20 model building



*Figure b: Texas Tech 1:20 building model*





*Figure c: Cobra probe location at the turn table center*



*A Resource for the State of Florida*

## SECTION 4

### Wind Flow Separation of T-Shape Bluff Bodies

*Principal Research Assistant:*

Chia Mohammadjani – FIU CEE Graduate Student

*Support Students:*

Manuel Matus – FIU EEI Research Specialist and CEE Graduate Student  
Bennard Amponsah (NSF REU Student - Rensselaer Polytechnic Institute)

*Principal Investigator:*

Ioannis Zisis, PhD ([izisis@fiu.edu](mailto:izisis@fiu.edu))

Department of Civil and Environmental Engineering  
Florida International University

*In Partnership with*

The International Hurricane Research Center (IHRC)  
Florida International University

July 2022

## Executive Summary

Wind engineering research aims at minimizing the impact of extreme wind events on people and the built environment. For instance, prediction of peak pressure coefficients on the surface of buildings is critical in understanding their behavior during a storm event and minimizing wind related damage to the building's envelope and structural system. The motivation for this project, was the 2016 FL Division of Emergency Management (DEM) funded research on canopies attached to mid-rise buildings. Some of the findings of that research revealed an unconventional distribution of pressures/suction on the canopies.

The focus of the current research was the concept of synchronous flow separation on T-shaped bluff bodies. This very specific flow phenomenon occurs when wind separates simultaneously due to interaction with both the main bluff body (e.g., building) and with the attached plate (e.g., canopy or balcony). Right after the flows are separated a very complex interaction is initiated that results in non-conventional wind-induced loading patterns on the surfaces of both the bluff body and the plate. Thus, this phenomenon could have great influence on aerodynamic performance of the building itself as well as the building components that are attached to it.

The wind tunnel testing on 1:100 models provided valuable information on the flow characteristics and corresponding wind pressure patterns. The geometric ratios of the constructed models resulted in some significant differences and revealed the impact of the bluff body volume on the separated flow and its reattachment on both the bluff body as well as the flat plate. The high suction zones were observed to move downwind and further from the leading edges which has some direct implications on the characterization of the design zones in typical north American building codes and wind standards. The findings proved that further research is needed to better understand the complexity of such fluid-structure interaction.

## 1. Introduction

One of the most dominant natural hazard in the United States is related to extreme wind events, such as hurricanes, tornadoes and downbursts. Based on National Oceanic and Atmospheric Administration (NOAA) 76.5% of Florida State population is living in coastal areas, that is over 15 million people that are exposed to wind and water related hazards. The coastal areas employs 6.2 million people annually who earn a total of \$302.8 billion per year which would become \$760 billion in gross domestic product (NOAA). Between 2010 and 2021 there have been 21 hurricanes that made landfall in the US, with 6 of them being of Category 3 or above (NOAA, 2021). Also, 8 of them – approximately 38% - occurred after 2020. The most intense event was the category 5 hurricane Michael with 160 m/h winds, storm surge up to 15 feet and estimated total economic loss at \$25.2 billion.

Wind engineering research aims at minimizing the impact of extreme wind events on people and the built environment. For instance, prediction of peak pressure coefficients on the surface of buildings is critical in understanding their behavior during a storm event and minimizing wind related damage to the building's envelope and structural system. Accurate modelling of response to wind, which relies largely on our knowledge of bluff body aerodynamics and aeroelasticity, is required to ensure structural stability and integrity against the wind demands. Civil engineering structures, like low-rise houses, urban buildings, warehouses, bridges etc., are bluff bodies (i.e., not streamlined) which are greatly affected by the turbulent wind flow. Because wind loads affect structures in repeated cycles, fatigue related failures could also be a great issue. It is paramount to have a very good understanding of wind-structure interaction and of the resulting wind loading schemes on the surface of the various structures to be able to safely design them against strong wind events. Wind engineering research has been translated into building codes and wind standards over the past several decades and has resulted in major advancements in this area. Nevertheless, there is a continuous need for improvement and innovation in both fundamental research topics as well as more applied engineering principles.

The motivation for this project, was the 2016 FL Division of Emergency Management (DEM) funded research on canopies attached to mid-rise buildings. Some of the findings of that research revealed an unconventional distribution of pressures/suction on the canopies. These findings were partially justified by assuming that a more complex wind-structure interaction exists on bluff bodies that are joined in less conventional ways (e.g., a flat plate attached perpendicularly on a large volume). For the purpose of this study, the term “*T-shaped bluff body*” will be utilized to describe these complex group of shapes/structures. From a practical standpoint, it is necessary to properly and effectively forecast flow structures related with such complex bluff bodies. Canopy-like configurations may be relevant to residential and commercial building applications, e.g., balconies, rooftop attachments/equipment, podiums, and several other types of structures.

Of particular interest is the concept of synchronous flow separation on T-shaped bluff bodies. This very specific flow phenomenon will occur when wind separates simultaneously due to interaction with both the main bluff body (e.g., building) and with the attached plate (e.g., canopy or balcony). This occurs mostly for flow that is parallel to the body-to-plate interface and results in separated flows that are initially at a 90-degree angle. Right after the flows are separated

a very complex interaction is initiated that results in non-conventional wind-induced loading patterns on the surfaces of both the bluff body and the plate. Thus, this phenomenon could have great influence on aerodynamic performance of the building itself as well as the building components that are attached to it. While previous studies on the flow around canopies have provided valuable insights into vortex shedding from the elongated bluff body itself, there is a lack of knowledge regarding the vortex formation mechanism on vertical T-shaped bluff bodies and its impact on aerodynamic performance of buildings and potentially other civil engineering structures. This project aims to carry out a preliminary wind tunnel study and investigate the corresponding loading mechanisms.

## 2. Theoretical Concepts

### 2.1 Fundamental Flow Separation Theories

Based on the nature of the flow and physical characteristics of the impediment the flow separations could be categorized into the subdivisions of steady-unsteady and laminar-turbulent separations. According to the Moore-Rott-Sears (MRS) theory, the unsteady separation occurs when the wall-component of the shear disappears and the local streamwise velocity equals the velocity of the moving separation structure (Haller, 2004). The unstable separation points, according to Lagrangian definition, are found at boundary locations at which time-average of skin friction disappears. Flow separation might be advantageous or disadvantageous based on the circumstances. Flow separation, for instance, can cause unstable aerodynamic loads, acoustic noise, and vibration (e.g., in pipelines and low-rise structures). Knowledge of flow separation and reattachment requires understanding of effects of surface roughness on turbulent boundary layers. For instance, a previous study showed that the upstream wall roughness will increase the boundary layer thickness and turbulence intensity and will result in early mean flow reattachment over a forward-facing step (FFS). This study also looked into the separation bubble unsteadiness over the forward-facing step (Kumahor, Fang, & Tachie, 2021).

#### *Separation and Reattachment on Turbulent Boundary Layer (TBL)*

Unlike the smooth wall scenario, Kumahor et al. (Kumahor et al., 2021) recorded discrete zones of considerably higher vertical Reynolds normal stress and Reynolds shear stress upstream of the step for the entirely rough wall scenario. Prior research has found that alterations in the approaching TBL have little effect on the mean upstream separation bubble (Awasthi, Devenport, Glegg, & Forest, 2014; Graziani, Lippert, Uystepuyst, & Keirsbulck, 2017; Largeau & Moriniere, 2006) which testifies on the importance of separated shear layer over the plates. These results indicate that mean reattachment length over the step ( $L_T$ ) will decrease if  $\delta/h$  would increase. Essel et al. (2015) did an experimental investigation of the influence of upstream roughness and Reynolds number on the recirculation zone over a smooth forward-facing step. Turbulent transport and unsteadiness of separated shear layer over an FFS and the interactions with large-scale motions in oncoming TBLs was the goal of this project. At the leading edge of the step, the Reynolds shear stress and onset of turbulent kinetic energy both displayed strong negative values, suggesting counter gradient diffusion. The results of this research show that the mass fluxes of the approach boundary layer decrease by the roughness while the reattachment length for the smooth wall increases. However, when they were plotted against

Reynolds number, these reattachments fail to merge into a global curve. Therefore, the resulting reduction in the mean velocity and turbulence level of critical shear layer may decrease the reattachment lengths. Another study examined the quasi-periodic sequence of the separated shear layer, where the dominant frequency of the turbulence motion in the oncoming TBL proved to have a profound influence on its low frequency flapping motion (Fang & Tachie, 2019).

#### *Separation Bubble in a TBL*

Adrian et al. (Adrian, Meinhart, & Tomkins, 2000) found that expansion and contraction of the separation bubble will be influenced from low velocity and high velocity regions. They described a structure buried in the turbulent boundary layer with extended alternating positive and negative velocity areas. The unsteady nature of the separation bubbles upstream of a turbulent boundary layer will be influenced by the large-scale motion (LSM) in the upcoming TBL. Using time-resolved particle image velocimetry (PIV), the impacts of LSM on the spatio-temporal dynamics of separated shear layers from TBL were explored by Fang & Tachie (Fang & Tachie, 2019). A turbulent boundary layer over a surface of 6.5 times its thickness was considered where the primary frequency of stream fluctuating velocity in the TBL has happened. Using a reverse flow area method, the unsteady characteristics of the separation bubbles upstream and downstream was investigated. They found that for the upcoming TBL the primary frequency of the downstream separation bubble is similar to the primary frequency of the streamwise fluctuating velocity and therefore, both separation bubbles had low frequency flapping motion. The TBL found to have conclusive impact on the unsteady characteristics of the separation bubble. The separation bubble had a low frequency of  $St = 0.07$  which agreed with the primary frequency of TBL and a fairly higher subdominant frequency of  $St = 0.17$ . by increasing the upstream wall thickness the upstream peak magnitudes and their vertical locations would be increased. The highest height of the mean separating streamline relates to the vertical location of these peak values, which are a result of the strong shear layer recirculating bubble and the external high velocity flow. These vertical peak values were studied by a handful of researchers including (Adrian et al., 2000; Ren & Wu, 2011).

#### *Edge Separation and Vortex Shedding*

The flow field and, consequently, the aerodynamic response of a bluff body can be dramatically influenced by flow separation out from the leading edge. Depending on the surface, the separated flow may eventually become reattached and separate again along the surface. The effects of leading-edge separation on the vortex induced vibration (VIV) was studied by Duan et al. (Duan, Laima, Chen, & Li, 2021) on an elongated bluff body using wind tunnel tests. The laser displacement system and particle image velocimetry (PIV) techniques were utilized to monitor the vibration signals and flow field especially the upper surface boundary layer. The experiments led to a critical height to thickness ratio where the VIV's emerge. These VIV's would be generated by back-to-back vortex shedding from the edge. Vortex evolution in the top layer boundary flow (above the model) as well as vortex shedding in the wake flow were explored in this study. In a separate study by Duan et al. (Duan, Laima, Chen, & Li, 2020) for reattachment of leading-edge separation flows, the critical height was found as  $h/t = 0.5$  using PIV. Therefore, by increasing the height of wind facing object the flow separation becomes more influential because of the way the pressure would distribute over the

surface. Further, the lower layers of flow separation show minimal impacts on the upper layers. The frequency spectrum of the wake velocity was based on vortex shedding frequency  $f_v$  and led to primary frequency of the flow structure because the vortex shedding in the wake causes the velocity oscillations. The effects of leading-edge geometry of a bluff body corresponding to Reynolds numbers between  $Re = 4 \times 10^4$  to  $Re = 7.5 \times 10^4$  has been explored by Taylor et al. (Taylor, Gurka, & Kopp, 2014). The research found that the vortex shedding frequency linearly decreases up to 40% because of larger leading-edge separation by alternating the leading-edge separation angle from  $0^\circ$  to  $90^\circ$ . Laima et al. (Laima, Li, Chen, & Ou, 2018) carried out an experimental study on flow pattern, pressure distribution, VIV and vortex shedding frequency over box girders. They found that due to large leading separation resulted from attachments unlike bare deck girders, the leading flow separations and VIV's in twin box girders would be variable.

### *Reynolds Number and Flow Separation*

Kumahor et al. (Kumahor et al., 2021) and Ebenezer. E et al. (Essel, Nematollahi, Thacher, & Tachie, 2015) argued that in a step with height of  $h$ , increases in  $L_T$  are caused by raising the Reynolds number depending on step height ( $Re_h = hUe/\nu$ , where  $\nu$  is the kinematic viscosity of the working fluid), until critical values of  $Re_h = 8500$  and  $6380$  are reached, after which  $L_T$  becomes nearly independent of  $Re_h$ . In a different manner Camussi. et al. (Camussi et al., 2008) claimed that for values of  $Re_h$  that were an order greater than the critical values of  $Re_h$ ,  $L_T$  rose with rising  $Re_h$ .

Jones et al. (G. Jones, Santer, Debiassi, & Papadakis, 2018) did investigations on flow separation control around airfoils at low Reynolds numbers. Unlike those airfoils which the geometry leads to higher Reynolds numbers, in airfoils with lower  $Re$ , large separated regions with wide wakes were experienced. At Reynolds number below  $Re = 500,000$  laminar boundary layers formation at top surface of an airfoil will extend to pressure recovery region. Jones. et al. (Gareth Jones, Santer, & Papadakis, 2018) did a separate research on airfoils at  $Re$  around  $5 \times 10^4$  and  $0^\circ$  angle of attack. For this flow condition, vortices were observed in separating shear layer at frequency of 4.9. The natural breakdown of the separated shear layer resulted in turbulence which indicated that the shear layer, which is located distant from the airfoil surface, is where significant turbulence kinetic energy (TKE) and Reynolds stress happen. TKE and Reynolds stress plots over time demonstrated that this would cause to swap an area of strong momentum in the near-wall area which instantaneously energizing the boundary layer. Based on Michel's criterion this transition will happen when the Reynolds number from momentum thickness pass the critical  $Re_\theta$  depending on Reynolds number (Prasad & Dimitriadis, 2017). This criterion could be found from Eq.1.

$$Re_\theta > 1.174 \left( 1 + \frac{22400}{Re_x} \right) Re_x^{0.46} \quad \text{Eq.1}$$

Ayed et al. (Ayed, Ragab, & Hajj, 2016) checked the application of active flow control over a surface for different Reynolds numbers to decrease high pressure coefficients and loads. Based on those Reynolds numbers, they allocated flux injection strategies in two flow regimes. The best reduction in pressure coefficient for a Reynolds number  $R = 10^3$  was 50% of the peak pressure coefficients. For a Reynolds number of  $R = 10^4$  the reduction factor for peak pressure coefficients did not go beyond 25%. Greenblatt et al. (David Greenblatt, 2004) concluded that the flow will accelerate at upstream of a slot while the pressure decreases downstream due to suction when a suction regime was applied to the

top of a wall mounted hump. They further realized that this process will be more convincing by using bigger Reynolds numbers. The  $C_p$  coefficients were similar and the experiments with higher Reynolds number has longer bubbles. Weldon et al. (Weldon et al., 2008) conducted experimental and numerical study into flow separation of unsteady two-dimensional rotor-oscillator flow. Using a kinematic theory of unsteady separation there has been a reported change from fixed to movable separation. In an unsteady flow, material spikes which are signs of unstable manifolds may have time varying locations. However, separation point is proven to be fixed for flows with a well-defined steady mean, even while the separation spike changes shape with time. During altering flow conditions, like increased Reynolds numbers in a flow past a cylinder, moving separation points might be noticed.

### *Laminar and Turbulent Separations*

The laminar boundary layer (LBL) will have significant harmful impacts by causing lift and drag. On an airfoil for example when the inherently unstable separated shear layers transit from a laminar to turbulent condition, the flow will reattach to the airfoil surface again. When the Reynolds number is low these separated shear layer could not reattach and therefore a wake will be generated. However, if the Reynolds number is big enough the separated shear layer will reattach causing a laminar separation bubble (Yarusevych, Sullivan, & Kawai, 2009). When the flow is in subcritical state there will be flow transitioning between the shear layers. The high force raises the flow turbulence stage while raising the momentum coefficient, and therefore the flow transition process is pushed ahead to generate turbulent shear layers, which are advantageous for separation delay (Feng & Wang, 2014). Christopher et al. (Christopher, Peter, Kloker, & Hickey, 2020) studied the turbulent boundary layer on a flat plate by solving the compressible Navier-Stokes equations at low Mach number conditions. The results showed that for the blowing wall the level of turbulence increases by spread on the inner scaling. Additionally, they investigated the cooling of foreign-gas films into laminar and turbulent supersonic boundary layers. The turbulent nature of unsteady vortices was checked and due to the development of these vortices, the turbulent heat transfer was altered. The rise in turbulent heat transfer caused by these vortices was shown to affect in a reduction in cooling efficacy.

## **2.2 Flow Separation in Flat Plates**

A flat plate is a relatively aerodynamic type of bluff body that has a plethora of applications and uses in common civil engineering structures. Flat plates could be compared to thin airfoils that have been used to maintain lift force with small angles of attack. Asymmetry of the flow system is created by any slope in flat plates, yielding in a nonzero mean lift on the plate. There are several applications of flat plates in buildings, such as canopies, balconies, rooftop attachments, wind partitions etc. Flat plates have also extensive applications in bridge engineering.

### *Characteristics of Vortex Shedding*

Different methodologies have been used to investigate the characteristics of vortex shedding behind a flat plate. Lam et al. (Lam & Wei, 2014) modelled vortex shedding flow over a flat plate with varying angle of attack - between  $20^\circ$  to  $45^\circ$  - and Reynolds number  $Re = 2 \times 10^4$ . The CFD turbulent model revealed two trains of vortices at both plate edges which ejected from the plate's trailing end. The separation shear layer accumulated near the plate trailing edge, resulting



in the formation of these vortices. Fluctuating forces were reported on the plate as a result of incorporation of upper shear layer provoking pressure on the plate.

Uniform streams can cause rotational oscillations in a flat plate which eventually induce subharmonic and harmonic vortex shedding. These types of shedding was the target of Fang et al. (Yuan-Cheng Fang, 2000) experimental work by explaining surface pressure and vortical structure of the near wake. Most of bluff bodies may experience vortex streets under different Reynolds numbers. Substantial fluctuating forces are produced by these vortices which cannot be overlooked and, in some cases, have a frequency similar to the characteristic frequencies of the body. This similarities in characteristic frequencies will excite resonance and trigger damage to the plate. Amplification in body oscillation magnitude has mutual relation with increases in shedding frequencies. Vortex lock-on happens when a bluff body's normal shedding frequency is replaced by the disturbance's forcing frequency (Shigehiko Kaneko, 2014). The lock-on state is affected by the vortex shedding and the forces resulted from oscillation.

#### *Angles of Attack and Flutter Analysis*

Wu et al. (Wu et al., 2020) conducted forced vibration tests on instability of flutter derivatives of a flat plate for wind flows in different angles. The aim of this study was to consider the response of flutter to using different flutter derivatives at different angles. The carbon made thin plate was  $1.1 \times 0.4$  m in dimensions and 10 mm of thickness. The oscillations were set up from 0 to 20 Hz and the wind angle of attacks were from  $0^\circ$  to  $7^\circ$  in  $1^\circ$  intervals. Instability related to flutter will cause undesirable impacts on flexible structures which magnifies the importance of aeroelastic criterion called flutter derivatives. Chowdhury et al. (Chowdhury & Sarkar, 2003) have developed the modified iterative least squares (MILS) procedure which unlike the iterative least squares (ILS) procedure would help to calculate the damping coefficient matrix and coupled stiffness in a more precise manner. The experimental set up consisted of a three degree of freedom elastic suspension system to be tested at Iowa State University wind tunnel facility. A NACA 0020 airfoil model was installed on the elastic suspension system. As a part of system of 3 degrees of freedom the lateral, vertical and torsional springs had different frequencies. At the beginning 18 flutter derivatives were calculated for the airfoils using the ILS procedure. The multiple DOF mixture helped to obtain true damping of lateral displacement. The authors reported that by increasing degrees of freedom from 2D to 3D the errors were increased. A modification to iterative least squares method (ILS) was proposed to pin down all 18 flutter derivatives.

Flutter derivatives of thin flat plates under wind flows from different angles have also been investigated by Wu et al. (Wu et al., 2020). For different AOAs a forced vibration test procedure was adopted to study the flat plates flutter derivatives. The wind tunnel test results showed that flutter derivatives undergone considerable changes from negative to positive for angle of attack equal to  $5.5^\circ$ . Varied AOAs emphasized on the performance of flat plates and helped to better recognize the flutter instability characteristics.

#### *Separation Bubble*

Long and thin recirculation bubbles could be traced in many structures which are exposed to the wind flows including thin and membrane airfoils, wind deflectors, yacht sails, small wind turbine generators, orientation fins, microair

vehicles, missile and rocket fins. A physically compound flow has characteristics like separated shear layer, primary leading-edge bubble, secondary leading-edge bubble, transition to turbulence, reattachment and a boundary layer zone formation after the reattachment. Long recirculation bubbles around a thin flat plate were investigated using finite numerical simulations by Luiz Eduardo B. Sampaio et al. (Sampaio, Luiz T. Rezende, & O. Nieckele, 2014). After the flat plate had experienced a boundary layer separation, at the vicinity of the edge a thin layer of recirculation of a turbulent structure was observed.

### 2.3 Atmospheric Boundary Layer (ABL) flow

Earth's atmosphere is made of several layers of air with different density, temperature and pressure properties. The lower part of the atmosphere is called Troposphere which starts from Earth's surface up to the average altitude of approximately 12 km. The atmospheric boundary layer (ABL) is the lowest part of the Troposphere which is in contact with the planetary layer and Earth's surface. The thickness of the ABL is not fixed and depending on the wind speed, roughness of the terrain and the flow next to the ABL, the height could achieve a few hundred meters to some kilometres. Based on the table 26.11-1 of the ASCE 7-22 the nominal height of the atmospheric boundary layer ( $z_g$ ) for exposure categories B, C and D are 1000 m, 750 m and 590 m respectively (ASCE7, 2022). The nominal height which also known as the gradient height could be even higher in large synoptic storms and achieve up to 2 to 4 kilometers than the  $z_g$  values defined by the ASCE 7. Wind speeds in these storms will increase above the  $z_g$  heights defined by the ASCE 7.

#### *Averaging times and wind speed profiles*

The wind flow in the ABL is not laminar but it experiences ongoing turbulent fluctuations and as a result the mean wind speed varies as a function of elevation and depends on the averaging time. The peak 3-second gust speed and the hourly wind speed are the two most commonly used averaging times that are used in wind engineering to calculate wind speeds from the wind time histories obtained from field observations. The logarithmic law which was originally developed by Prandtl for turbulent flow over a flat plate is applicable to the atmospheric boundary layer near the Earth's surface (Holmes, 2007) and has long superseded the power law. However, ASCE 7 is still using the power law to calculate the wind speed profile by introducing the  $\hat{\alpha}$  exponent which will be used for 3s gust speeds ( $V_{3s}$ ). The gradient height ( $z_g$ ) and peak power law exponent ( $\hat{\alpha}$ ) are values which have been used by the ASCE 7 to produce 3-second wind speed figures at the reference height ( $z_{open} = 10$  m) known as the basic wind speeds. The classical equation of power law at height ( $z$ ) relative to the reference height ( $z_{ref}$ ) is based on exponent  $1/\alpha$  and depends on the roughness of the surface and the averaging time (Simiu & Yeo, 2019).

#### *ABL Turbulence*

Wind in the ABL layer is mostly turbulent (except in very low wind speeds) with fluctuations in time and space. In structural engineering the ABL flow turbulence affects the wind velocity measurements. Additionally, the wind flow around a structure could be affected by the turbulence when particles from flow regions with high momentum convey into low-speed regions which is important in measuring the aerodynamic pressures on the structure surface (Simiu et

al., 2019). This necessitates the importance of true simulation of the turbulence in the wind tunnel and compliance with the full-scale turbulence features in the atmospheric boundary layer.

### 3. Previous Studies

Canopies attached to low- or mid-rise buildings suffer from wind-induced damage and are often detached from the structure they are attached to (the parent structure) acting as potential missiles that cause additional damage on surrounding structures. Before 2016, the American Society of Civil Engineers Wind Standard (ASCE 7) provided little guidance on the design of canopies attached to structures of varying height. Recent research in the US and Canada provided valuable information on the wind-induced loads on canopies for both low- and mid-rise buildings. The research findings guided the development of more accurate design recommendations and formed the basis for the current research project. For bluff bodies such as buildings, when flow separates the highest suction is found nearest to the edge where the separation occurs (Holmes, 2007). However, when a canopy is placed at the corner of a building, the highest suction was found near the center of the canopy – see Fig. 1 (Naeiji et al., 2022). This research hypothesized that the interaction between separation bubbles produced by the flow separating around the canopy and the flow separating around the corner of the building are causing this interaction.

Additional useful results were observed in previous research related to canopies attached to low- or mid-rise buildings. Zisis et al. (Ioannis Zisis, Farzaneh Raji, & Jose D. Candelario, 2017a) considered the pressure distribution over the canopy surface with emphasis on dimensions and direction of wind. The height of canopy was found out to have profound impact on the peak pressures on its surface, whereas the canopy lengths and its horizontal orientation had negligible influence on the peak pressures. Zisis et al. (Candelario, Stathopoulos, & Zisis, 2014) further experimentally monitored wind pressure and wind loads on canopies attached to a wall in a different study. Some contradictory results were observed against existing design guidelines in standards like AS/NZS 1170.2. Based on this publication  $hc/h$  (height of canopy to eave height) showed to have a great impact on uplift  $GC_{p,net}$ . Wen et al. (Wen, Hatakeyama, Sato, & Uematsu, 2020) did experiments on large canopies supported by beams. The distribution of pressure along the center and edge lines both on the top and bottom surfaces of canopy were assessed by conducting winds ranging from  $\theta = 0^\circ$  to  $\theta = 360^\circ$ . The maximum and minimum pressure coefficients were happened at angles between  $\theta = 0^\circ$  to  $\theta = 150^\circ$ . There are more researches on wind loads on canopies and the pressure distribution over canopy roofs and arch-roof industrial buildings (Paluch, Loredou-Souza, & Blessmann, 2003; Uematsu, Stathopoulos, & Iizumi, 2008; Zisis & Stathopoulos, 2010).

#### *Research Gap*

As previously discussed, flow separation is a well understood area of fluid mechanics. It is considered when designing all modern buildings, however there is no research on the interaction between separation bubbles. All current research suggests that when flow separation occurs in the ABL, the strongest suction pressures due to the separation occur on the windward edges (Holmes 2015). However, when flow separation occurs simultaneously at two perpendicularly attached bluff-bodies, then the loading scheme appears to be significantly affected. Although,

absolute peak pressures might not be affected significantly due to this interaction, the location that these peak pressures occur might be very different than more conventional cases (e.g., roof or wall surface). This effect might have a direct implication on how we design more complex structures mostly due to the existing zoning convention that is adopted in building codes and wind standards. Therefore, more attention is required to better understand potential loading mechanisms that are due to flow separated flows on T-shaped bluff bodies.

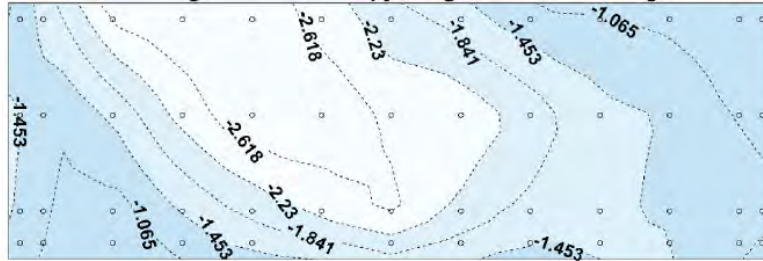


Fig. 1: High suction zone located towards the center of the canopy (from Naeiji et al., 2022)

## 4. Facility and Experimental Procedure

### 4.1 Experimental Set-up

In total 4 models were constructed and tested in the wind tunnel using a geometric scale of 1:100. Model-1 and Model-2 represented a bluff body with a vertical rectangular prism splitter plate on top of it, while Models 3 and 4 represented bluff bodies with horizontal splitter plates attached to their wall. Pressure taps were fitted on the surface of both the bluff bodies and splitter plates (Fig. 2). The models were placed on top of the turntable in the wind tunnel and were tested for different wind directions (Fig. 3). The geometry information and number of pressure taps for all four models is presented in Table.1. It should be noted that for this report, due to a sensor malfunction only results from models 2, 3 and 4 will be reported.

Table.1: Model 1-4 details

	Bluff Body					Splitter Plate						
	Geometry Dimentions			Dimention Ratios		Geometry Dimentions				Dimention Ratios		Number of Pressure Taps
	X	Y	Z	X/Y	X/Z	x	y	z	t	x/y	x/z	
	(mm)	(mm)	(mm)			(mm)	(mm)	(mm)	(mm)			
Model-1	240	240	240	1.00	1.00	240	120	-	10	2.00	-	144
Model-2	120	120	240	1.00	0.50	120	60	-	10	2.00	-	88
Model-3	240	240	240	1.00	1.00	240	-	120	10	-	2.00	144
Model-4	240	120	120	2.00	2.00	240	-	120	10	-	2.00	108
	X: Bluff Body Length					x: Splitter Plate Length						
	Y: Bluff Body Height					Y: Splitter Plate Height						
	Z: Bluff Body Width					Z: Splitter Plate Width						

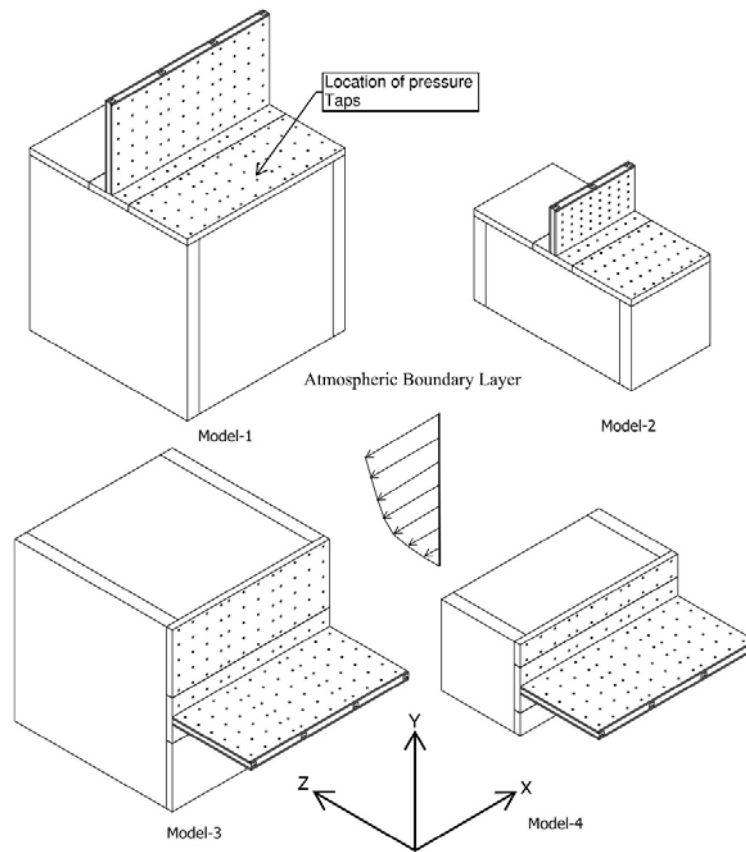


Fig. 2: Models schematics

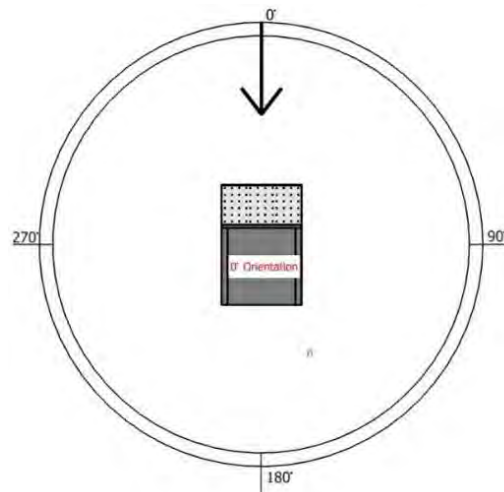


Fig. 3: Model-3 in the wind tunnel and a plan view of the model showing 0-360-degree wind direction

#### 4.2 Boundary Layer Simulation

The tests were carried out in the newly constructed Atmospheric Boundary Layer Wind Tunnel (ABLWT) in the Laboratory for Wind Engineering Research (LWER), located at Florida International University (FIU). The wind tunnel has a test section of 8 feet wide by 6 feet high and 60 feet overall length. The turntable, placed downwind of the wind tunnel, allows for housing the models and testing them in different wind directions. The spires and roughness

elements can be manually adjusted to achieve the desired exposure (open, suburban, or urban). The configuration chosen for the spires and roughness elements were adjusted to reproduce an open terrain profile and the scale of the models was set to 1:100. To calculate wind velocity profiles and turbulence intensity profiles and the power spectra, cobra probes were installed at different heights. Cobra probes sampling frequency was 2500 Hz and wind velocities were measured for a 60 s time duration. Reference height for the wind tunnel velocities was set at  $Z_g = 800$  mm which is approximately the gradient height for the particular wind tunnel. The mean wind speed and turbulence intensity profiles are shown in Fig. 4. The profiles agree well with the theoretical power law for  $\alpha = 0.14$  and Engineering Science Data Unit (ESDU).

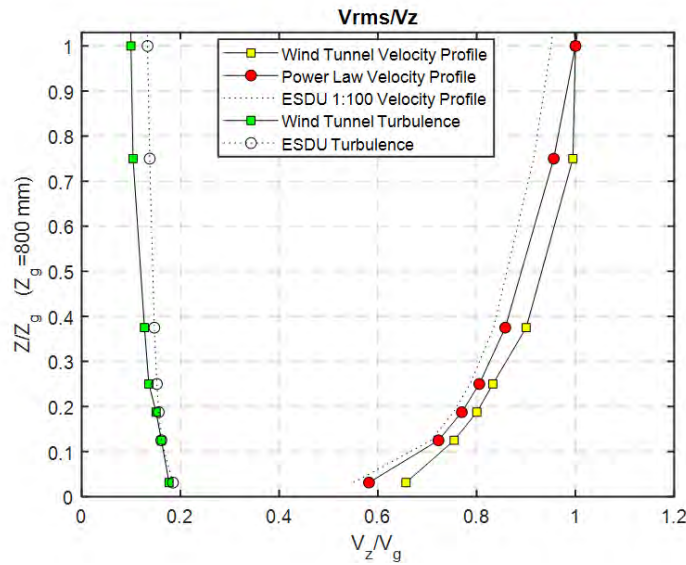


Fig. 4: Mean velocity and turbulence intensity profiles for small scale wind tunnel against the power law and ESDU (open terrain).

### 4.3 Pressure Coefficients

For mean pressure coefficient ( $\bar{C}_p$ ) and for peak negative and positive pressure coefficients ( $\hat{C}_{p\ min}$  and  $\hat{C}_{p\ max}$ ) Eq.2 and Eq.3 were used. The wind speed was referenced at the mean roof height for each model and the pressure time histories were recorded using Scanivalve's ZOC system. To eliminate signal distortions due to the tubing used to connect the pressure taps to the pressure scanners, a transfer function was used.

$$\bar{C}_p = \frac{\Delta p}{\frac{1}{2} \rho \bar{V}_{ref}^2} \quad \text{Eq.2} \quad \hat{C}_p = \frac{\Delta p}{\frac{1}{2} \rho V_{3s}^2} \quad \text{Eq.3}$$

For the extreme positive and negative peak pressure coefficients the BLUE WIND method (NIST) was used which utilizes Best Linear Unbiased Estimate of Lieblein's Blue (Lieblein, 1974). The process would be based on applying blue method to n epochs to estimate extreme negative and positive pressure coefficients using time-history pressure data recorded at the wind tunnel for the specified duration.

## 5. Results and Discussion

In this report data for models 2,3 and 4 for a wind direction of 90 degrees case were processed in order to evaluate the pressure coefficients when the wind is blowing parallel to the splitter plate. This wind direction was the most desired wind direction to evaluate the peak pressure formations due to flow separation on the bluff body and the flat plate. Mean and peak pressure coefficient are evaluated on the surface of all 3 models using pressure coefficient contour plots. Moreover, a line of selected pressure tap results at the middle of each surface was selected to study the pressure distributions in more detail.

### 5.1 Mean pressure coefficients $\bar{C}_p$

Fig. 5, Fig. 6 and Fig. 7 illustrate contour plots of mean pressure coefficients for Model-2, Model-3 and Model-4 for 90 °wind direction.  $\bar{C}_p$  represents mean pressure coefficients on one side of the bluff body and one side of the splitter plate surfaces ( $Z_{ref}=120$  mm for Model-2 and Model-4,  $Z_{ref}=240$  mm for Model-3).

Model-2 and Model-3 have different plate dimensions, plate orientations and therefore, separated flows have opposite directions (Fig. 5, Fig. 6). Separation bubble is initiated from the windward direction of both models but in Model-2 begins at the bottom windward edge of the splitter plate moving up away from the plate-bluff body interface. Mean pressure coefficients in Model-3 had close values to the Model-2 but unlike Model-2, the separation bubble starts from top windward edge on the bluff body moving down towards the plate-bluff body interface and penetrates the horizontal surface of the splitter plate while maintaining the same direction.

The splitter plate experienced another flow separation at its windward edge (Fig. 6-bottom) which is similar to the separated flow at the roof height of the bluff body in Model-2. Model-3 and Model-4 share the same splitter plate dimensions and orientation (horizontal) with the different bluff body height (Y) to plate width (Z) ratios where  $Y/Z_{(Model-3)} = 1$  and  $Y/Z_{(Model-4)} = 0.5$ . Mean values of pressure coefficients on the vertical surface of the bluff body in the Model-4 are less than Model-3 and the separation bubble in Model-4 is not as clear as in Model-3. The smaller ratio of bluff body height to splitter plate width ( $Y/Z = 0.5$ ) in Model-4 has likely affected the flow separation formation on its bluff body surface. Mean pressure coefficients of the splitter plate of Model-4 had smaller values than Model-3 with the same separation bubble direction, however, the penetration of separation bubble in Model-3 was longer than the penetration in Model-4.

Fig. 8a shows results of mean pressure coefficients  $\bar{C}_p$  selected from a row of 12 pressure taps at the middle of Model-3 and Model-4 surfaces (Fig. 6 & Fig. 7 - right) for the 90°wind direction. The edge mean pressure coefficients of Model-3 show some significant difference in comparison to Model-4. In this graph pressure taps 12 are located at the windward side of the surfaces and clearly the mean pressure of the Model-3 plate has shifted away from the leading edge. Mean pressure coefficient for this plate has a value of approximately -0.55 for pressure tap#9 which is an indication of separation bubble formation at the location on the surface of the Model-3 splitter plate. The presence of the bluff body had great influence on the mean pressure coefficients on the surfaces of splitter plates. The shorter height

of bluff body in Model-4 did not result in a strong wake formation on its surface as it has happened in Model-3 where a complete separation bubble due to bigger volume of the bluff body had penetrated the splitter plate surface causing higher suction on its surface.

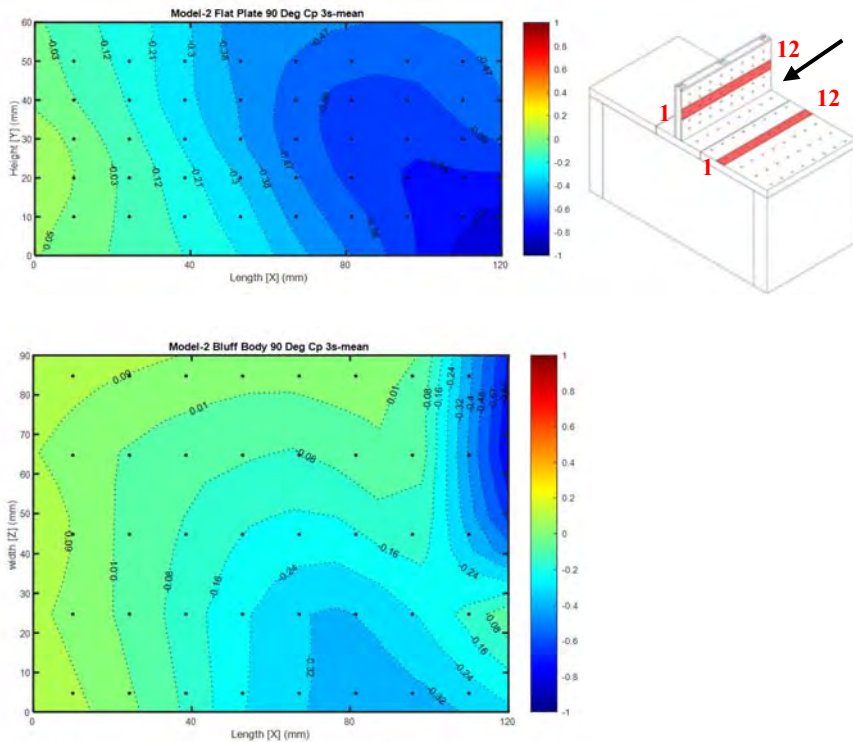
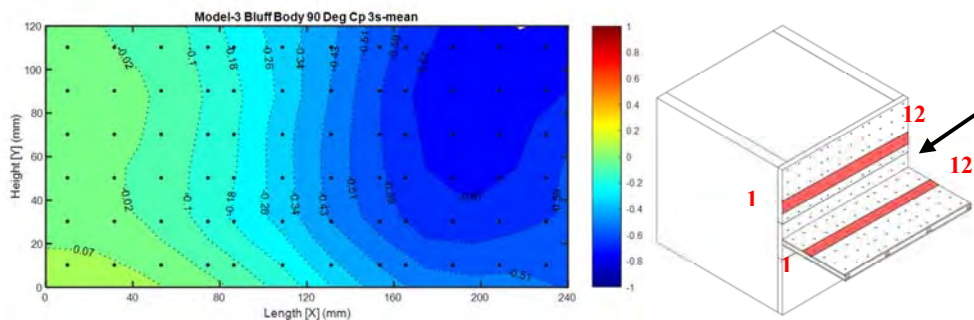


Fig. 5: Model-2,  $\bar{C}_p$  – 90 deg





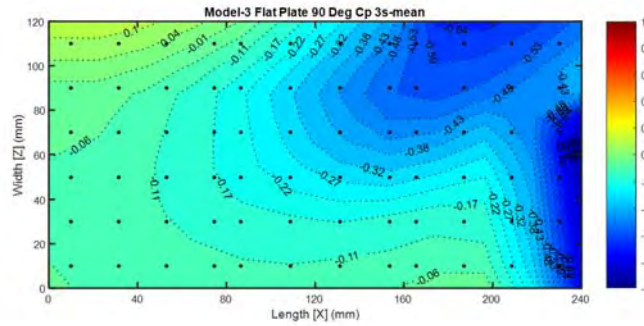


Fig. 6: Model-3,  $\bar{C}_p$  – 90 deg

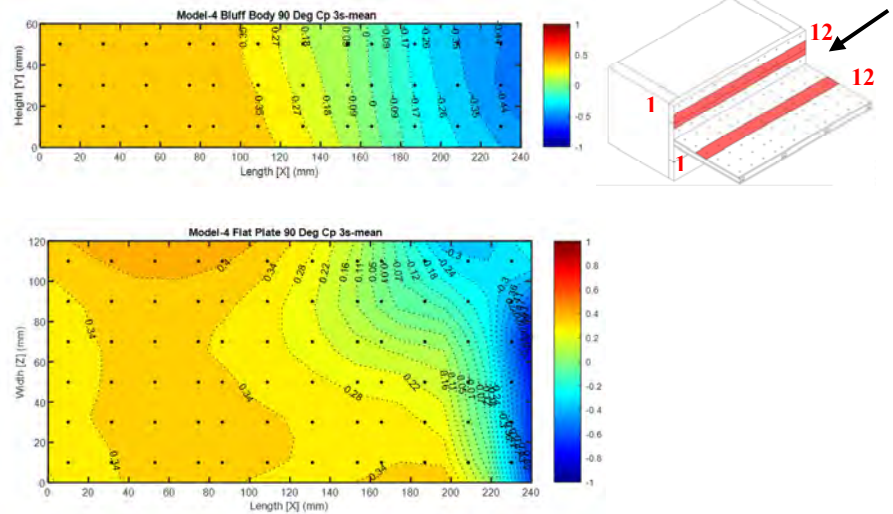


Fig. 5: Model-4,  $\bar{C}_p$  – 90 deg

The interaction between the splitter plate and the bluff body will yield reciprocal impacts on mean pressure coefficient values on both sections surface. By referring to Fig. 8a, bluff bodies for Model-3 and Model-4 had approximate closer mean pressure coefficient values  $\bar{C}_p_{Model-3} = -0.51$ ,  $\bar{C}_p_{Model-4} = -0.7$  which indicates a 36% difference between the two surfaces for pressure tap 12 at the leading edge. The difference between mean pressure coefficients for the two surfaces, however, at the pressure tap#9 location is almost 75% and unlike the leading edge where both bluff body edges had negative mean pressure coefficients, the pressure in Model-4 has become positive, whereas, in Model-3 was still negative. Again, the whole subassembly of Model-3 has negative mean coefficients for all pressure taps, but the subassembly of Model-4 is starting to experience positive mean pressure coefficient from pressure tap#9 back to pressure tap#1.

In both models the separation bubbles have shifted away from the leading edge with negative mean pressure coefficients at the location (pressure taps#12 to #8). Pressure coefficients became positive at lower taps (#4 to #1) which reveals the reattachment of separated flows at the downstream of surfaces. In both models mean pressure coefficients of the plate and the bluff body have intersection points at around the middle of models (pressure tap#6 for

Model-3 and #7 for Model-4) and similar values for taps located at the leeward side (tap#3 to tap#1). Flow mixtures from the separated flows of both surfaces could have happened at the intersection point producing a single flow with similar values and signs as a result of it. The similar values could have been due to the mixture of vortices from both surfaces causing a single vortex and positive values indicate the reattachment of the new vortex.

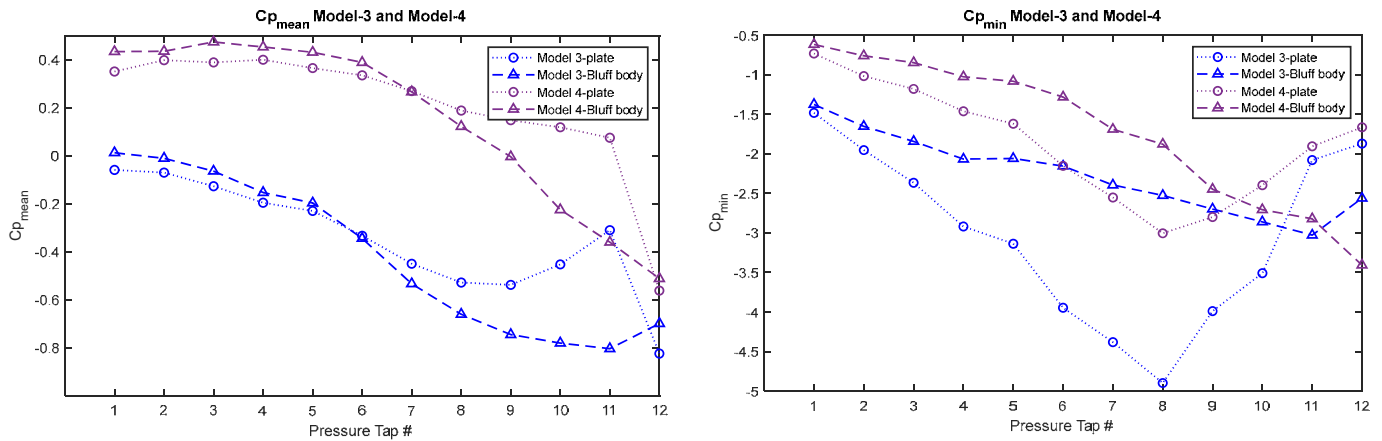


Fig. 6 : a) Mean pressure coefficients ( $\bar{C}_p$ ) and b) peak minimum pressure coefficients ( $\hat{C}_{p,min}$ ) right selected from middle surfaces of Model-3 and Model-4 for wind direction =  $90^\circ$

## 5.2 Peak pressure coefficients $\hat{C}_{p,min}$

Fig. 9 to Fig. 11 illustrate peak pressure coefficients for Model-2, Model-3 and Model-4 where left plots represent minimum peak pressure coefficient ( $\hat{C}_{p,min}$ ) and right plots represent maximum peak pressure coefficient ( $\hat{C}_{p,max}$ ) contour plots for 90 degrees wind direction. The highest peak negative pressure coefficients occurred on the splitter plates of Model-3 and Model-4 at the vicinity of the plate-bluff body interface where  $\hat{C}_{p,min,Model-3} = -4.51$  and  $\hat{C}_{p,min,Model-4} = -4.28$  respectively (Fig. 10 and Fig. 11 bottom left). The maximum pressure coefficients in Model-4 occurred at the middle of the bluff body surface and in Model-2 at the edge of the bluff body with  $\hat{C}_{p,max,Model-4} = 1.47$  and  $\hat{C}_{p,max,Model-2} = 1.56$  respectively.

The peak negative pressure contour plots show that separation bubbles and high suction zones have different patterns between the examined models. In Model-2 for instance, where the plate height to the bluff body width ratio was  $\frac{y}{z} = \frac{60}{120} = 0.5$ , a large high suction zone was observed on the bluff body roof top. However, there were also some localized high suction zones at the bottom of the leading edge of the plate and a high suction zone at the middle of the splitter plate away from the leading edge. Model-3 and Model-4 (horizontal plate) had a partially similar pressure distribution that indicated that the flow structure was influenced by the presence of the bluff body but to a different degree. The contours on these two models differ mostly due to the longer length of both surfaces in Model-4. In Model-4 the separation bubble can be seen on the horizontal surface of the splitter plate at the windward end of the plate-bluff body interface and then follow a path at an approximately  $45^\circ$  direction towards the end of the plate surface. The pressure gradient moves to positive values towards the end of the plate, indicating a flow reattachment, due to the extended

length of the surface in comparison to the bluff body height. Model-3 peak negative pressure coefficients location on the horizontal surface of the splitter plate is similar to that of Model 4 but there is no indication of flow reattachment due to the larger volume of the bluff body (Fig. 10). Separation bubbles formed on the splitter plate surface in Model-3 and Model-4 away from the leading edge which is in compliance with the previous research study done at the Wall of Wind on the wind-induced loads on canopies attached to mid-rise buildings (Naeiji et al., 2022).

Fig. 8b shows results of peak pressure coefficients selected from a row of 12 pressure taps at the middle of Model-3 and Model-4 surfaces for the 90° wind direction. For the selected group of pressure taps the trends are similar for both the wall surface of the bluff body and the flat plate. However, the plate in Model-3 experienced the most critical negative peak coefficient which was -4.9 for pressure tap#8.

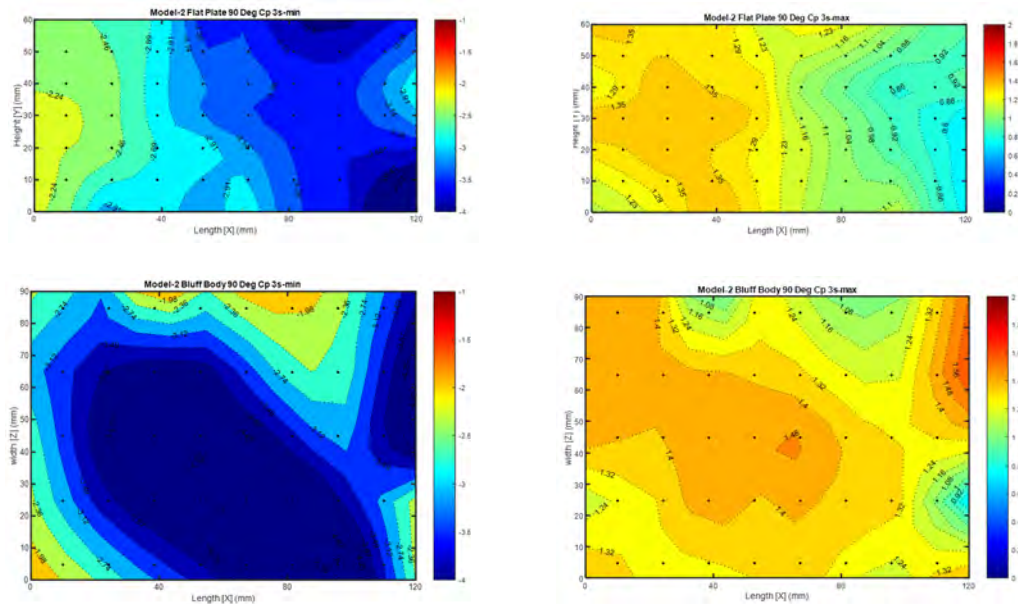
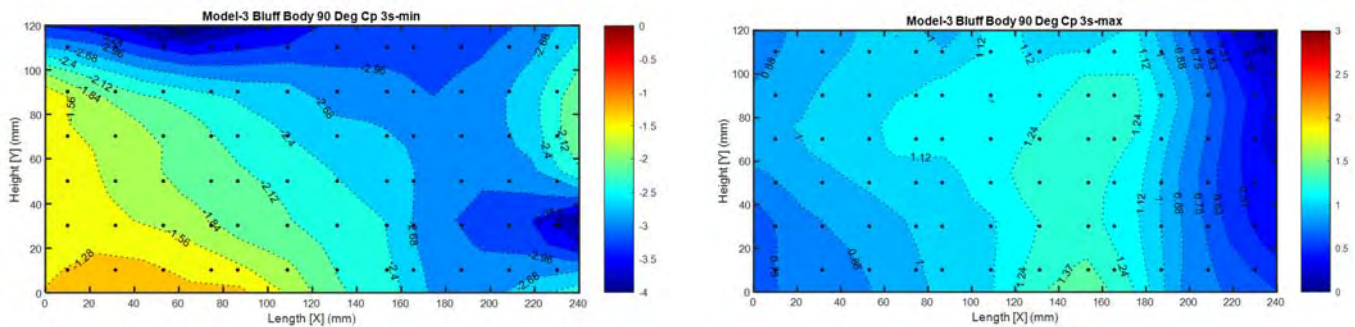


Fig. 9: Model-2, peak pressure coefficients  $C_{p\ min}$  left and  $C_{p\ max}$  right – 90 deg wind direction



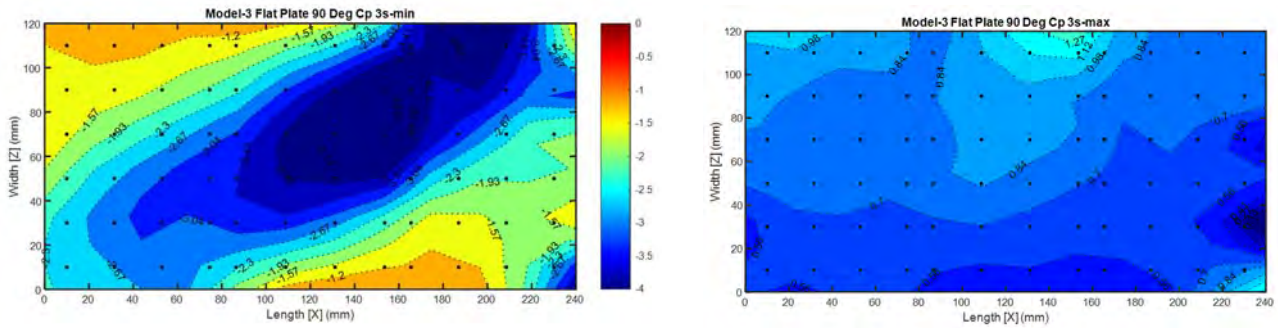


Fig. 10: Model-3, peak pressure coefficients  $\hat{C}_{p\ min}$  left and  $\hat{C}_{p\ max}$  right – 90 deg wind direction

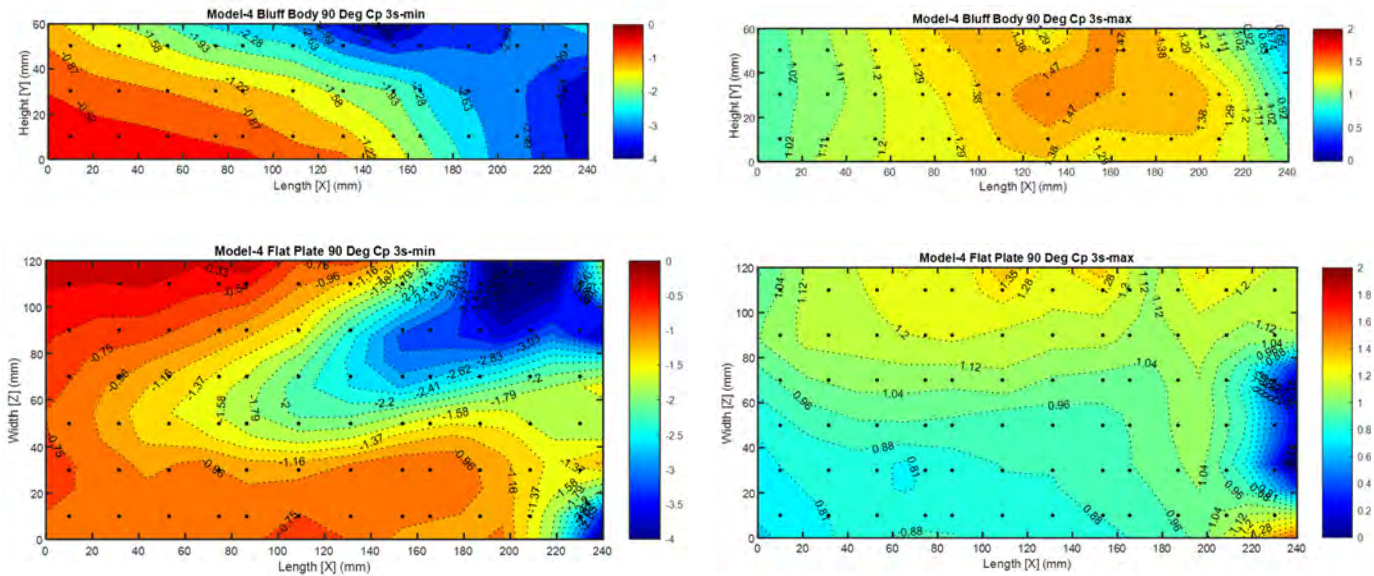


Fig. 7: Model-4, peak pressure coefficients  $\hat{C}_{p\ min}$  left and  $\hat{C}_{p\ max}$  right – 90 deg wind direction

## 6. Conclusions and Benefits to the State of Florida

This research project aimed to investigate the aerodynamic performance of T-shaped bluff bodies. Such bodies are comprised of a rectangle prism and a connected splitter plate in either a vertical or horizontal orientation. When the subassembly is exposed to the wind blowing parallel to the plate, flow separates from both surfaces and results in more complex separation bubble structure that have direct implication on the wind-induced pressures on the structure's surfaces.

Wind tunnel testing on 1:100 models provided valuable information on the flow characteristics and corresponding wind pressure patterns. The geometric ratios of the constructed models resulted in some significant differences and revealed the impact of the bluff body volume on the separated flow and its reattachment on both the bluff body as well as the flat plate. The high suction zones were observed to move downwind and further from the leading edges which has some direct implications on the characterization of the design zones in typical north American building codes and wind standards. The findings proved that further research is needed to better understand the complexity of such fluid-structure interaction. Flow visualization techniques (e.g. Particle Image Velocimetry - PIV) are expected to shed more

light into the structure of the separation bubble and its time and space resolution. A more comprehensive testing campaign will allow to draw safer conclusions about potential high suction zones farther from the edge of the plate or the bluff body. These zones can then be compared to the established wind standard methodology (e.g. ASCE 7) and provide valuable input on whether a revised design methodology is required for such complex structures.

In summary, the current research project has a two-fold benefit to the State of Florida and more broadly to the wind engineering field of study. The findings helped us shed more light on a fundamental building aerodynamic phenomenon – i.e. flow separation – from a novel standpoint. The wind tunnel tests showcased and confirmed a not so well researched wind-induced loading mechanism that might have been responsible for significant damage in different wind-structure interaction examples (e.g. rooftop equipment, canopies, parapets, overhangs etc.). Ultimately the findings from this research are expected to generate new knowledge that will help us achieve wind resilient design and/or mitigation strategies.

## References

- Adrian, R. J., Meinhart, C. D., & Tomkins, C. D. (2000). Vortex organization in the outer region of the turbulent boundary layer. *Journal of Fluid Mechanics*, 422, 1-54. doi:10.1017/s0022112000001580
- ASCE7. (2022). American Society of Civil Engineers, SEI-Society of Structural Engineering. *Minimum Design Loads and Associated Criteria for Buildings and Other Structures*. U.S.A.:
- Awasthi, M., Devenport, William J., Glegg, Stewart A. L., & Forest, Jonathan B. (2014). Pressure fluctuations produced by forward steps immersed in a turbulent boundary layer. *Journal of Fluid Mechanics*, 756, 384-421. doi:10.1017/jfm.2014.405
- Ayed, S. B., Ragab, S. A., & Hajj, M. R. (2016). Flow Control of Extreme Pressure Loads Associated with Flow Separation. *Journal of Engineering Mechanics*, 142(2). doi:10.1061/(asce)em.1943-7889.0000973
- Camussi, R., Felli, M., Pereira, F., Aloisio, G., & Di Marco, A. (2008). Statistical properties of wall pressure fluctuations over a forward-facing step. *Physics of Fluids*, 20(7). doi:10.1063/1.2959172
- Candelario, J. D., Stathopoulos, T., & Zisis, I. (2014). Wind Loading on Attached Canopies: Codification Study. *Journal of Structural Engineering*, 140(5). doi:10.1061/(asce)st.1943-541x.0001007
- Candelario José, D., Stathopoulos, T., & Zisis, I. (2014). Wind loading on attached canopies: Codification study. *Journal of Structural Engineering, ASCE*, 140(5).
- Chowdhury, A. G., & Sarkar, P. P. (2003). A new technique for identification of eighteen flutter derivatives using a three-degree-of-freedom section model. *Engineering Structures*, 25(14), 1763-1772. doi:10.1016/j.engstruct.2003.07.002
- Christopher, N., Peter, J. M. F., Kloker, M. J., & Hickey, J.-P. (2020). DNS of turbulent flat-plate flow with transpiration cooling. *International Journal of Heat and Mass Transfer*, 157. doi:10.1016/j.ijheatmasstransfer.2020.119972
- David Greenblatt, K. B. P., Chung-Sheng Yao, Jerome Harris, Norman W. Schaeffler, Anthony E. Washburn. (2004). *A separation control CFD validation test case, Part 1 Baseline and steady suction*. Paper presented at the American Institute of Aeronautics and Astronautics, AIAA, 2nd AIAA Flow Control Conference, June 28 – July 1, 2004, Portland, OR.
- Duan, G., Laima, S., Chen, W., & Li, H. (2020). Effects of leading-edge separation on the vortex shedding and aerodynamic characteristics of an elongated bluff body. *Journal of Wind Engineering and Industrial Aerodynamics*, 206. doi:10.1016/j.jweia.2020.104356
- Duan, G., Laima, S., Chen, W., & Li, H. (2021). Effects of leading-edge separation on the vortex-induced vibration of an elongated bluff body. *Journal of Wind Engineering and Industrial Aerodynamics*, 209. doi:10.1016/j.jweia.2020.104500
- Essel, E. E., Nematollahi, A., Thacher, E. W., & Tachie, M. F. (2015). Effects of upstream roughness and Reynolds number on separated and reattached turbulent flow. *Journal of Turbulence*, 16(9), 872-899. doi:10.1080/14685248.2015.1033060
- Fang, X., & Tachie, M. F. (2019). On the unsteady characteristics of turbulent separations over a forward-backward-facing step. *Journal of Fluid Mechanics*, 863, 994-1030. doi:10.1017/jfm.2018.962
- Feng, L.-H., & Wang, J.-J. (2014). Modification of a circular cylinder wake with synthetic jet: Vortex shedding modes and mechanism. *European Journal of Mechanics - B/Fluids*, 43, 14-32. doi:10.1016/j.euromechflu.2013.06.011
- Graziani, A., Lippert, M., Uystepuyst, D., & Keirsbulck, L. (2017). Scaling and flow dependencies over forward-facing steps. *International Journal of Heat and Fluid Flow*, 67, 220-229. doi:10.1016/j.ijheatfluidflow.2017.08.009

- Haller, G. (2004). Exact theory of unsteady separation for two-dimensional flows. *Journal of Fluid Mechanics*, 512. doi:10.1017/s0022112004009929
- Holmes, J. D. (2007). *Wind loading of structures*: CRC press.
- Jones, G., Santer, M., Debiiasi, M., & Papadakis, G. (2018). Control of flow separation around an airfoil at low Reynolds numbers using periodic surface morphing. *Journal of Fluids and Structures*, 76, 536-557. doi:10.1016/j.jfluidstructs.2017.11.008
- Jones, G., Santer, M., & Papadakis, G. (2018). Control of low Reynolds number flow around an airfoil using periodic surface morphing: A numerical study. *Journal of Fluids and Structures*, 76, 95-115. doi:10.1016/j.jfluidstructs.2017.09.009
- Kumahor, S., Fang, X., & Tachie, M. F. (2021). The Effects of Upstream Wall Roughness on the Spatio-Temporal Characteristics of Flow Separations Induced by a Forward-Facing Step. *Journal of Fluids Engineering*, 143(7). doi:10.1115/1.4050206
- Laima, S., Li, H., Chen, W., & Ou, J. (2018). Effects of attachments on aerodynamic characteristics and vortex-induced vibration of twin-box girder. *Journal of Fluids and Structures*, 77, 115-133. doi:10.1016/j.jfluidstructs.2017.12.005
- Lam, K. M., & Wei, C. T. (2014). Numerical Simulation of Vortex Shedding from an Inclined Flat Plate. *Engineering Applications of Computational Fluid Mechanics*, 4(4), 569-579. doi:10.1080/19942060.2010.11015342
- Largeau, J. F., & Moriniere, V. (2006). Wall pressure fluctuations and topology in separated flows over a forward-facing step. *Experiments in Fluids*, 42(1), 21-40. doi:10.1007/s00348-006-0215-9
- Lieblein, J. (1974). *Efficient Methods of Extreme Value Methodology*. Retrieved from Washington, DC
- Naeiji, A., Raji, F., & Zisis, I. (2017). Wind loads on residential scale rooftop photovoltaic panels. *Journal of Wind Engineering and Industrial Aerodynamics*, 168, 228-246.
- NIST. BLUE Extreme Value Type I Estimation. Retrieved from <https://www.itl.nist.gov/div898/winds/datasets.htm>
- NOAA. National Oceanic and Atmospheric Administration, Office for Coastal Management, Retrieved from <https://coast.noaa.gov/states/florida.html>
- NOAA. (2021). National Oceanic & Atmospheric Administration, Continental United States Hurricane Impacts 1851-2021, H. R. Division, Atlantic Oceanographic & Meteorological Laboratory, Retrieved from [https://www.aoml.noaa.gov/hrd/hurdat/All\\_U.S.\\_Hurricanes.html](https://www.aoml.noaa.gov/hrd/hurdat/All_U.S._Hurricanes.html)
- Paluch, M. J., Loredo-Souza, A. M., & Blessmann, J. (2003). Wind loads on attached canopies and their effect on the pressure distribution over arch-roof industrial buildings. *Journal of Wind Engineering and Industrial Aerodynamics*, 91(8), 975-994. doi:10.1016/s0167-6105(03)00047-3
- Prasad, C. S., & Dimitriadis, G. (2017). Application of a 3D unsteady surface panel method with flow separation model to horizontal axis wind turbines. *Journal of Wind Engineering and Industrial Aerodynamics*, 166, 74-89. doi:10.1016/j.jweia.2017.04.005
- Ren, H., & Wu, Y. (2011). Turbulent boundary layers over smooth and rough forward-facing steps. *Physics of Fluids*, 23(4). doi:10.1063/1.3576911
- Sampaio, L. E. B., Luiz T. Rezende, A., & O. Nieckele, A. (2014). The challenging case of the turbulent flow around a thin plate wind deflector, and its numerical prediction by LES and RANS models. *Journal of Wind Engineering and Industrial Aerodynamics*, 133, 52-64. doi:10.1016/j.jweia.2014.07.007
- Shigehiko Kaneko, T. N., Fumio Inada, Minoru Kato, Kunihiko Ishihara, Takashi Nishihara, Mikael A. Langthjem, (2014). *Flow-induced Vibrations (Second Edition)* (T. N. Shigehiko Kaneko, Fumio Inada, Minoru Kato, Kunihiko Ishihara, Takashi Nishihara, Mikael A. Langthjem, Ed.).
- Simiu, E., & Yeo, D. (2019). *Wind effects on structures: Modern structural design for wind*: John Wiley & Sons.

- Taylor, Z. J., Gurka, R., & Kopp, G. A. (2014). Effects of leading edge geometry on the vortex shedding frequency of an elongated bluff body at high Reynolds numbers. *Journal of Wind Engineering and Industrial Aerodynamics*, 128, 66-75. doi:10.1016/j.jweia.2014.03.007
- Uematsu, Y., Stathopoulos, T., & Iizumi, E. (2008). Wind loads on free-standing canopy roofs: Part 1 local wind pressures. *Journal of Wind Engineering and Industrial Aerodynamics*, 96(6-7), 1015-1028. doi:10.1016/j.jweia.2007.06.047
- Weldon, M., Peacock, T., Jacobs, G. B., Helu, M., & Haller, G. (2008). Experimental and numerical investigation of the kinematic theory of unsteady separation. *Journal of Fluid Mechanics*, 611, 1-11. doi:10.1017/s0022112008002395
- Wen, L., Hatakeyama, T., Sato, K., & Uematsu, Y. (2020). Wind force coefficients for the design of supporting systems of large canopies attached to low- and middle-rise buildings with flat roofs. *Journal of Wind Engineering and Industrial Aerodynamics*, 207. doi:10.1016/j.jweia.2020.104429
- Wu, B., Wang, Q., Liao, H., Li, Y., & Li, M. (2020). Flutter derivatives of a flat plate section and analysis of flutter instability at various wind angles of attack. *Journal of Wind Engineering and Industrial Aerodynamics*, 196. doi:10.1016/j.jweia.2019.104046
- Yarusevych, S., Sullivan, P. E., & Kawall, J. G. (2009). On vortex shedding from an airfoil in low-Reynolds-number flows. *Journal of Fluid Mechanics*, 632, 245-271. doi:10.1017/s0022112009007058
- Yuan-Cheng Fang, J. M. C. (2000). Experimental study of vortex shedding and subharmonic lock-on for a rotationally oscillating flat plate. *Journal of Wind Engineering and Industrial Aerodynamics*, 84, 163-180.
- Zisis, I., Raji, F., & Candelario, J. D. (2017a). Large-Scale Wind Tunnel Tests of Canopies Attached to Low-Rise Buildings. *Journal of Architectural Engineering*, 23(1). doi:10.1061/(asce)ae.1943-5568.0000235
- Zisis, I., Raji, F., & Candelario, J. D. (2017b). Large-scale wind tunnel tests of canopies attached to low-rise buildings. *Journal of Architectural Engineering*, 23(1), B4016005.
- Zisis, I., & Stathopoulos, T. (2010). Wind-Induced Pressures on Patio Covers. *Journal of Structural Engineering*, Vol. 136, No. 9,(1172-1181). doi:10.1061/共ASCE弄ST.1943-541X.0000210





*A Resource for the State of Florida*

## **Section 5**

# **Investigation and Incorporation of WOW testing outputs in the Florida Public Hurricane Loss Model**

**FINAL REPORT  
(Period: 2021-2022)**

*A Research Project Funded by:*  
**The State of Florida Department of Emergency Management**

**Investigators:** Kurt Gurley, Ph.D.  
Professor of Civil and Coastal Engineering  
Engineering School for Sustainable Infrastructure and Environment  
University of Florida  
[kgurl@ce.ufl.edu](mailto:kgurl@ce.ufl.edu)

Jean-Paul Pinelli, P.E., Ph.D.  
Professor  
Department of Civil Engineering  
Florida Institute of Technology  
[pinelli@fit.edu](mailto:pinelli@fit.edu)

**Graduate Students:** *Christian Bedwell*  
*Zhuoxuan Wei*  
*Roberto Vicente Silva de Abreu*

## **Executive Summary**

One of the key components of a better mitigated and therefore more disaster-resilient Florida involves recovery and reconstruction funding for homeowners, and a key element of that funding derives from insurance coverage, which is increasingly driven by cost considerations. The Florida Public Hurricane Loss Model (FPHLM), which has been supported by the State, provides a means of evaluating hazard insurance rate requests independently of the proprietary models used by private insurers. The model is continually refined to both satisfy the standards issued by the Florida Commission on Hurricane Loss Projection Methodology, and incorporate the current state-of-knowledge in the methodologies employed by the meteorological, engineering, actuarial, statistical, and computer science teams.

The Wall of Wind (WOW) research is largely focused on filling critical gaps in the engineering state-of-knowledge on building performance in hurricane winds via experimental methods. Recent FDEM-funded WOW work included the uplift loads on roof to wall connections of residential buildings, the influence of construction defects and their associated leakage paths on the building internal pressure during high winds, and the exterior building loads experienced by non-rectangular plan low-rise buildings. In a recent report the FPHLM research team evaluated the suitability of these research outputs for incorporation in the FPHLM. The conclusion was that they could be incorporated in the FPHLM with further research.

For the current performance period, four tasks, corresponding to four sections in this report, were proposed to investigate the possible incorporation of recent FIU wall of wind (WOW) experimental outcomes within the FPHLM.

### **Sections 1 to 3.**

This sections of the report focus on possible updates to the FPHLM in response to both recent data provided by the FIU WOW facility, and changes to the Florida Building Code (FBC) as a response to adopting ASCE 7-16 Wind Load Provisions. FIU WOW research on the distribution of roof uplift loads to roof to wall (r2w) connections was used to verify the current assumptions employed in the FPHML. This expedited the development of a new variant in the strong residential model to reflect appropriate changes to component capacities that result in less vulnerable structures. This new strong variant will be submitted in the 2022 model certification cycle with the Florida Commission on Hurricane Loss Prediction Methodology (FCHLPM). The FIU WOW investigation of internal pressure for enclosed buildings was the basis for an investigation into the assumptions currently used in the FPHLM. The work from the 2020-2021 DEM report was updated to include the influence of model internal pressure modifications on overall vulnerability functions. The implementation of the new modeling schemes with modified internal pressure will be compared with new hurricane loss insurance claims data in the coming year to determine the disposition of this internal pressure modification. The FIU WOW investigation of loads and roof decking vulnerability on non-rectangular shaped residential structures guided the creation of a roadmap to determine the efficacy of developing non-rectangular models within FPHLM. As a part of future model calibrations based on new insurance claims data, alternative shapes will be considered to add an additional degree of freedom to the calibration process.

### **Section 4**

With support from the FDEM, the WoW tested water ingress through a full-scale sliding glass door system installed on a large-scale building mock-up in 2021. The FPHLM models non-breach related leakage paths for sliders and other components to account for water ingress. In this report the FPHLM engineering team compared the WoW test outputs against the FPHLM water leak model. The comparisons centered on the rate of water penetration, expressed in volume of water per unit of effective area of the slider and per unit of time.

The water penetration in a non-breached component is a function of the size of the defect if any, the wind driven rain (WDR) impinging on the component and its associated run-off, the wind speed, and the wind direction. Similarly to what is observed in nature, the wind driven rain (WDR) rates for different storm durations in the FPHLM rain hazard model are not uniform. In fact, the mean WDR rates from the rain model are much smaller than the ones used in the WoW tests for the same wind speeds. The comparisons of the water penetration rate through the slider defects indicate that the FPHLM estimates higher water intrusion at low wind speeds and lower intrusion at high wind speeds.

Further research is needed to understand the discrepancy between the test results and the numerical model. That additional research could include WoW tests with different combinations of wind speed, wind direction, and duration, but with WDR rates similar to the FPHLM, and for different types of breaches to reflect the different strengths of the FPHLM models.

## **SECTION 1**

The FPHLM is expected to be re-evaluated for certification in Florida based on a planned fall 2022 model submission. A significant portion of the upgrades to FPHLM scheduled for development before fall 2022 is to develop a vulnerability model that utilizes ACSE 7-16 C&C loading to best reflect the latest state-of-knowledge. This is a long term effort that extends beyond the performance period of this SOW, and will incorporate overhauls of several FPHLM vulnerability components. The WOW testing of R2WC loads will be among the primary sources of benchmark data during this development, during the first 11 months of this effort in the 2021/2022 academic year.

### **Response**

The Florida Building Code adopted ASCE 7-16 in its 2020 edition and began enforcing it January 2021. In the pursuit of accurately simulating wind-induced loading, and ensuring that modeled structures represent constructed buildings, the engineering team has continued the process of integrating the ASCE 7-16 loading scheme into the FPHLM. Along with these loading changes, a new strong model has been developed. This model is designed to reflect structures built in compliance with the new Florida Building Code. During this preliminary stage of development, the new loading scheme and the new model were developed for a single building type: a timber-frame, gable-roof, single-story, personal residential model.

The most notable changes in the ASCE 7-16 component & cladding loading method are the new pressure zones and coefficients for roof uplift loads. As noted in Figure 1, the ASCE 7-16 map of pressure zones includes new regions along the ridge-line for gable-roof structures. The new roof pressure coefficients, depicted in Figure 2, result in higher uplift loads across the roof.

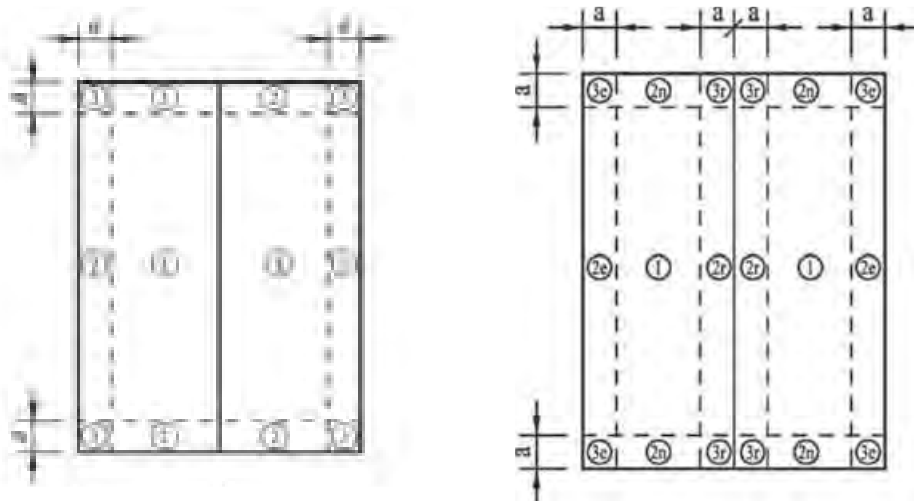


Figure 1: Diagram of gable roof pressure zones from ASCE 7-10 (left), and ASCE 7-16 (right)

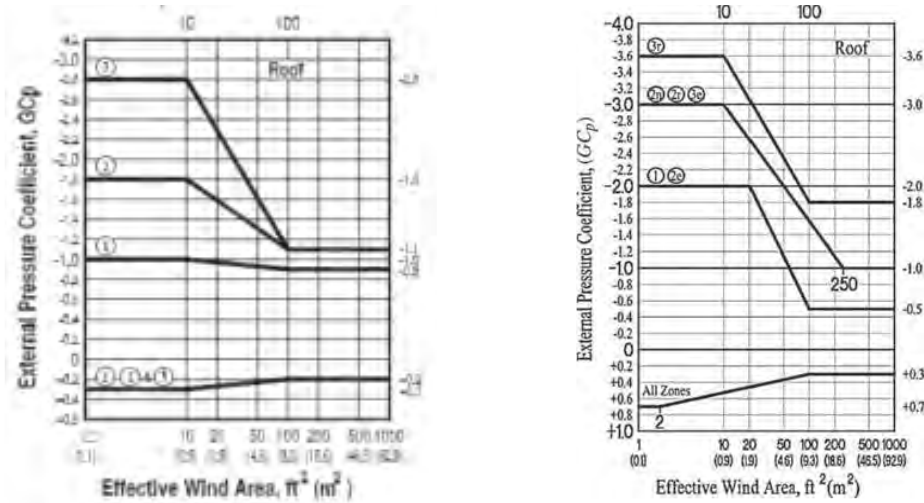


Figure 2: Plot of External Pressure Coefficient vs. Effective Wind Area for roof C&C from ASCE 7-10 (left) and ASCE 7-16 (right)

Because ASCE 7 pressure zones are defined without considering the angle of approach, a method was developed to produce directionalized pressure zone maps. Since the FPHLM evaluates models in  $45^\circ$  increments, pressure zone maps were produced for winds parallel to the ridgeline, winds perpendicular to the ridgeline, and cornering winds. This procedure was originally developed for ASCE 7-98 pressure zones (which remained unchanged through ASCE 7-10), and was adapted for the ASCE 7-16 pressure zones. Directionalized maps for ASCE 7-98 and ASCE 7-16 can be seen in Figure 3.

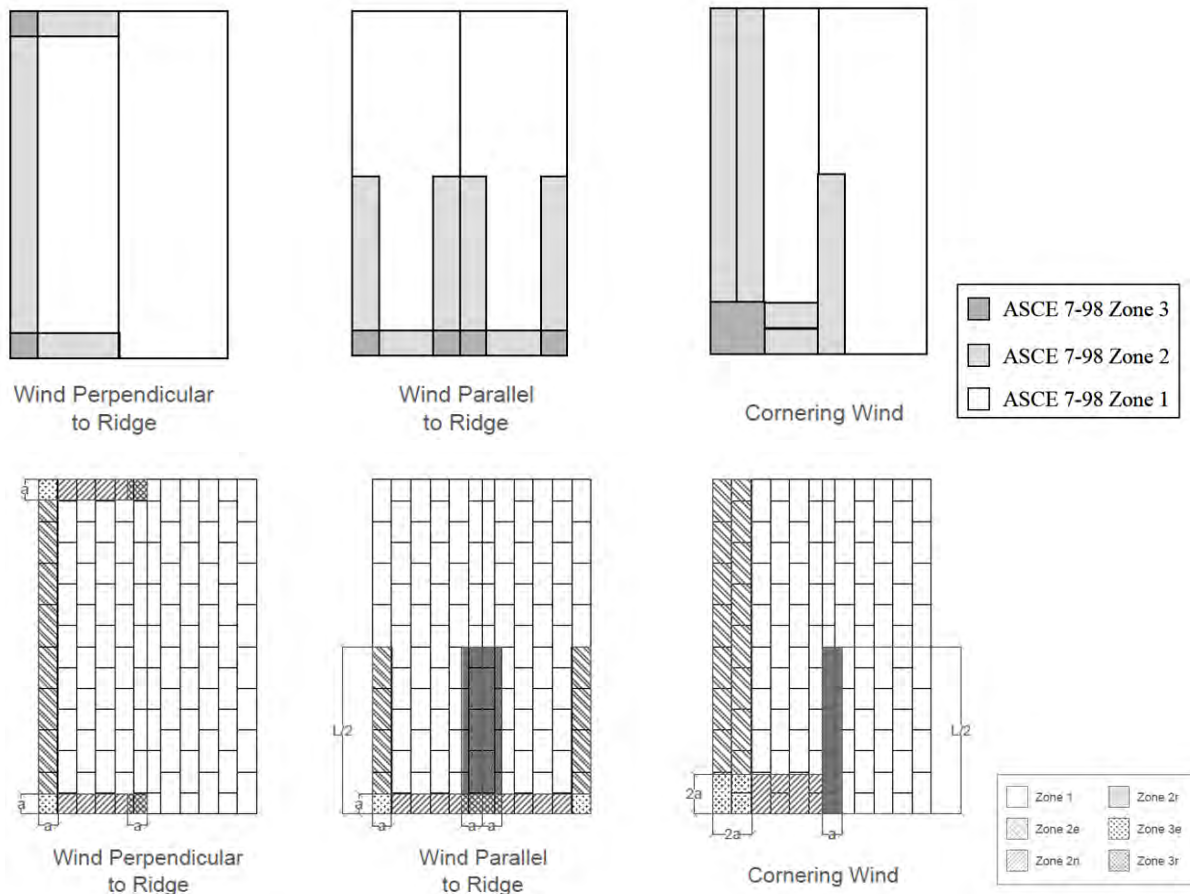


Figure 3: Diagrams of directionalized ASCE pressure zone maps for FPHLM gable roof, pre-ASCE 7-16 (above), ASCE 7-16 (below)

Several models were evaluated under both ASCE 7-10 and ASCE 7-16 loading. As expected, the increase in uplift loads resulted in increased vulnerability. Once the models diverge, the difference in vulnerabilities between models exposed to ASCE 7-10 and ASCE 7-16 loading remains stable.

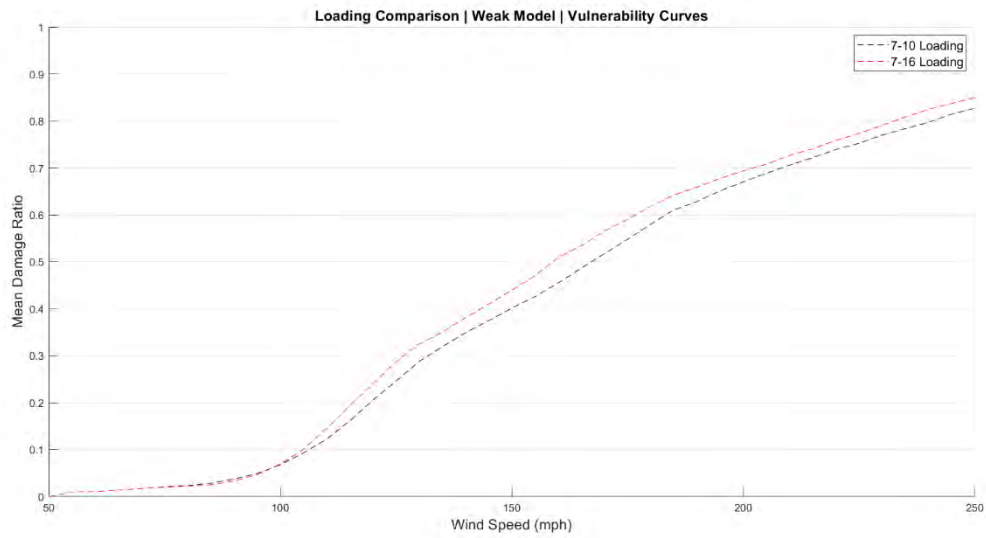


Figure 4: Vulnerability curves for weak model, comparing ASCE 7-10 vs. ASCE 7-16 loading

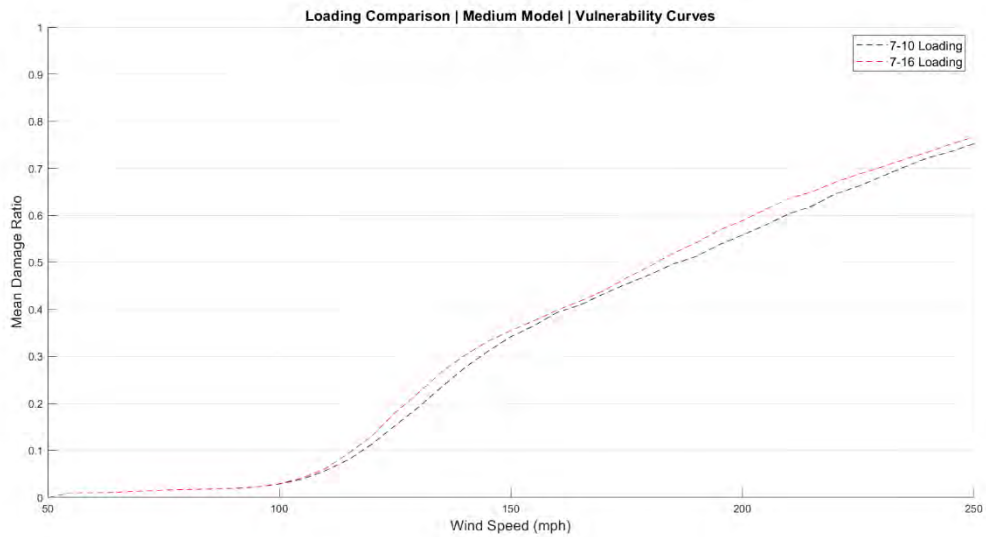


Figure 5: Vulnerability curves for medium model, comparing ASCE 7-10 vs. ASCE 7-16 loading

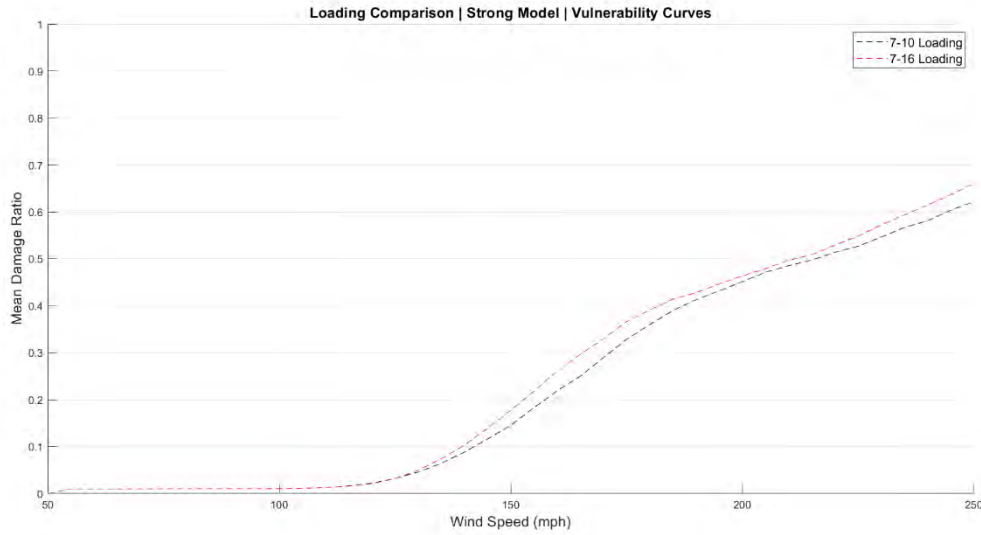


Figure 6: Vulnerability curves for inland strong model, comparing ASCE 7-10 vs. ASCE 7-16 loading

The new strong model was developed to reflect the changes in building construction practice in response to the Florida Building Code 7<sup>th</sup> Ed. Some of these changes to construction practice will be prescriptive (a recipe with specific instructions such as maximum allowable nail spacing), while others may be more case-specific to a given engineer, firm, or region. Prescriptive examples include changes to roof sheathing thickness and fastener spacing. In ASCE 7-10, minimum sheathing thickness was a function of truss spacing; in ASCE 7-16 minimum sheathing thickness is a function of wind speed. Other substantive changes include the nailing schedule

Rafter or Beam Spacing (in)	Minimum Net Thickness (in)
4	5/8
48	1 ½ Tongue & Groove
60	
72	

required to attach decking to the roof truss system. Such changes are relatively straight forward to implement in the FPHLM engineering model by offering additional (larger) capacity values for various connections holding the structure together.

Table 1: Minimum Roof Sheathing Thickness, FBCR 2017 (left), FBCR 2020 (right, excerpt)

Truss Spacing 24" o.c.	Wind Speed		
	115 mph	120 mph	130 mph
Minimum Sheathing Thickness (in) Exposure B	7/16	7/16	7/16
Minimum Sheathing Thickness (in) Exposure C	7/16	7/16	15/32
Minimum Sheathing Thickness (in) Exposure D	15/32	19/32	19/32

The new strong model was designed as a modified version of the inland strong model. In compliance with the new FBC provisions regarding roof sheathing fasteners and spacing, the new strong model was designed using ring-shank nails at 6" spacing,



rather than the strong models 8d nails at 6” spacing. This capacity change is quantified in the model as an increase in sheathing uplift capacity from 130 psf to 200 psf. Because higher uplift loads across the roof were expected, the roof-to-wall connection was also upgraded from hurricane straps to a high-wind connector from Simpson Strong Tie. This change resulted in a capacity increase from 1240 lb. to 2250 lb.

The development of the new strong model requires an iterative approach in order to ensure that the model behaves logically when compared to other models. For example, the model plotted in Figure 7 was designed using the previously-described upgrades to sheathing fasteners and roof-to-wall connections. By increasing the capacity of these components, uplift loads are transferred to the stud-to-sill connections at high windspeeds. This behavior results in the new strong model becoming more vulnerable than the original strong model at high wind speeds. The probability of wind speeds of this magnitude are low enough that this behavior will not significantly impact the model’s projected losses. Regardless, continued development of the new strong model is ongoing, in the pursuit of a model which is less vulnerable than the original strong model at all simulated wind speeds.

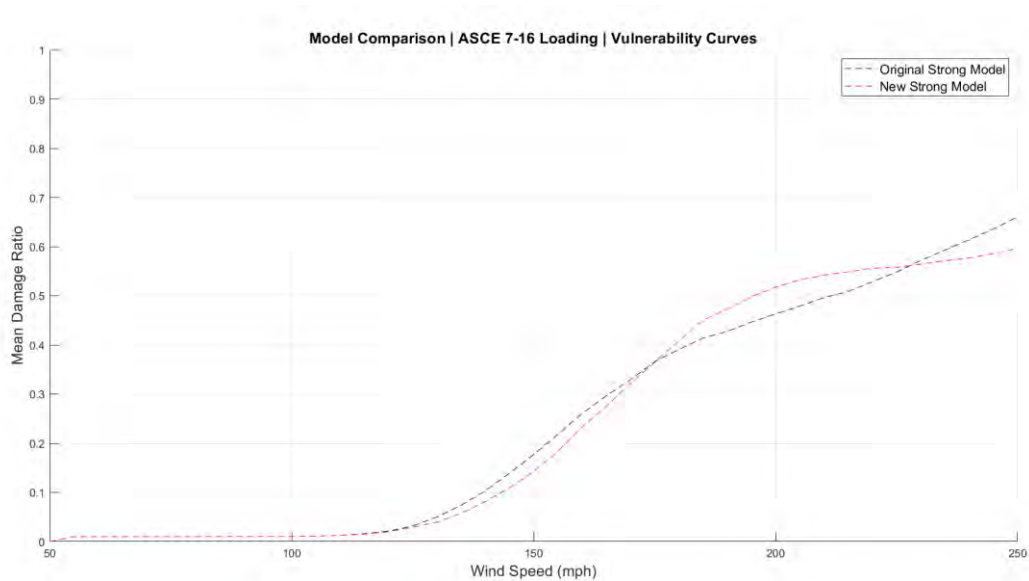


Figure 7: Vulnerability curves comparing the strong and new strong models under ASCE 7-16 loading.

In the 2020-2021 DEM Report, the results of the Florida International University (FIU) Wall of Wind (WOW) tests on the distribution of roof-to-wall connection loads were discussed in the context of the FPHLM physical damage module. The tests involved instrumenting a 1:4 scale model gable-roof residential building with load cells at the roof-to-wall connections and subjecting the model to turbulent winds at various approach angles. Using that model’s geometry, calculations were performed using ASCE Main Wind Force Resisting System (MWFRS) and ASCE Components & Cladding (C&C) approach. The report concluded that the ASCE C&C method of calculating and distributing uplift loads was an effective approximation when compared to the FIU WOW results.

The previously discussed modifications to the FPHLM, notably the new loading scheme and new strong model, do not affect the way uplift loads are distributed to roof-to-wall connections. The new strong model includes upgraded capacities for various structural components. The new loading scheme results in a significant increase in the uplift load across the roof, but has no impact on the way those loads are distributed to roof-to-wall connections. The conclusion of the UF report on the WOW tests, that the ASCE C&C loading method is an effective approximation of load distribution, remains unchanged in the light of the modifications made to the FPHLM.

## SECTION 2

Non-breach related leakage paths (defects) have long been incorporated in the FPHLM to account for water ingress, but the influence of such paths on internal pressure is not yet well understood nor implemented in the FPHLM. The WOW sequence of tests on internal pressure due to varying controlled aperture sizes provided an initial benchmark to develop an internal pressure model that is sensitive to both approach wind direction and defect size. An important outcome from the 2019/2020 study is that the modification in internal pressure model to accommodate non-breach leakage paths does influence the FPHLM modeled vulnerability of most building components. The influence appears to be a universal increase in building vulnerability to some degree. As the incorporation of ASCE 7-16 throughout the model is developed over the next year, this internal pressure modification, based on WOW testing, will be included in this development.

### Response

In the 2020-2021 DEM report, the engineering team discussed the Wall of Wind (WOW) tests focused on breaches and internal leakage, and the implementation of the results of those tests into the FPHLM physical damage model. The WOW tests involved instrumenting a scale model residential structure with internal pressure taps and comparing different configurations of defects in the building envelope. The internal pressure of each configuration at each approach angle was measured, and the peak internal pressure coefficient was calculated using the partial turbulence simulation approach to account for the absence of low-frequency eddies caused by size restrictions. The results of these tests are plotted in Figure 8.

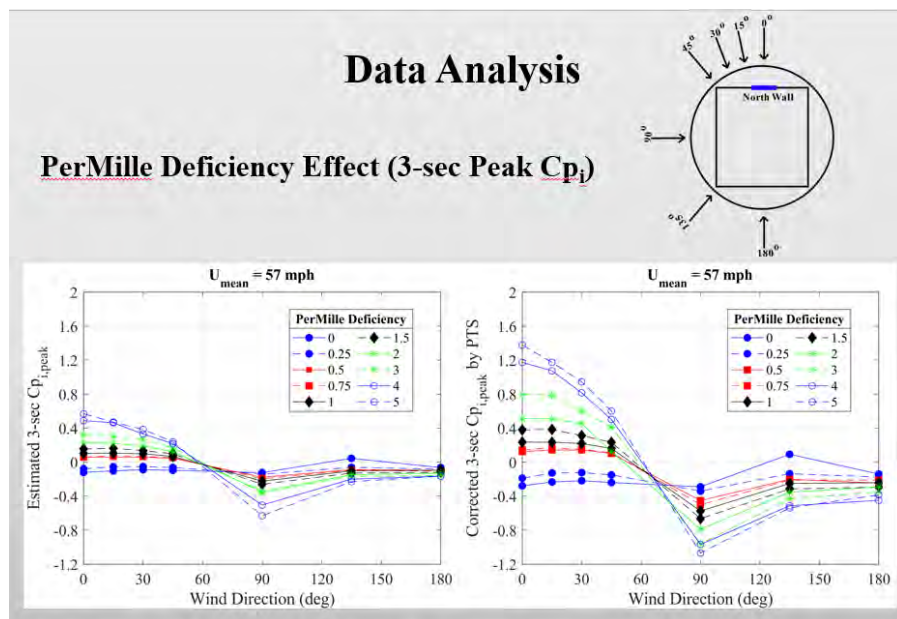


Figure 8: Screen capture from Erwin et al. (2020) FIU WOW report on internal pressure on buildings with controlled aperture sizes.

A beta-version of the FPHLM was developed, utilizing the results of these tests to modify the method of calculating internal pressure. The weak, medium, and strong models were assigned defect ratio values of 0.5%, 0.3%, and 0.2%, where each value represents the percentage of wall area with permeable defects. For each model, the initial value for internal pressure was calculated using these angle-dependent peak pressure coefficient from the WOW test rather than the ASCE internal pressure coefficient. Analysis of the weak, medium, and strong models was performed, comparing component damage to structures with and without the modified internal pressure calculation (Figures 9-11).

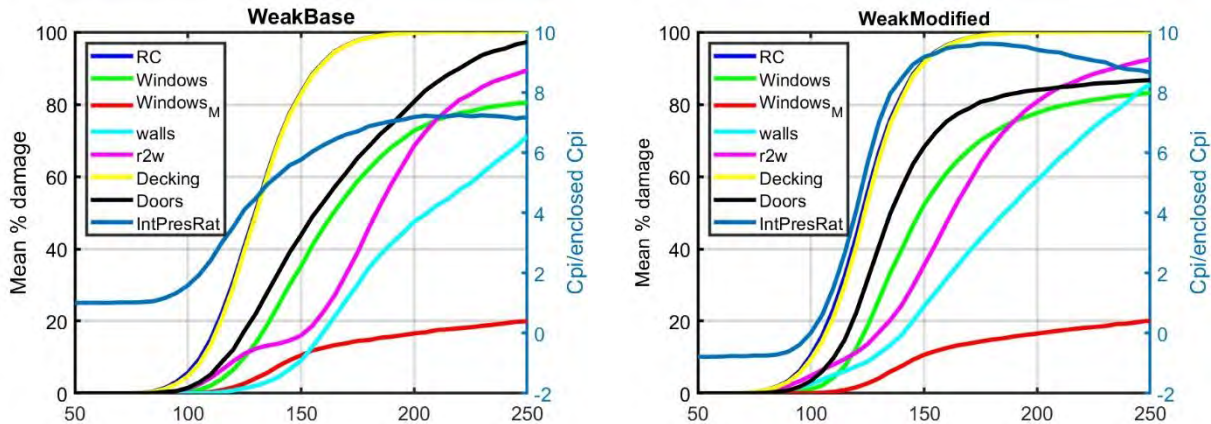


Figure 9: Weak Model - Six component vulnerabilities as a function of wind speed, and actual internal pressure coefficient in ratio with the fixed ASCE 7-98 internal pressure coefficient. Left: prior to modification to internal pressure model (Base). Right: After modification to internal pressure model (Modified).

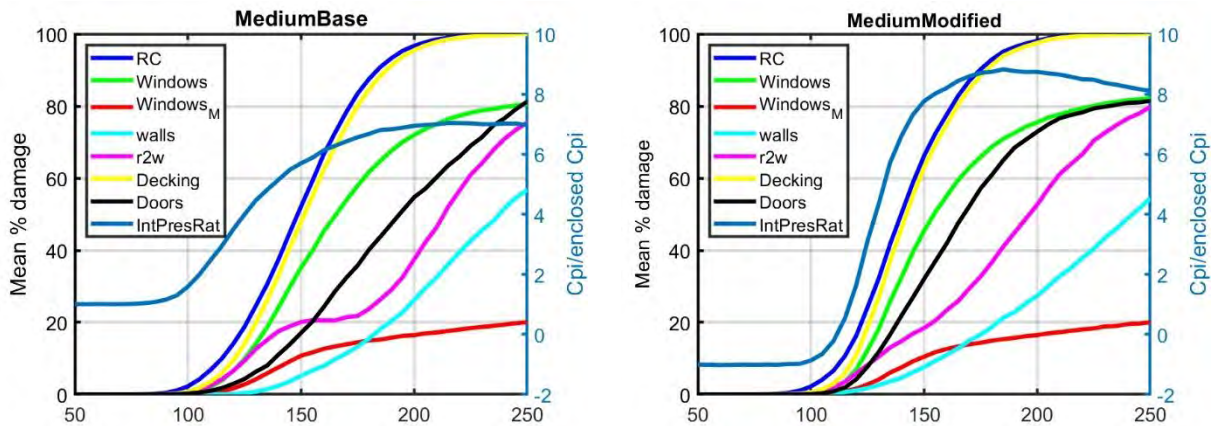


Figure 10: Medium Model - Six component vulnerabilities as a function of wind speed, and actual internal pressure coefficient in ratio with the fixed ASCE 7-98 internal pressure coefficient. Left: prior to modification to internal pressure model (Base). Right: After modification to internal pressure model (Modified).

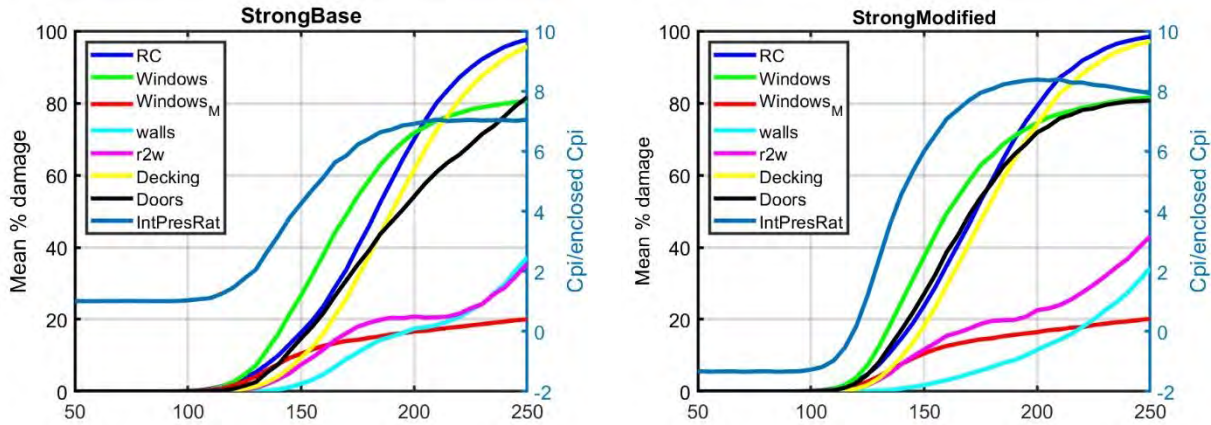


Figure 11: Strong Model - Six component vulnerabilities as a function of wind speed, and actual internal pressure coefficient in ratio with the fixed ASCE 7-98 internal pressure coefficient. Left: prior to modification to internal pressure model (Base). Right: After modification to internal pressure model (Modified).

After the ASCE 7-16 loading scheme was developed, a version of the FPHLM was assembled which integrated both the new loading scheme and the modified internal pressure method. The weak, medium, and strong models were tested, using the same values for the peak internal pressure coefficient as before. In addition to analyzing physical component damage (Figures 12-14), the damage matrices were also processed by the personal residential vulnerability module to produce vulnerability curves (Figures 15-17).

The modified internal pressure calculation lead to an increase in the vulnerability of all models. In the medium and strong models, this vulnerability increase was most extreme between 125-200 mph. Unlike the medium and strong models, the weak models diverged at 125 mph and never converged to a similar trend. The failure to converge can be attributed to the sharp increase in damage to the exterior wall at high wind speeds; this behavior is most extreme in the weak model, and is insignificant in the other models.

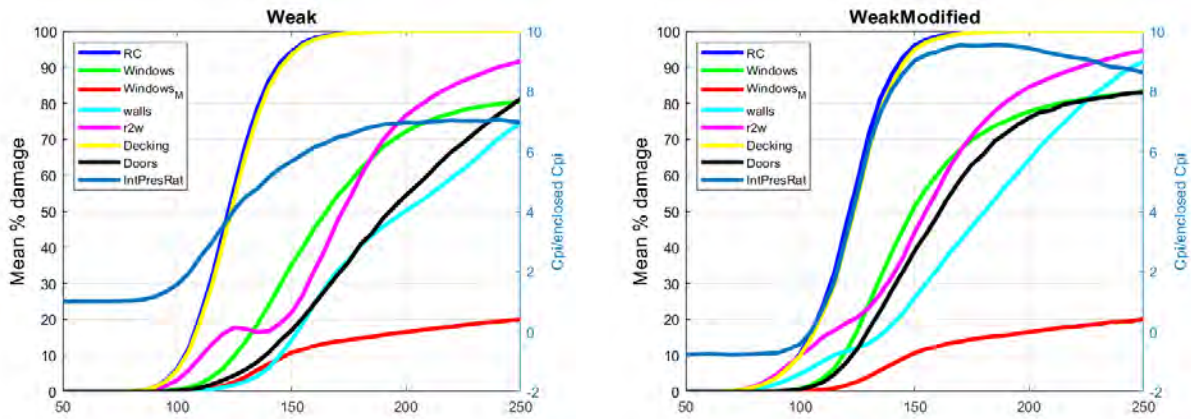


Figure 12: Weak Model, ASCE 7-16 Loading - Six component vulnerabilities as a function of wind speed, and actual internal pressure coefficient in ratio with the fixed ASCE 7-16 internal pressure coefficient. Left: prior to modification to internal pressure model (Base). Right: After modification to internal pressure model (Modified).

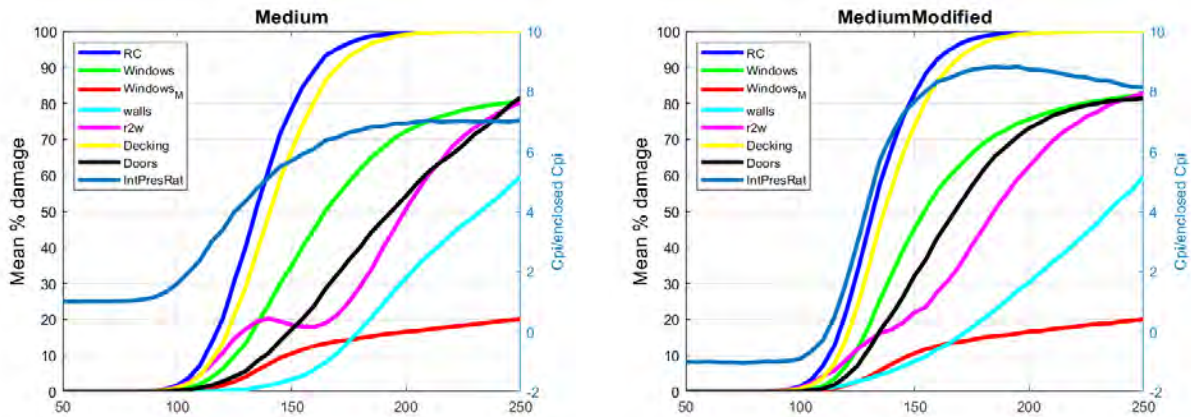


Figure 13: Medium Model, ASCE 7-16 Loading - Six component vulnerabilities as a function of wind speed, and actual internal pressure coefficient in ratio with the fixed ASCE 7-16 internal pressure coefficient. Left: prior to modification to internal pressure model (Base). Right: After modification to internal pressure model (Modified).

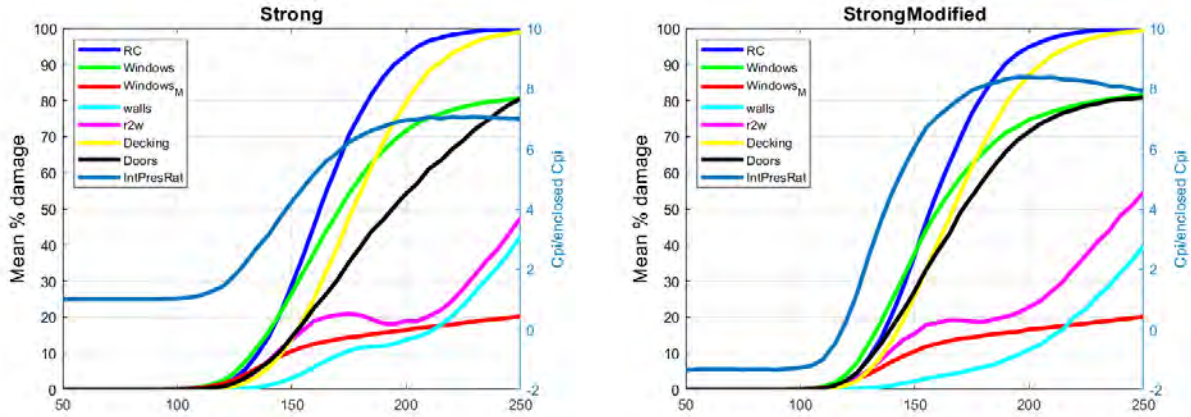


Figure 14: Strong Model, ASCE 7-16 Loading - Six component vulnerabilities as a function of wind speed, and actual internal pressure coefficient in ratio with the fixed ASCE 7-16 internal pressure coefficient. Left: prior to modification to internal pressure model (Base). Right: After modification to internal pressure model (Modified).

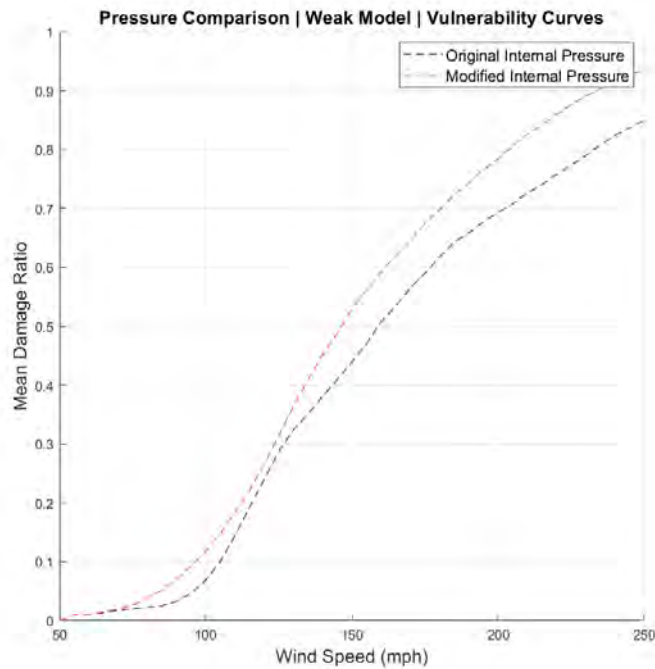


Figure 15: Vulnerability curves for the weak model under ASCE 7-16 loading with and without internal pressure modification.

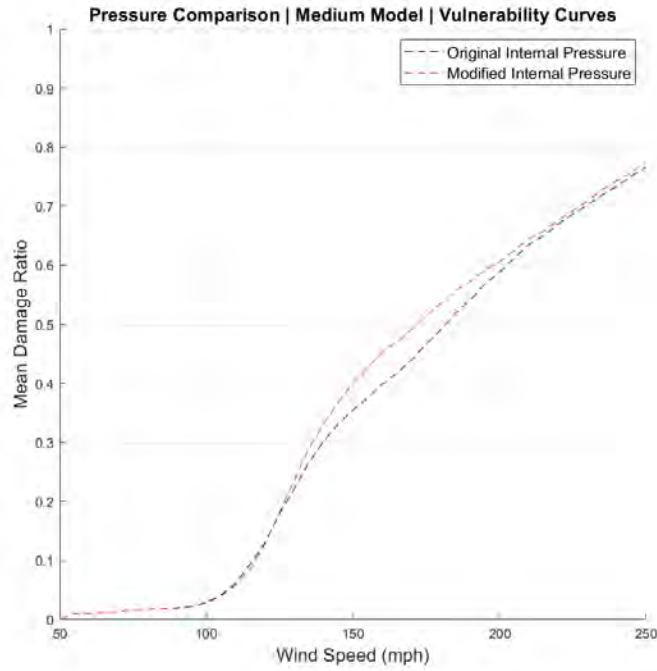


Figure 16: Vulnerability curves for the medium model under ASCE 7-16 loading with and without internal pressure modification.

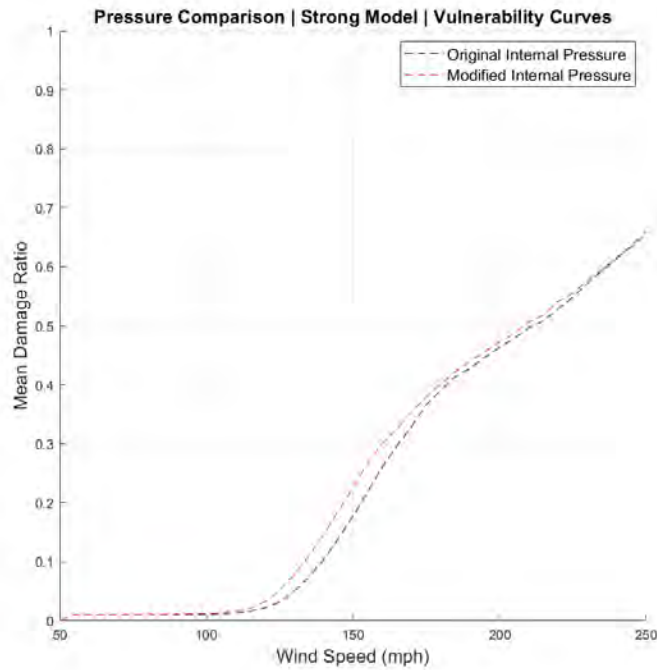


Figure 17: Vulnerability curves for the strong model under ASCE 7-16 loading with and without internal pressure modification.



### **SECTION 3**

Ongoing WOW research concerning pressure loads on non-rectangular building plans offers a potentially significant expansion to the library of rectangular models currently employed in the FPHLM. Results of this WOW research will be evaluated to determine whether non-rectangular models should be developed for the FPHLM. This will be conducted in three phases. 1) Compare rectangular and non-rectangular pressure loads to evaluate any trends worthy of pursuit. 2) If so, develop a simple roof-cover-only failure investigation to get a sense of the impact on current FPHLM loss projections. 3) If significant, develop a roadmap for the development of full non-rectangular models for the FPHLM (implementation of roadmap is beyond the current scope, but may be pursued in future funding cycles).

#### **Response**

The FPHLM vulnerability model employs a directional wind load scheme when determining building damage using Monte Carlo simulation. This directional scheme allows the differentiation of damage as a function of approaching wind direction. The scheme developed is based on modifications to the directionally enveloped ASCE 7 pressure coefficient maps. The recent updates to this FPHLM scheme were discussed earlier in this report, inspired by the FBC adoption of ASCE 7-16 Wind Load Provisions, which includes substantial changes to the directionally enveloped maps. All such ASCE 7 pressure loading guidance is presented for rectangular roof shapes only.

Although most of the existing low-rise residential infrastructure in Florida is not rectangular in roof shape, the FPHLM has only explicitly modeled simple rectangular shapes. This is due to a confluence of five considerations:

- 1) The FPHLM intent is to represent loss predictions in an aggregate sense. It is not intended to be applied as an accurate predictor for any given individual structure. If the aggregate losses predicted are verifiable against claims data, the utility of developing non-rectangular roof models is limited.
- 2) ASCE 7, the root of the FPHLM loading scheme, only presents wind load guidance on rectangular structures. Two reasons for this: a) It has been assumed in the past that rectangular roof guidance can be extrapolated to other shapes, but no how-to guidance exists. b) Expanding beyond rectangular shapes in ASCE 7 would open the doors to an large list of roof shapes that would require wind tunnel testing to derive directionally enveloped pressure coefficients to determine design loads.
- 3) Item b) in the previous paragraph applies also to the FPHLM library of existing structures. It is not feasible to develop hundreds of variants of models to account for the hundreds of roof shapes that do exist. Thus, rectangular was chosen, and model variations do account for construction relating to include age, material, roof shape (hip vs gable only), region.
- 4) The literature to date does not demonstrate that the non-rectangular shape of a roof would influence the vulnerability of that building. For example, it has not been shown that the roof cover damage to an L-shaped building and a rectangular building of the same roof

slope and square footage would differ. This observation may well be invalidated in the peer reviewed literature soon based on recent work at FIU WOW, to be discussed.

- 5) In actual model operation, the portfolios (collections of actual insured properties to be analyzed) provided by insurers generally do not include enough detail to determine roof shape specifics. Thus, non-rectangular models cannot be properly assigned during model operation.

The references by Sarma et al. (2021) and Zisis and Matus (2021) form the basis for this section of the report on the development of non-rectangular building models for the FPHLM. Although neither of these documents are peer reviewed literature, the findings presented therein are likely to be peer reviewed in 2022.

We now discuss the three phases of this effort and the response to each:

Phase 1) Compare rectangular and non-rectangular pressure loads to evaluate any trends worthy of pursuit:

Response: The work by Zisis and Matus (2021) provides a comparative study of pressure loads on roofs of various shapes (rectangular, C, T and L shaped). This experimental work provides guidance for developing modifications to the FPHLM wind loading schemes, and led to the study by Sarma et al. (2021) discussed next.

Phase 2) If so, develop a simple roof-cover-only failure investigation to get a sense of the impact on current FPHLM loss projections

Response: Sarma et al. (2021) explored this task in the framework of damage to roof sheathing rather than roof cover. Figure 18 below shows a screen capture from the Sarma et al. (2021) document, where the roof sheathing vulnerability as a function of wind speed is presented for four roof shapes (L, T, C, and Rectangular shapes). The horizontal axis is 3-second gust wind speed in m/s, converted to mph by multiplying by 2.236 (50 m/s = 111 mph, 70 m/s = 156 mph). Observe that the separation between roof shapes is minor at lower wind speeds, and becomes more distinct by 70 m/s. This analysis of roof sheathing loss provides the critical path toward next steps.

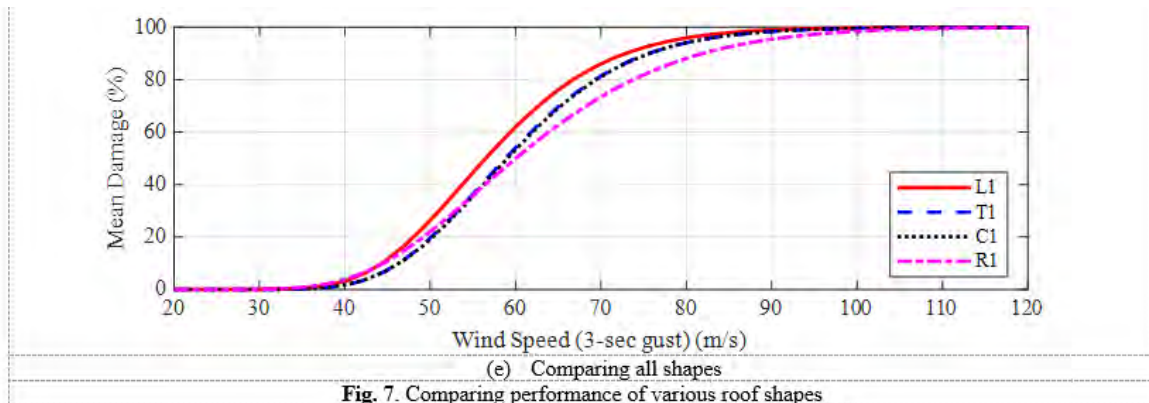


Figure 18: Copy/paste from Sarma et al. (2021). Comparison of roof sheathing loss (vertical axis) vs wind speed (horizontal axis) for four different roof shapes:

L1: L-shaped roof    T1: T-shaped roof    C1: C-shaped roof    R1: rectangular roof

Phase 3) If significant, develop a roadmap for the development of full non-rectangular models for the FPHLM (implementation of roadmap is beyond the current scope, but may be pursued in future funding cycles)

Response: The Figure above indicates that the largest separation of damage is between the rectangular and L-shaped buildings, and this difference is more significant at higher wind speeds with a corresponding lower probability of occurrence. Based on the work to date, it is *not* obvious that pursuing the development of models with alternative roof shapes will influence the current predictive capabilities of the FPHLM. However, a rational roadmap forward in future efforts would be:

Develop an L-shaped model to complement the existing rectangular model for one specific subset classification (e.g. old construction, timber frame gable roof one story)

Investigate the differences in damage probabilities of all model components (roof cover, roof sheathing, openings, walls, etc.) between these shapes

Input the physical damage results into the costing model to produce relative vulnerability models (overall loss ratio vs wind speed) for comparative analysis

The above future efforts would be conducted concurrent with the pursuit of up to data infrastructure exposure data from insurance companies and tax appraisers to see whether the determination of roof shape will be available for portfolio analysis. Finally, new insurance claims data is being secured soon. This provides a new means of validating the performance of the existing FHPLM and determining whether roof shape would be a useful degree of freedom to add to the calibration procedures.

**References:**

Matus M, Zisis I. Investigation of irregular-shaped buildings and their pressure distribution. 6th AAWE Workshop, 2021.

Zisis I, Feng C, Matus M. Investigation of wind-loads on irregular shaped low-rise buildings. Engineering Mechanics Institute Conference, 2021.

Sarma H, Zisis I, Matus M. Effect of roof shape on wind vulnerability of roof sheathing panels. Manuscript in preparation for submission to peer review, 2021.

Zisis I, Matus M. Codification of Wind induced loads on irregular shaped buildings – Phase II. A Report Submitted to: The State of Florida Division of Emergency Management. July 2021.

## **SECTION 4:**

Recent hurricane in Florida and elsewhere have shown the vulnerability of low-rise and mid/high-rise residential buildings to rainwater ingress (Kennedy et al., 2020; Pinelli et al., 2018). WDR is the main factor causing interior damage (Mileti, 1999). Especially mid/high-rise buildings which are made of engineered steel and concrete structures, suffer few significant structural failures (Eamon et al., 2007). However, even for low-intensity events, with no damage to the openings, fenestration, especially sliding doors, experience a large amount of water leaks (Pita et al., 2016) and wind driven rain is proved to be the predominant source of interior related losses (Chowdhury et al., 2011; Mullens et al., 2006). For instance, when Hurricane Irma passed through South Florida, wind speeds were far less than the wind speed required by the Florida Building Code. Notwithstanding this, a remarkable amount of water passed through the fenestrations of buildings, bringing about millions of dollars in interior damage.

In 2021 a WoW project funded by the Florida Division of Emergency Management (FDEM) investigated water intrusion through a full-scale sliding glass door system installed on a large-scale building model. To accomplish the goals, wind-driven-rain (WDR) tests were conducted for multiple wind directions, test durations and wind speeds to study their effects on water intrusion through the sliding glass door system.

The Florida Public Hurricane Loss Model, funded by the Florida Office of Insurance Regulation (OIR), incorporates non-breach related leakage paths to estimate the water ingress through the defects of sliders. The objective of this research is to compare the results of the WoW tests to the results of the FPHLM water leak model for sliders. The research team first compared the WDR rates derived from the rain hazard model of FPHLM against the WoW WDR rates, and then compared the water penetration rates from the leakage path model for sliders of the FPHLM against the WoW test results.

## **Background**

### ***WoW Tests***

The WoW has a long history of research on WDR and its effects on building under hurricane conditions. Researchers simulated the interaction between WDR and building envelope, in the 12-fan WoW at Florida International University (FIU) (Chowdhury et al., 2017). The WoW facility can generate a boundary layer profile of up to a Category 5 (Saffir-Simpson scale) hurricane and simulate associated WDR (Aly et al., 2011). Baheru et al., (2014, b; 2015) created a ¼ scale test model of a residential building to measure the rain deposition characteristics under simulated hurricane conditions. Figure 1 shows the schematic-diagram of the 12-fan WoW with a test structure, which can be rotated to a required direction. This test quantified two metrics: Rain Admittance Factor (RAF) and Surface Runoff Coefficient (SRC) and provided the distribution of RAF and SRC on the façade of the low-rise building model.

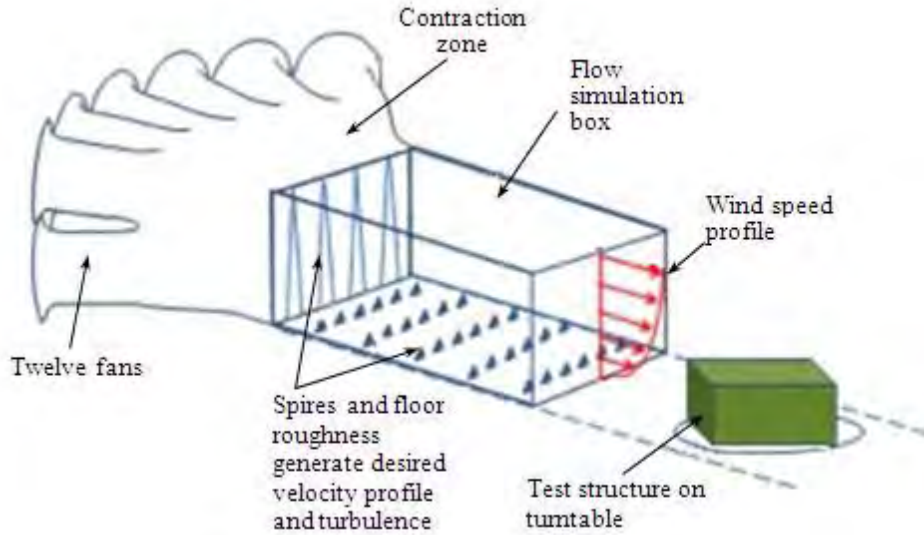


Figure 1. Schematic-diagram of 12-fan Wall of Wind (WoW) from Baheru et al. (2014, b)

Raji (2018) and Raji et al. (2019; 2020) tested building models at the WoW with a 1:4 scale with a 5:12 roof pitch and both hip and gable roofs. They divided the interior layout of the building into 6 interior and 6 attic compartments with exact same dimensions and investigated the distribution of water ingress between partitions and flooring with different damage states of the building given different wind directions.

In 2021, FDEM funded a WoW project to expose a full-scale sliding glass door – installed on a full-scale test model – to wind and wind-driven rain conditions generated by the WoW (see Figure 2). The test protocol for the study was established to investigate the effects of wind speed, wind direction, experiment duration, and the potential sheltering effect of two common shuttering systems – aluminum storm panels and accordion shutters – on the volume of water intrusion accumulated inside the building model. The protocol considered three wind directions,  $0^\circ$ ,  $22.5^\circ$ , and  $45^\circ$ . This research reported the observed water intrusion as the total volume of water intrusion, symbolized here as  $RR_{b,tot}$  with the Equation 1. Table 1 shows the mean  $RR_{b,tot}$  and the corresponding wind speed, shutter type and wind direction.

$$RR_{b,tot} = \frac{V_{tot}}{A_e t} \quad (1)$$

Where:

- $V_{tot}$  is the total value of water ingress through the slider.
- $A_e$  is the effective area calculated as area of the sliding glass door itself (direct impinging raindrop region) plus the area of the wall directly above the sliding glass door (surface runoff region). In this test  $A_e$  are  $8640 \text{ inch}^2$ ,  $10376 \text{ inch}^2$ , and  $10129.6 \text{ inch}^2$  for the slider without shutter, with accordion shutter, and with storm panel respectively.
- $t$  is the duration of the WDR event.



Figure 2. Large-scale building model with full-scale sliding glass door

Table 1. Results of mean  $RR_{b,tot}$  from WoW test

Wind speed (mph)	Shutter Type	Wind direction (deg)	$RR_{b,tot}$ (cm/hr)
65	None	0	0.0014
100	None	0	0.6383
130	None	0	1.0040
65	None	45	0.0008
65	Accordion	0	0.0003
100	Accordion	0	0.0084
130	Accordion	0	0.6793
65	Accordion	45	0.0000
65	Storm Panel	0	0.0000
100	Storm Panel	0	0.5101
130	Storm Panel	0	1.0108
65	Storm Panel	45	0.0000

Among all research above, Baheru et al. (2014, a & b), Raji (2018) and 2021 FDEM-funded WoW test provided the combinations of WDR rates and wind speeds which are compared against the results from the rain hazard model (introduced in next section) in Chapter Results.

### ***FPHLM - Rain Hazard Model***

The FPHLM interior damage model incorporates the results of the tests described above, Baheru et al. (2014, b), Raji (2018).

Pita et al. (2012) estimated the amount of WDR during hurricane events via simulation of a large number of synthetic hurricanes. A number of stations are placed uniformly across each synthetic hurricane at a given distance from the coast. The simulation records the time history of rain rate and wind speed at each station for all synthetic hurricanes resulting in the distributions of WDR at 10-meter height as a function of maximum 3-sec gust wind speed at 10-meter height for actual terrain (WS). The model separates accumulated WDR into two parts:  $WDR_1$  defined from beginning of a hurricane to the moment of maximum wind speed,  $V_{max}$ , and  $WDR_2$  defined from the moment of  $V_{max}$  ( $t_{V_{max}}$ ) to the end of a hurricane (Pita et al., 2012; Johnson et al., 2018). As a result of the rotation of the hurricane, the values of  $WDR_1$  and  $WDR_2$  are distributed in ratios  $\alpha$  and  $\beta$  over the eight possible wind direction octants (Johnson et al., 2018) (see Figure 3). The outputs of Pita et al. (2012) and Johnson et al. (2018) are incorporated into the vulnerability model of FPHLM to estimate the amount of water ingress during hurricane events. The amount of accumulated wind-driven rain for each wind direction octant equals to the product of  $WDR_1$  or  $WDR_2$  and the corresponding  $\alpha$  or  $\beta$  (see Equations 2 and 3).

$$V_i = WDR_1 \cdot \alpha_i \quad (2)$$

$$V_j = WDR_2 \cdot \beta_j \quad (3)$$

where,  $V_i$  and  $V_j$  are the amount of accumulated WDR before and after  $t_{V_{max}}$  for the  $i$ -th and  $j$ -th octants respectively.

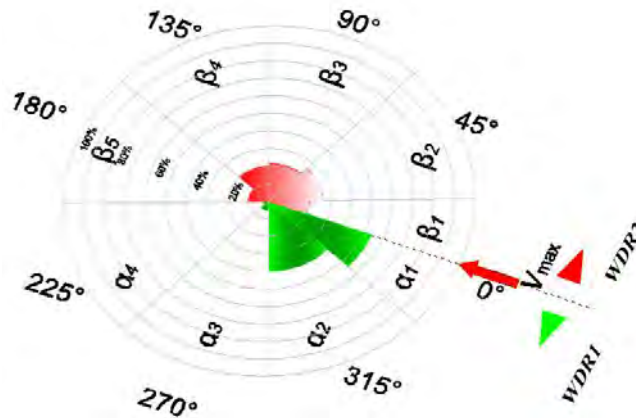


Figure 3. Distribution of WDR as a function of wind direction

### ***FPHLM - Non-breach Related Leakage Paths***

Johnson et al. (2018) estimated water intrusion through the defects of sliders in the FPHLM vulnerability model. The total volume of water intrusion during a hurricane event is divided into four parts: direct impinging rain before  $t_{V_{max}}$  ( $V_{DI1}$ ), surface runoff before  $t_{V_{max}}$  ( $V_{SR1}$ ), direct impinging rain after  $t_{V_{max}}$  ( $V_{DI2}$ ), and surface runoff after  $t_{V_{max}}$  ( $V_{SR2}$ ).

As the storm rotates before and after  $t_{V_{max}}$ , it subjects any given surface to fractions of impinging rain corresponding to the different wind directions (or octants) from the storm rotation. In the



FPHLM there is no occurrence of any breach in the exterior damage model for that simulation before the  $t_{Vmax}$ . The total volume of impinging rain penetrating through a component defect area  $A_d$  is the sum of the corresponding fractions of impinging rain over the wind direction octants  $\theta_m$ , as the storm rotates from its start to  $t_{Vmax}$ . Because the defect locations are unknown, the mean  $RAF_{\theta_m}$  and  $SRC_{\theta_m}$  values are applied to each slider. Similarly, the total volume of surface runoff water penetrating through a defect is the sum of the corresponding fractions of surface runoff water over the wind direction octants  $\theta_m$  as the storm rotates from its start to  $t_{Vmax}$ . Equation 4 and 5 illustrate the estimate of  $V_{DI1}$  and  $V_{SR1}$ , respectively.

$$V_{DI1} = \left[ \sum_{m=1}^4 RAF_{\theta_m} \cdot \alpha_m(V_{max}) \right] \cdot WDR_1(V_{max}) \cdot A_d \quad (4)$$

$$V_{SR1} = \left[ \sum_{m=1}^4 SRC_{\theta_m} \cdot \alpha_m(V_{max}) \cdot A_{SR_{\theta_m}} \right] \cdot WDR_1(V_{max}) \quad (5)$$

where,  $A_{SR_{\theta_m}}$  = reference surface area for defects which is a function of the wind direction.

After  $t_{Vmax}$ , the total amount of impinging rain penetrating through the remaining defect area of slider is the sum of the corresponding fractions of impinging rain over the wind direction octants  $\theta_n$  as the storm rotates from  $t_{Vmax}$  to its end. Similarly, the total value of surface run-off penetrating through the remaining defects of slider is the sum of the corresponding fractions of surface runoff water over the wind direction octants  $\theta_n$  as the storm rotates from  $t_{Vmax}$  to its end. Equations 6 and 7 illustrate the estimate of  $V_{DI2}$  and  $V_{SR2}$ .

$$V_{DI2} = \left[ \sum_{n=1}^5 RAF_{\theta_n} \cdot \beta_n(V_{max}) \right] \cdot WDR_2(V_{max}) \cdot A_d \cdot survival \quad (6)$$

$$V_{SR2} = \left[ \sum_{n=1}^5 SRC_{\theta_n} \cdot \beta_n(V_{max}) \cdot A_{SR_{\theta_n}} \right] \cdot WDR_2(V_{max}) \cdot survival \quad (7)$$

where, *survival* is the survival function = 1 – damage ratio of slider.

## **Methodology**

### ***Introduction***

To compare the outputs of the 2021 FDEM-funded WoW tests to the FPHLM estimates, the FPHLM research team produced two parameters from the model including WDR rates and water penetration rates through the defects of a slider. The WDR rate is the amount of accumulated wind-driven rain water per unit time. The water penetration rate is the amount of water intrusion through a slider per unit time, and per unit of effective area of the slider, as defined in above. These parameters are compared against the results of the WoW test in next Chapter.

### ***Storm Duration Evaluation***

As introduced in section FPHLM - Rain Hazard Model and section FPHLM - Non-breach Related Leakage Paths, the rotation and time history of a hurricane event are embedded in the vulnerability model with the  $\alpha$ 's and  $\beta$ 's derived from the rain hazard model. To deal with the uncertainty of wind direction and building orientation, the vulnerability model loops over the wind direction of the maximum wind speed and estimates the amount of accumulated wind-driven rain for each octant with Equations 2 and 3.

To calculate the WDR rate and water penetration rate, the total storm duration and the duration of the storm per each octant are required. The FPHLM research team updated the rain hazard

model and extracted the combination of maximum 3-sec gust wind speed at 10 meters height (WS) in mph, direction of maximum wind speed (WD) from 1 to 8 representing 0° to 315° with a 45° interval, the amount of accumulated WDR ( $V_{\alpha i}$  or  $V_{\beta i}$ ) in inches, and the duration ( $t_{\alpha i}$  or  $t_{\beta i}$ ) in hour for all stations and hurricane simulations. There are 2,104,191 simulations in total. Table 2 shows a part of the results. Table 3 shows the mean time for each octant and the entire hurricane event as a function of maximum wind speed. Note that what is not shown in this table is that the wind speeds for each octant are different.

Table 2. Example of accumulated WDR and duration of all octants

Simulation number	35	36	37	38	39	40	41
<b>WS</b>	54	52	50	52	58	61	62
<b>WD</b>	5	5	5	8	8	8	7
<b><math>V_{\alpha 1}</math></b>	0.49	0.45	0.41	1.22	1.26	1.81	3.69
<b><math>V_{\alpha 2}</math></b>	0.51	0.44	0.38	4.23	4.47	4.43	2.26
<b><math>V_{\alpha 3}</math></b>	0.00	0.00	0.00	0.96	1.33	0.00	0.00
<b><math>V_{\alpha 4}</math></b>	0.00	0.00	0.00	0.00	0.00	0.00	0.00
<b><math>V_{\beta 1}</math></b>	0.45	0.41	0.38	0.98	0.97	0.93	1.07
<b><math>V_{\beta 2}</math></b>	0.53	0.46	0.39	2.58	2.51	1.57	0.99
<b><math>V_{\beta 3}</math></b>	0.00	0.00	0.00	1.60	2.23	3.42	1.45
<b><math>V_{\beta 4}</math></b>	0.00	0.00	0.00	0.00	0.00	1.28	4.11
<b><math>V_{\beta 5}</math></b>	0.00	0.00	0.00	0.00	0.00	0.00	0.00
<b><math>t_{\alpha 1}</math></b>	4.3	4.5	4.7	3.5	2.7	0.6	32.9
<b><math>t_{\alpha 2}</math></b>	4.5	4.2	3.9	31.2	32.1	32.9	0.0
<b><math>t_{\alpha 3}</math></b>	0.0	0.0	0.0	0.0	0.0	0.0	0.0
<b><math>t_{\alpha 4}</math></b>	0.0	0.0	0.0	0.0	0.0	0.0	0.0
<b><math>t_{\beta 1}</math></b>	0.1	0.1	0.1	0.4	0.4	1.8	0.9
<b><math>t_{\beta 2}</math></b>	4.4	4.7	4.9	4.0	3.2	2.3	1.5
<b><math>t_{\beta 3}</math></b>	4.6	4.1	3.8	31.2	32.1	33.0	1.6
<b><math>t_{\beta 4}</math></b>	0.0	0.0	0.0	0.0	0.0	0.0	33.8
<b><math>t_{\beta 5}</math></b>	0.0	0.0	0.0	0.0	0.0	0.0	0.0

Table 3. Mean time for each octant and entire hurricane as a function of WS

WS	$t_{\alpha 4}$	$t_{\alpha 3}$	$t_{\alpha 2}$	$t_{\alpha 1}$	$t_{\beta 1}$	$t_{\beta 2}$	$t_{\beta 3}$	$t_{\beta 4}$	$t_{\beta 5}$	sum
50	0.00	0.56	17.71	5.93	1.64	7.18	17.37	0.48	0.11	50.97
55	0.00	0.63	18.30	5.62	1.46	6.43	17.99	0.78	0.18	51.40
60	0.00	0.71	18.62	5.54	1.27	5.60	18.37	1.33	0.32	51.77
65	0.01	0.79	18.41	5.92	1.12	4.88	18.22	2.19	0.55	52.10
70	0.02	0.86	17.79	6.64	1.03	4.27	17.67	3.28	0.84	52.39
75	0.03	0.89	16.73	7.70	0.97	3.72	16.70	4.57	1.21	52.51
80	0.04	0.89	15.41	8.97	0.96	3.24	15.46	5.98	1.61	52.55
85	0.04	0.85	14.03	10.29	0.98	2.85	14.17	7.37	1.99	52.56
90	0.04	0.82	12.86	11.34	0.98	2.57	13.07	8.41	2.33	52.42

95	0.04	0.80	11.69	12.40	1.03	2.37	11.95	9.49	2.60	52.39
100	0.05	0.80	10.71	13.32	1.08	2.23	11.02	10.36	2.86	52.42
105	0.06	0.84	10.03	13.83	1.10	2.18	10.36	10.88	2.99	52.28
110	0.06	0.95	9.41	14.14	1.10	2.20	9.75	11.09	3.18	51.87
115	0.06	1.14	8.96	14.33	1.10	2.31	9.28	11.19	3.31	51.69
120	0.06	1.33	8.86	14.30	1.08	2.47	9.16	11.13	3.34	51.73
125	0.08	1.70	8.64	14.05	1.08	2.77	8.88	10.81	3.40	51.40
130	0.05	1.93	8.84	13.56	1.01	2.96	9.05	10.30	3.40	51.10

### ***WDR Rates from Rain Hazard Model***

After the storm duration evaluation, the FPHLM research team calculated the WDR rate of each octant for each simulation, which is defined as  $V_{\alpha i}$  or  $V_{\beta j}$  divided by  $t_{\alpha i}$  or  $t_{\beta j}$ , and derived the mean WDR rate as a function of WS. Figure 4 displays the mean WDR rates for octant  $\alpha 1$ ,  $\beta 1$  and the mean WDR rate of the combination of  $\alpha 1$  and  $\beta 1$  which is the sum of  $V_{\alpha 1}$  and  $V_{\beta 1}$  divided by the sum of  $t_{\alpha 1}$  and  $t_{\beta 1}$ . In octant  $\alpha 1$  and  $\beta 1$  the wind direction is 0 degree of  $V_{max}$  and the wind speed is equal to  $V_{max}$  (see Figure 3). Note the WDR rate is not uniform in the model as it is not in nature.

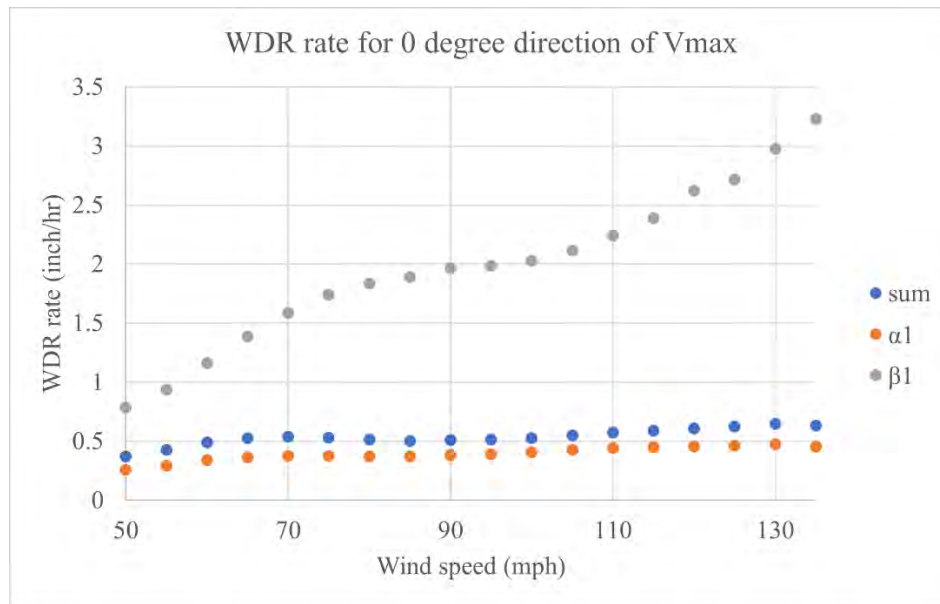


Figure 4. WDR rate for 0 degree direction of  $V_{max}$

### ***Water Penetration Rates from the FPHLM***

To produce comparable water penetration rates against the mean  $RR_{b, tot}$  from FDEM-funded WoW test, the FPHLM research team derived the total volume of water intrusion through defects of a slider for octant  $\alpha 1$  and  $\beta 1$  given the direction of  $V_{max}$  perpendicular to the façade of the building as well as  $45^\circ$  to the building façade. Equations 4 to 7 illustrates the estimation of the water intrusion in FPHLM. The selection of the direction of  $V_{max}$  and octants makes it convenient

to obtain matched combinations of wind speed, wind direction and water penetration rates to the values in Table 1 without a big change of the vulnerability model.

The  $V_{max}$  in FPHLM as an input parameter is the 3-sec gust wind speed at 10 meters height (around 3-story height), while the wind speed in Table 1 is 3-sec gust wind speed at the slider height (note: it is not clear to the FHPLM team is the WoW reported wind speed is the actual wind speed at the slider height or at the COBRA probe. If it is the later an additional adjustment is needed). A correction factor  $f_{log}$  is necessary to account for wind variation with story height, in the FPHLM model. The variation of wind speed with story height is calculated based on a log-law:

$$f_{log}(z) = \frac{\ln(\frac{z}{z_0})}{\ln(\frac{10}{z_0})} \quad (8)$$

where,  $z$  is the story height in meters. Each story is defined as 3.33 m in FPHLM.  $z_0$  is the roughness factor defined as 0.45 m in FPHLM.

The 1-story low-rise building (LR) model of FPHLM has sliders on the first floor. In order to obtain the amount of water intrusion at 65 mph, 100 mph, and 130 mph on the first floor,  $V_{max}$  is defined as 80 mph, 125 mph, and 160 mph respectively in the LR model. The mid/high-rise building (MHR) model has sliders on every story. The water intrusion of the selected combination of story number and  $V_{max}$  is derived with the MHR model resulting in the mean volume of water intrusion for each combination of wind speed and wind direction. Table 4 shows the combinations of targeted wind speed on the first floor, story number of the apartment unit, and  $V_{max}$ . So, for example, in the case of a  $V_{max} = 55$  mph at 10 m, units on the 9<sup>th</sup> floor will experience actual winds of 65 mph.

Table 4. Combinations of targeted wind speed,  $V_{max}$ , and story number

Targeted wind speed (mph)	$V_{max}$ (mph)	Story number
65	55	9
65	60	5
65	65	3
65	70	2
100	85	8
100	90	6
100	95	4
100	100	3
130	110	9
130	115	7
130	120	5
130	125	4
130	130	3
130	140	2

After the total volume of water intrusion of octant  $\alpha_1$  and  $\beta_1$ ,  $V_{\alpha_1\beta_1}$ , is available, the FPHLM research team calculated the water penetration rates,  $WPR$ , for each combination of wind speed and wind direction as:

$$WPR = \frac{V_{\alpha_1\beta_1}}{(t_{\alpha_1} + t_{\beta_1}) \cdot A_e} \quad (9)$$

## Results and Discussion

### *Comparison of WDR Rates*

USGS (2019) provides common horizontal rain rates ( $RR_h$ ) for very heavy rain and violent shower as 0.315 in/hr (8 mm/hr) and 1.969 in/hr (50 mm/hr) respectively. Pita et al. (2012) provided equations to convert  $RR_h$  to vertical rain rates ( $RR_v$ ), which we refer to as WDR rates in this report. These equations would yield the WDR shown in **Error! Reference source not found.**. The WDR rates can vary dramatically based on  $RR_h$  in nature.

Table 5. WDR rates given WS and RR

WS (mph)	RR <sub>h</sub> (in/hr)	
	0.315	1.969
60	1.29	8.061
65	1.83	8.681

Baheru et al. (2014,a) proposed wind-driven rain rates for a range of wind speeds shown in Figure 5, assuming a  $RR_h$  equal to 1 in/hr, which is between the range of Table 6.

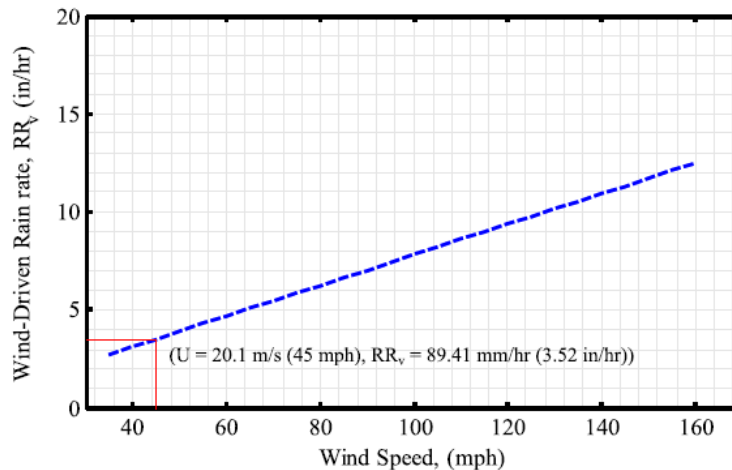


Figure 5. WDR rates as a function of wind speed from Baheru et al. (2014, a)

Table 6 shows the combinations of wind speed and WDR rates from subsequent WoW tests. Table 5 shows WDR rates for information purposes. They are not directly comparable since the scale of the different tests were not the same. The FPHLM team needs more input from the WoW team to understand how to bring these different rates to the same scale. It is understood

that the slider test WDR rate is a full-scale rate. However, it does not coincide with the proposed relationship in Figure 5.

Table 6. Combinations of wind speed and WDR rate measured in previous WoW tests

WoW test	Scale	Wind speed (mph)	WDR rate (inch/hr)
Baheru et al., 2014 b	1/4	59.28	14.80
Raji, 2018	1/4	30.00	3.39
FDEM-funded test	1	65	9.3

Figure 4 provide the mean WDR rates for octants  $\alpha_1$  and  $\beta_1$ , as well as the mean WDR rate for the combination of  $\alpha_1$  and  $\beta_1$ . Table 7 shows the WDR rates given wind speed equal to 60 mph and 65 mph.

Table 7. Combinations of wind speed and WDR rate from the rain model

Wind speed (mph)	WDR rate for $\alpha_1$ (inch/hr)	WDR rate for $\beta_1$ (inch/hr)	Combined WDR rate (inch/hr)
60	0.34	1.16	0.49
65	0.36	1.39	0.53

The comparison between WDR rates in Table 6 and **Error! Reference source not found.** i indicates that the WDR rate for the WoW slider tests are much higher than those from the FPHLM rain hazard model which hinders the comparisons between test and model results. In addition, the WDR rate in the model is not uniform as it is not in nature. In other words, all these facts and statistics need to inform the comparisons.

### ***Comparison of Water Penetration Rates***

This section compares the water penetration rates (WPR) from the commercial residential low-rise (CR-LR) and mid/high-rise (CR-MHR) models against the results from FDEM-funded WoW test separately.

For the CR-LR model, the FPHLM research team produced the results for the building classes with the combinations of factors: 1-story or 3-story, timber or masonry, weak model or strong model, with or without shutter. Figure 6 to Figure 14 show these comparisons. The comparison indicates that WPR from the WoW test is close to nothing for 65 mph wind speed, which is obviously smaller than the FPHLM WPR. On the contrary, when the wind speeds are 100 mph and 130 mph, the WPR from the WoW test are consistently much higher than that from the model.

It is difficult to interpret these comparisons, since the WDR rate from the model is much lower than that from the WoW test, which probably explains the large differences between FPHLM and tests at high wind speeds. In addition, the existence of shutters does not impact the FPHLM WPR. The CR-LR model does not take into account the effect of the shutter for the estimation of water intrusion through slider defects. Finally, there are differences in the CR-LR models in WPR, based on strength of the model, which take into account quality and age of the building. The strong model has less water intrusion through slider defect compared to the weak model.

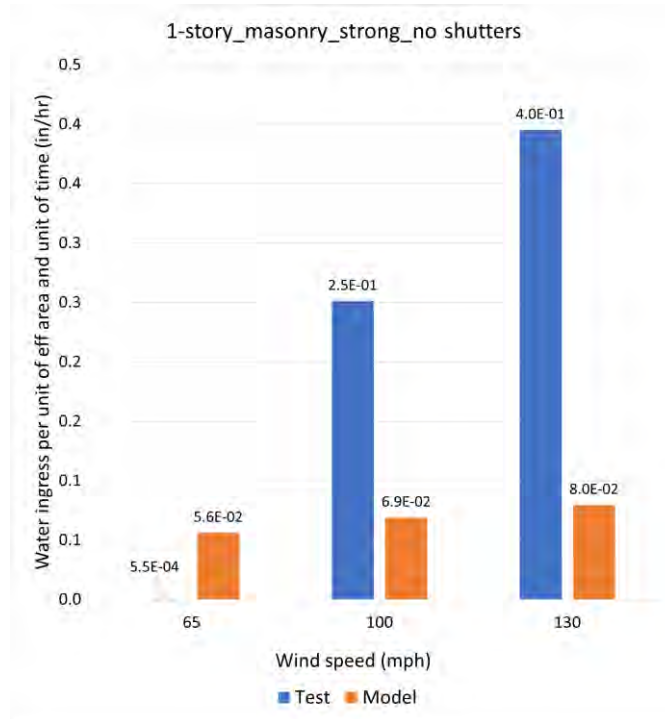


Figure 6. Comparison between WPR from WoW test and WPR from FPHLM for 1-story masonry building without shutter in strong model at 0° wind direction

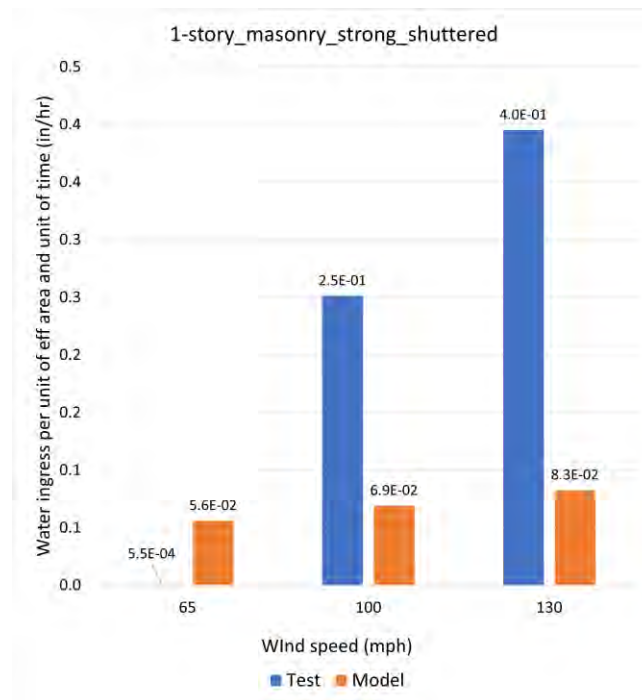


Figure 7. Comparison between WPR from WoW test and WPR from FPHLM for 1-story masonry building with shutter in strong model at 0° wind direction

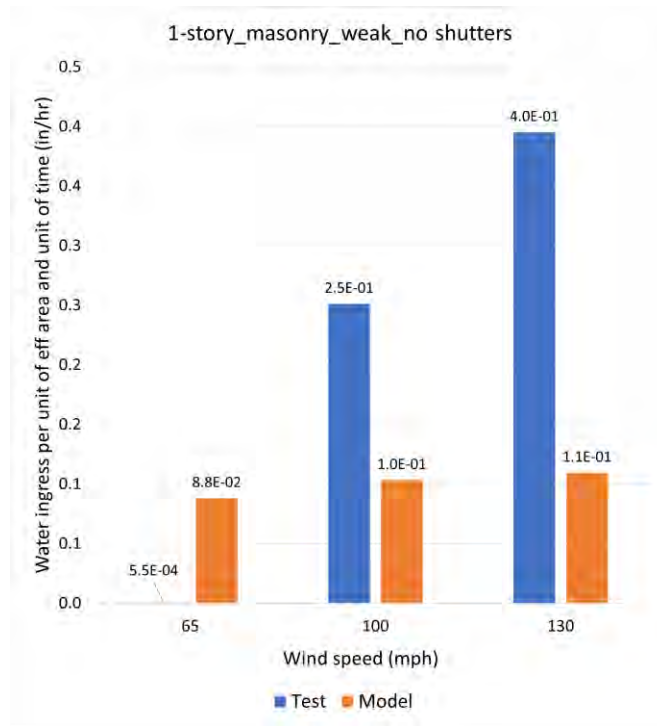


Figure 8. Comparison between WPR from WoW test and WPR from FPHLM for 1-story masonry building without shutter in weak model at 0° wind direction

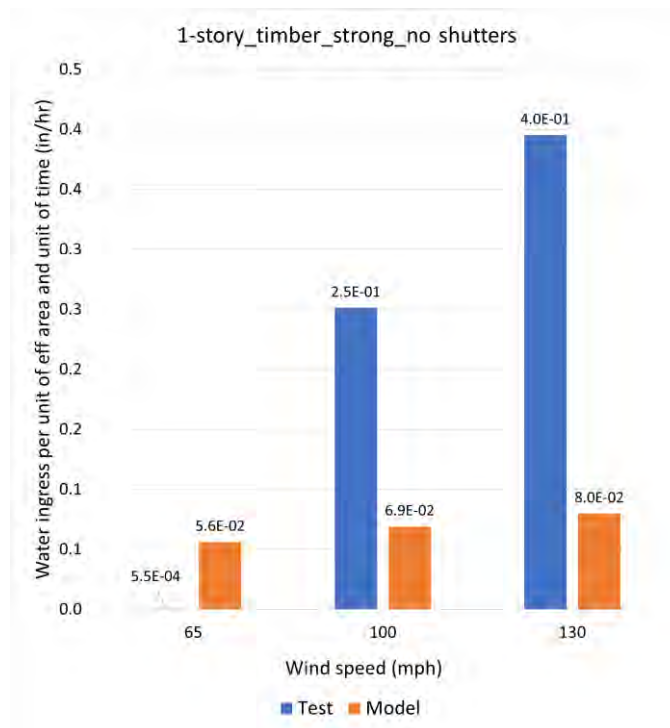


Figure 9. Comparison between WPR from WoW test and WPR from FPHLM for 1-story timber building without shutter in strong model at 0° wind direction



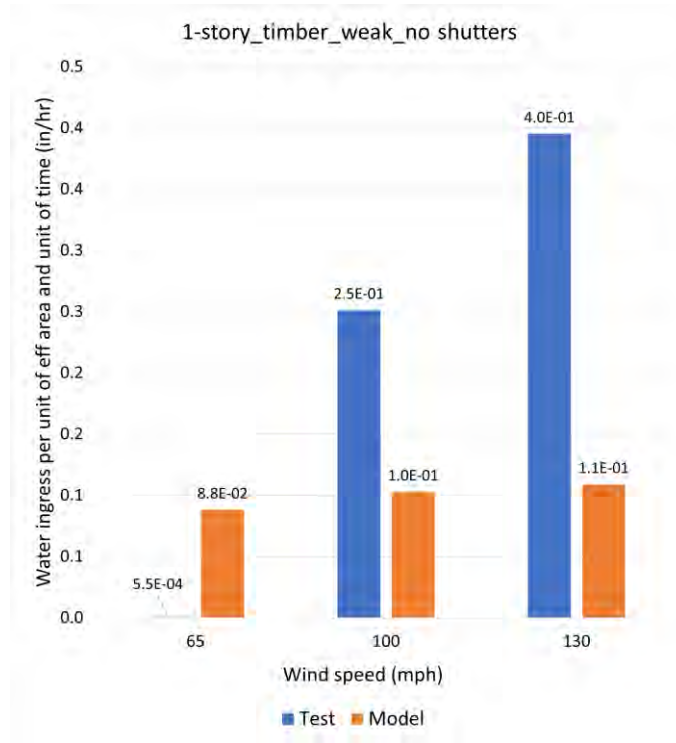


Figure 10. Comparison between WPR from WoW test and WPR from FPHLM for 1-story timber building without shutter in weak model at 0° wind direction

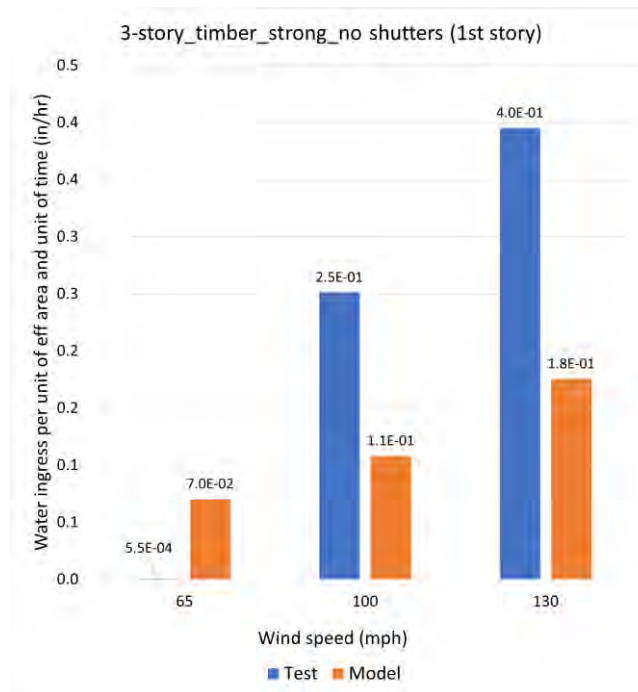


Figure 11. Comparison between WPR from WoW test and WPR from FPHLM for 3-story timber building without shutter in strong model at 0° wind direction on the first story

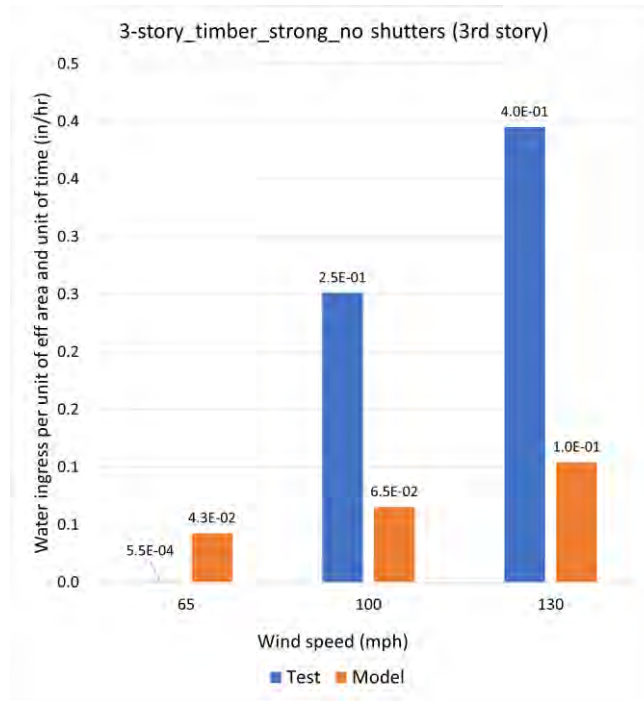


Figure 12. Comparison between WPR from WoW test and WPR from FPHLM for 3-story timber building without shutter in strong model at 0° wind direction on the third story

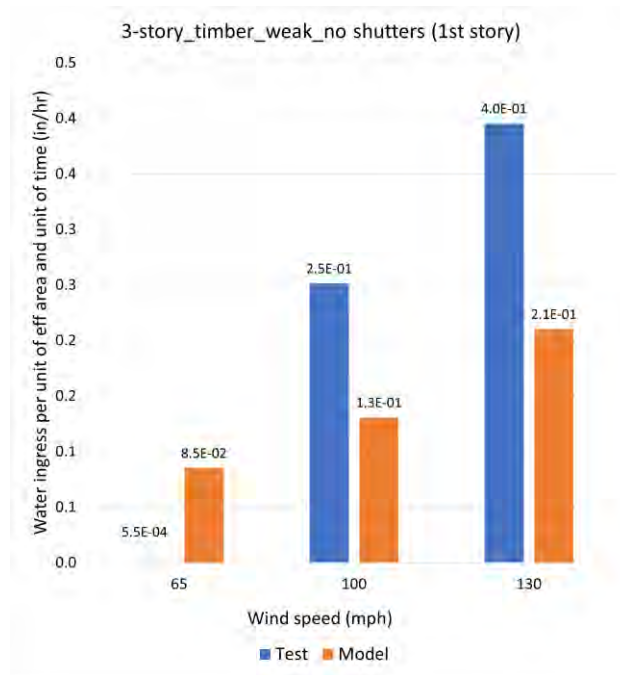


Figure 13. Comparison between WPR from WoW test and WPR from FPHLM for 3-story timber building without shutter in weak model at 0° wind direction on the first story

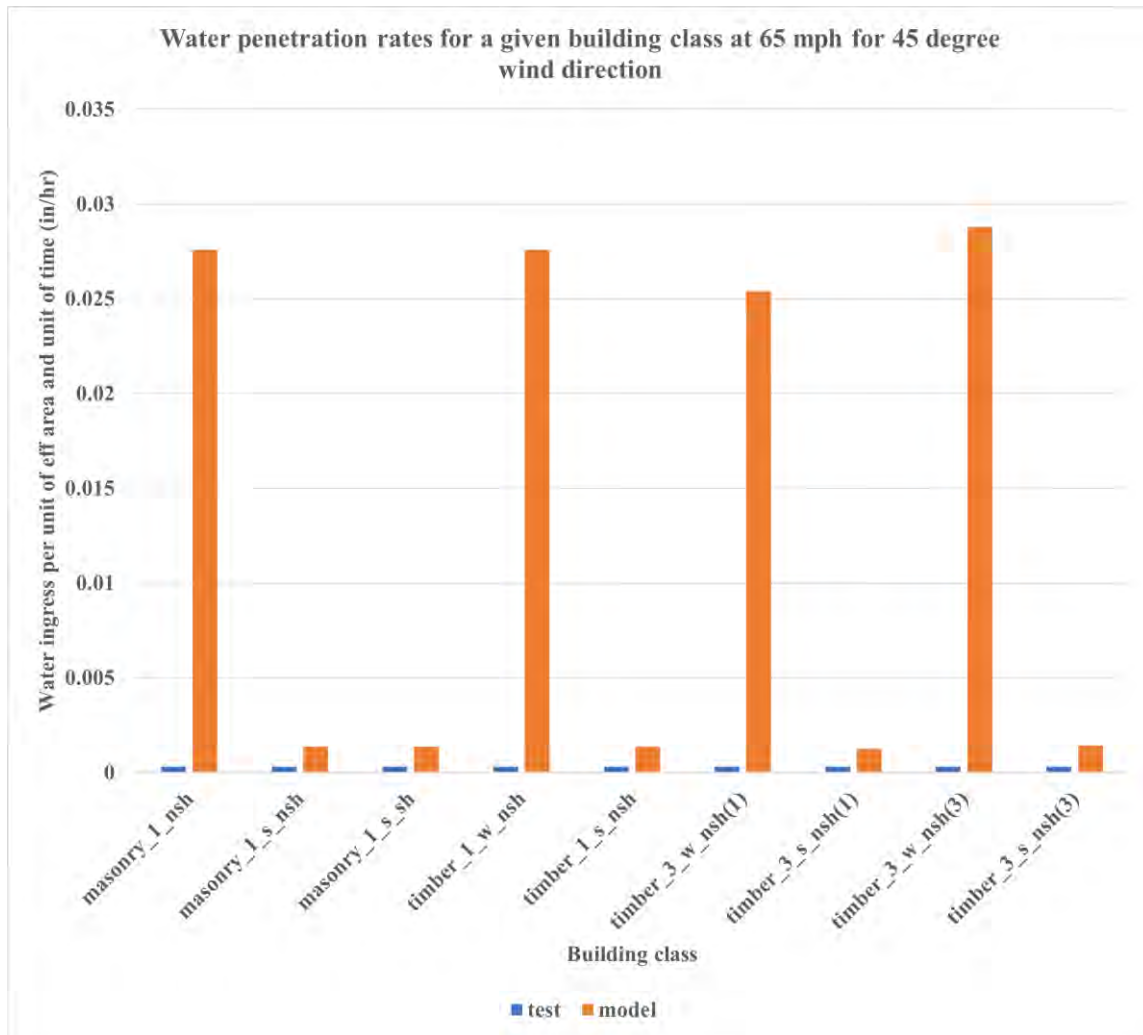


Figure 14. Comparison between WPR from WoW test and from FPHLM at 65 mph for 45° wind direction\*

\*Legend explanation: timber/masonry\_1-story/3-story building\_weak/strong model\_no shutter/shutter. (1) means the value for 1-st story and (3) means the value for 3-rd story.

For the CR-MHR model, the FPHLM research team produced WPR for building classes with the combinations of the following factors: 5-story or 10-story building, and with or without shutter. Figure 15 to Figure 18 show these comparisons. The conclusions are similar to the CR-LR model: the model estimates higher water intrusion through slider defects at low wind speed but estimates lower water intrusion through slider defects at high wind speed. The main difference compared to LR model is that, all other things being equal, a unit in the same story but in a taller buildings has more water intrusion than a unit in the same story but in a shorter building. According to Equation 5 and 7, the taller building has a greater surface runoff area for slider (more stories upstream).

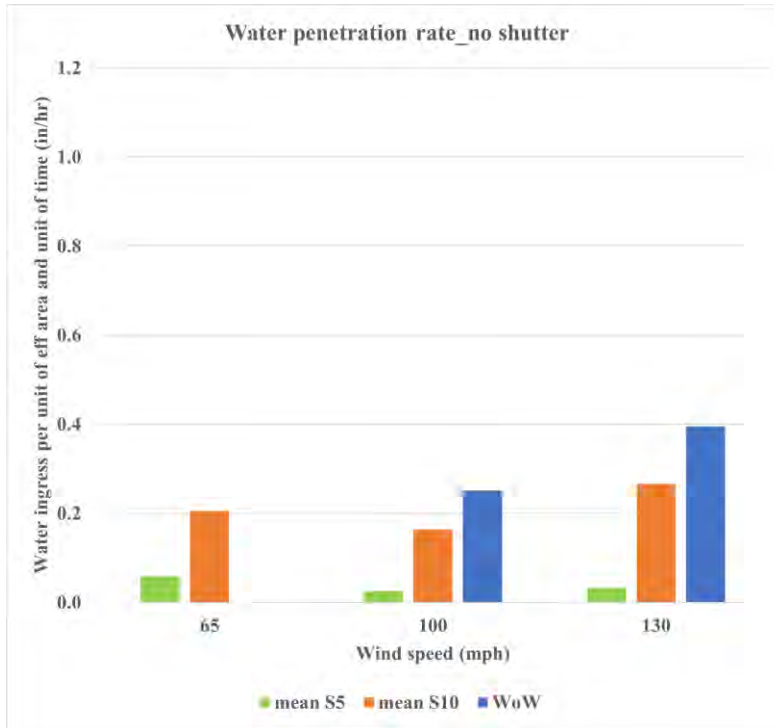


Figure 15. Comparison between WPR from WoW test and WPR from FPHLM for 5-story and 10-story building without shutter at 0° wind direction

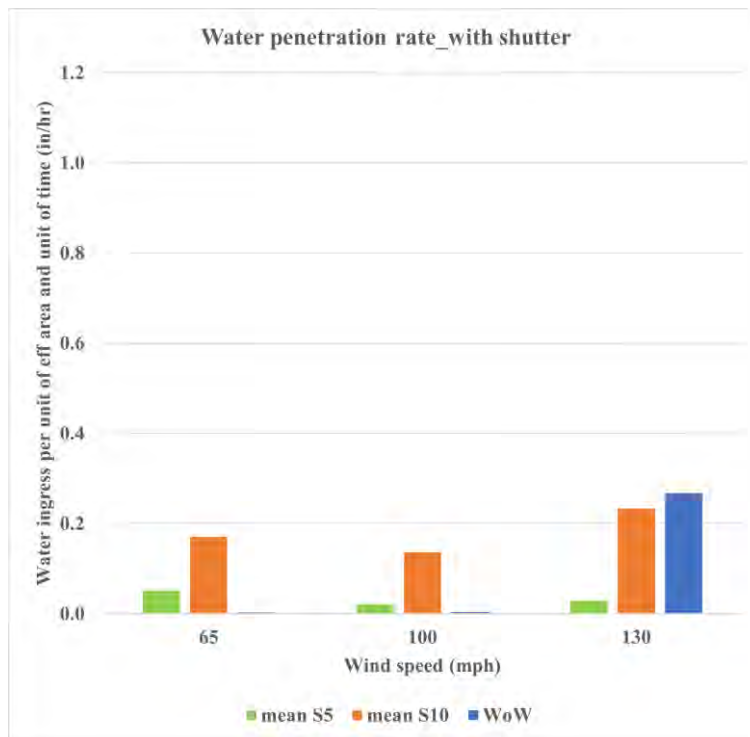


Figure 16. Comparison between WPR from WoW test and WPR from FPHLM for 5-story and 10-story building with shutter at 0° wind direction

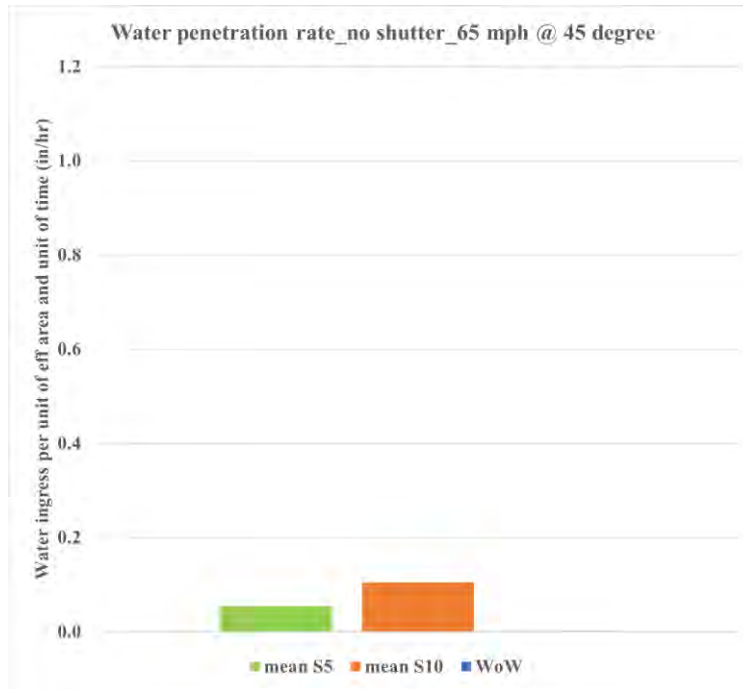


Figure 17. Comparison between WPR from WoW test and WPR from FPHLM for 5-story and 10-story building without shutter in 65 mph at 45° wind direction

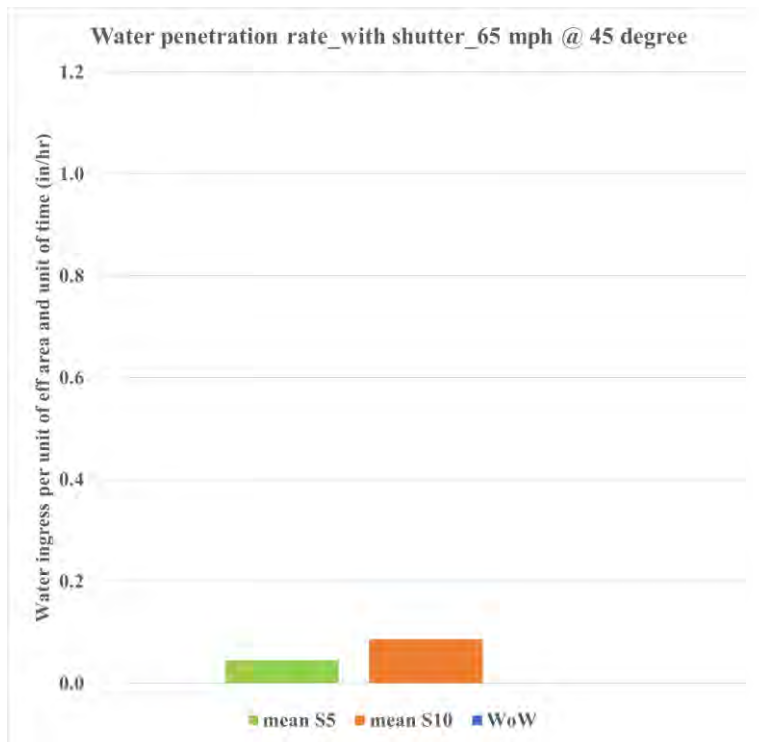


Figure 18. Comparison between WPR from WoW test and WPR from FPHLM for 5-story and 10-story building with shutter in 65 mph at 45° wind direction

## **Conclusions**

### ***Summary***

The FPHLM team calculated hurricane durations and accumulated wind-driven rain for each wind direction octant and calculated the resulting WDR rates which are compared against the WDR rate used in the WoW tests. The WDR rate from the FPHLM rain hazard model is substantially smaller than the one used in the WoW tests.

The comparisons between the water penetration rates from the vulnerability model of FPHLM and those from the WoW tests indicate that the FPHLM estimates higher water intrusion through slider defects when maximum wind speed is low while estimates lower water intrusion through slider defects when maximum wind speed is high. The later is not surprising given the differences in WDR rates. The other indicates that the model and the tests differ in their quantification of the mechanisms of water penetration at low wind speed.

### ***Recommendations for Further Studies***

More WoW tests could be performed to obtain more data with respect to different wind speed and wind direction, and different defect conditions to reflect different quality and age of components. It would be useful if the tests would use WDR rates similar to the ones modeled in the FPHLM.

In parallel to these efforts, the FPHLM meteorology team is working on a new rain hazard model which might results in better simulations of the rain hazard.

It is worth to investigate further the mechanism of the impact of wind speed and wind pressure on the water penetration through defect area. The defect area might increase with the increase of wind speed and wind pressure.

## **References**

- Aly, A. M., Chowdhury, A. G., & Bitsuamlak, G. (2011). Wind profile management and blockage assessment for a new 12-fan Wall of Wind facility at FIU. *Wind & Structures*, 14(4), 285-300.
- Baheru, T., Chowdhury, A. G., Bitsuamlak, G., Masters, F. J., & Tokay, A. (2014, a). Simulation of wind-driven rain associated with tropical storms and hurricanes using the 12-fan Wall of Wind. *Building and Environment*, 76, 18-29.
- Baheru, T., Chowdhury, A. G., Pinelli, J. P., & Bitsuamlak, G. (2014, b). Distribution of wind-driven rain deposition on low-rise buildings: Direct impinging raindrops versus surface runoff. *Journal of Wind Engineering and Industrial Aerodynamics*, 133, 27-38.
- Baheru, T., Chowdhury, A. G., & Pinelli, J. P. (2015). Estimation of wind-driven rain intrusion through building envelope defects and breaches during tropical cyclones. *Natural Hazards Review*, 16(2), 04014023.
- Chowdhury, A. G., Bitsuamlak, G. T., Fu, T. C., & Kawade, P. (2011). Study on roof vents subjected to simulated hurricane effects. *Natural Hazards Review*, 12(4), 158-165.
- Gan Chowdhury, A., Zisis, I., Irwin, P., Bitsuamlak, G., Pinelli, J. P., Hajra, B., & Moravej, M. (2017). Large-scale experimentation using the 12-fan wall of wind to assess and mitigate hurricane wind and rain impacts on buildings and infrastructure systems. *Journal of Structural Engineering*, 143(7), 04017053.

- Eamon, C. D., Fitzpatrick, P., & Truax, D. D. (2007). Observations of structural damage caused by Hurricane Katrina on the Mississippi Gulf Coast. *Journal of Performance of Constructed Facilities*, 21(2), 117-127.
- Johnson, T., Pinelli, J. P., Baheru, T., Chowdhury, A. G., Weekes, J., & Gurley, K. (2018). Simulation of rain penetration and associated damage in buildings within a hurricane vulnerability model. *Natural Hazards Review*, 19(2), 04018004.
- Kennedy, A., Copp, A., Florence, M., Gradel, A., Gurley, K., Janssen, M., ... & Silver, Z. (2020). Hurricane Michael in the area of Mexico Beach, Florida. *Journal of Waterway, Port, Coastal, and Ocean Engineering*, 146(5).
- Mileti, D. (1999). *Disasters by design: A reassessment of natural hazards in the United States*. Joseph Henry Press.
- Mullens, M., Hoekstra, B., Nahmens, I., & Martinez, F. (2006). Water intrusion in central Florida homes during Hurricane Jeanne in September 2004. *UCF Housing Constructability Lab*, Orlando.
- Pinelli, J. P., Roueche, D., Kijewski-Correa, T., Plaz, F., Prevatt, D., Zisis, I., Elawady, A., Haan, F. Pei, S., Gurley, K. & Rasouli, A. (2018). Overview of damage observed in regional construction during the passage of Hurricane Irma over the state of Florida. *Proc., ASCE Forensic*, 18.
- Pita, G., Pinelli, J. P., Cocke, S., Gurley, K., Mitrani-Reiser, J., Weekes, J., & Hamid, S. (2012). Assessment of hurricane-induced internal damage to low-rise buildings in the Florida Public Hurricane Loss Model. *Journal of wind engineering and industrial aerodynamics*, 104, 76-87.
- Pita, G. L. (2012). Hurricane vulnerability of commercial-residential buildings (Vol. 73, No. 289, p. 2012).
- Pita, G. L., Pinelli, J. P., Gurley, K., Weekes, J., Cocke, S., & Hamid, S. (2016). Hurricane vulnerability model for mid/high-rise residential buildings. *Wind and Structures*, 23(5), 449-464.
- Raji, F. (2018). Interior damage of residential building due to wind-driven rain intrusion.
- Raji, F., Zisis, I., & Pinelli, J. P. (2019, September). Intrusion and propagation of hurricane induced rain water in building interior. *In Proc., 15th Int. Conf. on Wind Engineering. Kanagawa, Japan: International Association for Wind Engineering*.
- Raji, F., Zisis, I., & Pinelli, J. P. (2020). Forthcoming "A wind tunnel study to quantify the wind-driven rain propagation in the interior of residential structures,". *ASCE Journal of Structural Engineering*, 146(7).
- USGS. (2019) Rainfall calculator, metric units How much water falls during a storm?. <https://water.usgs.gov/edu/activity-howmuchrain-metric.html#:~:text=Slight%20rain%3A%20Less%20than%200.5,than%208%20mm%20per%20hour> : retrieved 07/25/2022



*A Resource for the State of Florida*

***SECTION 6***  
***Education and Outreach Programs to Convey the  
Benefits of Various Hurricane Loss Mitigation Devices  
and Techniques***

A Report Submitted to:  
The State of Florida Division of Emergency Management

*Prepared By:*  
Erik Salna

The International Hurricane Research Center (IHRC)  
Florida International University

July 31, 2022



## **Executive Summary:**

The FIU International Hurricane Research Center developed and coordinated education and outreach activities to build on the foundation of previous work under this grant and showcased the hurricane-loss mitigation objectives of the HLMP.

For the 2021-2022 performance period, the below mentioned educational partnerships, community events, and outreach programs were developed:

### ***Executive Summary:***

#### ***Wall of Wind Mitigation Challenge (WOW! Challenge): Thursday, March 31st, 2022***

(The 2022 competition was done virtually.)

The International Hurricane Research Center (IHRC), located on the campus of Florida International University (FIU), has developed the Wall of Wind Mitigation Challenge (WOW! Challenge), a judged competition for South Florida high school students. As the next generation of engineers to address natural hazards and extreme weather, this STEM education event features a competition between high school teams to develop innovative wind mitigation concepts and real-life human safety and property protection solutions. The mitigation concepts are tested live at the FIU NSF-NHERI Wall of Wind (WOW) Experimental Facility (EF), located on FIU's Engineering Campus.

- The objective for the 2022 Wall of Wind Mitigation Challenge was for students to reduce the wind-induced force on a building's foundation, by optimizing its overall shape.
- The student teams prepared three components for the competition: a physical test, an oral presentation, and a written technical paper.
- The competition included teams from six South Florida high schools.
- *First Place* was awarded to Miami Coral Park Senior High School.  
*Second Place* was awarded to North Miami Senior High School.  
*Third Place* was awarded to G. Holmes Braddock Senior High School.
- A complete scoring summary can be found on the following link:  
[https://www.ihrc.fiu.edu/wp-content/uploads/2022/05/2022\\_WOW\\_CHALLENGE\\_RESULTS\\_SUMMARY.pdf](https://www.ihrc.fiu.edu/wp-content/uploads/2022/05/2022_WOW_CHALLENGE_RESULTS_SUMMARY.pdf)

Media exposure resulted in great positive visibility for the IHRC, FIU and FDEM's message of mitigation:

- NSF-NHERI DesignSafe News: <https://www.designsafe-ci.org/community/news/2022/june/fiu-wall-wind-mitigation-challenge-inspires-next-gen-engineers/>

#### ***Eye of the Storm (Science, Mitigation & Preparedness) In-Person Event: May 14th, 2022***

The Museum of Discovery & Science (MODS), located in Fort Lauderdale, FL, assisted the IHRC in planning, coordinating and facilitating this free admission public education event that showcased special hands-on, interactive activities and demonstrations teaching hurricane science, mitigation and preparedness.

- A record 3,897 visitors attended Eye of the Storm, showcasing special interactive activities and demonstrations teaching hurricane science, mitigation and preparedness.

- A Participant Post Survey showed 86% of respondents increased their knowledge about wind engineering and mitigating hurricane damage and 90% will be taking steps to mitigate hurricane damage.
- Media Release and Flyer: [2022 Eye of the Storm – Hurricane \(Science, Mitigation & Preparedness\) Free Museum Event, Saturday, May 14th, 10am to 5pm | IHRC Website \(fiu.edu\)](#)

Special Guests:

- Grant Goodwin, HLMP Program Manager, Florida Division of Emergency Management
- Dana McGeehan, Region 7 Recovery Coordinator, Florida Division of Emergency Management

Media exposure resulted in great positive visibility in the community for the IHRC, FIU and FDEM's message of mitigation.

- [FIU News Website "University helps community prepare for hurricane season,"](#) June 7, 2021.

***NOAA Hurricane Awareness Tour: IHRC did not participate because there was not a Florida city on this year's tour. The tour conducted two events near Washington D.C. and in New York City.***

***Get Ready, America! The National Hurricane Survival Initiative: Cancelled due to lack of sponsorships.***

## **Education and Outreach Programs:**

***Wall of Wind Mitigation Challenge (WOW! Challenge): Thursday, March 31st, 2022***

### Overview of Wall of Wind Mitigation Challenge:

The International Hurricane Research Center (IHRC), located on the campus of Florida International University (FIU), has developed the Wall of Wind Mitigation Challenge (WOW! Challenge), a judged competition for South Florida high school students. As the next generation of engineers to address natural hazards and extreme weather, this STEM education event features a competition between high school teams to develop innovative wind mitigation concepts and real-life human safety and property protection solutions. The student teams prepare three components for the competition: a physical test, an oral presentation, and a written technical paper. The mitigation concepts are tested live at the FIU NSF-NHERI Wall of Wind (WOW) Experimental Facility (EF), located on FIU's Engineering Campus.

The WOW! Challenge requires problem solving, teamwork, and creativity, and it includes aspects of science, technology, engineering, mathematics, architectural design, and business entrepreneurship. The high school students are inspired to pursue STEM education and careers in wind engineering and hurricane mitigation. The competition has real world applications and benefits society as a whole by developing hurricane mitigation techniques that can lead to enhanced human safety, property loss reduction, insurance cost reduction, and a culture of

hurricane preparedness. There is no other competition like it in the entire country, and it's a once in a lifetime opportunity for the high school students – *an experience they never forget.*

2022 Wall of Wind Mitigation Challenge: (The 2022 competition was done virtually.)

The objective for the 2022 FIU Wall of Wind (WOW) Mitigation Challenge was to reduce the wind-induced force on a building's foundation, by optimizing its overall shape. A schematic diagram of this interaction is shown in Figure 1. Mitigation solutions should demonstrate a sound comprehension of aerodynamic principles. Teams were tasked with developing a mitigation solution to improve a building's aerodynamic performance in order to reduce the reaction forces and moments on a scale model of the building. The mitigation solution could be created by re-shaping an allowable portion of the building model. The goal was to construct a building model that would remain upright, not blown over, to as high a wind speed as possible.

Students prepared three components for the competition: a written technical paper, an oral presentation, and a physical test of a building model. All of the details of the rules and guidelines for the three required components are on the WOW! Challenge web page located at: <http://www.ihrc.fiu.edu/outreach-education/wall-of-wind-challenge/>.

Teams from six South Florida high schools participated in the competition. They were from Booker T. Washington Senior High School, G. Holmes Braddock Senior High School, Jose Marti MAST Academy, Miami Coral Park Senior High School, North Miami Senior High School, and TERRA Environmental Research Institute.

Each school watched their building model get tested live on Zoom by the NSF-NHERI Wall of Wind at FIU to evaluate the effectiveness of the mitigation solution. Here are the recorded Zoom tests:

- [2022 WOW Challenge - Booker T. Washington .mp4](#)
- [2022 WOW Challenge - G HOLMES BRADDOCK .mp4](#)
- [2022 WOW Challenge - Jose Marti MAST 6-12 Academy.mp4](#)
- [2022 WOW Challenge - Coral Park.mp4](#)
- [2022 WOW Challenge - North Miami .mp4](#)
- [2022 WOW Challenge - TERRA Environmental Research Institute.mp4](#)

Each student team was provided \$50 for buying additional materials and supplies, sponsored by DDA Forensics.

Scale Building Model Requirements and Restrictions Described for the Student Teams:

- The building model will be a minimum of 32 inches high (i.e. total height), which includes a gold painted wooden base (8 inches x8 inches x1.5 inches) which will be provided for each team; see Figure 2.
- Above the lowest 1.5 inches of the building model, which is the provided wooden base, and up to at least 30.5 inches above the base, the building model must have a minimum solid (i.e. not porous; no air can pass through) width of 8 inches, or wider; see Figure 2.
- The weight of the building model must be no greater than 40 lbs., including the provided square base. The center of gravity must be directly above the center of the 8 inch square base (+/- 0.5 inches) and must be within +/- 1 inch of the mid-height of the model

building, measured from the bottom of the provided base to the top of the highest element on the building model. See Figure 2.

- Any shape above the lowest 1.5 inches of the provided base can be used as long as it always has a minimum solid width of 8 inches when viewed from any and all directions; see Figure 3 for shape examples.
- All building models will be tested for two wind directions at 90 degrees to each other; see Figure 3 for example wind directions on various shapes. The building model will be prevented from sliding during the Wall of Wind tests by a small 0.75-inch-high stop that will be placed at the back and side edges of the gold base.
- The goal is to have a building model shape that has the least tendency to be blown over by the wind when tested for the two directions at 90 degrees to each other. The wind speed for each of the two directions will be gradually increased until the model blows over. The higher the wind speed at which this happens will result in a higher score for the team.

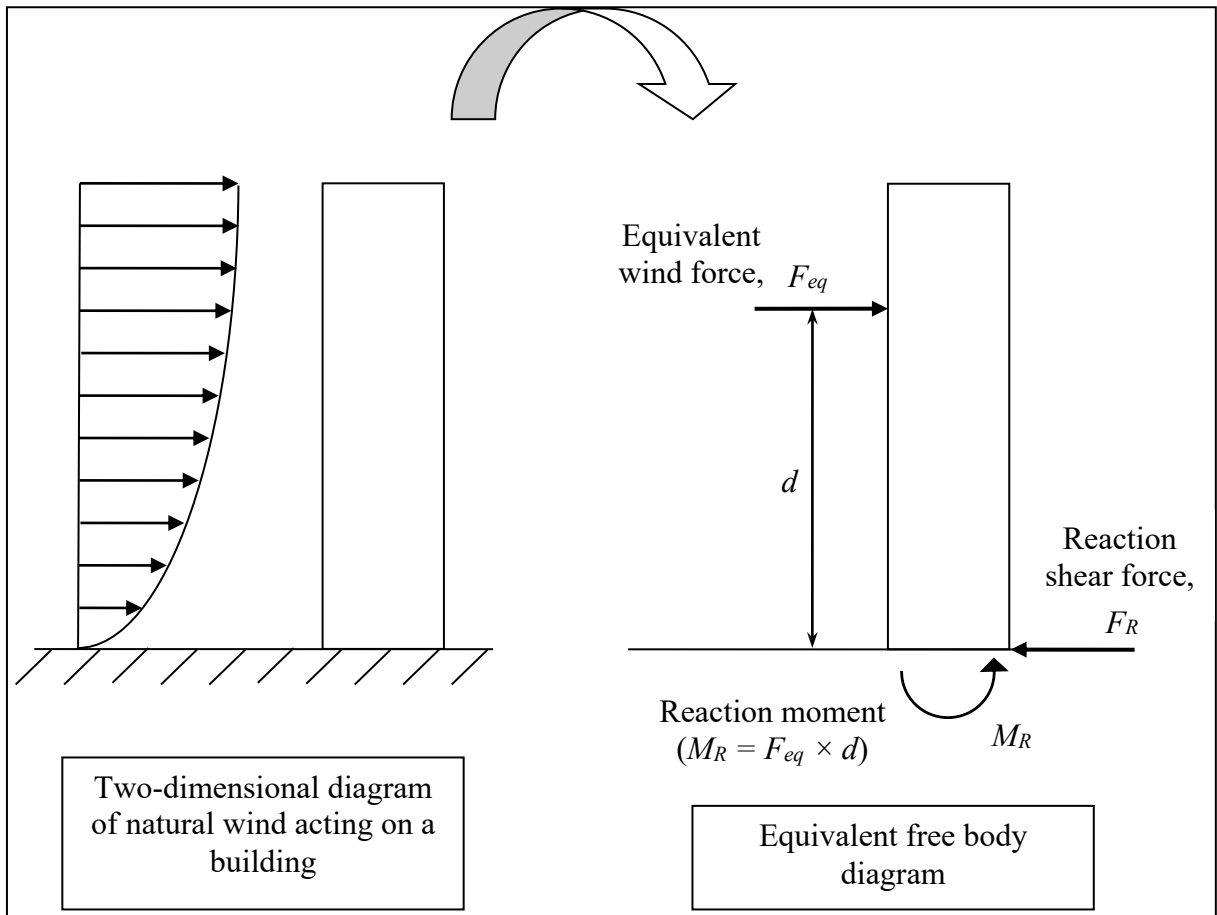
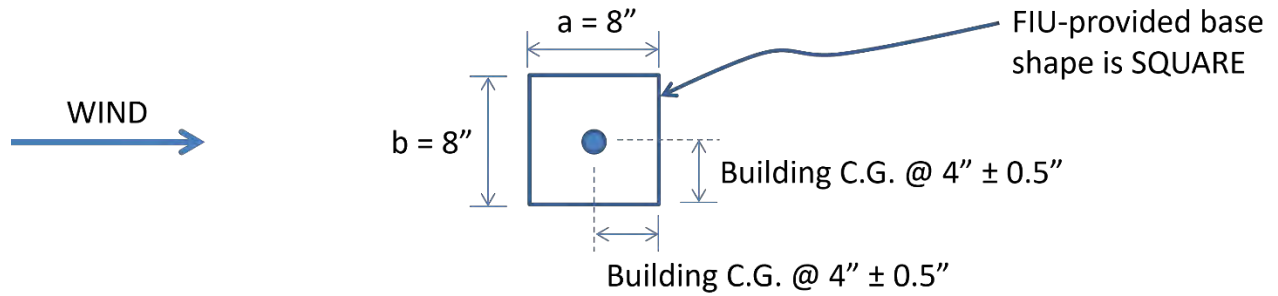
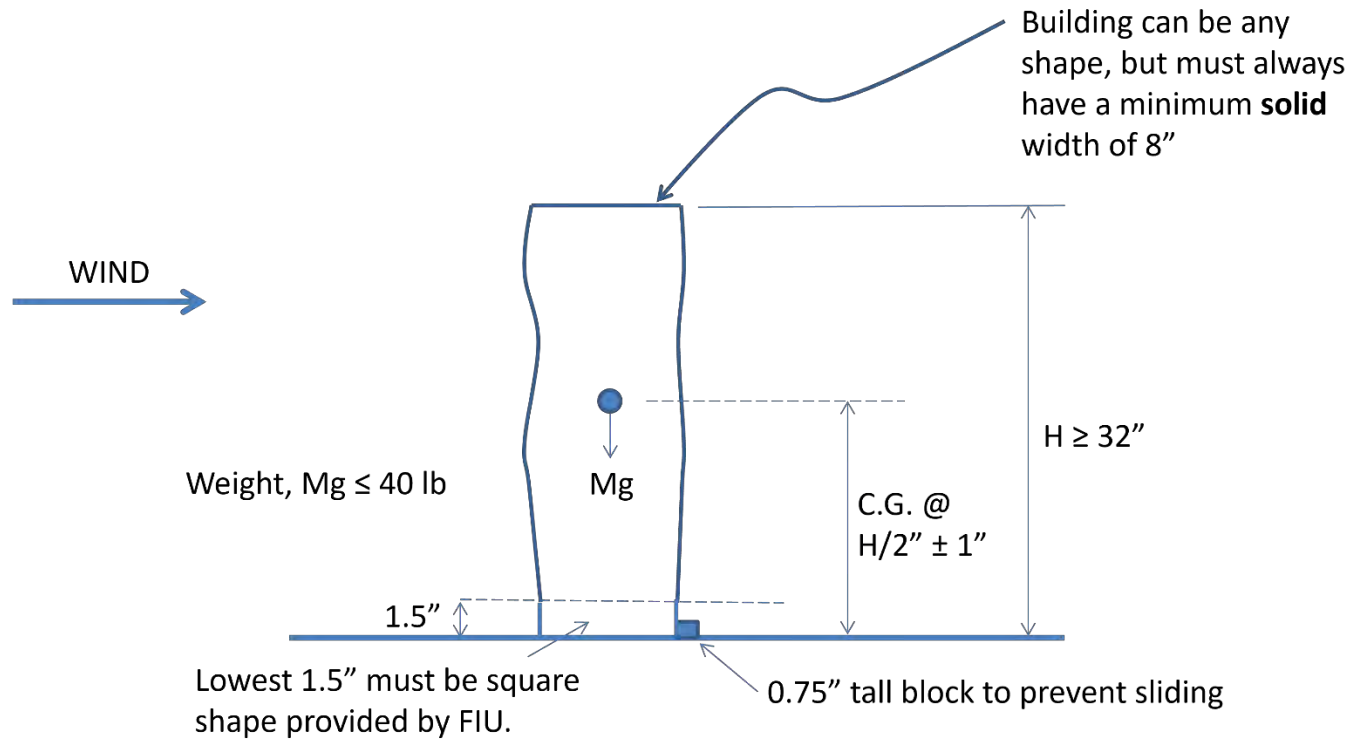


**Figure 1:** Simplified two-dimensional schematic diagram of wind acting on a tall building, and the equivalent free body diagram. Note: across wind forces and moments may also exist, and will act into or out of the building.



**PLAN VIEW**



**ELEVATION VIEW**

**Figure 2:** Schematic diagram of the building model, showing variable shape above the provided square base.

# Examples of cross-section shapes

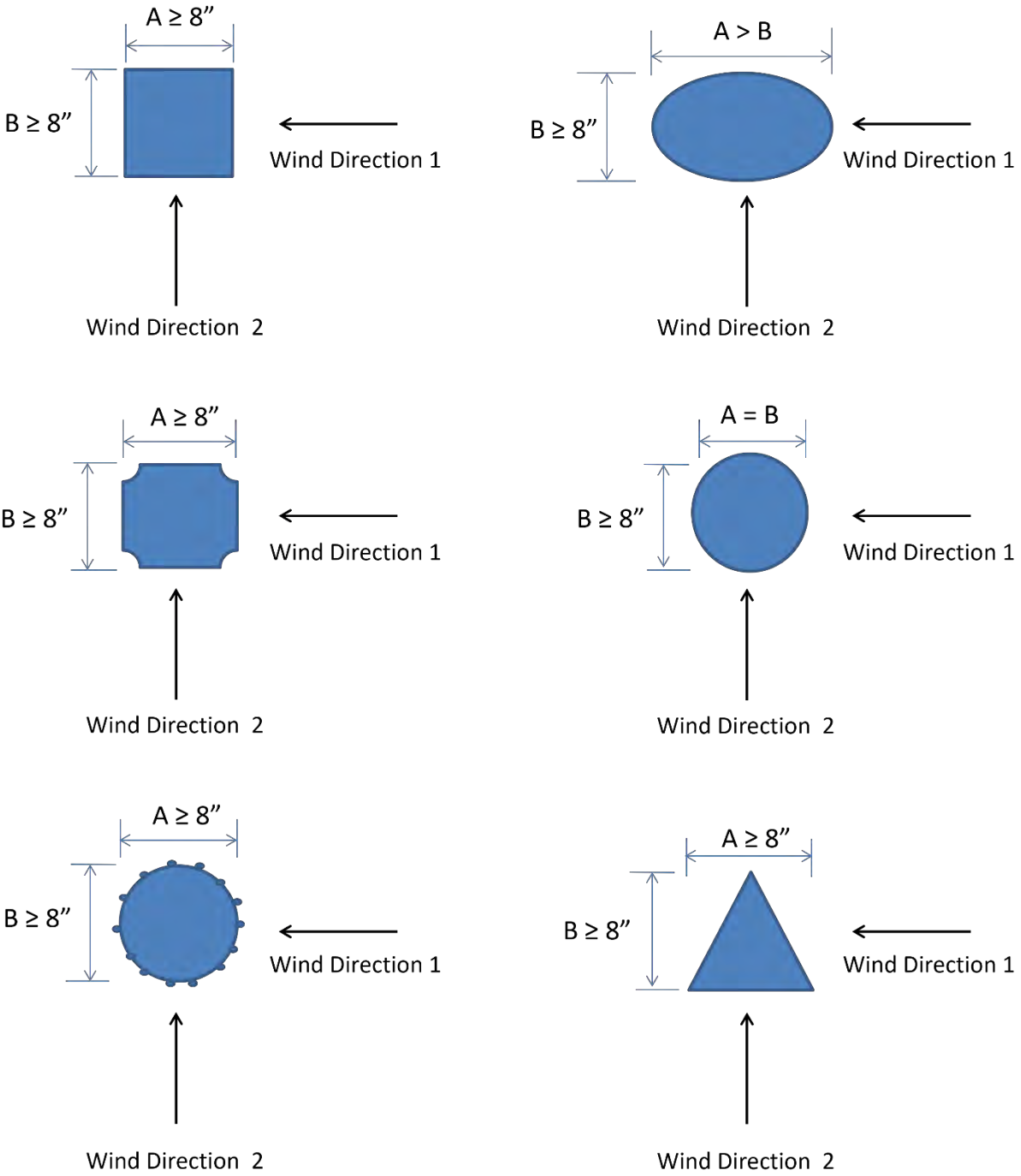


**Figure 3:** Examples of allowable cross-section shapes and wind directions that will be tested at the NSF-NHERI Wall of Wind at FIU.

#### The Oral Presentation Description:

- Oral presentations were done virtually by a recorded Zoom video and judged by the IHRC NSF-NHERI Wall of Wind faculty and research team.
- Oral presentations were to be no more than 7 minutes.

#### Oral presentations and written technical papers had to include these items:

- Effectively communicate some scientific process or analysis and include any scientific or mathematical analysis involved with the development of their hurricane wind mitigation solution for their building model.
- What is hurricane wind mitigation?
- What is the importance of hurricane wind mitigation?
- How is hurricane wind mitigation being addressed with your building model?
- In addition to wind engineering, presentations could also include disciplines such as architecture, business, economics, finance, marketing, geosciences, insurance, political science, sociology, and urban planning.

All three required components of the competition were judged and scored by the IHRC NSF-NHERI Wall of Wind faculty and research team.

#### The judges were:

- Seung Jae Lee, PhD, Associate Professor, Department of Civil & Environmental Engineering, College of Engineering and Computing, International Hurricane Research Center, Extreme Events Institute, Florida International University
- Ioannis Zisis, PhD, Assistant Professor, Department of Civil & Environ. Engineering, Co-Director, Lab. Wind Engineering Research, Extreme Events Institute, Florida International University
- Steven W. Diaz, PhD, PE, Program Director/Site Operations Manager, NSF-NHERI Wall of Wind Experimental Facility, International Hurricane Research Center, Extreme Events Institute, Florida International University
- Walter Conklin, B.S., Laboratory and Health and Safety Manager, NSF-NHERI Wall of Wind Experimental Facility, International Hurricane Research Center, Extreme Events Institute, Florida International University
- James Erwin, M.S., NSF-NHERI Wall of Wind Research Specialist II, International Hurricane Research Center, Extreme Events Institute, Florida International University
- Manuel A. Matus M.Sc., Research Specialist, NSF-NHERI Wall of Wind Experimental Facility, International Hurricane Research Center, Extreme Events Institute, Florida International University
- Dejiang Chen, Ph.D., Research Specialist, NSF-NHERI Wall of Wind Experimental Facility, International Hurricane Research Center, Extreme Events Institute, Florida International University
- Erik Salna, M.S., Associate Director for Education and Outreach, International Hurricane Research Center, Extreme Events Institute, Florida International University

The judges used a cumulative and weighted scoring point scale for the written technical paper (25%), oral presentation (25%), and physical test of the building model (50%) to determine the top three teams. The final results were as follows:

- *First Place* was awarded to Miami Coral Park Senior High School.
- *Second Place* was awarded to North Miami Senior High School.
- *Third Place* was awarded to G. Holmes Braddock Senior High School.

A complete scoring summary can be found on the following link:

[https://www.ihrc.fiu.edu/wp-content/uploads/2022/05/2022\\_WOW\\_CHALLENGE\\_RESULTS\\_SUMMARY.pdf](https://www.ihrc.fiu.edu/wp-content/uploads/2022/05/2022_WOW_CHALLENGE_RESULTS_SUMMARY.pdf)

The Wall of Wind Mitigation Challenge was supported by media. This media exposure resulted in great positive visibility for the IHRC, FIU and FDEM’s message of mitigation. The following media representative participated:

- NSF-NHERI DesignSafe News: <https://www.designsafe-ci.org/community/news/2022/june/fiu-wall-wind-mitigation-challenge-inspires-next-gen-engineers/>

Evaluation and Assessment:

- All teachers gave an overall rating of *Excellent* for the competition experience.
- Teachers rated all aspects of the Wall of Wind Mitigation Challenge – materials, communication, educational value - from *Good to Excellent*.
- Students expressed considerable interest in studying wind engineering at the college level.
- Teachers said that the Wall of Wind Mitigation Challenge contributed to an increase in knowledge of wind engineering.

The Wall of Wind Mitigation Challenge received positive feedback from the teachers:

Booker T. Washington Senior High School:

- *“The FIU WOW challenge helped create more awareness in the students to engage their peers, family members, and community on issue of hurricane mitigation and preparedness.”* Mr. Bidokwu D.O, Chemistry, Physics and Engineering Teacher, Booker T. Washington Senior High School

North Miami Senior High School:

- *“Excellent overall experience. Students learned how to make decisions, collaborate online, and work together in a large group setting. Working with different personalities helped them understand how inter-personal relationships at work are important. Lastly, seeing the Wall of Wind in person was an invaluable experience that propelled all of their interests in engineering disciplines.”* Timothy Ferri, Lead Teacher, Academy of Engineering, North Miami Senior High School

G. Holmes Braddock Senior High School:

- *“This was an excellent learning experience for my students. They got to dive deep into wind engineering and practice practical applications.”* Lacey Simpson, Science Department, G. Holmes Braddock Senior High School



Jose Marti MAST Academy:

- *“I truly enjoy using real world simulations for the students to experience the design engineering process and compete so that they can reflect on their work compared to peers in other schools.”* Carmen L. Garcia, NBCT, Teacher, Jose Marti MAST Academy

Miami Coral Park Senior High School:

- *“This is a great competition to teach students about wind mitigation as well as so many other STEM lessons. One of my favorite competitions!”* Charlie Delahoz, Engineering/Architecture Magnet Teacher, Miami Coral Park Senior High School

NSF-NHERI Wall of Wind (WOW) Experimental Facility (EF):

- *“The WOW Challenge is a platform to educate high school students in our community with regards to hurricane engineering and community resilience. Student teams are given real-world wind engineering problems and they conceive and validate wind mitigation concepts to solve such problems. The WOW Challenge informs students about the importance of mitigation and community resilience to prepare them as future leaders in disaster mitigation. We see these young students become motivated toward STEM careers and possibly enrolling at FIU with the dream of performing research at our national, shared-use NHERI WOW experimental facility”.* Arindam Gan Chowdhury, PhD, Professor, Dept. of Civil & Environ, Engineering PI and Director, NHERI Wall of Wind (WOW) Experimental Facility (EF), Co-Director, Lab. Wind Engineering Research, Extreme Events Institute, Florida International University



*Jose Marti MAST Academy Model Drawings*



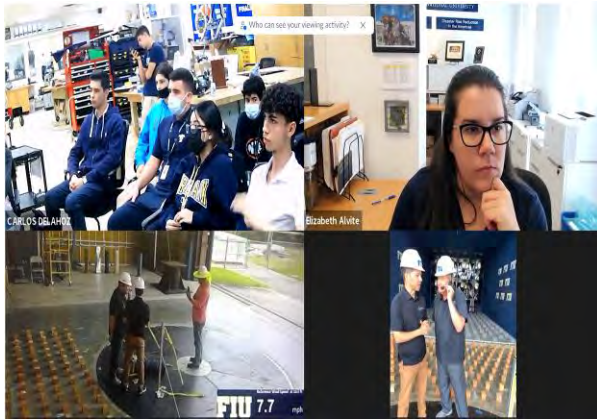
*Jose Marti MAST Academy Actual Model*



*North Miami Team working on model.*



*Wall of Wind building model test set-up.*



*Miami Coral Park H.S. live Zoom test.*



*Building Models in Wall of Wind Challenge.*



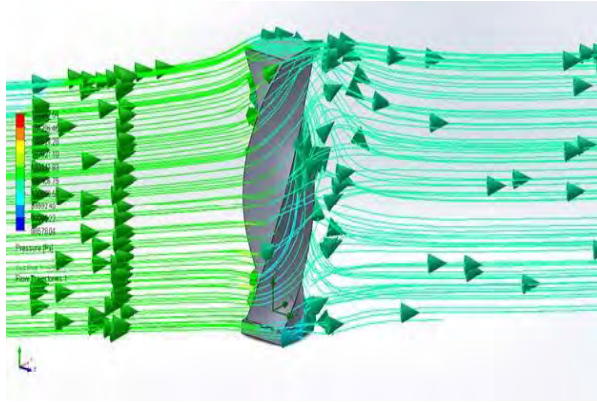
*1st Place: Miami Coral Park*



*2nd Place: North Miami*



*3rd Place: G. Holmes Braddock*



*Miami Coral Park Air Flow Simulation*



*1st Place Team: Miami Coral Park. H.S.*



*2nd Place Team: North Miami H.S.*



*3rd Place Team: G. Holmes Braddock H.S*

***Eye of the Storm (Science, Mitigation & Preparedness) Event: May 14th, 2022***

Overview:

The Museum of Discovery & Science (MODS), located in Fort Lauderdale, FL, assisted the IHRC in planning, coordinating and facilitating this free admission public education event. A record 3,897 visitors attended Eye of the Storm, showcasing special interactive activities and demonstrations teaching hurricane science, mitigation and preparedness. This included special learning activities for parents and children providing family fun throughout the day.

- Media Release and Flyer: [2022 Eye of the Storm – Hurricane \(Science, Mitigation & Preparedness\) Free Museum Event, Saturday, May 14th, 10am to 5pm | IHRC Website \(fiu.edu\)](#)

**Key Messages Communicated to the Public:**

- 1. Know Your Risk*
- 2. Know Your Evacuation Zone*
- 3. Complete Your Hurricane Plan*
- 4. Address Any Special Needs*

5. *Assemble Your Supply Kit*
6. *Prepare Your Pets*
7. *Get an Insurance Check-Up*
8. *Protect Your Home*
9. *Help Your Neighbor*

This collaborative community education outreach project partnered the IHRC and MODS with:

- Florida Division of Emergency Management
- Broward County Emergency Management
- Broward County CERT
- City of Fort Lauderdale Emergency Management
- City of Fort Lauderdale Fire Rescue and Fire Explorers
- City of Fort Lauderdale Police Department
- NOAA National Hurricane Center
- NOAA Atlantic Oceanographic and Meteorological Laboratory and Hurricane Research Division
- NOAA National Weather Service – Miami Office
- BECON-TV (Broward Education Communications Network)
- International Hurricane Protection Association
- Florida Power & Light
- Many other organizations and non-profits

Special guests:

- Grant Goodwin, HLMP Program Manager, Florida Division of Emergency Management
- Dana McGeehan, Region 7 Recovery Coordinator, Florida Division of Emergency Management

Various distinguished hurricane experts participated:

- Daniel Brown, Senior Hurricane Specialist, NOAA's National Hurricane Center
- Neal Dorst, Hurricane Researcher, NOAA/AOML/HRD
- Stanley B. Goldenberg, Research Meteorologist, NOAA/AOML/HRD
- Dr. Frank D. Marks, Director of Hurricane Research Division, NOAA/AOML/HRD
- Robert Molleda, Warning Coordination Meteorologist, National Weather Service-Miami

Special interactive exhibits and demonstrations included:

- IHPA Live Air Cannon Demonstrations Showing Debris Impact of Shutters and Windows
- Weather Jeopardy Game
- BECON-TV Hurricane Broadcast Center
- Live Tropical Weather Briefings by NOAA's National Hurricane Center
- FIU NSF-NHERI Wall of Wind Exhibit
- MODS Live Weather Science Demonstrations
- Special Showings of Built to Last? Resilience Documentary in IMAX Theater

Special live interactive theater presentations:

- Tsunami Tim Live Weather Education Theater Shows

Partner Mascots:

- *Sparky the Fire Dog* - City of Fort Lauderdale Emergency Management
- *Joey the Otter* - Museum of Discovery and Science Joey the Otter Mascot
- *Roary the Panther* - Florida International University

Assessment Activities:

Participant Post Survey Questions for Event Attendees:

1. Did you attend the 2022 Eye of the Storm event?
2. To what extent did this event increase your knowledge about how wind engineering can mitigate hurricane damage?
3. To what extent are you interested in learning more about wind engineering?
4. To what extent will you be taking to steps to mitigate hurricane damage to your property?
5. How many times have you attended the Eye of the Storm Event?

Positive Survey Results:

- 86% increased their knowledge about wind engineering and mitigating hurricane damage.
- 90% will be taking steps to mitigate hurricane damage.
- 77% would like to learn more about wind engineering.
- 76% were first time attendees of the event.

Message Board #1 During Event:

What did you learn today about protecting your home from hurricanes?

- “Taping your windows doesn’t protect them from breaking. Best is having impact windows and metal shutters.”
- “I learned that the hip roof was the best roof for the hurricanes.”
- “Make sure windows and doors are protected. Make sure you have supplies to keep everyone safe.”
- “Need window protection.”
- “Get water, food, flashlights, battery.”
- “Hurricanes can go from levels 1-5 and 5 is the most powerful. They cause floods and damage. When hurricanes happen, power can go out so go shopping to be prepared.”
- “You need to hide in the bathroom.”

Message Board #2 During Event:

Would you like to study wind engineering in school?

- “Yes, I would like to study wind engineering in school!!!”
- “Wind engineering sounds interesting and cool to learn”
- “Yes, because I would learn about hurricanes, how to prevent them, and know when they are coming.”
- “I think wind engineering is important as all other types of engineering are. They all serve a purpose which would help to understand hurricanes better, also giving us more data”

- “There’s an infinite amount of helpful possibilities in the field of wind engineering! From flight, to safety and solving eco issues!”

#### Kahoot! Education Quiz Questions Before Live Theater Shows:

- How many categories of hurricanes are there?
- What’s the most active month for hurricanes in Florida?
- What should you NOT do to mitigate hurricane damage?
- What items should you have in your hurricane emergency kit?
- Your action plan for hurricane preparedness should include?

#### Weather Jeopardy Categories:

- Hurricanes 101
- Know Your Zone
- Don’t Blow Away
- Whacky Weather

#### Media Coverage:

The following local South Florida media representatives participated in person:

- Phil Ferro, Meteorologist, WSVN-TV (FOX)
- Vivian Gonzalez, Meteorologist, WSVN-TV (FOX)

#### Digital Marketing Campaign Summary

- Views: 392,599
- Impressions: 7,098,310+
- Engagements and Clicks: 67,198
- Hours Watched: 8,665+

The Eye of the Storm received great coverage by the local South Florida media. This resulted in great positive visibility in the community for IHRC, FIU and FDEM’s message of hurricane preparedness and mitigation:

- Miami Standard website, “Eye of the Storm,” April 26, 2022. The website has monthly unique visitors of 121,830.
- Daily Advent website, “Eye of the Storm Event,” April 26, 2022. The website has monthly unique visitors of 1,178,400.
- Miami Community News website, “FIU’s International Hurricane Research Center, FDEM and the Museum of Discovery and Science to Host FREE Admission Eye of the Storm Event,” April 26, 2022. The website has monthly unique visitors of 42,990.
- The Sun Sentinel website, “Sunday calendar: Eye of the Storm,” April 29, 2022. The website has monthly unique visitors of 1,684,250.
- AroundTown, “Eye of the Storm,” May 6-19, 2022. The publication has a circulation of 20,000.
- The Sun Sentinel website, “Eye of the Storm,” May 6, 2022. The website has monthly unique visitors of 1,539,110.
- Sun Sentinel, “Eye of the Storm,” May 8, 2022. The publication has a circulation of 220,000.

- The Sun Sentinel website, “Weekly calendar: Community and entertainment events beginning May 11,” May 10, 2022. The website has a unique monthly circulation of 1,539,110.
- WTVJ-NBC website, “Eye of the Storm at Museum of Discovery and Science,” May 11, 2022. The website has a unique monthly circulation of 338,910.
- WTVJ-NBC website, “Museum of Discovery and Science Unveiling ‘Eye of the Storm’ Exhibit Saturday,” May 11, 2022. The website has monthly unique visitors of 338,910.
- Geeksscience.com, “Museum of Discovery and Science Unveiling ‘Eye of the Storm’ Exhibit.
- Saturday – NBC 6 South Florida,” May 14, 2022. The website has monthly unique visitors of 121,500.
- NBC Miami website, “Eye of the Storm,” May 11, 2022. The website has monthly unique visitors of 306,690.
- Newsbreak.com, “Museum of Discovery and Science Unveiling ‘Eye of the Storm’ Exhibit Saturday,” May 11, 2022. The website has monthly unique visitors of 2,791,402.
- Fior Reports website, “Museum of Discovery and Science Unveiling ‘Eye of the Storm’ Exhibit Saturday,” May 11, 2022. The website has monthly unique visitors of 9,580.
- MeinNews website, “Museum of Discovery and Science unveils ‘Eye of the Storm’ exhibit Saturday - NBC 6 South Florida,” May 11, 2022. The website has monthly unique visitors of 12,191.
- WSVN-FOX website, “Turning Hotter,” May 13, 2022. The website has monthly unique visitors of 345,990.
- International Hurricane Research Center at Florida International University website, “2022 Eye of the Storm - Hurricane (Science, Mitigation & Preparedness) Free Museum Event,” May 14, 2022.
- Greater Fort Lauderdale LGBT Chamber of Commerce website, “Eye of the Storm Calendar Listing,” May 14, 2022. The website has monthly unique visitors of 148,920.
- TheKidonthego.com, “Eye of the Storm Calendar Event,” May 14, 2022. The website has monthly unique visitors of 5,010.
- WTVJ-NBC news, “Eye of the Storm,” May 14, 2022. The segment aired at 6 a.m. The station has a Nielsen audience of 10,565.
- Go Riverwalk website, “Eye of the Storm Event Listing,” May 14, 2022. The website has monthly unique visitors of 8,850.
- Artscalendar.com, “Eye of the Storm Event Listing,” May 14, 2022. The website has monthly unique visitors of 5,370.
- AllEvents.in website, “Eye of the Storm Event Listing,” May 14, 2022. The website has monthly unique visitors of 840,540.
- Stay Happenings website, “Eye of the Storm Event Listing,” May 14, 2022. The website has monthly unique visitors of 575,550.
- Macaroni Kid website, “Eye of the Storm Event Listing,” May 14, 2022. The website has monthly unique visitors of 179,630.
- March of Museums website, “Eye of the Storm Event Listing,” May 14, 2022. The website has monthly unique visitors of 4,570.
- Visit Florida website, “Eye of the Storm Event Listing,” May 14, 2022. The website has monthly unique visitors of 364,500.

- Munchkin Fun Broward, “Eye of the Storm Event Listing,” May 14, 2022. The website has monthly unique visitors of 13,689.
- AARP FL website, “Eye of the Storm Event Listing,” May 14, 2022. The website has monthly unique visitors of 110,730.
- MiamiontheCheap.com, “Eye of the Storm Event Listing,” May 14, 2022. The website has monthly unique visitors of 24,690.
- Fortlauderdaleonthecheap.com, “Eye of the Storm Event Listing,” May 14, 2022. The website has monthly unique visitors of 24,450.
- Nextdoor website, “Eye of the Storm Event Listing,” May 14, 2022. The website has monthly unique visitors of 20,986,302.
- City of Fort Lauderdale website, “Eye of the Storm Event Listing,” May 14, 2022. The website has monthly unique visitors of 73,950.
- Condo Blackbook website, “Eye of the Storm,” May 14, 2022. The website has monthly unique visitors of 40,680.
- Schools&CollegeListings website, “Eye of the Storm,” May 14, 2022. The website has monthly unique visitors of 640,140.
- The Boca Raton Observer website, “Eye of the Storm,” May 14, 2022. The website has monthly unique visitors of 15,250.
- Greater Fort Lauderdale Chamber website “Eye of the Storm,” May 14, 2022. The website has monthly unique visitors of 148,920.
- WSVN-FOX news, “Eye of the Storm,” May 14, 2022. The segment aired at 10 p.m. The station has a Nielsen audience of 45,399.
- WSVN-FOX website, “7Weather’s Ferro, Gonzalez discuss hurricanes, storm preparedness at Museum of Discovery and Science,” May 14, 2022. The website has monthly unique visitors of 275,670.
- WSVN-FOX website, “Eye of the Storm,” May 14, 2022. The website has monthly unique visitors of 275,670.
- AllEvents.In website, “Eye of the Storm,” May 14, 2022. The website has monthly unique visitors of 840,540.
- CitySpark website, “Eye of the Storm,” May 14, 2022. The website has monthly unique visitors of 21,660.
- DesignSafe, “NHERI at Florida International University Takes Center Stage at Eye of the Storm Event,” July 1, 2022. The website has monthly unique visitors of 20,210.
- Cision website, “Flood Risk America Participates in the ‘Eye of the Storm 2022’ Hurricane Preparedness Event,” July 11, 2022. The website has monthly unique visitors of 551,910.
- Longview News-Journal website, “Flood Risk America Participates in the 'Eye of the Storm 2022' Hurricane Preparedness Event,” July 11, 2022. The website has monthly unique visitors of 38,310.
- Newsbreak.com, “Flood Risk America Participates in the 'Eye of the Storm 2022' Hurricane Preparedness Event,” July 11, 2022. The website has monthly unique visitors of 2,775,360.
- Bezinga website, “Flood Risk America Participates in the 'Eye of the Storm 2022' Hurricane Preparedness Event,” July 11, 2022. The website has monthly unique visitors of 79,440.



2020 Virtual Eye of the Storm: Update as of July 15th

The 2020 virtual Eye of the Storm, the 12-episode “evergreen” video series, was re-promoted in conjunction with the Eye of the Storm in-person event on May 14<sup>th</sup>. The video series continues to be promoted during the current hurricane season by MODS and IHRC.

All the videos are listed on the MODS virtual Eye of the Storm web-page:

[https://mods.org/?page\\_id=16093](https://mods.org/?page_id=16093)

All the videos are also listed on the following MyFloridaCFO web-page: [Plan Prepare Protect: Are You Disaster Ready? Eye of the Storm Videos \(myfloridacfo.com\)](https://myfloridacfo.com/plan-prepare-protect-are-you-disaster-ready-eye-of-the-storm-videos)

The virtual Eye of the Storm has resulted in a hugely successful digital marketing campaign and has expanded the reach and impact beyond South Florida to other states on the Gulf of Mexico and the U.S. eastern seaboard at risk of a hurricane landfall.

The Eye of the Storm virtual series is an outstanding success:

- A reach of more than 133,472,350+ impressions for the entire digital marketing and public relations campaign.
- Social media channels included Facebook, Twitter, Instagram, LinkedIn and YouTube.
- The Museum utilized Google Display and Search Ads and My Business Posts.
- Museum marketing included slides in the AutoNation IMAX Theater, article in the Museum’s What Will You Discover? magazine, emails to 75,000 subscribers, webpage with link to videos and Facebook event page.
- Calendar listings and articles were featured in 50 publications and media with a circulation of 45,328,368.



*Fort Lauderdale Police and FPL Vehicles*



*FDEM Weather Safety Live Theater Shows*



*FIU Wall of Wind Exhibit*



*BECON-TV Hurricane Broadcast Center*



*Florida Division of Emergency Management*



*Broward County Emergency Management*



*Broward County American Red Cross*



*Live Air Cannon Missile Demonstrations*



*Mitigation Education: Simpson Strong-Tie*



*Shutter Mitigation Education*



*Families Building Houses for Wind Testing*



*National Hurricane Center & NWS-Miami*



*Key Preparedness Messages*



*Fort Lauderdale CERT Team*



**FIU**

# Understanding Hurricane Effects on Manufactured Homes

Funded by the Florida Division of Emergency Management

*A*

**KU**

# Project PIs



## Florida International University



Dr. Arindam Chowdhury



Dr. Ioannis Zisis



Dr. Amal Elawady



## University of Kansas



Dr. Elaina Sutley



Dr. William Collins



## University of Alabama



Dr. Thang Dao





# Mobile Home, Manufactured Home, what are we studying?

**FIU**



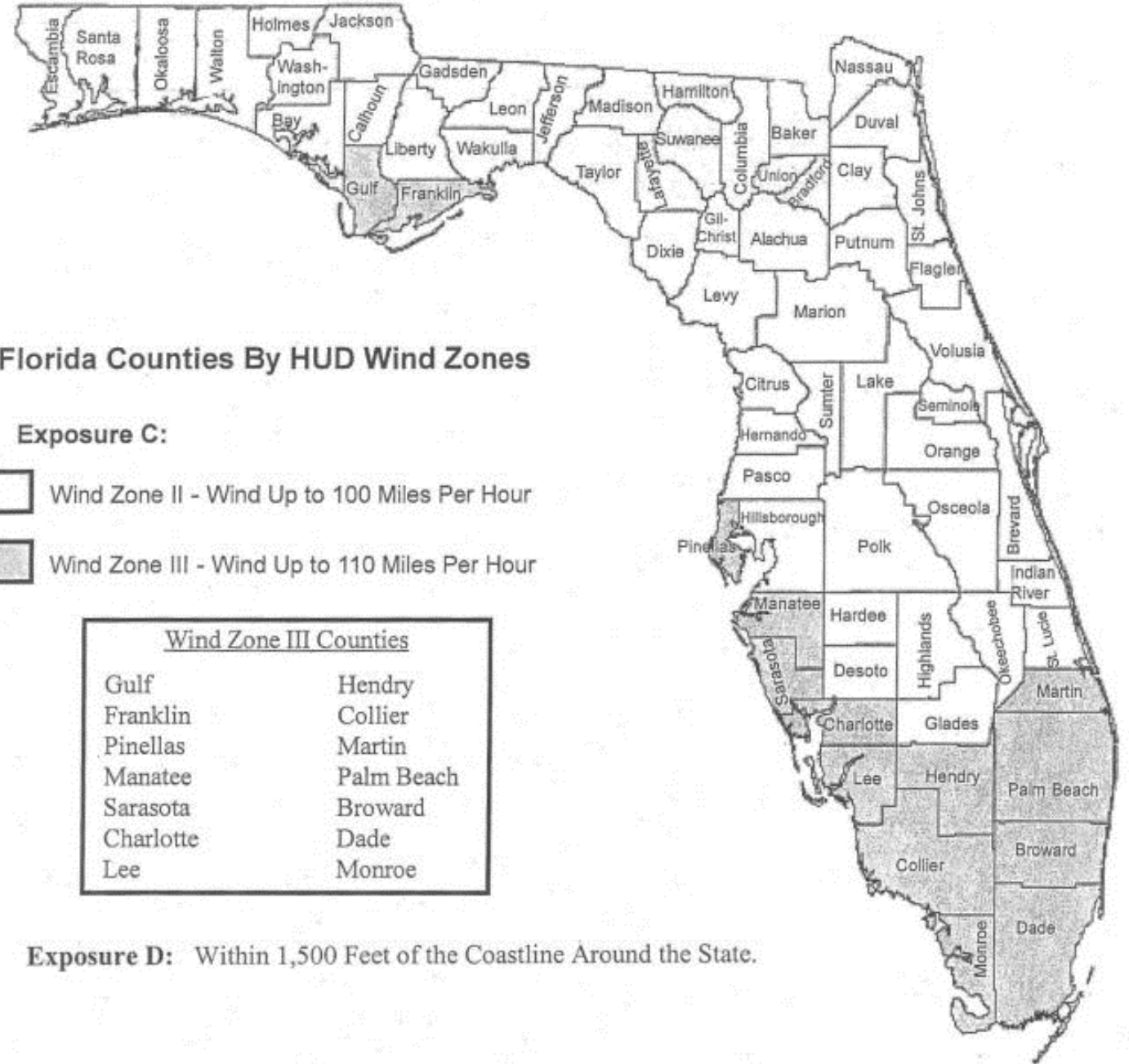
*A*

**KU**

# Manufactured Home Construction and Safety Standards

24 CFR 3280

commonly called the HUD Code



Florida Counties By HUD Wind Zones

**Exposure C:**

- Wind Zone II - Wind Up to 100 Miles Per Hour
- Wind Zone III - Wind Up to 110 Miles Per Hour

<u>Wind Zone III Counties</u>	
Gulf	Hendry
Franklin	Collier
Pinellas	Martin
Manatee	Palm Beach
Sarasota	Broward
Charlotte	Dade
Lee	Monroe

**Exposure D:** Within 1,500 Feet of the Coastline Around the State.

# Project Overview

- The overall goal of this research is to provide the fundamental knowledge needed to reduce the physical vulnerability of manufactured homes (MH) to wind events.
- The objective of the proposed research is to experimentally and numerically assess wind and wind-driven rain effects on MH units:
  - Develop a new dataset on aerodynamic effects on manufactured homes.
  - Develop detail-specific damage accumulation models for loading on MH fasteners and subassemblies.
  - Finite Element Modeling (FEM) of the non-linear behavior of MH units under moderate to extreme wind events.





Wall of Wind

NHERI Experimental Facility

# Large-scale Wind Tunnel Testing Program

**Florida International University**

Arindam Gan Chowdhury, PhD

Ioannis Zisis, PhD

Amal Elawady, PhD

# Wind-tunnel Testing

- Perform large-scale wind tunnel experimentation to investigate aerodynamic loading on Manufactured Homes.
- The study will also consider interference effects on grouped MHs for different wind directions.
- Wind tunnel testing will be conducted on scaled models of isolated and grouped MHs to measure aerodynamic pressures on the MH of interest.
- The pressure coefficient time histories will be later used to inform the FEM.

# Site Selection to be Modeled for Experiments



# Model Configuration

## MH dimensions:

- Width, length, and height
- Crawl space height
- Roof pitch
- Clear space between homes.

## Additions and attachments:

- Carport
- Overhangs



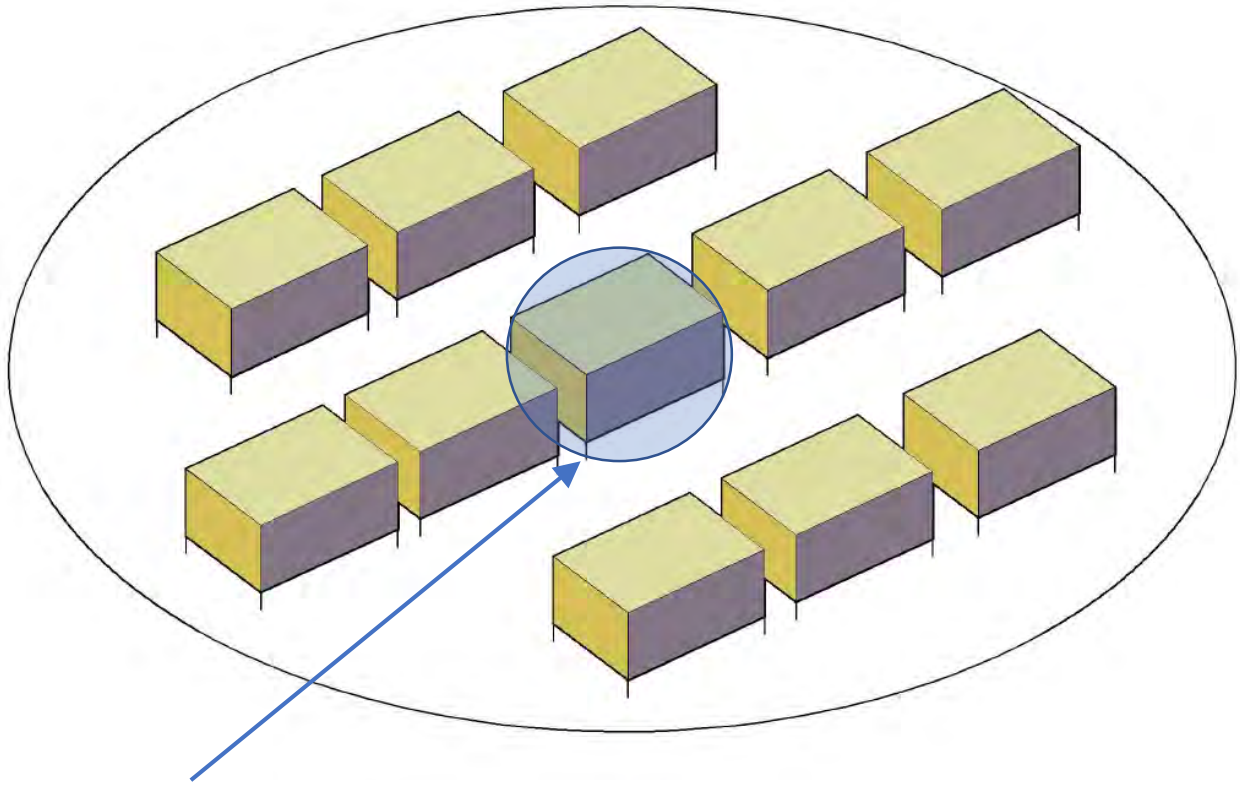
# Test Protocol

- Aerodynamic loading on roof, walls and floors
- Large-scale models: 1:10 and 1:5
- Varying wind directions
- Shielding effect



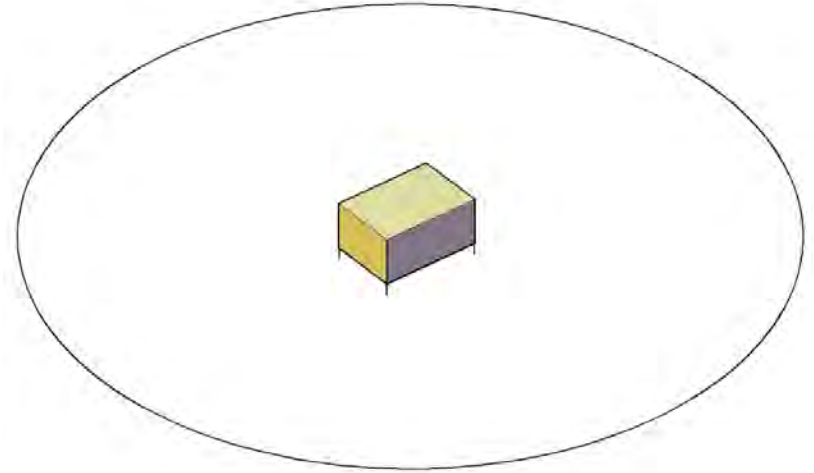
# Test Protocol

Configuration 1: Shielded (1:10 Scale)

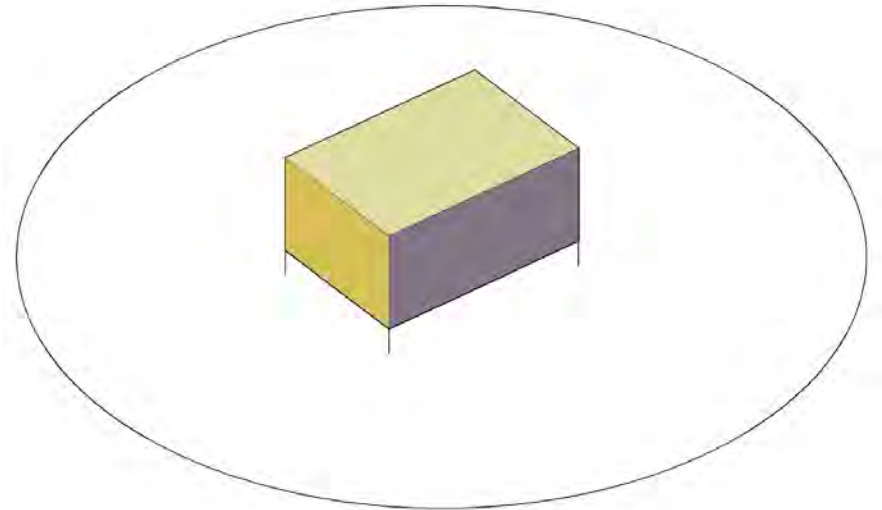


MH of interest

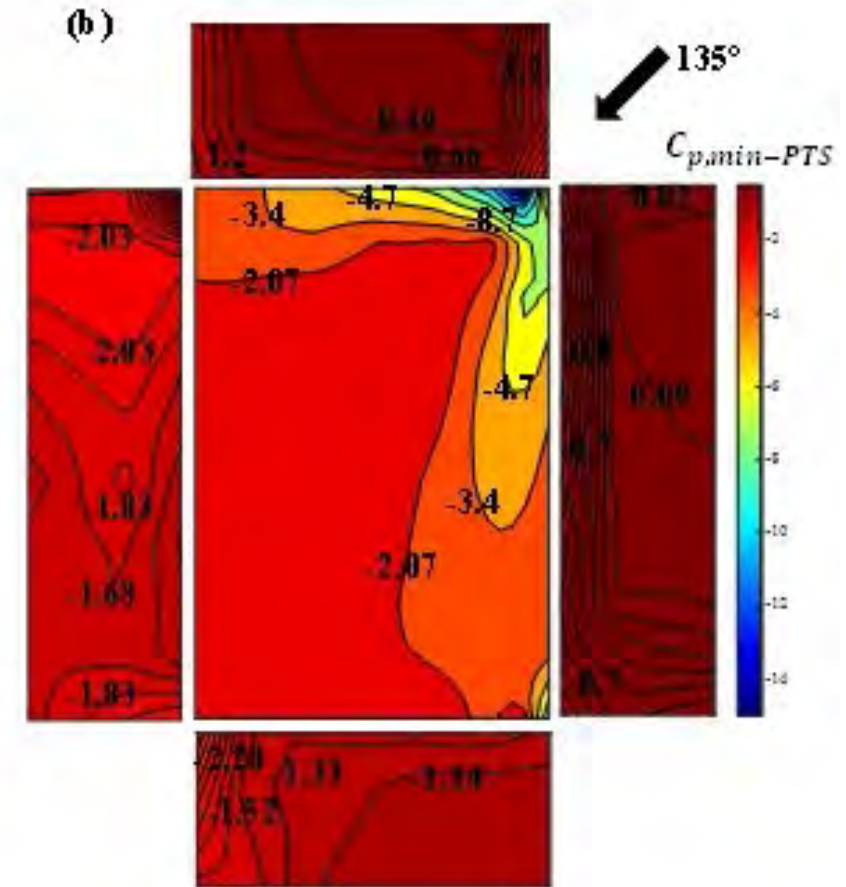
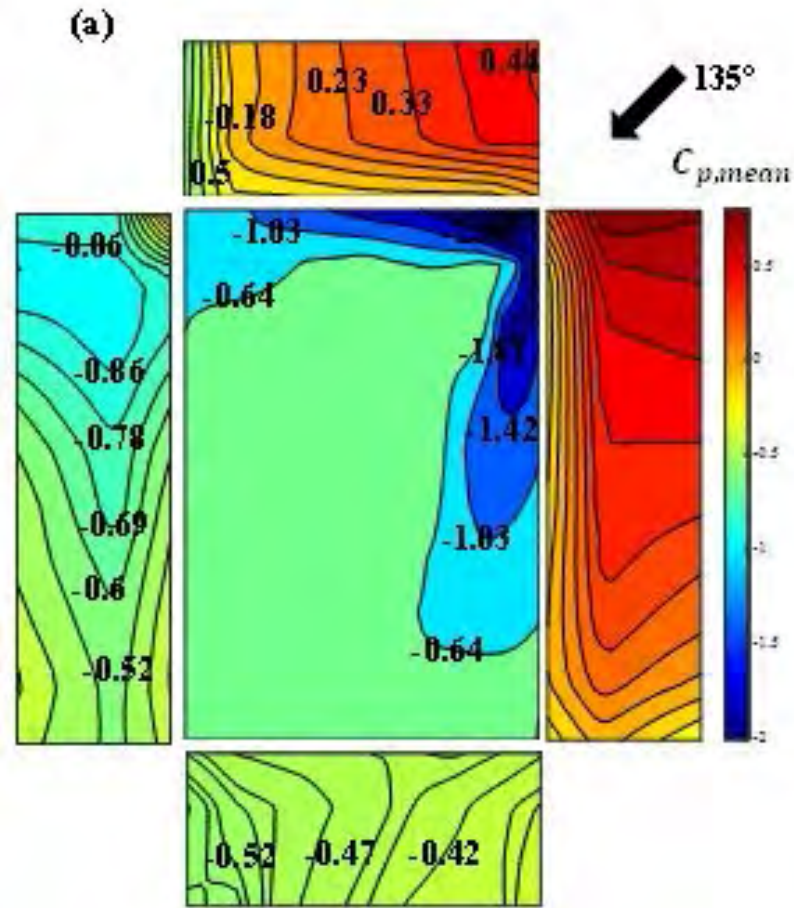
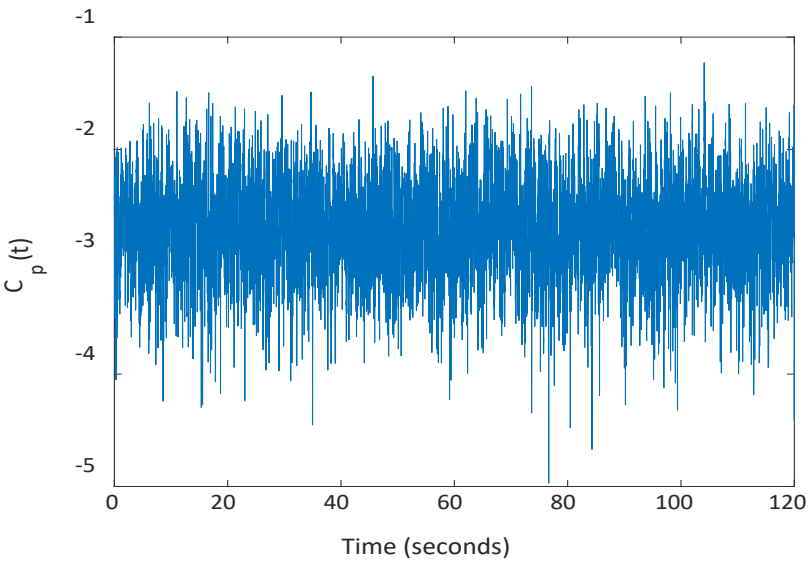
Configuration 2: Unshielded (1:10 Scale)



Configuration 3: Unshielded (1:5 Scale)



# Expected Outcomes





# Component-level Experimental Testing Program

**University of Kansas**

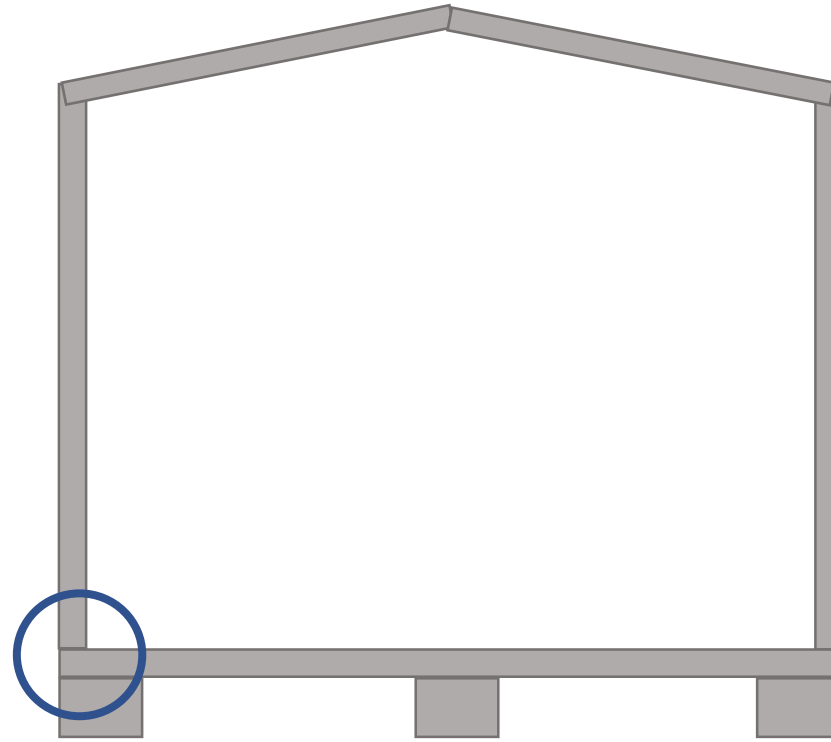
Afeez Badmus

William Collins, PhD

Elaina Sutley, PhD



# Wall to Floor Connection



## Wind zone III (older)

No exterior sheathing

2x4 studs

26 gauge straps run full wall height



## Wind zone III (newer)

OSB exterior sheathing

2x6 studs

Actual hurricane straps securing wall to foundation



# Wall to Floor Connection

Wind zone II



3 1/2" wood screw connecting bottom plate to stud, at every stud

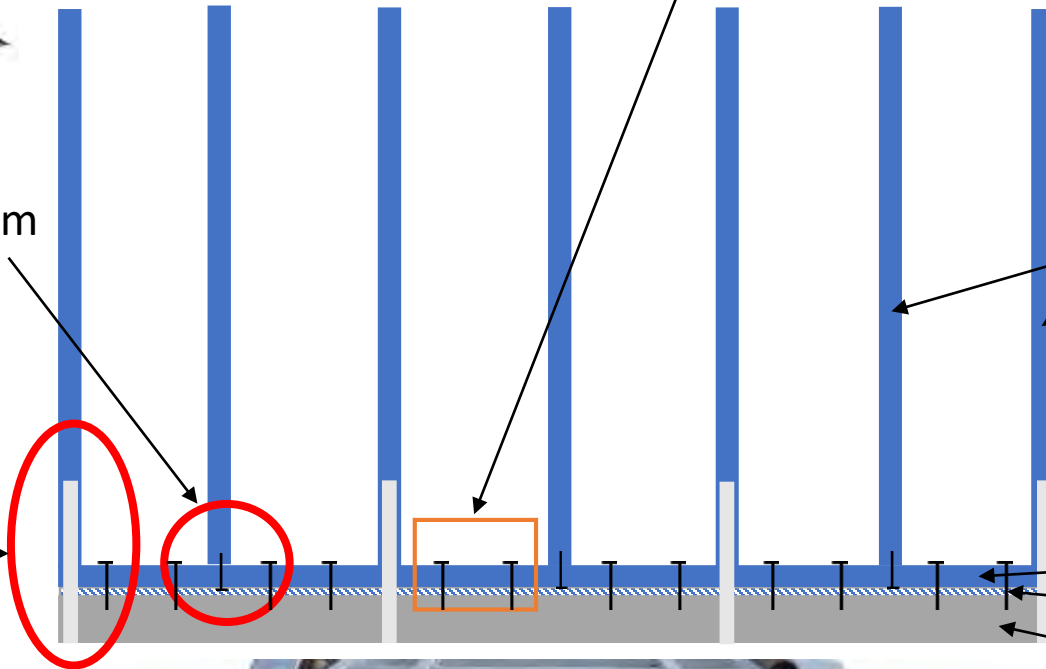
Screw connecting bottom plate to joist ?

2x4 stud @ 16" o.c.

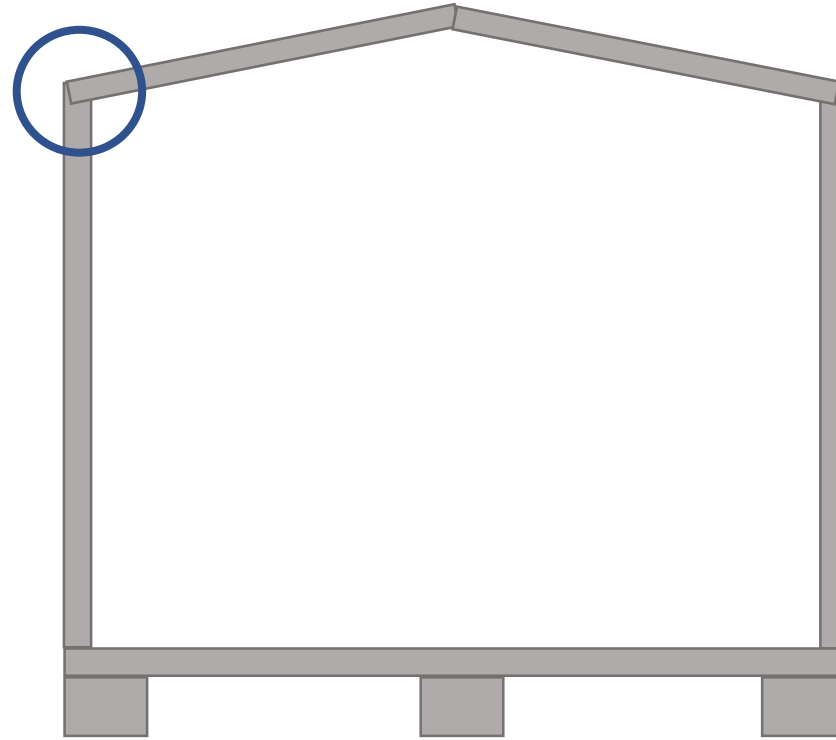
26 gauge steel strap stapled connection to joists to bottom plate to stud at every other stud

2x4 single bottom plate  
WSP subfloor  
2x6 joists at 16" o.c.

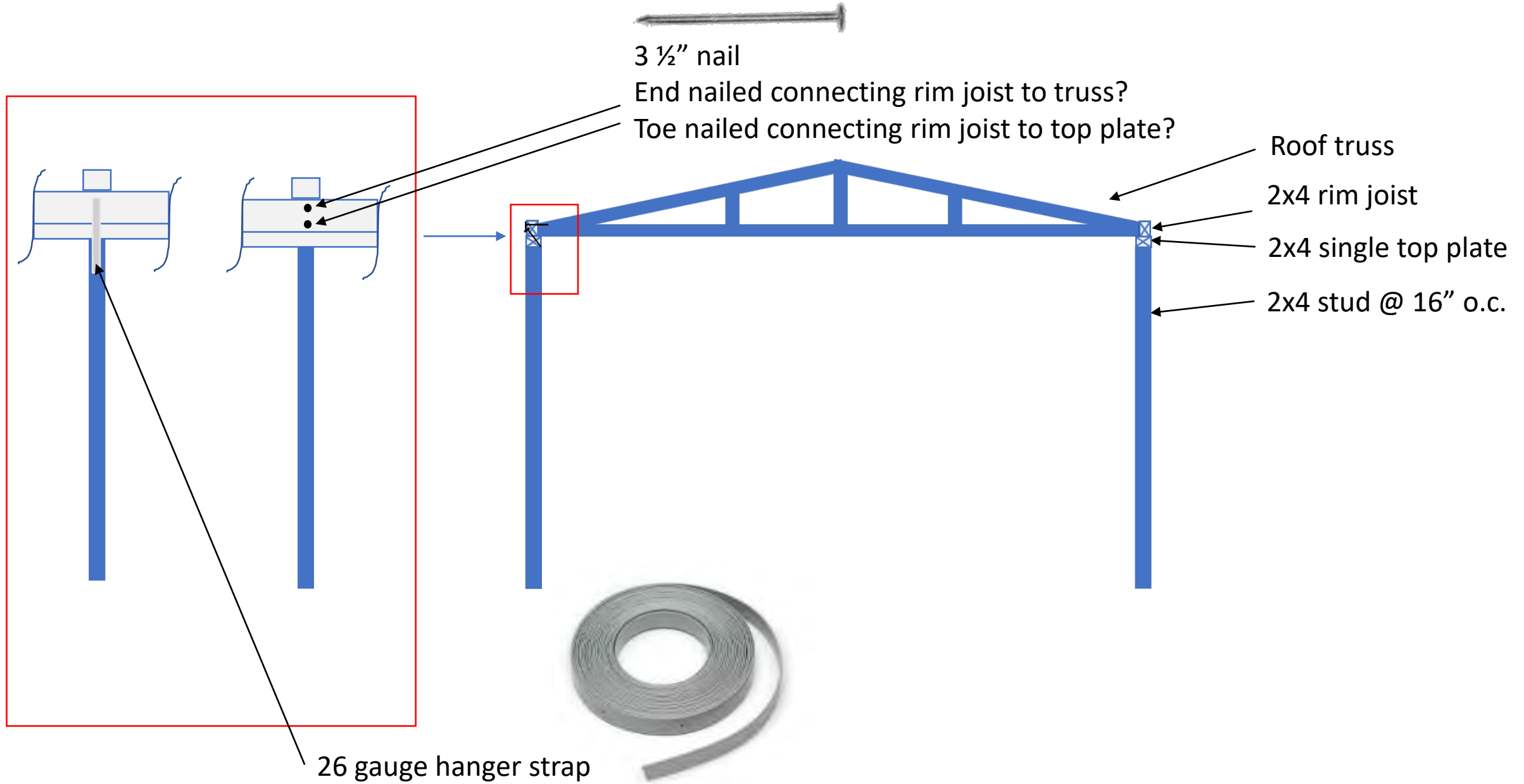
Steel chassis



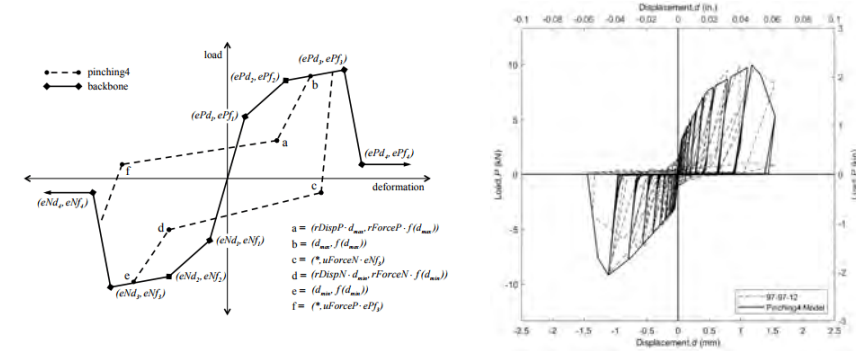
# Roof to Wall Connection



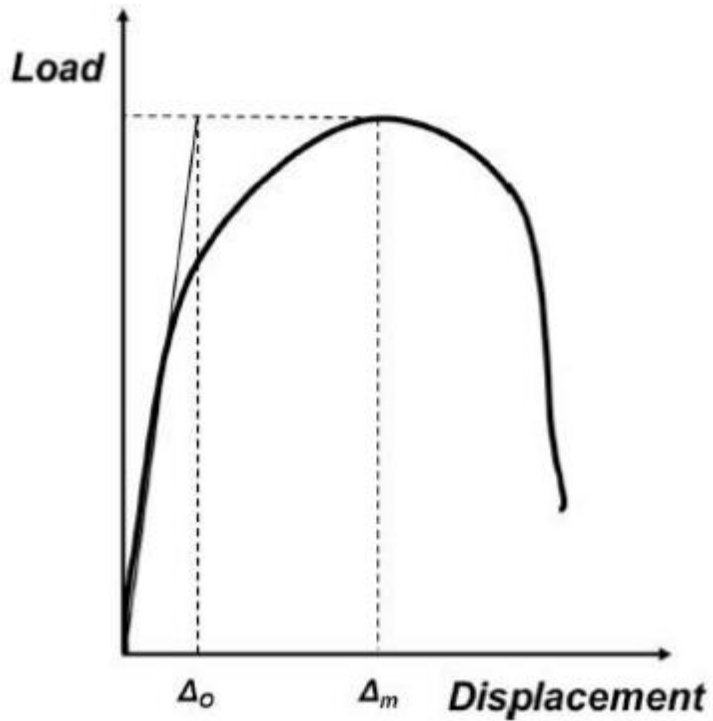
# Roof to Wall Connection



# Quasi-static Cyclic Test Protocol

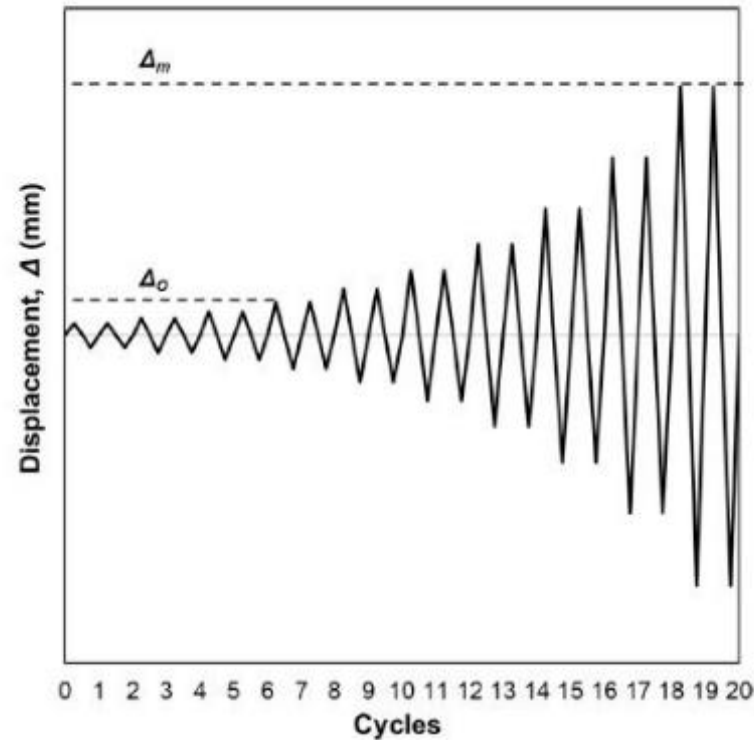


## Step 1: Monotonic Loading



Schematic representation of  $\Delta_0$  and  $\Delta_m$  from monotonic test result (Boadi-Danquah et al, 2021)

## Step 2: Cyclic Loading



Schematic cyclic displacement protocol in accordance with FEMA 461 (Boadi-Danquah et al, 2021)

$\Delta_0$  = initial state of damage, where initial linearity intersects with peak load.

Start with six cycles of displacement amplitude lower than amplitude at which the lowest damage state is first observed

$\Delta_m$  = Displacement at  $P_{max}$

For cyclic test, each step (displacement amplitude) consists of two cycles; then amplitude is increased by a factor of 1.4 until  $\Delta_m$  is reached

# Summary

- (2) variations of roof-to-wall connections, tested in pure tension
  - 12" long 26 gauge steel strap connecting rim joist to top plate to stud
  - 3 ½" nail toe-nailed connecting rim joist to top plate ?
- (2x2) variations of wall-to-floor connections, tested in pure tension and combined shear and tension
  - a) 3 ½" screw connecting bottom plate to floor system ?
  - b) (a) with 12" long 26 gauge steel strap connecting joist to bottom plate to stud
- Will produce fastener hysteresis and corresponding Pinching4 material model for FEM.





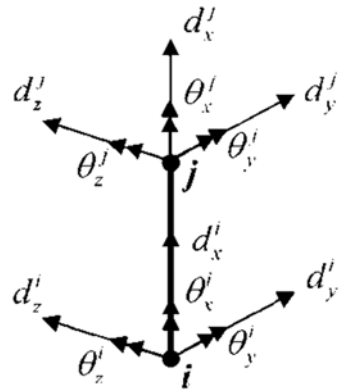
# Finite Element Modeling

**University of Alabama**

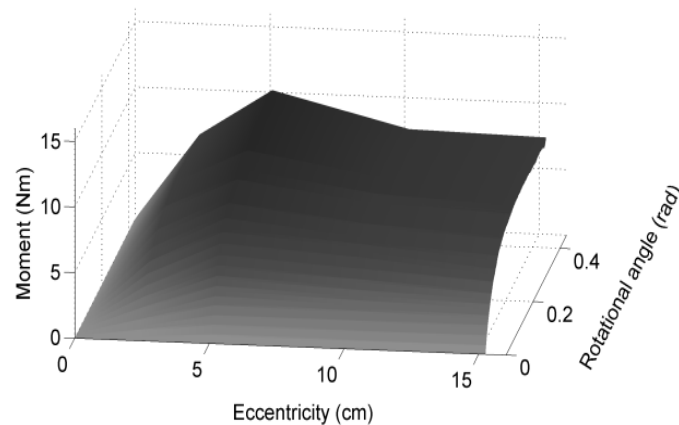
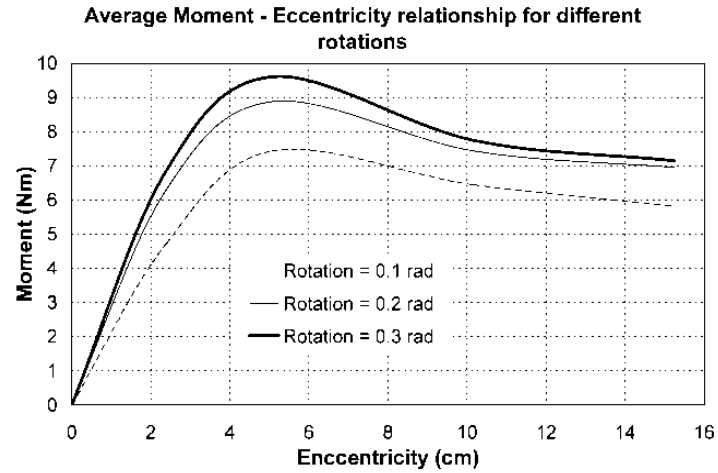
Thang Dao, PhD

# Numerical Model

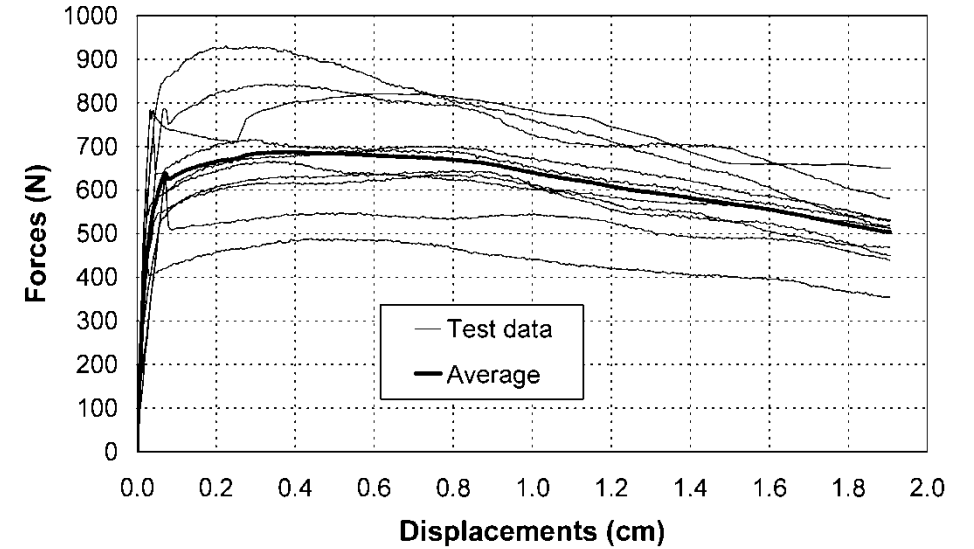
- Current fastener model:



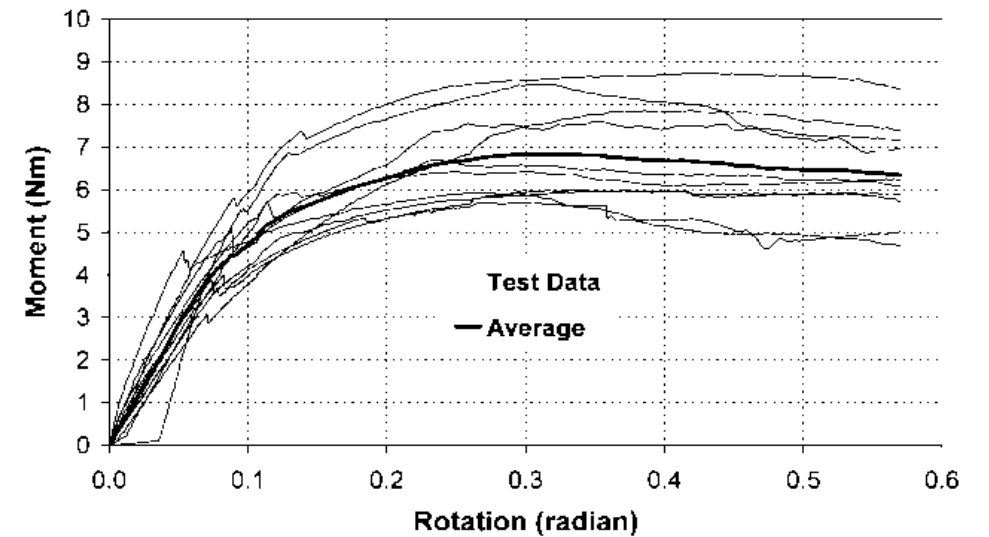
Degrees of freedom in nail model



8d-Box Nails - Withdraw Test

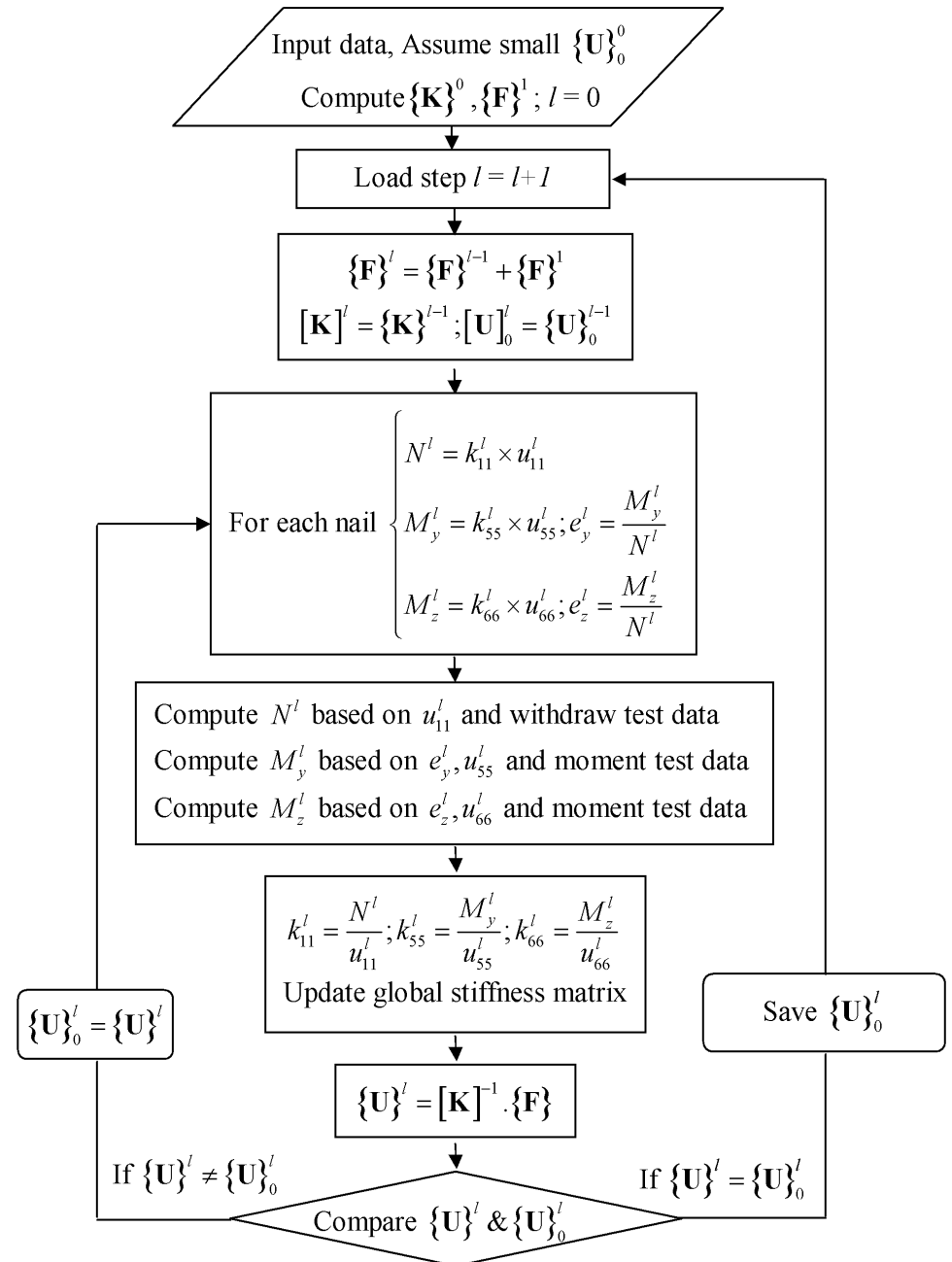
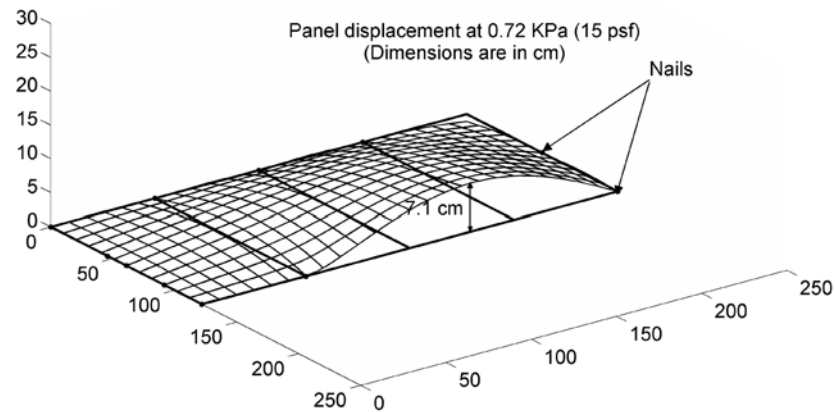
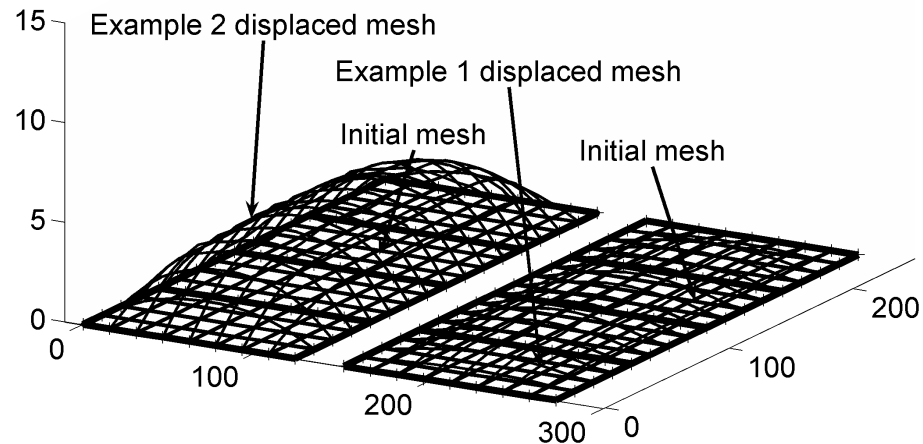


8d-Box Nail, M/N = 2.381cm (0.9375 inches)



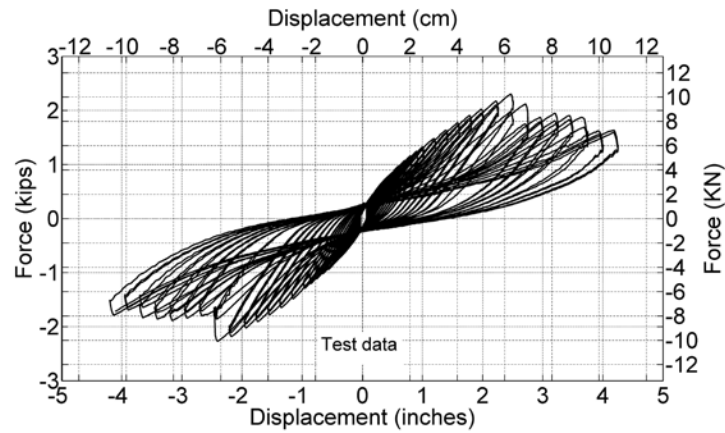
# Numerical Model (Cont.)

- Current fastener model (Cont.):

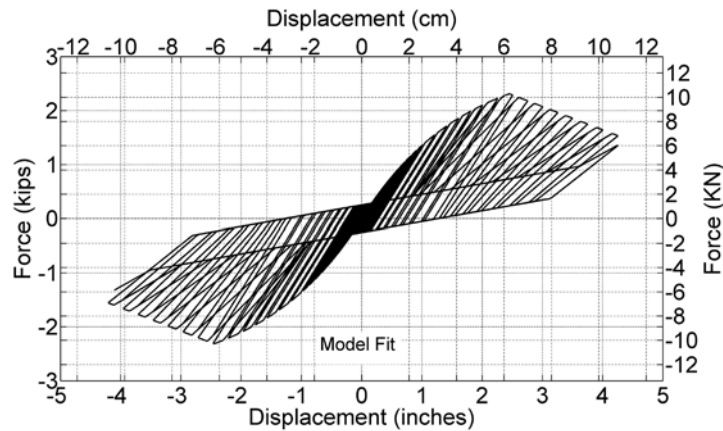


# Numerical Model (Cont.)

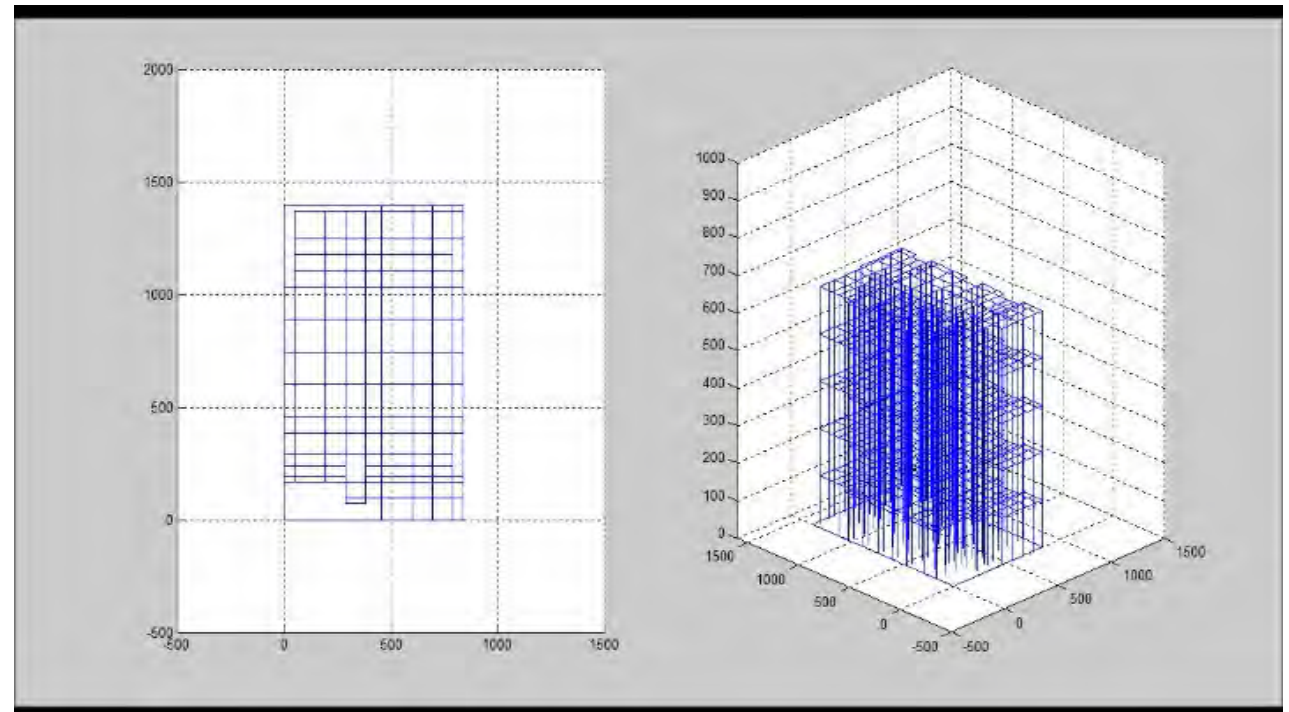
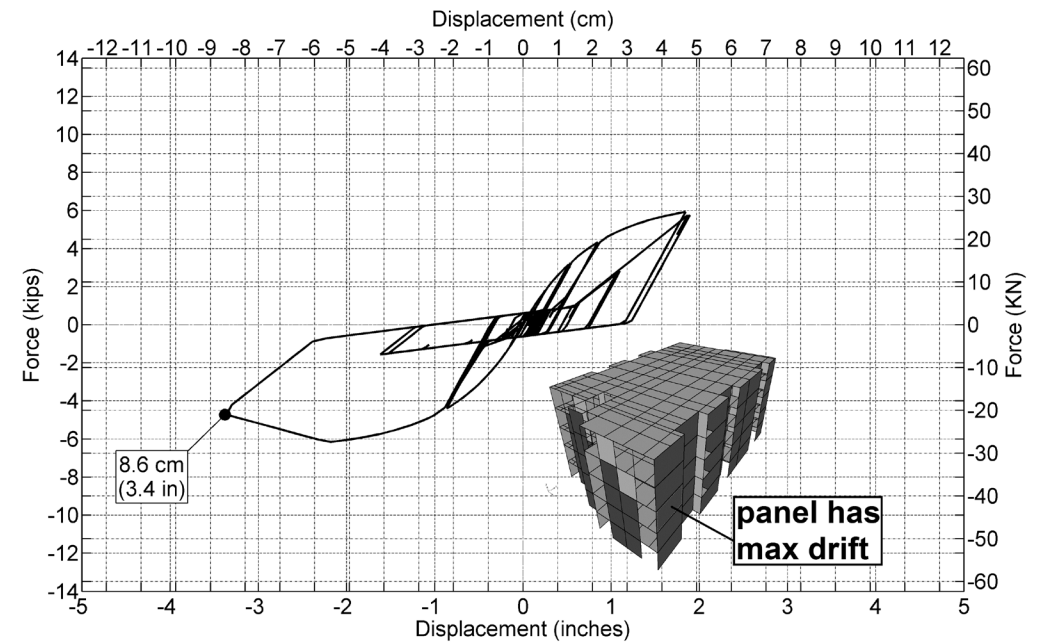
- New fastener model (from seismic):



Test data:

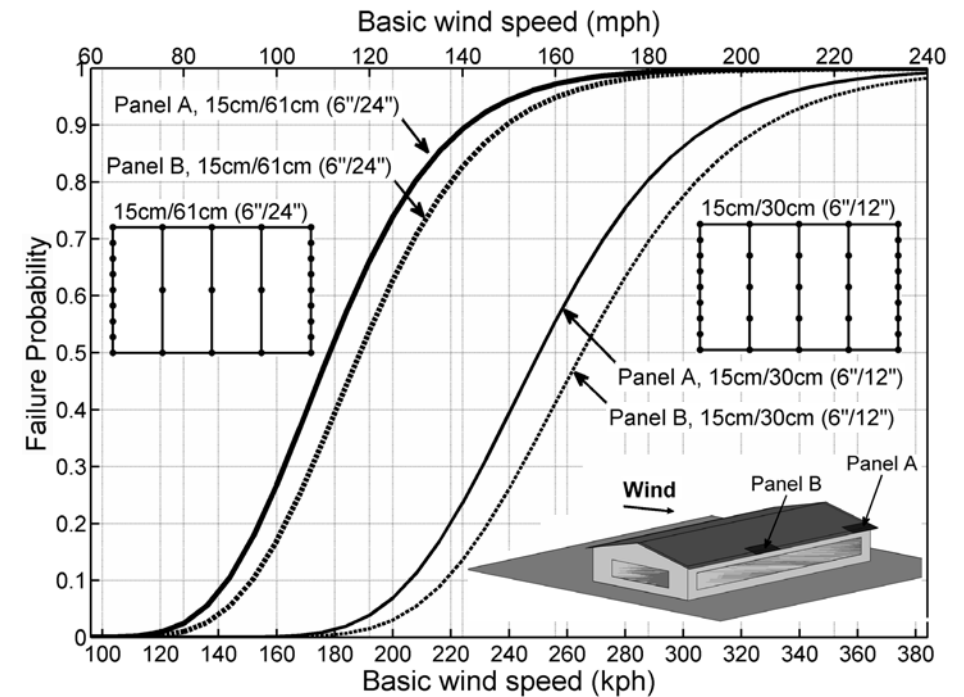
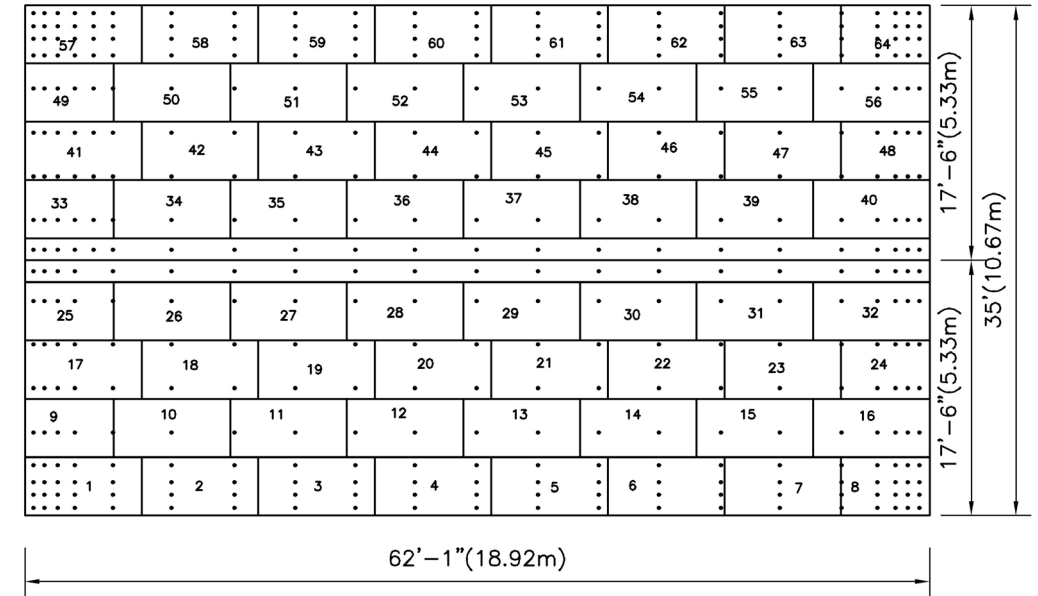
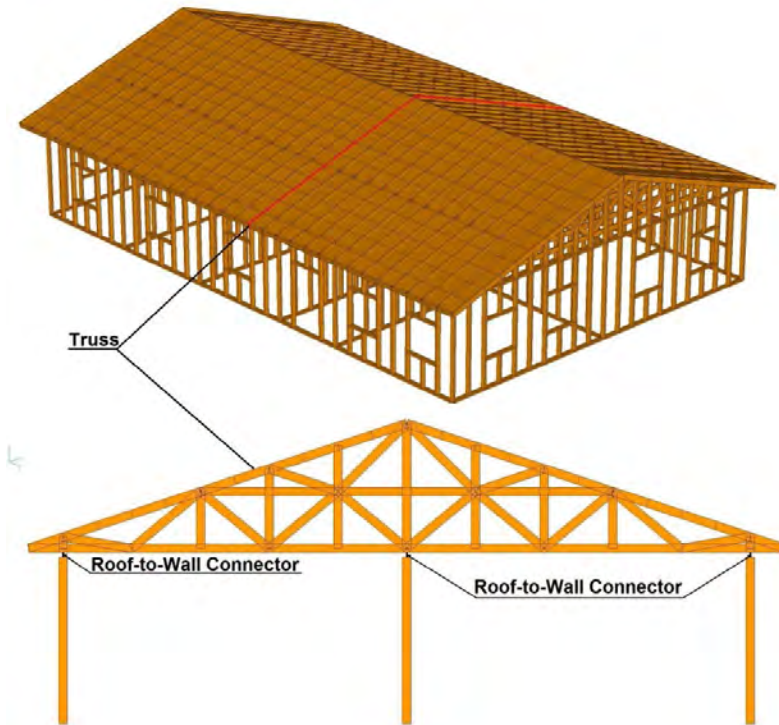


Model: Dao and van de Lindt, 2011



# Numerical Model (Cont.)

- Components and Building analysis:



Thank you!



**FIU**

# Understanding Hurricane Effects on Manufactured Homes

Funded by the Florida Division of Emergency Management

*A*

**KU**

# Project PIs



## Florida International University



Dr. Arindam Chowdhury



Dr. Ioannis Zisis



Dr. Amal Elawady



## University of Kansas



Dr. Elaina Sutley



Dr. William Collins



## University of Alabama



Dr. Thang Dao







# Mobile Home, Manufactured Home, what are we studying?

**FIU**



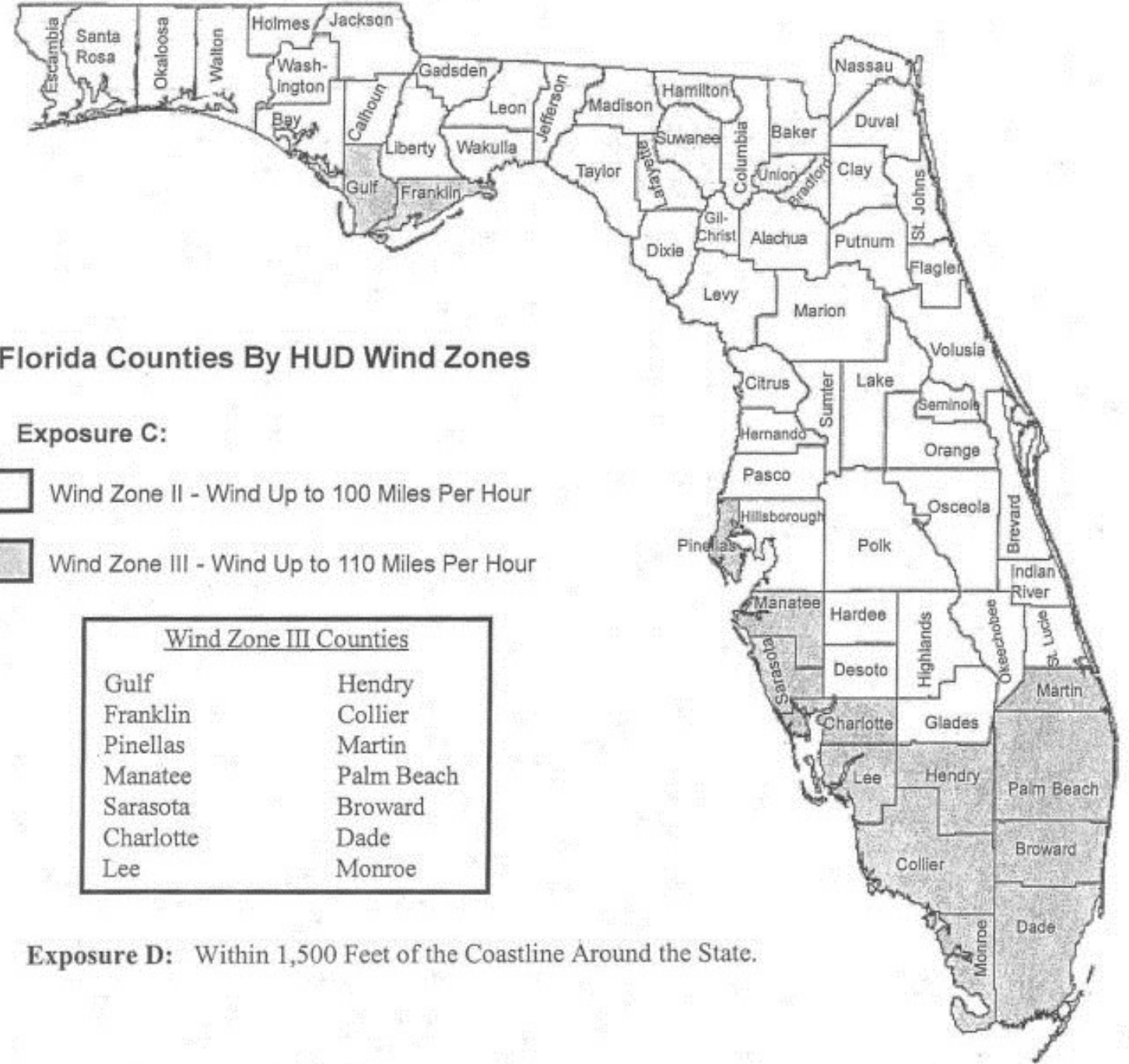
*A*

**KU**

# Manufactured Home Construction and Safety Standards

24 CFR 3280

commonly called the HUD Code



**Exposure D:** Within 1,500 Feet of the Coastline Around the State.

# Project Overview

- The overall goal of this research is to provide the fundamental knowledge needed to reduce the physical vulnerability of manufactured homes (MH) to wind events.
- The objective of the proposed research is to experimentally and numerically assess wind and wind-driven rain effects on MH units:
  - Develop a new dataset on aerodynamic effects on manufactured homes.
  - Develop detail-specific damage accumulation models for loading on MH fasteners and subassemblies.
  - Finite Element Modeling (FEM) of the non-linear behavior of MH units under moderate to extreme wind events.

# Aerodynamic Tests on Manufactured Home Communities

**Florida International University**

Arindam Gan Chowdhury, PhD

Ioannis Zisis, PhD

Amal Elawady, PhD

# Introduction

- Manufactured homes help fill a demand for affordable housing and currently shelter more than 20 million people in the US.
- More than 10% of the manufactured homes in the US are in coastal and hurricane prone areas.
- These homes are more vulnerable to extreme wind events than conventional residential houses.
- There is limited literature on the evaluation of realistic wind loads on manufactured homes and their communities, as well as wind resistance assessment of their envelope components.

# Research Aim

- Experimentally investigate the aerodynamics of manufactured homes and their communities using large-scale wind tunnel testing.
- Investigate interference effects on the wind loading of a manufactured home of interest.



# Selected Manufactured Home Configurations



Location 1: South Naples, FL

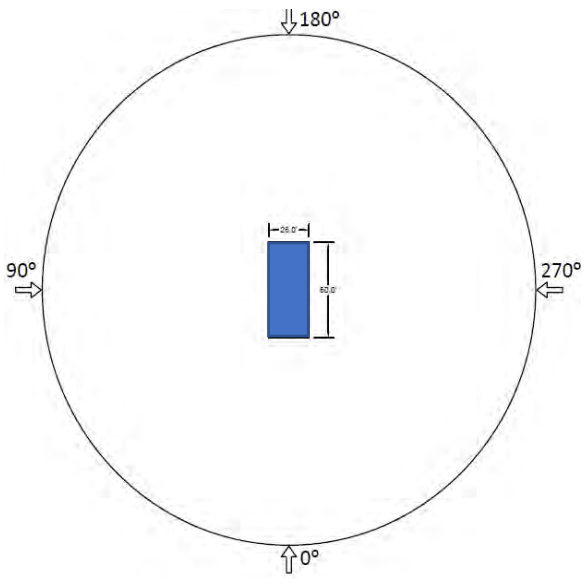


Location 2: Big Coppitt Key, FL

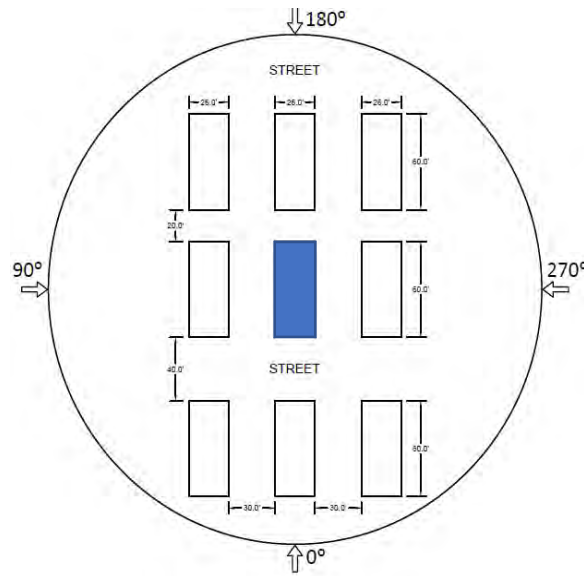


Location 3: Estero, FL

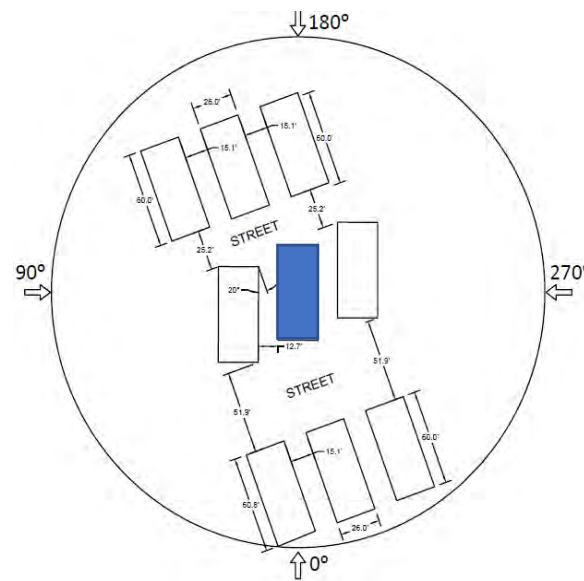
# Test Model Configurations



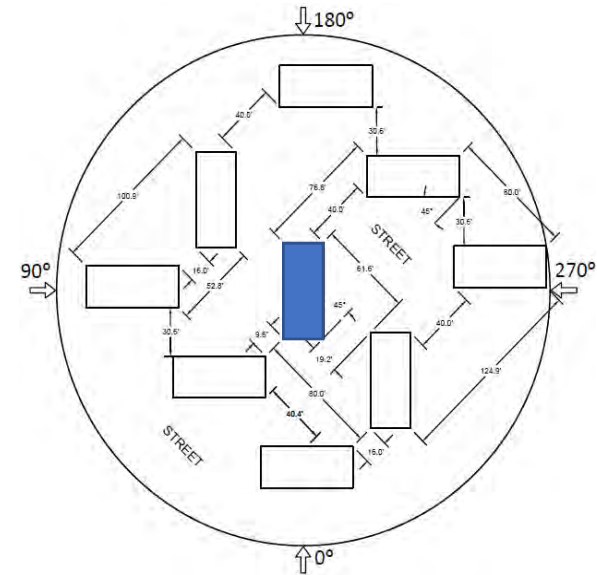
Isolated



Configuration 1



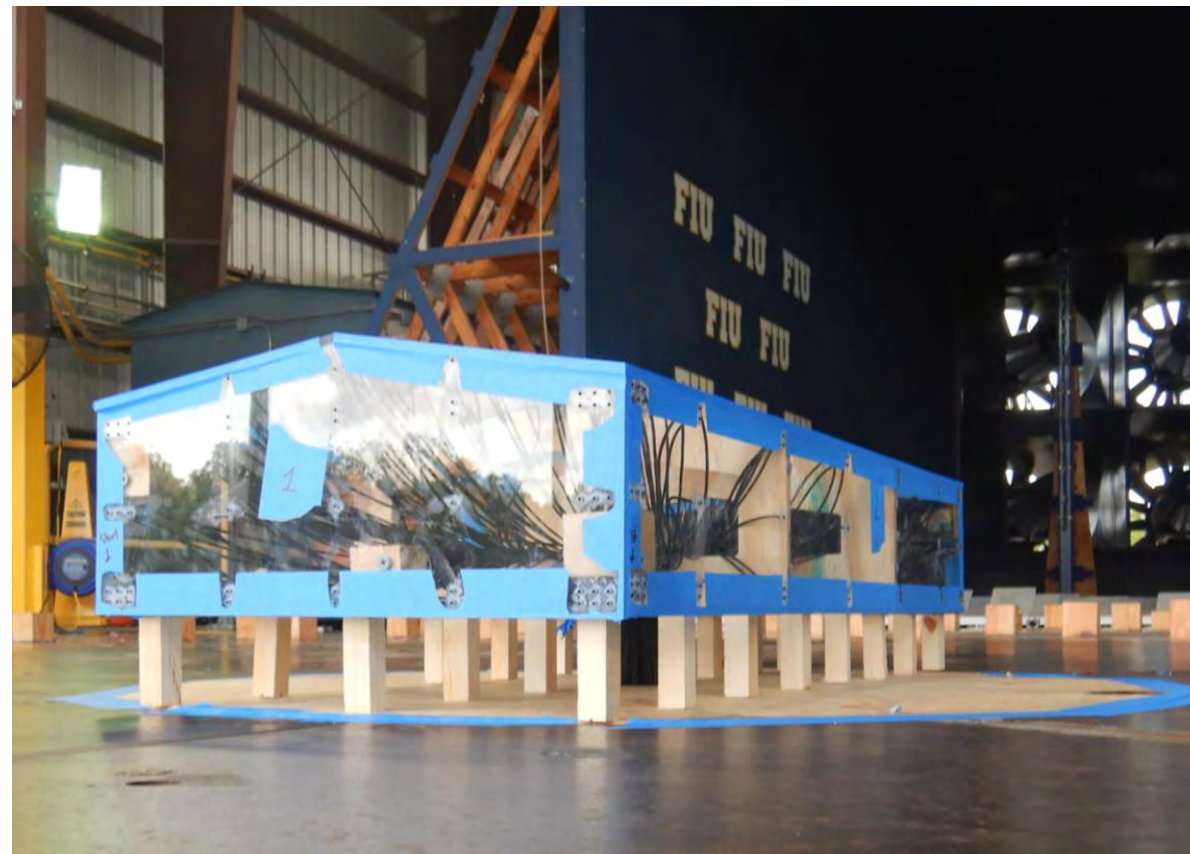
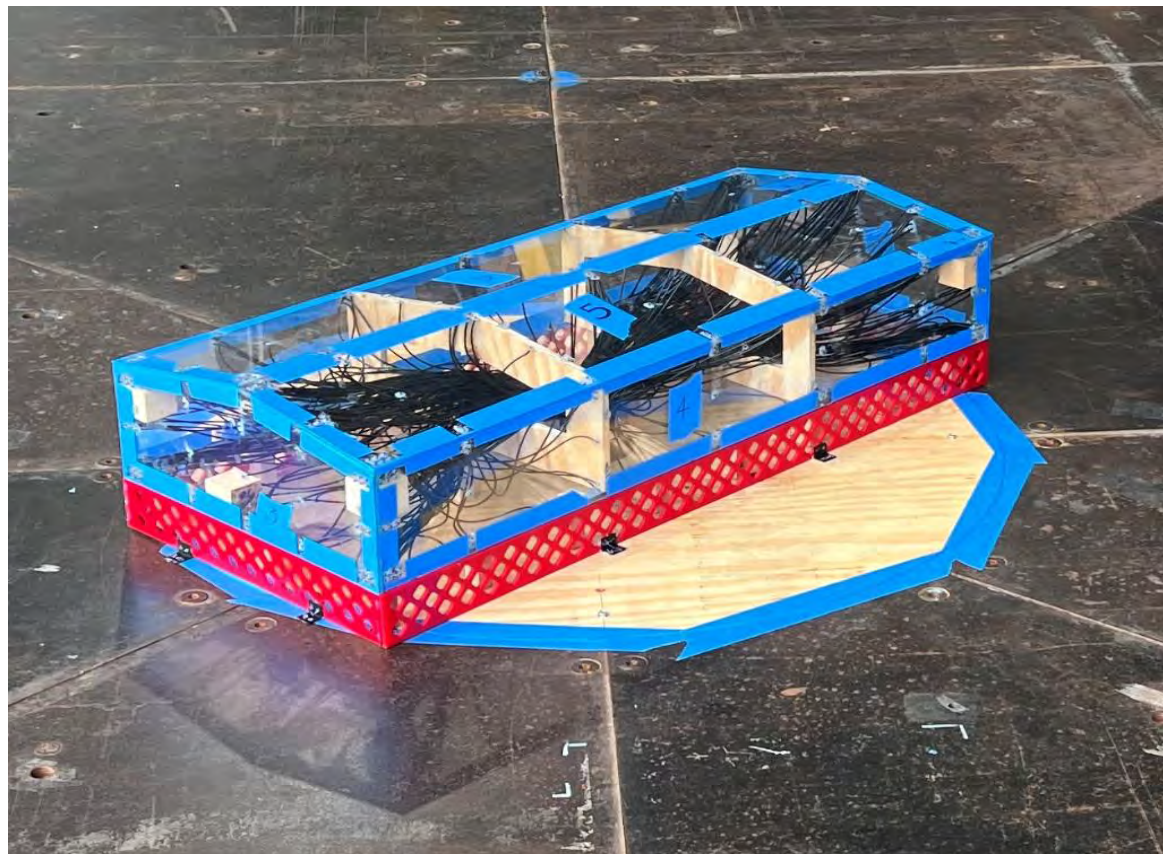
Configuration 2



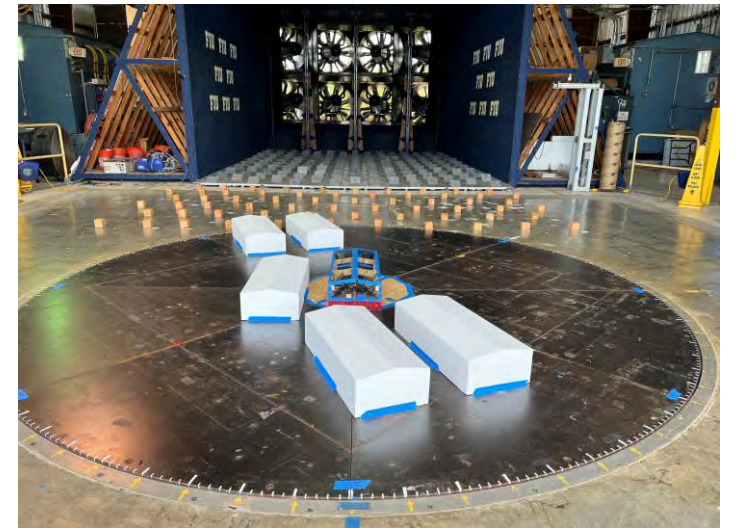
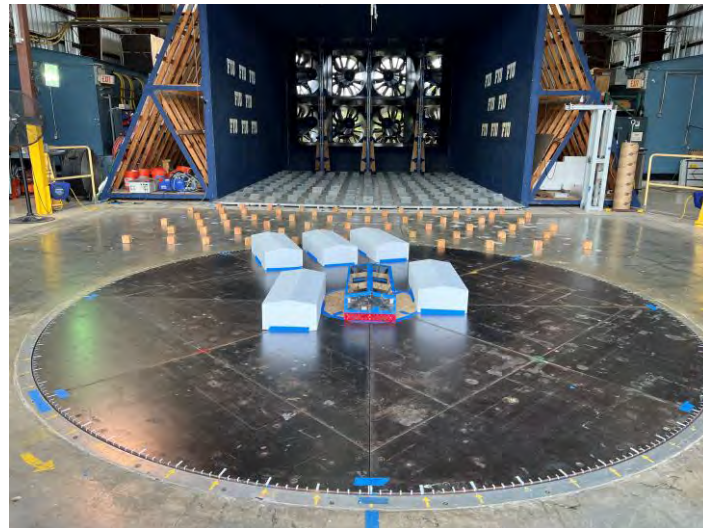
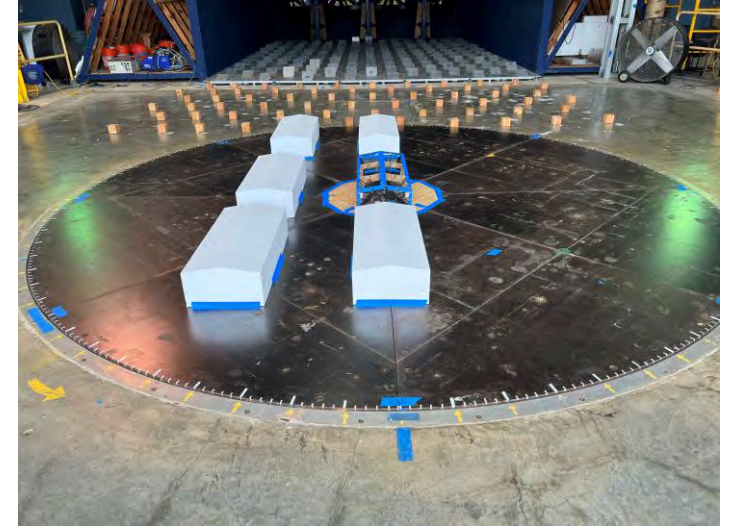
Configuration 3



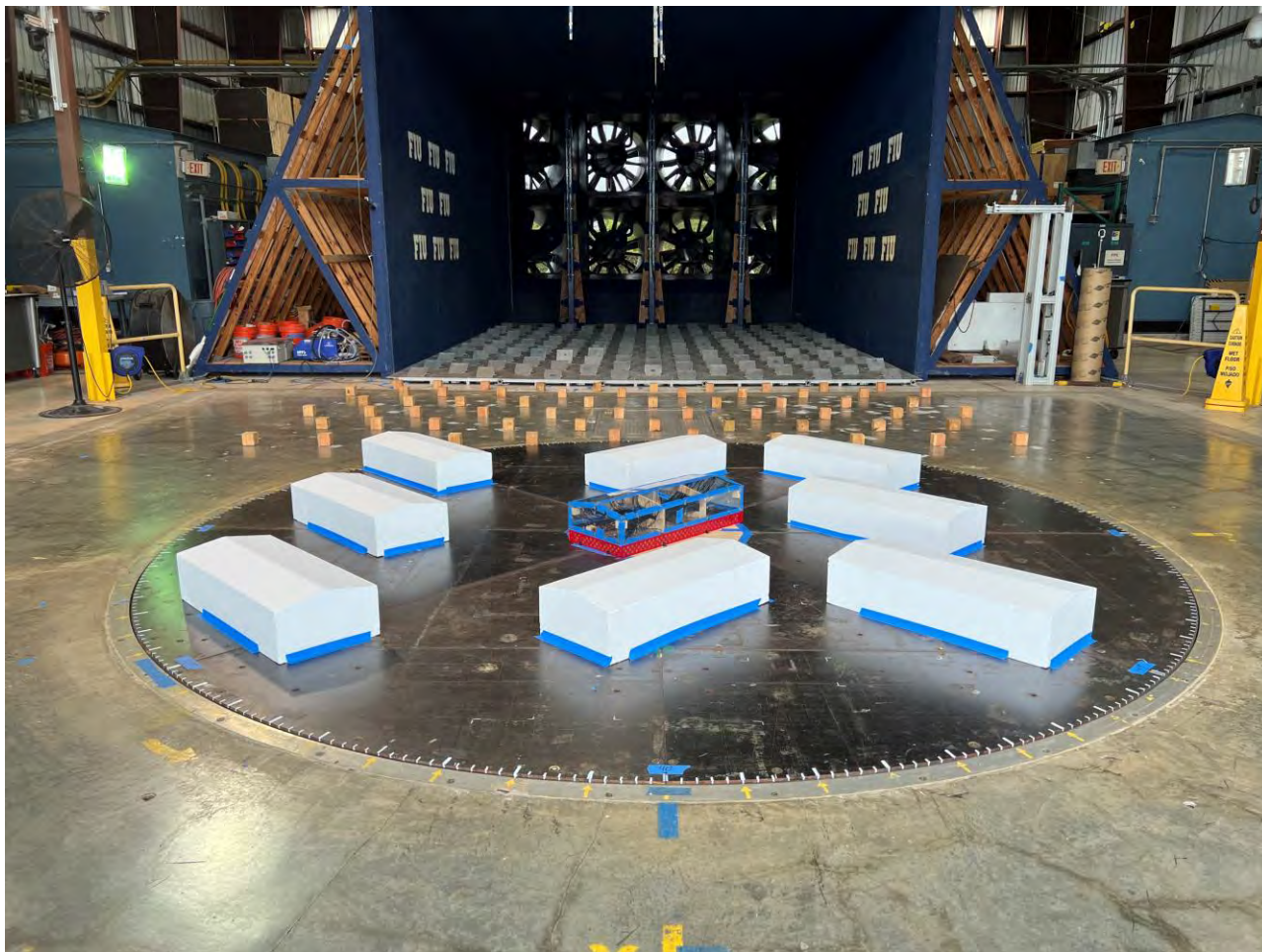
# Test Model Configurations



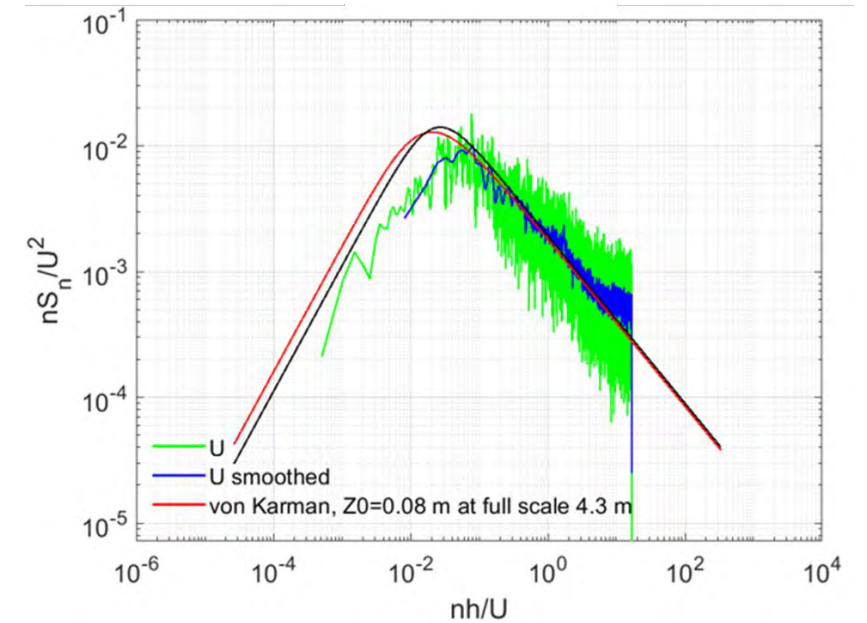
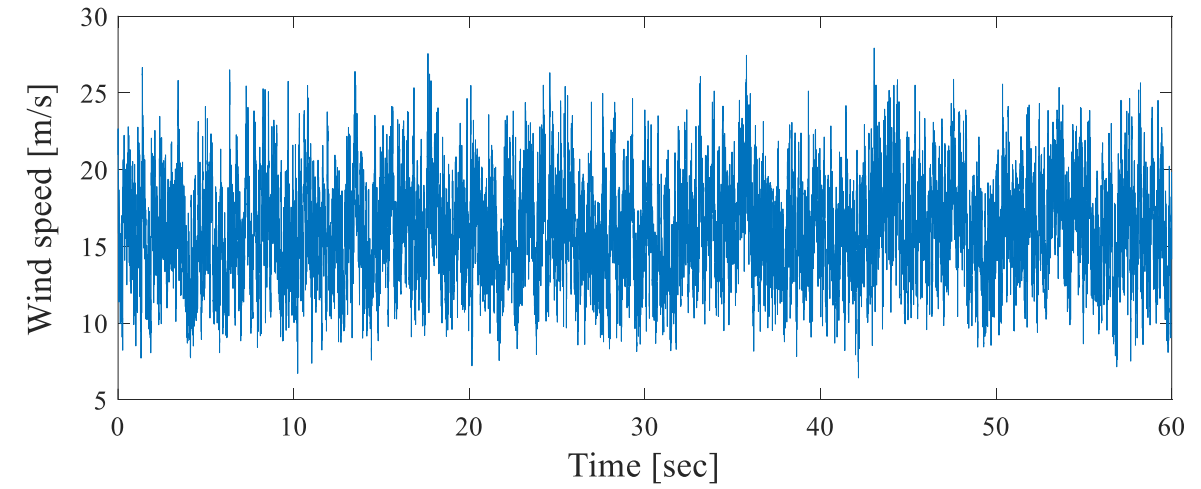
# Test Model Configurations



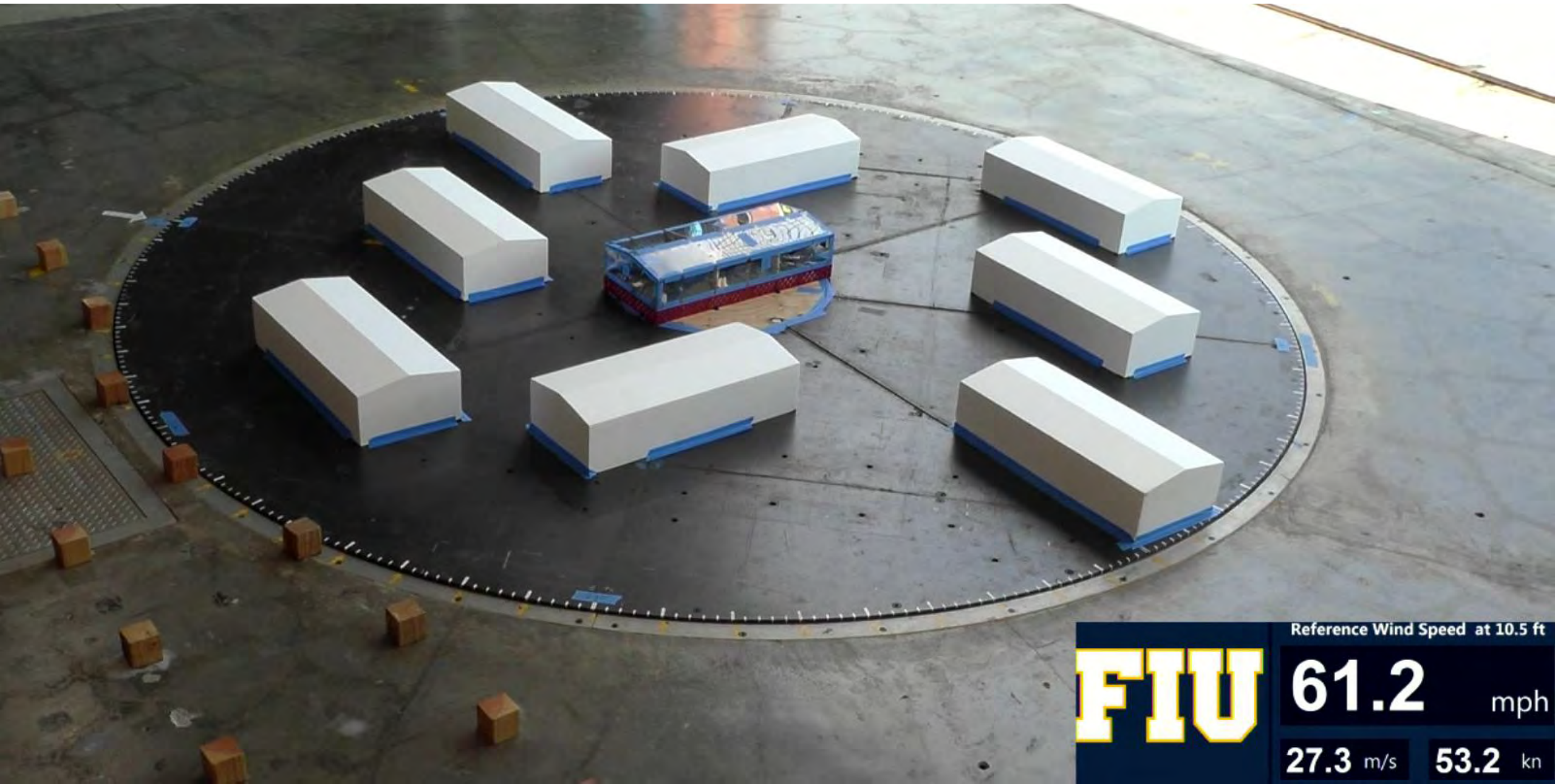
# Test Model Configurations



# Test Protocol



# Wind Tunnel Test

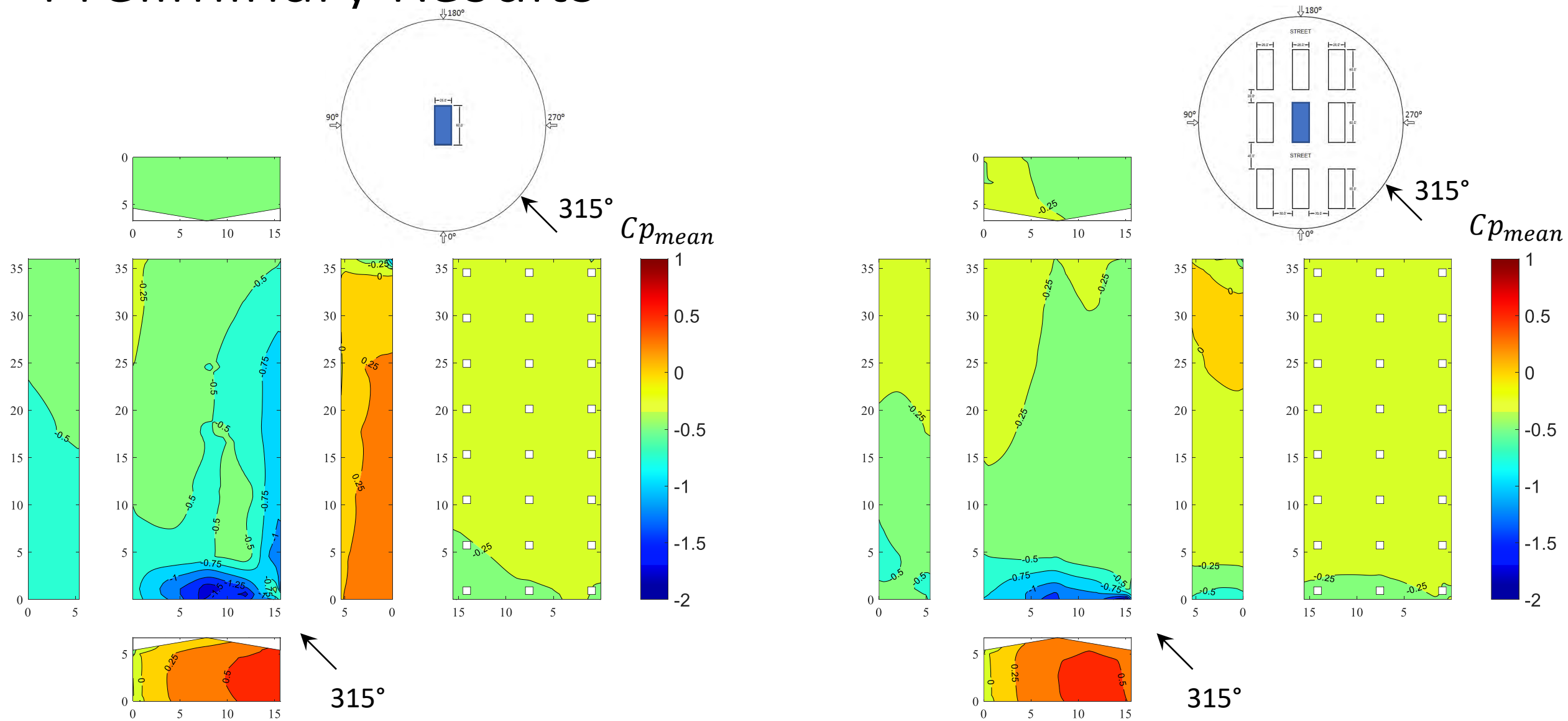


Reference Wind Speed at 10.5 ft

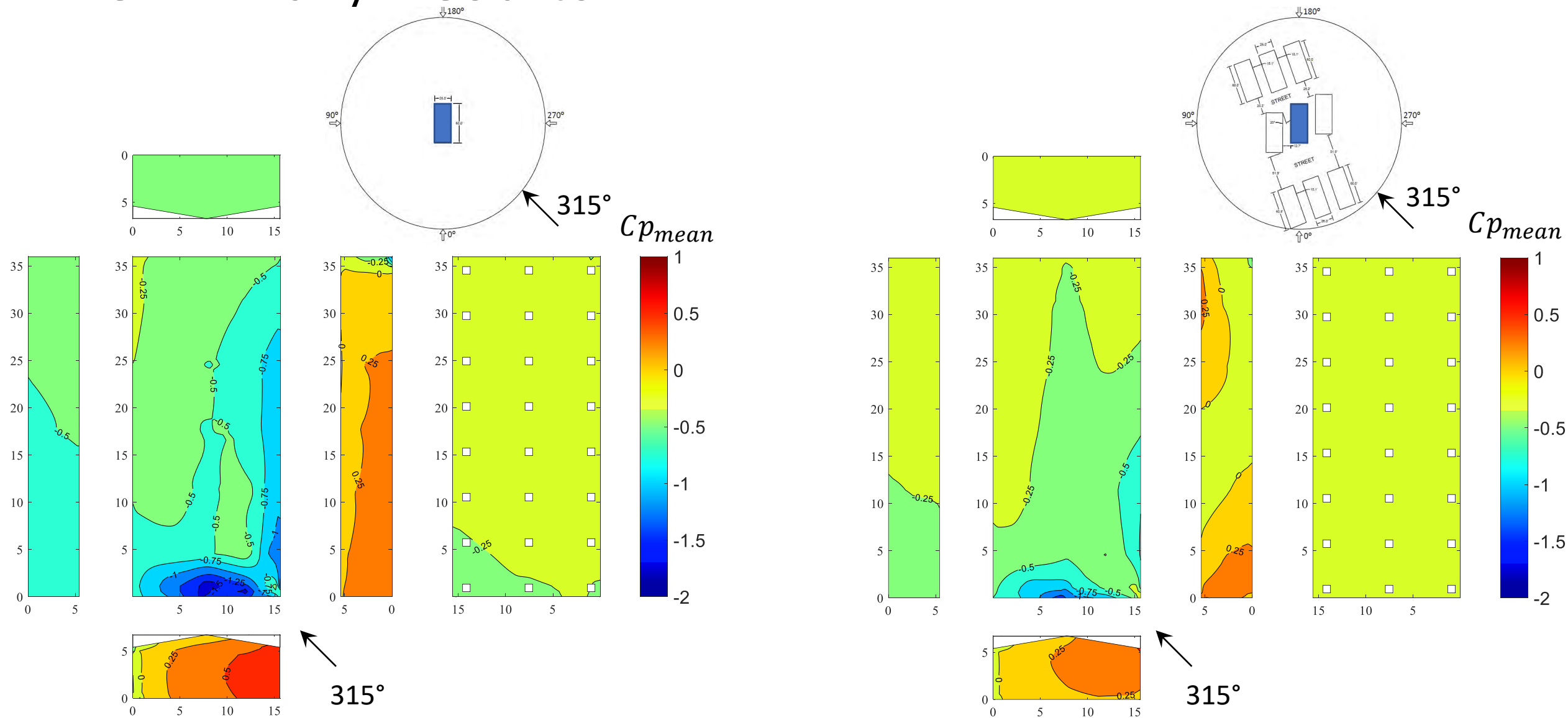
**FIU** **61.2** mph

27.3 m/s 53.2 kn

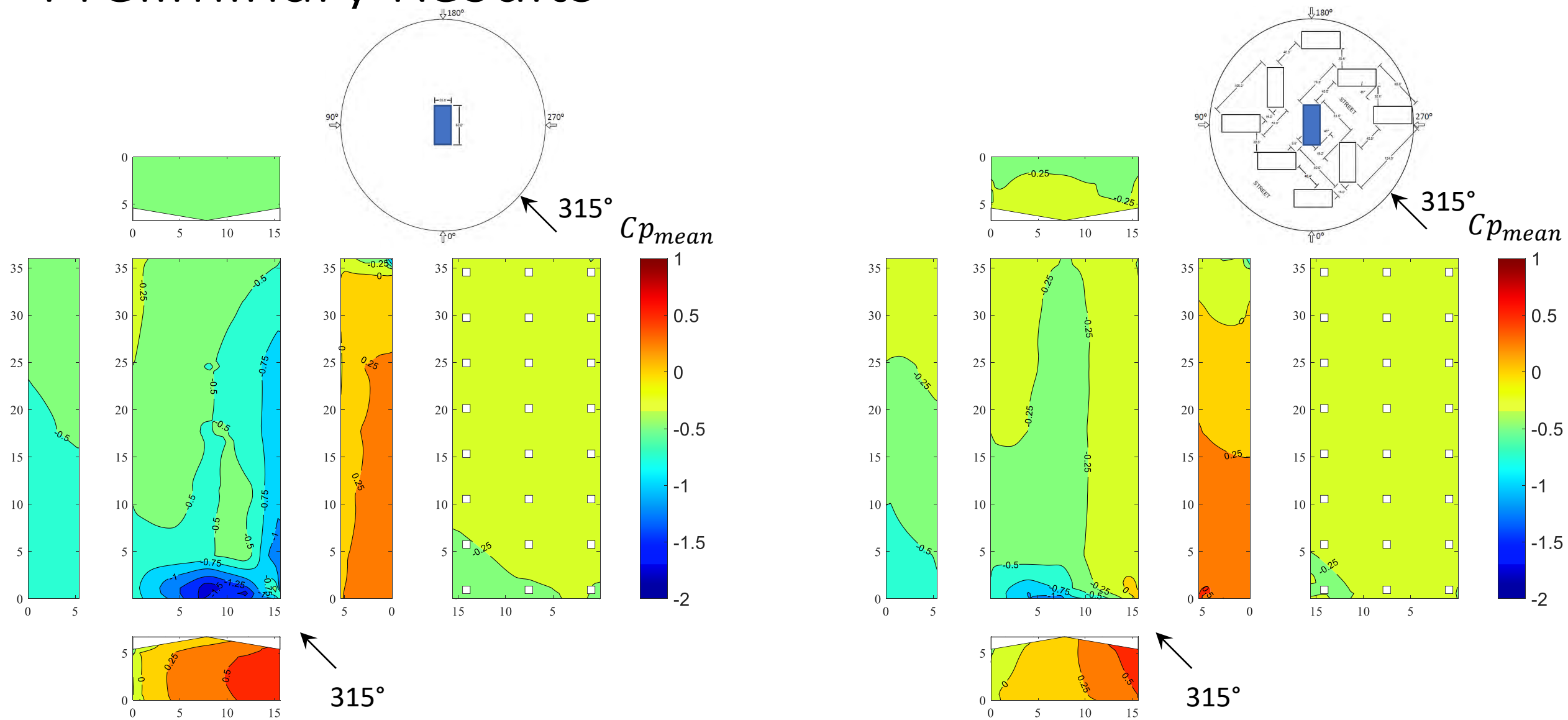
# Preliminary Results



# Preliminary Results

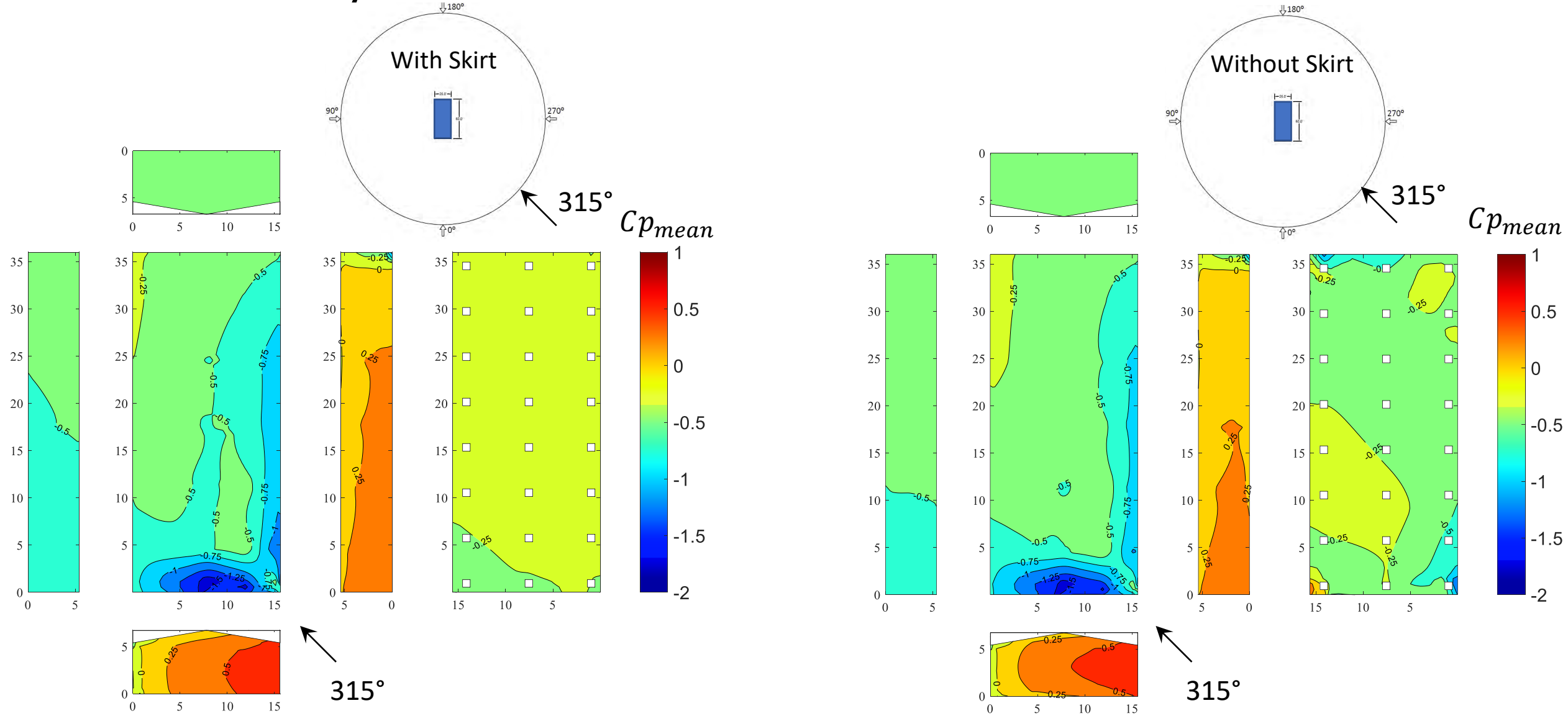


# Preliminary Results





# Preliminary Results



# Next Steps

- The pressure and force coefficient data obtained from this study will be used to inform building component testing and numerical simulations of the behavior of manufactured homes during extreme wind events.
- The findings of this study can be also used to help improve risk assessments of manufactured homes.



Thank you!

**Feedback and recommendations for future test phases are greatly appreciated!**



# Component-level Experimental Testing Program

**University of Kansas**

Afeez Badmus, PhD Student

Cyra Chronister, Undergraduate Student

William Collins, PhD

Elaina Sutley, PhD

# Critical connections

- Wall-to-floor
- Roof-to-wall
- Sheathing-to-rafter
- Foundation

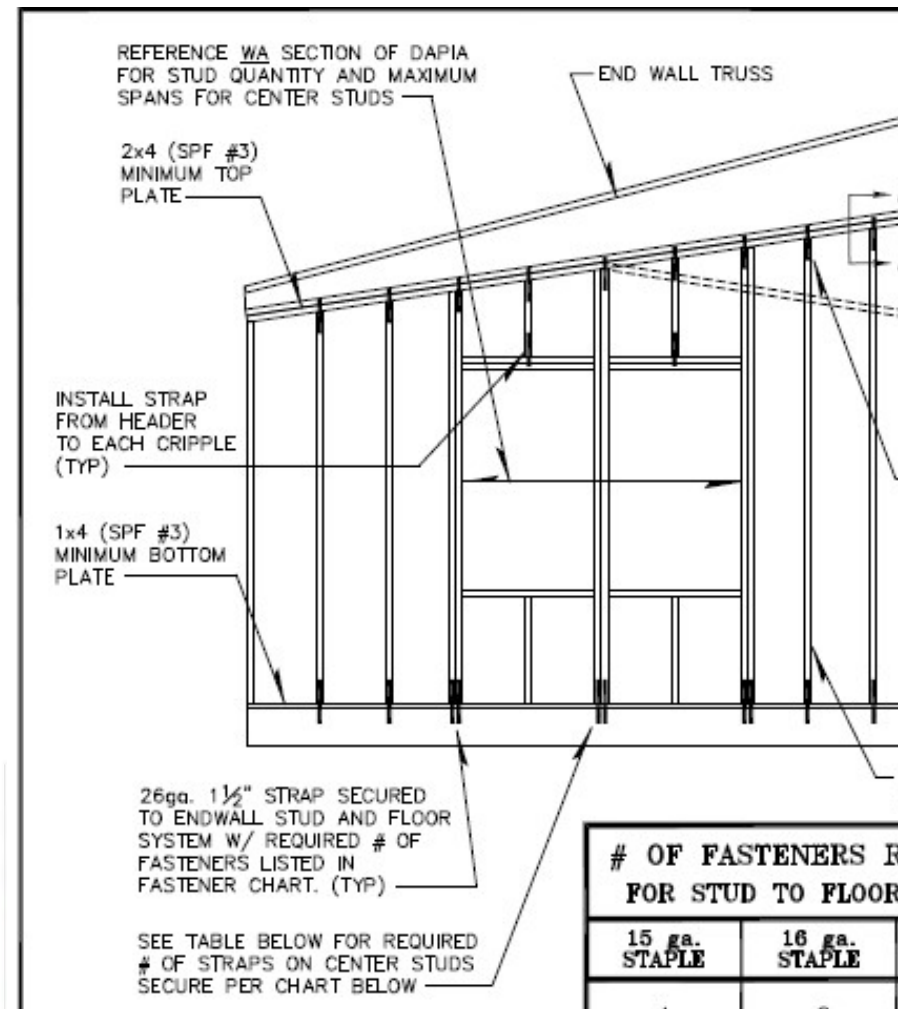
# Variability in structural details for Wind Zone II Homes

- Lumber
  - 2x4
  - 2x3
  - 1x4
- Fasteners
  - Nails (6d, 8d, 10d)
  - Screws
  - Staples
- 26 gage strap



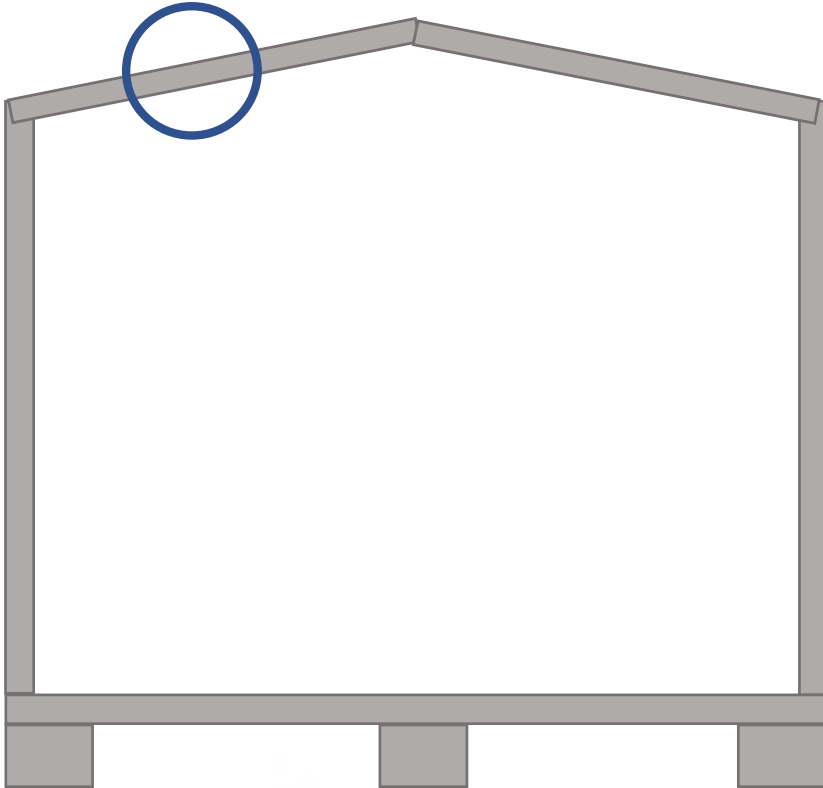
Click image to open expanded view

[Tie Down Engineering](#)  
 59155 Certified Galvanized Strapping - 37'  
 Brand: Tie Down  
 ⭐⭐⭐⭐⭐ 365 ratings  
 | 28 answered questions  
 \$30<sup>27</sup>  
 Save up to 8% with business pricing. Sign up for free Amazon Business account. Not eligible for Amazon Prime. Available with free Prime shipping from other sellers on Amazon.  
 Material Alloy Steel  
 Brand Tie Down  
 Number 12 of Pieces



# OF FASTENERS REQUIRED PER END OF STRAP FOR STUD TO FLOOR STRAPS LOCATED AT OPENINGS				
15 ga. STAPLE	16 ga. STAPLE	.131 NAIL	.113 NAIL	.099 NAIL
4	6	4	6	8

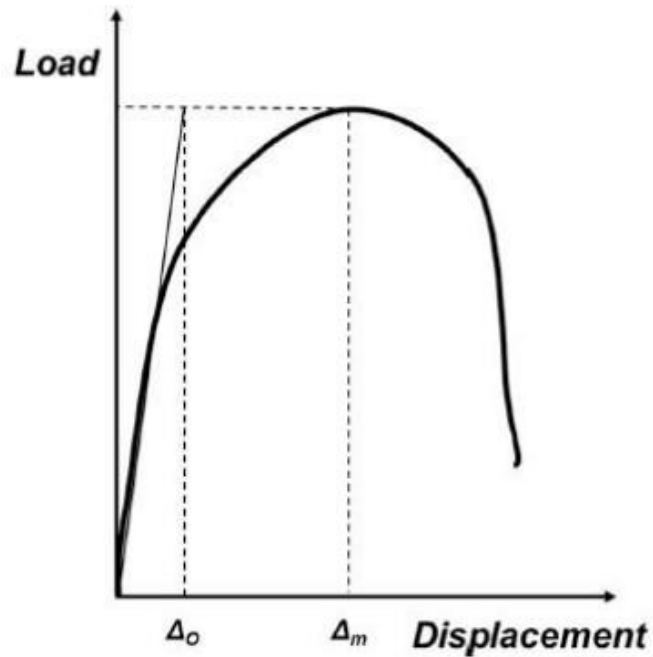
# Sheathing-to-Rafter Connection



- Identified as critical gap in knowledge
  - Cyclic behavior not quantified
- Various construction details
  - SPF vs SYP
  - OSB vs 3-ply Plywood (7/16" – 1/2")
  - #8 screw vs 8d common nail
- Different failure modes
  - Pull-out vs Pull-through

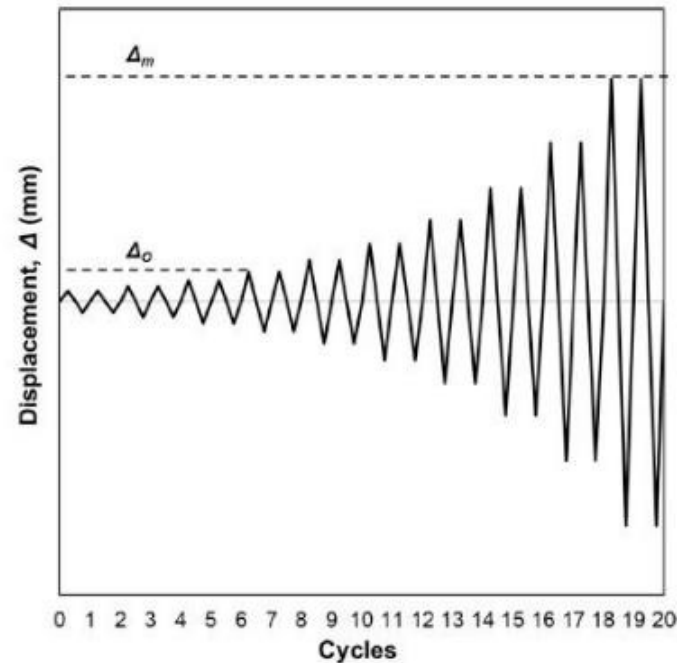
# Testing Protocol

## Step 1: Monotonic Loading

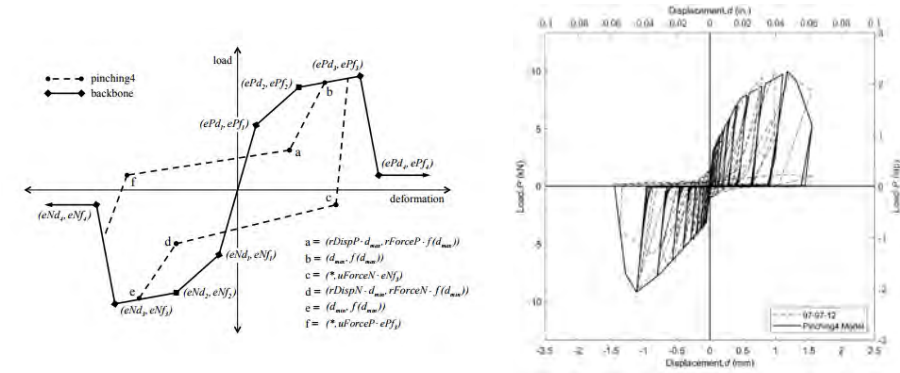


Schematic representation of  $\Delta_0$  and  $\Delta_m$  from monotonic test result (Boadi-Danquah et al, 2021)

## Step 2: Cyclic Loading



Schematic cyclic displacement protocol in accordance with FEMA 461 (Boadi-Danquah et al, 2021)



- What does cyclic behavior look like for roof wind loads?

$\Delta_0$  = initial state of damage, where initial linearity intersects with peak load.

- How do fasteners unload in wood roof systems?

$\Delta_m$  = Displacement at  $P_{max}$

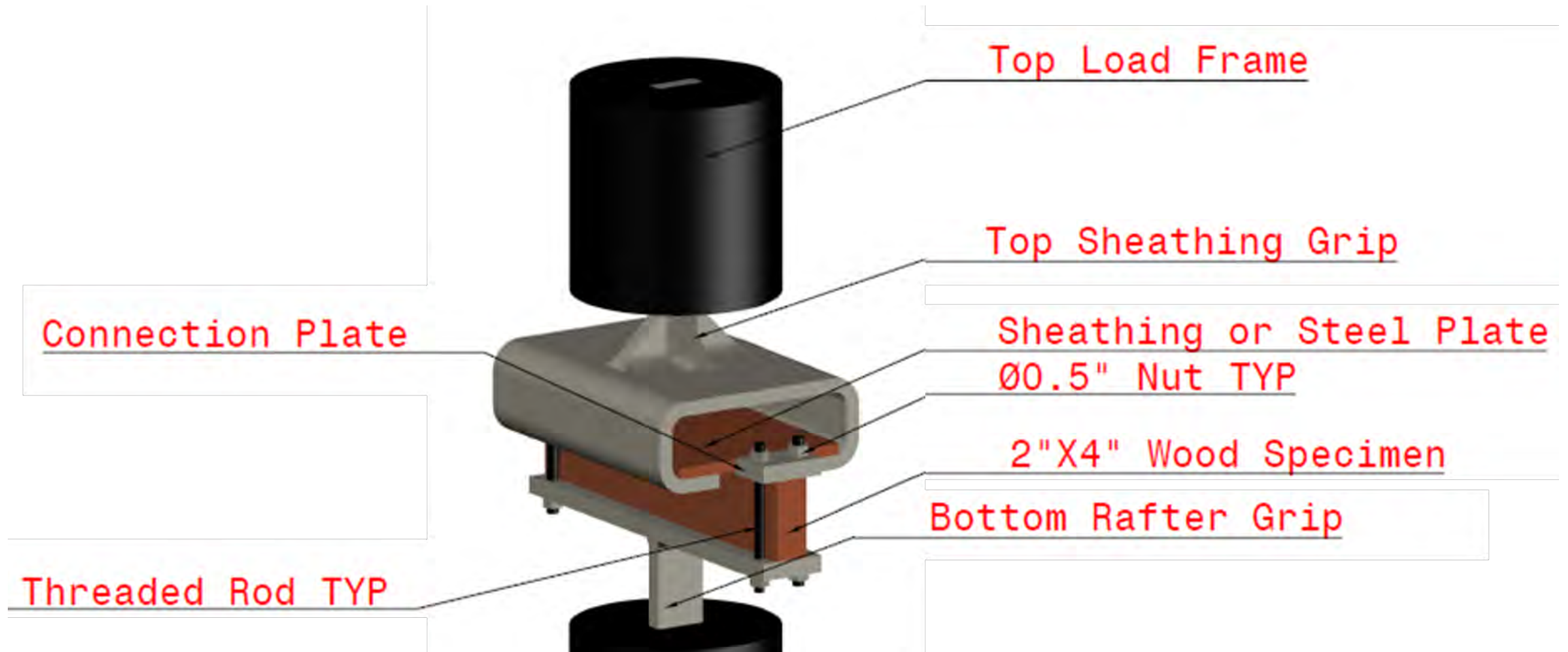
For cyclic test, each step (displacement amplitude) consists of two cycles; then amplitude is increased

- What are cyclic effects on pull-out? Pull-through?

Wu et al. 2014



# Test Fixture Setup



# Test Fixture Setup



Displacement measured at:

- Cross-head
- Sheathing centerline
- Fastener head

# Test Fixture Setup



Rafter Pull-out



Sheathing Pull-through

# Test Fixture Setup



Edge

Field

# Test Matrix

Sheathing Type	Sheathing Thickness (in.)	Rafter Type	Fastener Type	Fastener Size (in.)	Head Diameter (in.)	Monotonic Test		Cyclic Test	
						Field	Edge (2)	Field	Edge (2)
OSB	7/16	SPF	8d common	0.113" x 2.375"	0.281	5	5	5	5
		SYP				5	5	5	5
		SPF	#8 screw	0.164" x 2.0"	0.315	5	5	5	5
		SYP				5	5	5	5
		SPF	8d common	0.113" x 2.375"	0.281	5	5	5	5
		SYP	#8 screw	0.164" x 2.0"	0.315	5	5	5	5



# Nominal Capacity Calculations

Ultimate withdrawal capacity (pull-out),  $W_u$ :

$$W_u = 14250 G^2 D$$

$G$  = Specific Gravity of Wood ( $G = 0.42$  for SPF)

$D$  = Diameter of the screw shank ( $D = 0.164$ " for #8)

$$W_u = 412.25 \text{ lbf/in}$$

Embedded threaded length of screw = 1.299"

Pull-out:

$$W_u = \underline{\underline{536 \text{ lbf}}}$$

Fastener head pull-through,  $W_H$ :

$$W_H = 690 * \pi * D_H * G^2 * t_{ns}$$

$G$  = Specific Gravity of OSB ( $G = 0.5$ )

$D_H$  = Fastener head diameter ( $D_H = 0.315$ " )

$t_{ns}$  = Net side member thickness ( $t_{ns} = 7/16$ " )

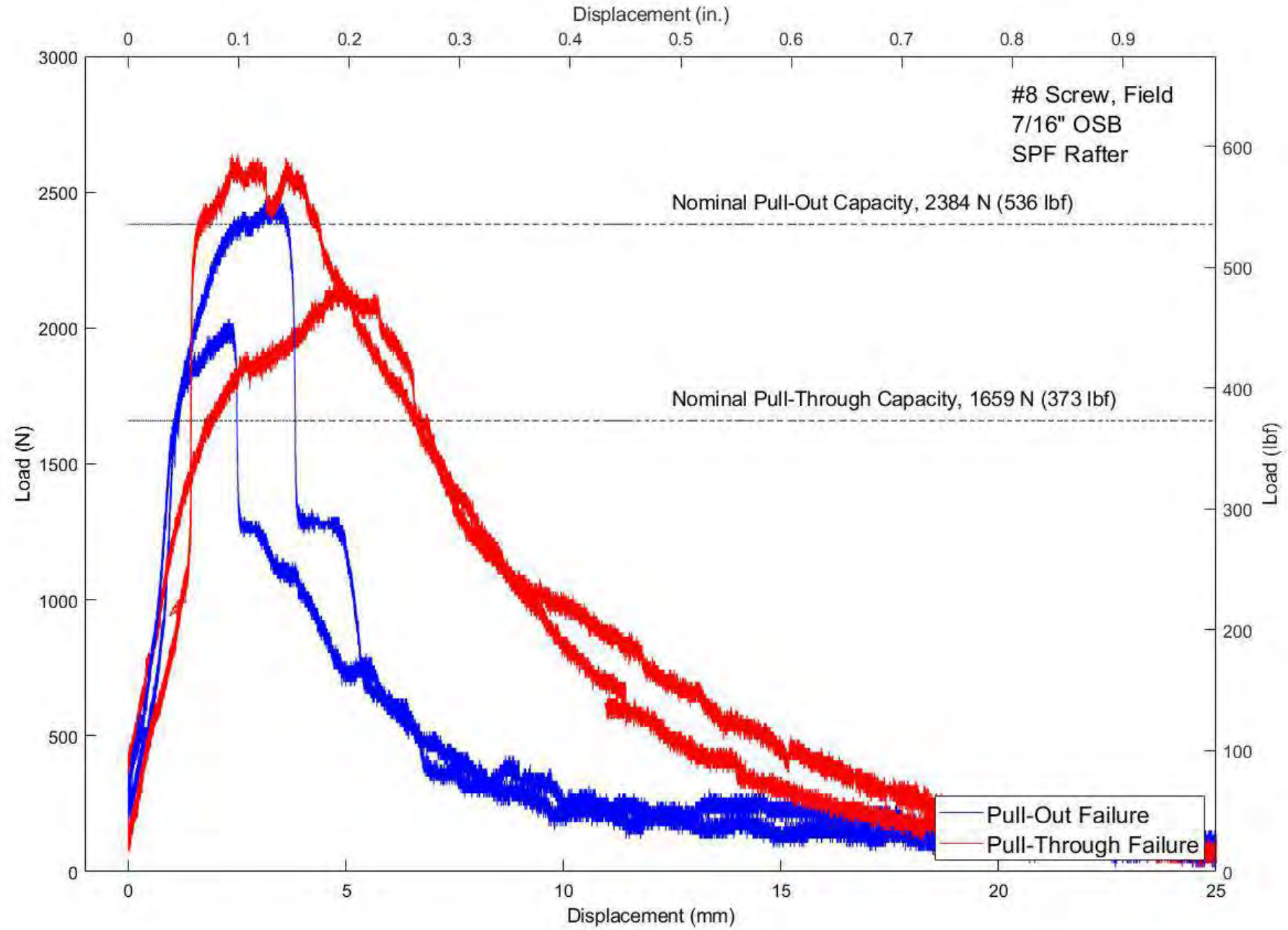
$$W_H = 74.68 \text{ lbf}$$

Empirical FOS ~5

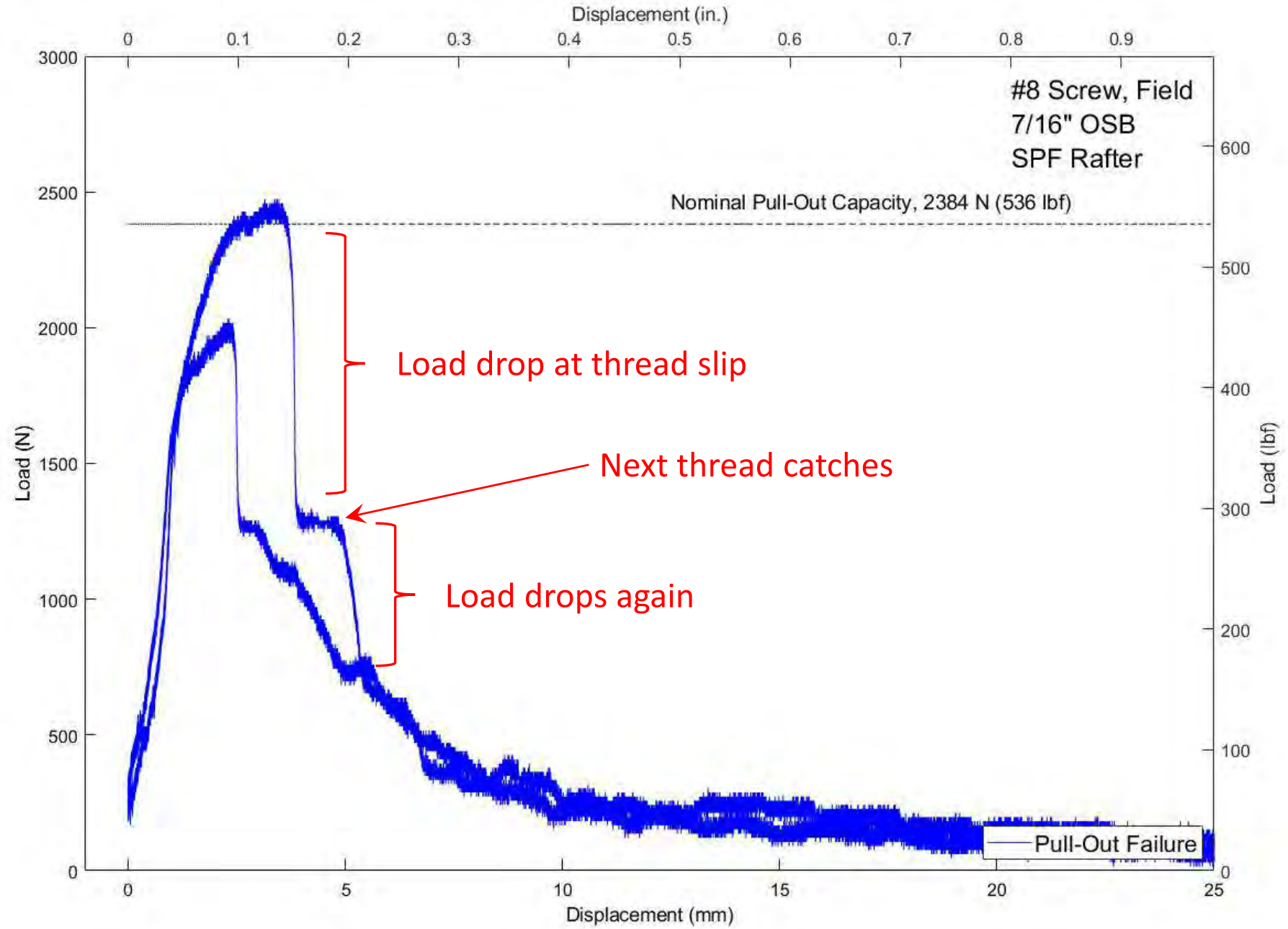
Pull-through:

$$W_H = \underline{\underline{373 \text{ lbf}}}$$

# Monotonic Testing

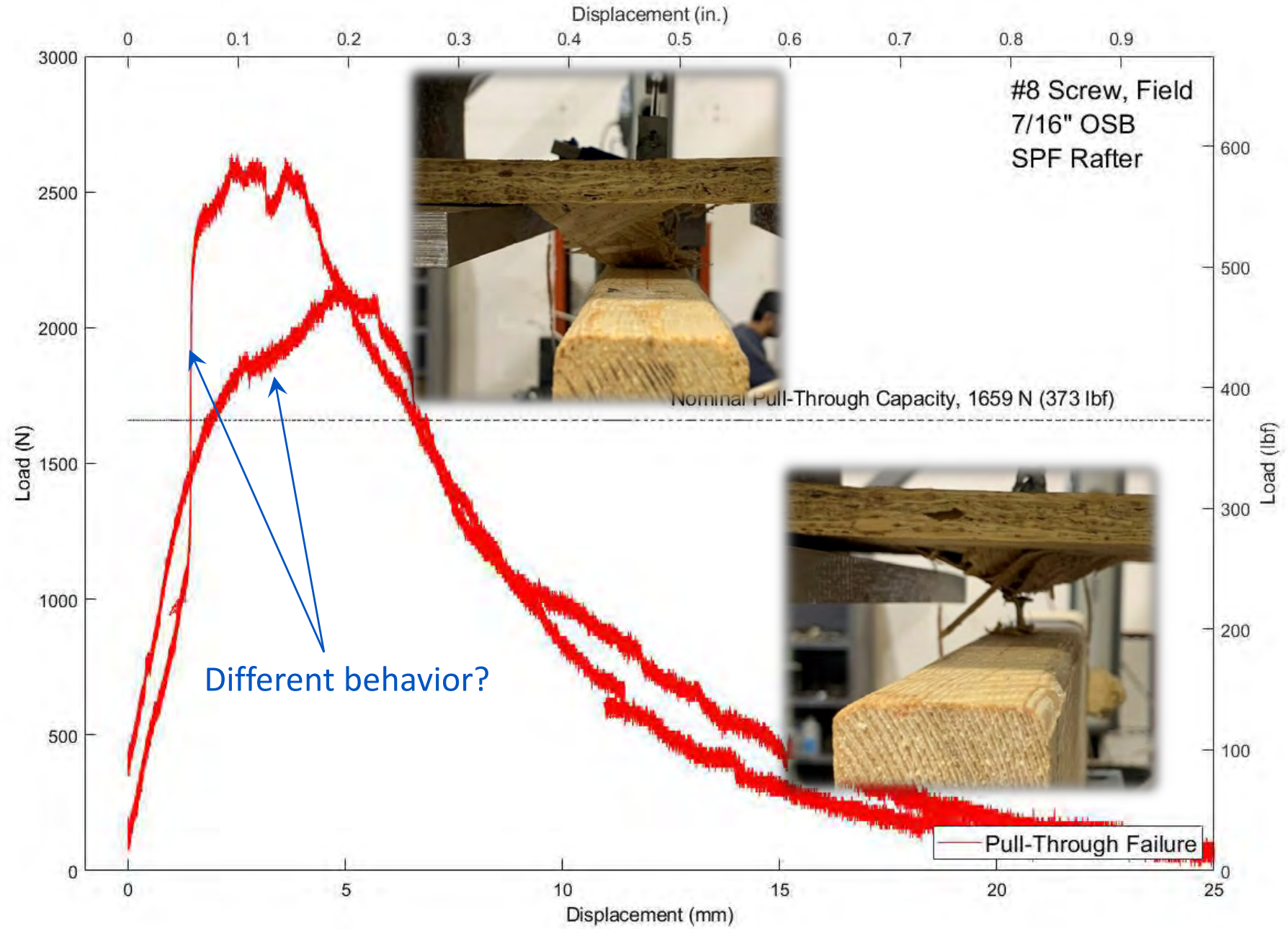


# Monotonic Testing

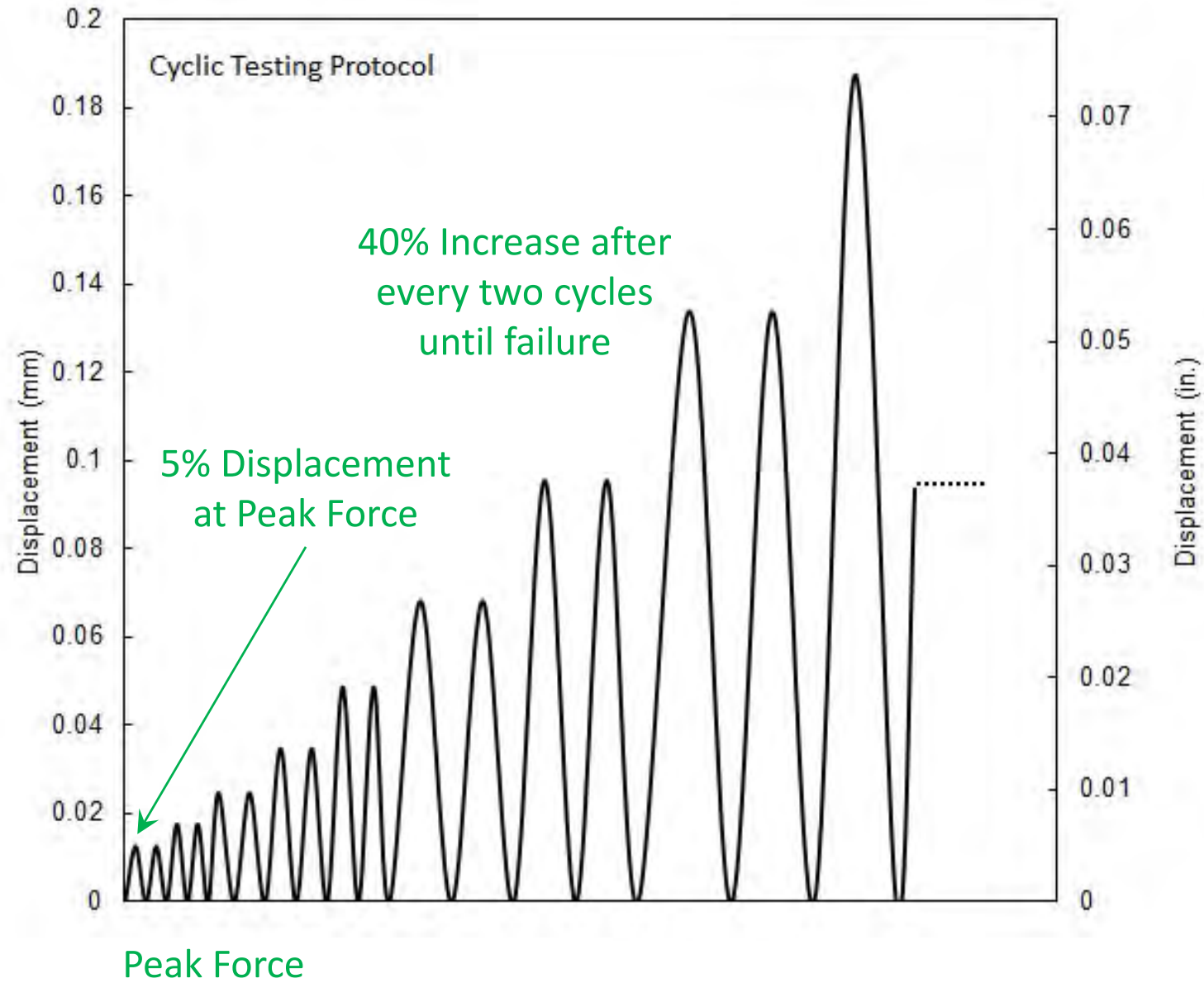




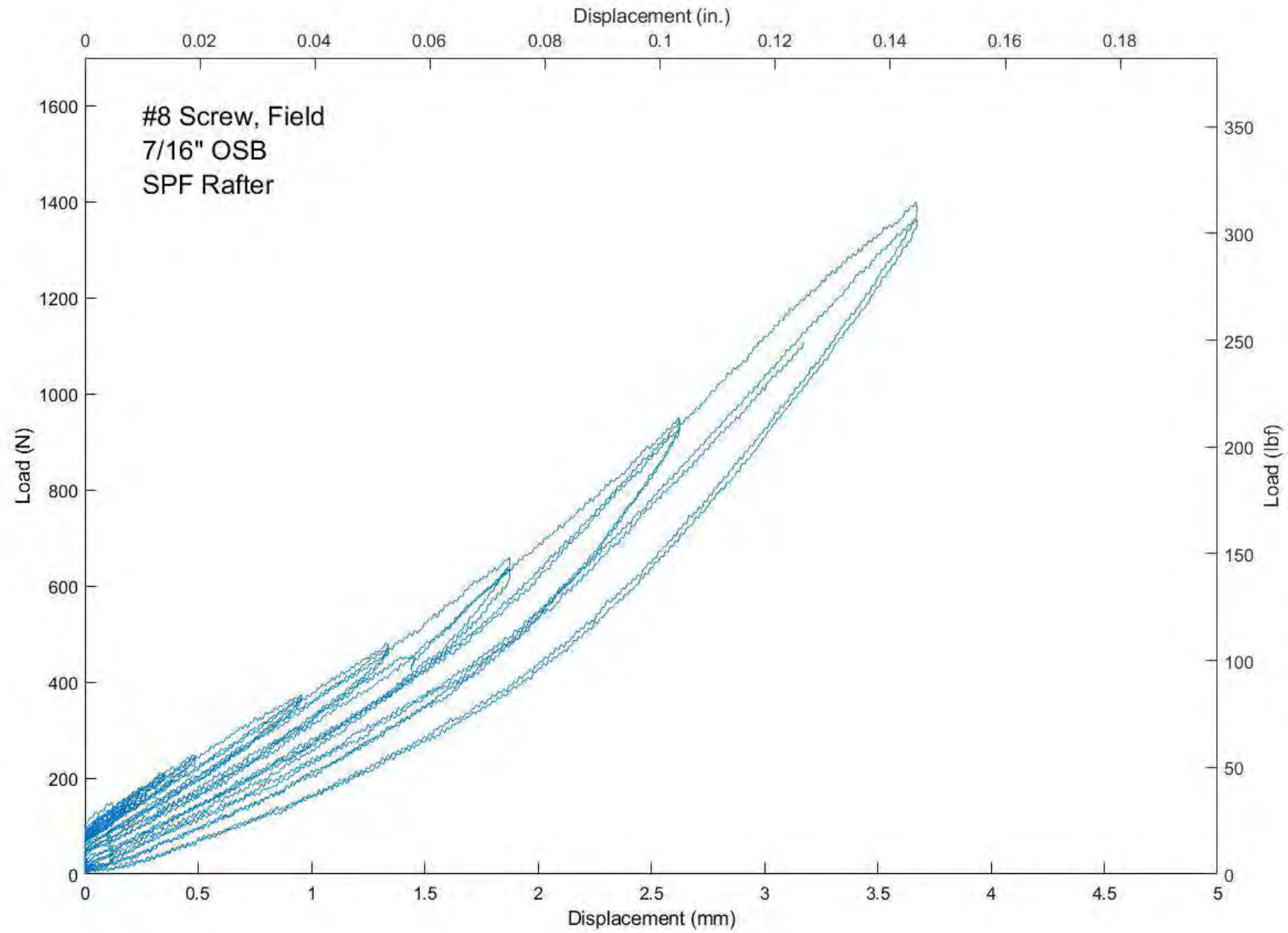
# Monotonic Testing



# Cyclic Testing



# Cyclic Testing



## Summary and Next steps

- Fastener tests in wood are highly variable
  - Both in terms of capacity and behavior
  - Need to adjust testing matrix to capture variability
  - Data does correspond to NDS values
- Nonlinearity/Damage under small displacements
  - Results in extremely long cyclic tests
- Being very intentional to isolate behavior to be able to send the best data to UA
- Already have materials purchased for other connections



**FIU**

Thank you!

*A*

**KU**

# Nonlinear Dynamic Analysis of Manufactured Homes subject to Hurricane-induced Wind Loads: Numerical Study

**Farhan A. Chowdhury, Thang N. Dao**

Department of Civil, Construction and Environmental Engineering  
The University of Alabama

June 28, 2022

# Overview

- Introduction
- Research Objective
- Previous Numerical Models
- Hysteresis Model
- Modeling Concept
- Results



Image Courtesy: Manufactured Housing Institute (MHI)

# Introduction

- Manufactured Home Units (MHU) gaining traction in US.
- Shortcomings in current building codes for MHUs.
- Limited work on LFWC, which is different from MHUs.
- Seismic vs. wind loads:
  - Lateral vs. vertical load paths and different failure modes.
  - Adjustments needed for hysteresis model (cyclic behavior).



# Research Objective

- Develop numerical (FE) model to study short-term damage on MHU under wind loads.
- Nonlinear load-deflection relationships for components.
- Calibration of hysteresis parameters from K.U. connection tests.
- Pressure coefficient time-histories from F.I.U. wind tunnel tests as input to numerical model.

# Previous Numerical Models

- Nonlinear roof sheathing fastener (nail) model for wind load by [Dao and van de Lindt](#) (2008; 2009).
- [Steven Cai](#) (LSU) and [Arindam Chowdhury](#) (FIU) lead studies (2018) on failure of low-rise timber buildings under extreme wind.
- 10 parameter hysteretic spring model [Folz and Filiatrault](#) (2001).
- Seismic performance of mid-rise CFS building frames by [Dao and van de Lindt](#) (2013; 2014).
- ASCE 7 static wind load vs. dynamic load from wind tunnel test.

# Hysteresis Model

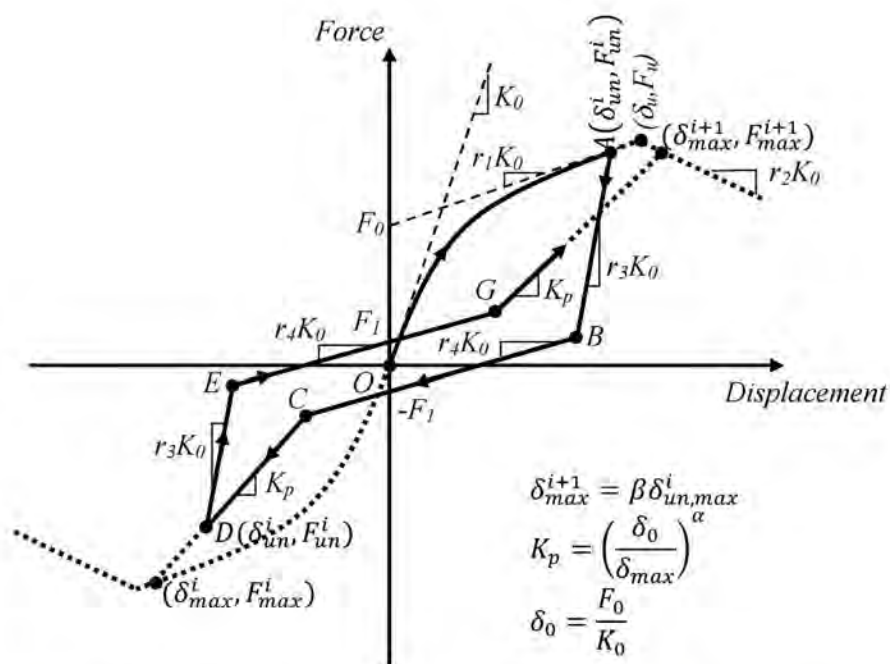
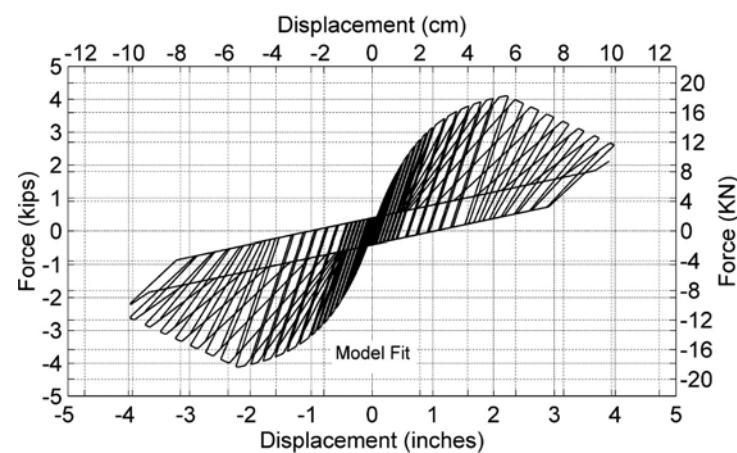


Fig. Ten-parameter hysteresis model (data from Folz and Filiatrault 2001)

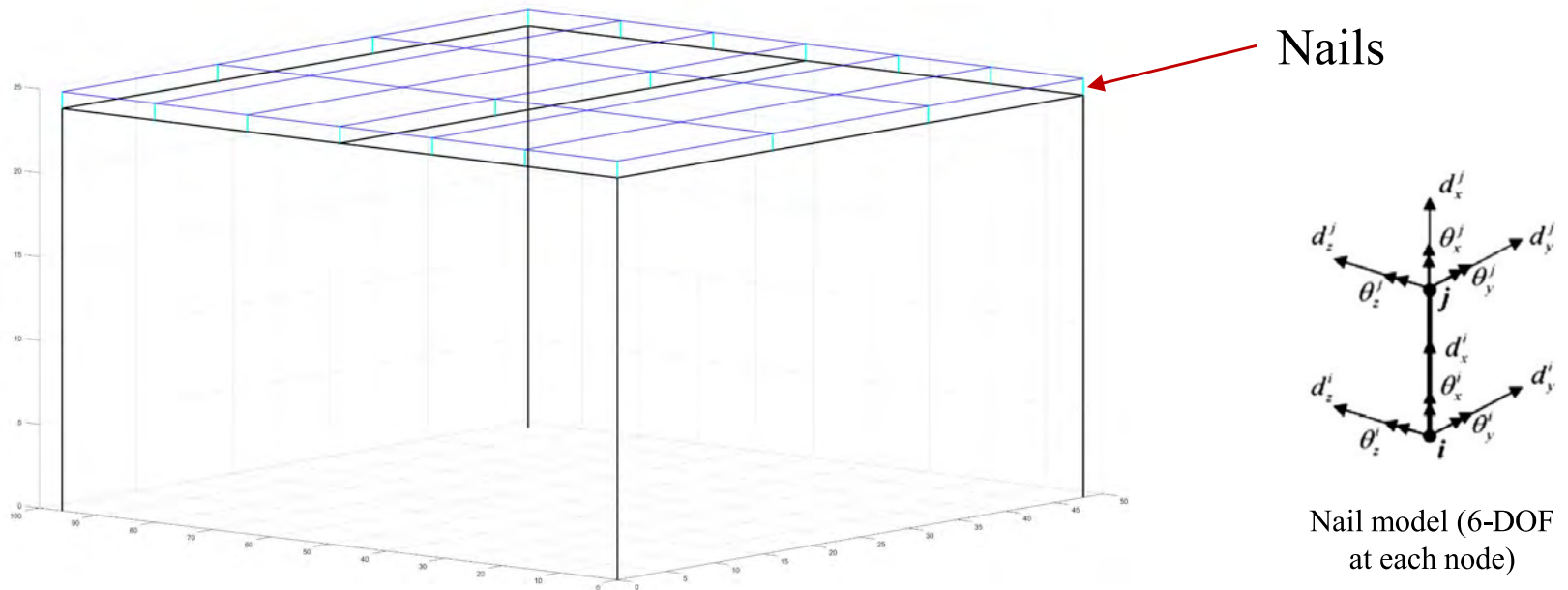
$$r_3 = r_3^{\delta u} \left( \frac{\delta_u}{\delta_{max}} \right)^\gamma$$

Dao and van de Lindt (2013)

- Modification needed for wind load application.
- For now, without connection test data, we are using hysteresis model from seismic application.

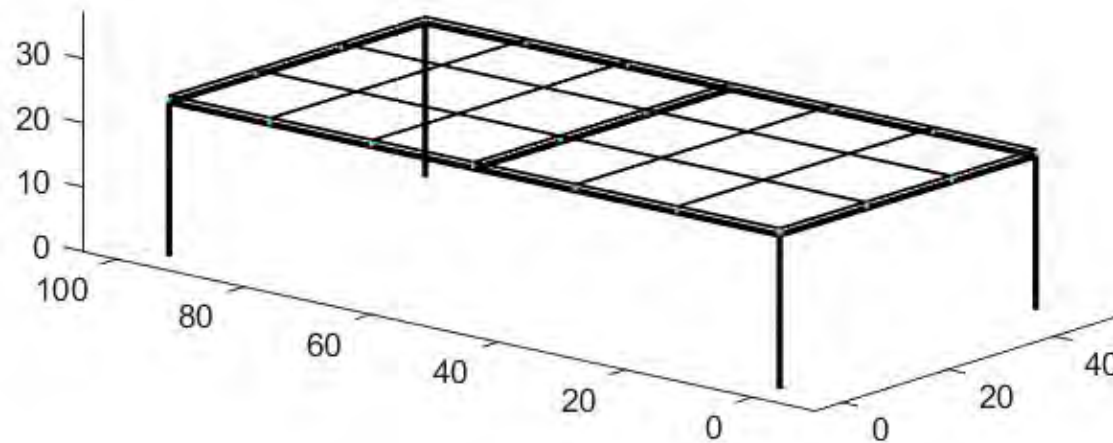


# Modeling Concept

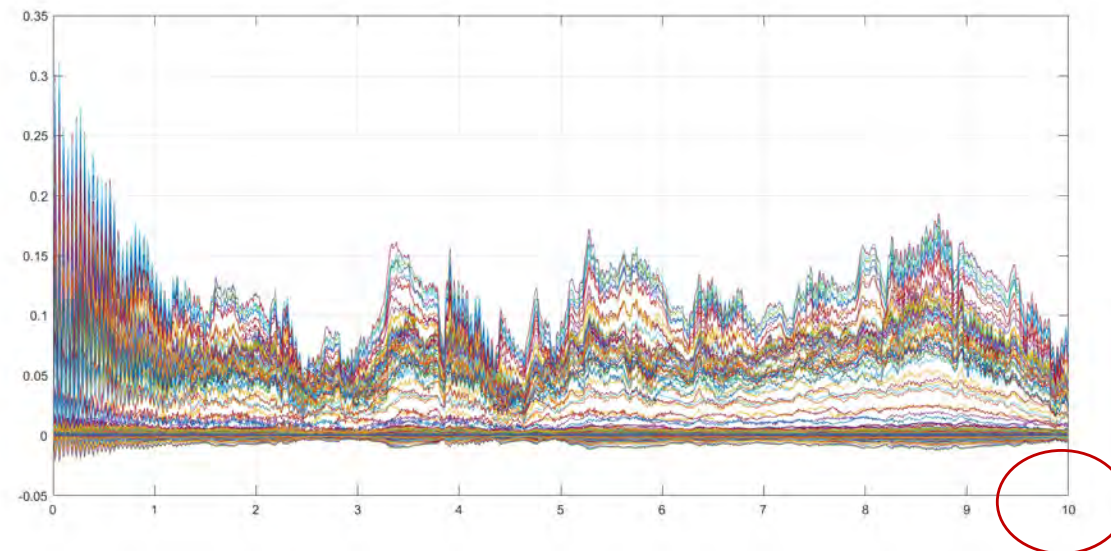
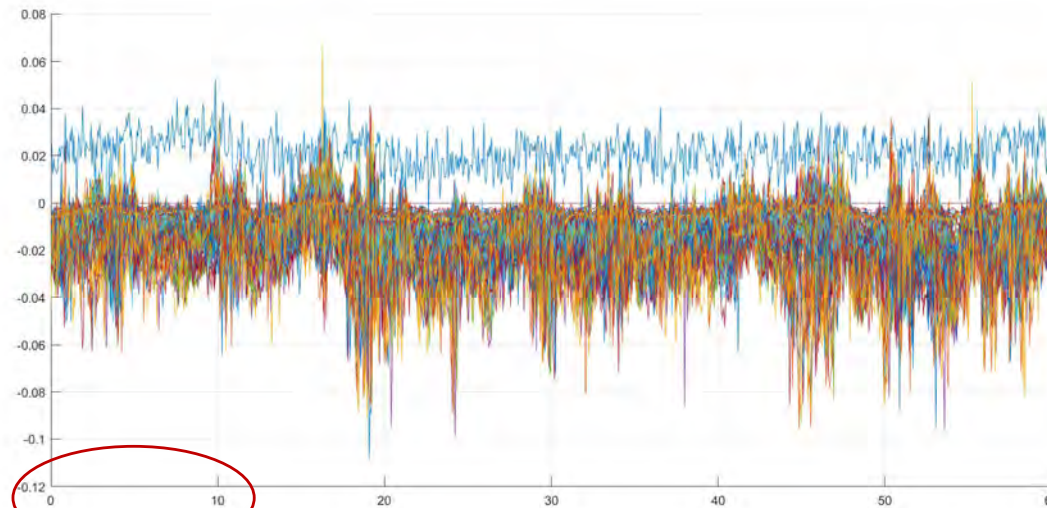


- FE model with single roof sheathing (4ft by 8ft) to prove the concept.
- Single story frame: 2x4 (beams) and 4x4 (columns).
- Plate elements (roof sheathing); beam elements (beams and columns).
- Nonlinear spring elements (nail connectors).

# Results (Soft-Frame): Video



# Results (Time-History Input & Response)



# Notes on Results

- Wind load time-history data at the nodes on the roof sheathing.
- Weight of sheathing is very light, so the sheathing has a high frequency, as seen from the time-history response.
- Because of high freq. (many cycles), we are looking at long-term damage, possible follow-up study on fatigue behavior at the connections.
- The time-history data used for this concept model is from a previous wind tunnel study. The new data from FIU is being processed.